

**The Pennsylvania State University**  
**The Graduate School**  
**College of Engineering**

**ACTIVE AND PASSIVE TECHNIQUES FOR TILTROTOR**  
**AEROELASTIC STABILITY AUGMENTATION**

A Thesis in  
Aerospace Engineering  
by  
Eric L. Hathaway

© 2005 Eric L. Hathaway

Submitted in Partial Fulfillment  
of the Requirements  
for the Degree of

Doctor of Philosophy

August 2005

The thesis of Eric L. Hathaway was reviewed and approved\* by the following:

Farhan Gandhi  
Associate Professor of Aerospace Engineering  
Thesis Adviser  
Chair of Committee

Edward C. Smith  
Professor of Aerospace Engineering

Joseph F. Horn  
Assistant Professor of Aerospace Engineering

Christopher D. Rahn  
Professor of Mechanical Engineering

George A. Lesieutre  
Professor of Aerospace Engineering  
Head of the Department of Aerospace Engineering

\*Signatures are on file in the Graduate School.

# Abstract

Tiltrotors are susceptible to whirl flutter, an aeroelastic instability characterized by a coupling of rotor-generated aerodynamic forces and elastic wing modes in high speed airplane-mode flight. The conventional approach to ensuring adequate whirl flutter stability will not scale easily to larger tiltrotor designs. This study constitutes an investigation of several alternatives for improving tiltrotor aerolastic stability. A whirl flutter stability analysis is developed that does not rely on more complex models to determine the variations in crucial input parameters with flight condition. Variation of blade flap and lag frequency, and pitch-flap, pitch-lag, and flap-lag couplings, are calculated from physical parameters, such as blade structural flap and lag stiffness distribution (inboard or outboard of pitch bearing), collective pitch, and precone. The analysis is used to perform a study of the influence of various design parameters on whirl flutter stability. While previous studies have investigated the individual influence of various design parameters, the present investigation uses formal optimization techniques to determine a unique combination of parameters that maximizes whirl flutter stability. The optimal designs require only modest changes in the key rotor and wing design parameters to significantly increase flutter speed. When constraints on design parameters are relaxed, optimized configurations are obtained that allow large values of kinematic pitch-flap ( $\delta_3$ ) coupling without degrading aeroelastic stability. Larger values of  $\delta_3$  may be desirable for advanced tiltrotor configurations. An investigation of active control of wing flaperons for stability augmentation is also conducted. Both stiff- and soft-inplane tiltrotor configurations are examined. Control systems that increase flutter

speed and wing mode sub-critical damping are designed while observing realistic limits on flaperon deflection. The flaperon is shown to be particularly effective for increasing wing vertical bending mode damping. Controller designs considered include gain scheduled full-state feedback optimal control, constant gain full-state controllers derived from the optimal controllers, and single-state feedback systems. The dominant feedback parameters in the optimal control systems are identified and examined to gain insight into the most important feedback paths that could be exploited by simpler reduced-order controllers.

# Contents

<b>List of Figures</b>	<b>ix</b>
<b>List of Tables</b>	<b>xviii</b>
<b>List of Symbols</b>	<b>xix</b>
<b>Dedication</b>	<b>xxi</b>
<b>Acknowledgments</b>	<b>xxii</b>
<b>1 Introduction</b>	<b>1</b>
1.1 Overview of tiltrotor aeroelastic and aeromechanical stability research . . .	3
1.2 Influence of passive design parameters on tiltrotor stability . . . . .	11
1.3 Application of active control to tiltrotor aircraft . . . . .	14
1.4 Summary . . . . .	17
<b>2 Objectives of Present Research</b>	<b>35</b>
2.1 Development of simple tiltrotor stability analysis . . . . .	35
2.2 Optimization of passive design parameters . . . . .	37
2.3 Active control of wing flaperons for stability augmentation . . . . .	38

<b>3</b>	<b>Description of Present Analysis</b>	<b>40</b>
3.1	Overview of formulation . . . . .	40
3.1.1	Aerodynamics . . . . .	42
3.1.2	Assembling rotor/wing equations . . . . .	44
3.2	Validation . . . . .	45
3.2.1	XV-15 . . . . .	45
3.2.2	Boeing Model 222 . . . . .	46
3.2.3	1/5-scale V-22 aeroelastic model . . . . .	46
3.2.4	WRATS model . . . . .	47
3.2.5	WRATS Semi-Articulated, Soft-Inplane rotor model . . . . .	48
3.3	Influence of unique model features . . . . .	50
3.3.1	Structural flap-lag coupling . . . . .	50
3.3.2	Gimbal/Blade flapping degrees of freedom . . . . .	54
3.3.3	Modeling blade pitch-flap and pitch-lag coupling . . . . .	56
3.4	Summary . . . . .	63
<b>4</b>	<b>Optimization of Rotor and Wing Design Parameters</b>	<b>86</b>
4.1	Wing model . . . . .	87
4.2	Parametric study . . . . .	88
4.2.1	Influence of individual rotor design parameters . . . . .	88
4.2.2	Influence of individual wing design parameters . . . . .	93
4.3	Parametric optimization . . . . .	95
4.3.1	Selection of objective function . . . . .	96
4.3.2	Optimization of rotor parameters . . . . .	99
4.3.3	Optimization of wing parameters . . . . .	102
4.3.4	Concurrent wing/rotor optimization . . . . .	105

<b>5</b>	<b>Active Control of Wing Flaperons for Stability Augmentation</b>	<b>127</b>
5.1	Flaperon active control formulation . . . . .	128
5.1.1	Limits on control gains . . . . .	130
5.1.2	Wing unsteady aerodynamic modeling . . . . .	131
5.2	Optimal Control Results . . . . .	135
5.2.1	XV-15 . . . . .	136
5.2.2	Model 222 . . . . .	137
5.3	Influence of Unsteady Aerodynamics . . . . .	138
5.4	Full-State Constant Gain Controller . . . . .	141
5.5	Effect of Rotor Speed on Flaperon Control . . . . .	142
5.6	Investigation of Key Feedback Parameters . . . . .	143
<b>6</b>	<b>Conclusions</b>	<b>162</b>
6.1	Optimization of rotor and wing design parameters . . . . .	163
6.2	Active control of wing flaperons . . . . .	165
6.3	Recommendations for future work . . . . .	167
6.3.1	Model Correlation . . . . .	167
6.3.2	Passive Design Optimization . . . . .	168
6.3.3	Active Control . . . . .	168
6.3.4	Active–Passive Hybrid Optimization . . . . .	170
	<b>Bibliography</b>	<b>171</b>
	<b>Appendix A. Analytical Model</b>	<b>179</b>
A.1	Degrees of Freedom . . . . .	179
A.2	Acceleration of a Point on the Blade . . . . .	180
A.3	Rotor Equations of Motion . . . . .	182
A.3.1	Blade flapping equations . . . . .	182
A.3.2	Blade lead-lag equations . . . . .	184

A.4	Blade Root Loads – Inertial Contribution . . . . .	186
A.5	Rotor Hub Loads – Inertial Components . . . . .	187
A.6	Rotor Aerodynamics . . . . .	189
A.6.1	Introduction . . . . .	189
A.6.2	Section aerodynamic forces . . . . .	189
A.6.3	Rotor aerodynamic forces and moments . . . . .	191
A.7	Gimbal/Rotor Speed Degrees of Freedom . . . . .	197
A.8	Rotor Equations of Motion . . . . .	198
A.9	Wing Models . . . . .	211
A.9.1	FEM wing structural model . . . . .	211
A.9.2	FEM wing aerodynamics . . . . .	218
A.9.3	FEM Wing assembly and pylon inertial contribution . . . . .	224
A.9.4	Modal wing representation . . . . .	225
A.10	Wing/Rotor Coupling . . . . .	227
<b>Appendix B. Wing Unsteady Aerodynamic Model</b>		<b>229</b>
B.1	Generating RFA model from frequency-domain data . . . . .	229
B.1.1	Optimal pole placement to improve fit . . . . .	233
B.1.2	Results of RFA fitting process . . . . .	234
B.2	Integration of RFA aero model with FEM wing . . . . .	234
B.2.1	Conversion to time domain . . . . .	235
B.2.2	Numerical integration across span of wing elements . . . . .	236



# List of Figures

1.1	The Bell/Boeing V-22 Osprey tiltrotor aircraft . . . . .	19
1.2	The Bell Eagle Eye tiltrotor UAV . . . . .	20
1.3	The Bell/Agusta BA-609 civilian tiltrotor . . . . .	21
1.4	Effect of Lag Frequency on Hub Loads (from Ref. 4) . . . . .	22
1.5	The Lockheed Electra turboprop airliner . . . . .	22
1.6	Simple propeller model used to validate analysis of Ref. 8 . . . . .	23
1.7	Pitch and Yaw Stiffness Required for Neutral Whirl Flutter Stability (from Ref. 7) . . . . .	24
1.8	Transcendental Model 1-G (from Ref. 10) . . . . .	25
1.9	Transcendental Model 2 (from Ref. 10) . . . . .	25
1.10	First flight of Bell XV-3 tiltrotor research aircraft, August 11, 1955 (from Ref. 10) . . . . .	26
1.11	Later configuration of XV-3 in airplane mode flight (from Ref. 10) . . . . .	27
1.12	XV-3 in the NASA Ames Research Center 40- by 80- ft. wind tunnel (from Ref. 10) . . . . .	28
1.13	Proprotor Whirl Flutter: Origin of destabilizing aerodynamic force (from Ref. 11) . . . . .	29
1.14	Bell Model 300 rotor in the Ames 40- by 80-ft wind tunnel (from Ref. 10) . . . . .	30
1.15	Boeing Model 222 rotor in the Ames 40- by 80-ft wind tunnel (from Ref. 10) . . . . .	31
1.16	XV-15 Tiltrotor Research Aircraft in hover . . . . .	32

1.17	WRATS wind tunnel model in NASA Langley TDT (from Ref. 39) . . . . .	33
1.18	Bell semi-articulated soft-inplane rotor installed on WRATS model (from Ref. 43) . . . . .	34
3.1	Degrees of freedom at hub attachment point . . . . .	70
3.2	Gimbal and blade flapping degrees of freedom . . . . .	70
3.3	Rotor azimuthal position and blade lead-lag degrees of freedom . . . . .	71
3.4	Semi-span XV-15 – Damping of wing vertical bending mode vs. airspeed .	71
3.5	Semi-span XV-15 – Damping of wing chordwise bending mode vs. airspeed	72
3.6	Semi-span XV-15 – Damping of wing torsion mode vs. airspeed . . . . .	72
3.7	Boeing Model 222 – Damping of wing vertical bending mode vs. airspeed .	73
3.8	Boeing Model 222 – Damping of wing chordwise bending mode vs. airspeed	73
3.9	Boeing Model 222 – Damping of wing torsion mode vs. airspeed . . . . .	74
3.10	1/5-scale V-22 model – Damping of wing vertical bending mode vs. air- speed (85% RPM, on-downstop, air) . . . . .	74
3.11	1/5-scale V-22 model – Damping of wing chordwise bending mode vs. airspeed (85% RPM, on-downstop, air) . . . . .	75
3.12	WRATS model – Damping of wing vertical bending mode vs. airspeed (742 RPM, off-downstop, air) . . . . .	75
3.13	WRATS model – Damping of wing vertical bending mode vs. airspeed (888 RPM, off-downstop, air) . . . . .	76
3.14	WRATS model – Damping of wing vertical bending mode vs. airspeed (770 RPM, on-downstop, air) . . . . .	76
3.15	WRATS model – Damping of wing vertical bending mode vs. airspeed (888 RPM, on-downstop, air) . . . . .	77
3.16	WRATS SASIP model – Damping of wing vertical bending mode vs. air- speed (550 RPM, on-downstop, air) . . . . .	77
3.17	WRATS SASIP model – Damping of wing vertical bending mode vs. air- speed (550 RPM, off-downstop, air) . . . . .	78

3.18	WRATS SASIP model – Damping of wing vertical bending mode vs. air-speed (742 RPM, on-downstop, air) . . . . .	78
3.19	WRATS SASIP model – Damping of wing vertical bending mode vs. air-speed (742 RPM, off-downstop, air) . . . . .	79
3.20	Arrangement of springs used to model blade Structural Flap Lag-Coupling (SFLC) . . . . .	79
3.21	Influence of blade Structural Flap-Lag Coupling (SFLC) on damping of wing vertical bending mode . . . . .	80
3.22	Influence of blade Structural Flap-Lag Coupling (SFLC) on damping of wing chordwise bending mode . . . . .	80
3.23	Influence of blade Structural Flap-Lag Coupling (SFLC) on damping of wing torsion mode . . . . .	81
3.24	Variation of rotor low-frequency lag mode frequency (Curve-fit variation of lag frequency from the rigid blade analysis of Ref. 1) . . . . .	81
3.25	Variation of rotor cyclic and collective flap frequencies (Explicit cyclic and collective modal frequencies from Ref. 2) . . . . .	82
3.26	Blade flap and lag angles inboard and outboard of pitch bearing . . . . .	82
3.27	Definition of forces and moments contributing to blade pitch equation of motion . . . . .	83
3.28	Variation of effective pitch-flap and pitch-lag coupling parameters . . . . .	83
3.29	Influence of blade pitch modeling on damping of wing vertical bending mode	84
3.30	Influence of blade pitch modeling on damping of wing chordwise bending mode . . . . .	84
3.31	Influence of blade pitch modeling on damping of wing torsion mode . . . . .	85
4.1	Modal damping of baseline system (b: wing beam mode, c: wing chord mode, t: wing torsion mode, $\beta_0$ : rotor coning mode, $\zeta - 1, \zeta + 1$ : cyclic lag modes, $\beta - 1, \beta + 1$ : cyclic flap (gimbal) modes) . . . . .	111
4.2	Modal Damping of Baseline System, no couplings due to pitch dynamics . . . . .	111

4.3	Variation of pitch-flap and pitch-lag coupling parameters (due to flexibility outboard of the pitch bearing) for baseline system . . . . .	112
4.4	Influence of blade flatwise bending stiffness on flutter speed . . . . .	112
4.5	Influence of blade chordwise bending stiffness on flutter speed . . . . .	113
4.6	Effect of reduced chordwise bending stiffness on pitch-lag coupling due to blade flexibility distribution $\tilde{K}_{P\zeta}$ (Eq. (3.25)) . . . . .	113
4.7	Influence of gimbal spring stiffness on flutter speed . . . . .	114
4.8	Influence of $\delta_3$ angle (pitch-gimbal coupling) on flutter speed (Baseline $\delta_3 = 15^\circ$ ) . . . . .	114
4.9	Influence of additional pitch-flap coupling on flutter speed . . . . .	115
4.10	Influence of additional pitch-lag coupling on flutter speed . . . . .	115
4.11	Influence of distribution of blade flatwise bending flexibility on flutter speed (Baseline $R_\beta = 1$ ) . . . . .	116
4.12	Influence of reduced $R_\beta$ on couplings due to blade flexibility distribution (Baseline $R_\beta = 1$ ) . . . . .	116
4.13	Influence of distribution of blade chordwise bending flexibility on flutter speed (Baseline $R_\zeta = 1$ ) . . . . .	117
4.14	Influence of control system stiffness on flutter speed . . . . .	117
4.15	Influence of wing vertical bending stiffness on flutter speed . . . . .	118
4.16	Influence of wing torsional stiffness on flutter speed . . . . .	118
4.17	Influence of wing chordwise bending stiffness on flutter speed . . . . .	119
4.18	Influence of wing vertical bending-torsion coupling on flutter speed . . . . .	119
4.19	Influence of wing chordwise bending-torsion coupling on flutter speed . . . . .	120
4.20	Illustration of two-stage optimization algorithm . . . . .	120
4.21	Rotor Optimization: Maximize damping from 200 to 500 kts (tight constraints) . . . . .	121
4.22	Rotor Optimization: Maximize damping from 200 to 500 kts (medium constraints) . . . . .	121

4.23	Rotor Optimization: Maximize damping from 200 to 500 kts (relaxed constraints)	122
4.24	Rotor Optimization: Variation of pitch-flap and pitch-lag couplings due to distribution of blade flexibility	122
4.25	Wing design optimization: Optimization unable to improve beam mode damping, due to chord mode and torsion mode instabilities at high speeds	123
4.26	Wing Optimization: Maximize damping from 200 to 300 kts (tight constraints)	123
4.27	Wing Optimization: Maximize damping from 200 to 300 kts (medium constraints)	124
4.28	Wing Optimization: Maximize damping from 200 to 300 kts (relaxed constraints)	124
4.29	Concurrent Wing/Rotor Optimization: Maximize damping from 200 to 500 kts (tight constraints)	125
4.30	Concurrent Wing/Rotor Optimization: Maximize critical flutter speed (tight constraints)	125
4.31	Concurrent Wing/Rotor Optimization: Maximize critical flutter speed (tight constraints, key parameters only)	126
5.1	XV-15: Modal damping vs. airspeed for uncontrolled system (b: wing beam mode, c: wing chord mode, t: wing torsion mode, $\beta_0$ : rotor coning mode, $\zeta - 1, \zeta + 1$ : cyclic lag modes, $\beta + 1$ : cyclic flap (gimbal) mode)	147
5.2	XV-15: Modal damping vs. airspeed with optimal wing flaperon control (flaperon deflection limit reached at 420 kts).	147
5.3	XV-15: LQR optimal controller gains	148
5.4	Model 222: Modal damping vs. airspeed for uncontrolled system (b: wing beam mode, c: wing chord mode, t: wing torsion mode, $\beta_0$ : rotor coning mode, $\zeta - 1, \zeta + 1$ : cyclic lag modes, $\beta - 1, \beta + 1$ : cyclic flap modes)	148

5.5	Model 222: Modal damping vs. airspeed with optimal wing flaperon control ( $\beta + 1$ mode reaches zero damping at 412 kts.) . . . . .	149
5.6	Model 222: LQR optimal controller gains . . . . .	149
5.7	XV-15: Modal damping vs. airspeed for uncontrolled system, including unsteady aerodynamic model . . . . .	150
5.8	XV-15: Modal damping vs. airspeed with optimal wing flaperon control and unsteady aerodynamics (flaperon deflection limit reached at 420 kts). . . . .	150
5.9	XV-15: LQR optimal controller gains when unsteady aerodynamic effects are included . . . . .	151
5.10	XV-15: Time history of wingtip vertical displacement and flaperon deflection, response to initial disturbance of wing vertical bending mode, quasi-steady aerodynamic model, airspeed = 350 knots . . . . .	151
5.11	XV-15: Time history of wingtip vertical displacement and flaperon deflection, response to initial disturbance of wing vertical bending mode, unsteady aerodynamic effects included, airspeed = 350 knots . . . . .	152
5.12	Model 222: Modal damping vs. airspeed for uncontrolled system, including unsteady aerodynamic model . . . . .	152
5.13	Model 222: Modal damping vs. airspeed with optimal wing flaperon control and unsteady aerodynamics ( $\beta + 1$ mode reaches zero damping at 412 kts.) . . . . .	153
5.14	Model 222: LQR optimal controller gains when unsteady aerodynamic effects are included . . . . .	153
5.15	XV-15: Modal damping vs. airspeed for wing flaperon control with unsteady aerodynamics, controller gains obtained using quasi-steady aero model	154
5.16	Model 222: Modal damping vs. airspeed for wing flaperon control with unsteady aerodynamics, controller gains obtained using quasi-steady aero model . . . . .	154

5.17	XV-15: Modal damping vs. airspeed for wing flaperon actuation with constant gains (optimally determined at 380 kts and 458 RPM) – rotor speed = 458 RPM (cruise) . . . . .	155
5.18	Model 222: Modal damping vs. airspeed for wing flaperon actuation with constant gains (optimally determined at 380 kts and 386 RPM) – rotor speed = 386 RPM (cruise) . . . . .	155
5.19	XV-15: Modal damping vs. airspeed for uncontrolled system – rotor speed = 565 RPM (hover) . . . . .	156
5.20	XV-15: Modal damping vs. rotor speed for uncontrolled system – airspeed = 380 kts . . . . .	156
5.21	XV-15: Modal damping vs. airspeed for wing flaperon actuation with constant gains (optimally determined at 380 kts and 458 RPM) – rotor speed = 565 RPM (hover) . . . . .	157
5.22	XV-15: Modal damping vs. rotor speed for wing flaperon actuation with constant gains (optimally determined at 380 kts and 458 RPM) – airspeed = 380 kts . . . . .	157
5.23	XV-15: Modal damping vs. airspeed for wing flaperon actuation with constant gains (optimally determined at 380 kts and 565 RPM) – rotor speed = 565 RPM (hover) . . . . .	158
5.24	XV-15: Modal damping vs. airspeed for wing flaperon actuation with constant gains (optimally determined at 380 kts and 565 RPM) – rotor speed = 458 RPM (cruise) . . . . .	158
5.25	XV-15: Modal damping vs. rotor speed for wing flaperon actuation with constant gains (optimally determined at 380 kts and 565 RPM) – airspeed = 380 kts . . . . .	159
5.26	Model 222: Modal damping vs. airspeed for wing flaperon actuation with constant gains (optimally determined at 380 kts and 386 RPM) – rotor speed = 551 RPM (hover) . . . . .	159

5.27	XV-15: Influence of rate feedback of wing vertical bending motion on flutter speed . . . . .	160
5.28	XV-15: Influence of position feedback of wing vertical bending motion on flutter speed . . . . .	160
5.29	XV-15: Influence of rate feedback of wing chordwise bending motion on flutter speed . . . . .	161
5.30	XV-15: Influence of position feedback of wing chordwise bending motion on flutter speed . . . . .	161
B.1	Velocity distributions corresponding to the generalized airfoil and flap motions used in unsteady aerodynamics formulation . . . . .	242
B.2	Comparison of state-space RFA model to frequency-domain aerodynamic model, coefficient of lift due to $W_0$ . . . . .	242
B.3	Comparison of state-space RFA model to frequency-domain aerodynamic model, coefficient of lift due to $W_1$ . . . . .	243
B.4	Comparison of state-space RFA model to frequency-domain aerodynamic model, coefficient of lift due to $D_0$ . . . . .	243
B.5	Comparison of state-space RFA model to frequency-domain aerodynamic model, coefficient of lift due to $D_1$ . . . . .	244
B.6	Comparison of state-space RFA model to frequency-domain aerodynamic model, pitching moment coefficient due to $W_0$ . . . . .	244
B.7	Comparison of state-space RFA model to frequency-domain aerodynamic model, pitching moment coefficient due to $W_1$ . . . . .	245
B.8	Comparison of state-space RFA model to frequency-domain aerodynamic model, pitching moment coefficient due to $D_0$ . . . . .	245
B.9	Comparison of state-space RFA model to frequency-domain aerodynamic model, pitching moment coefficient due to $D_1$ . . . . .	246
B.10	Comparison of state-space RFA model to frequency-domain aerodynamic model, hinge moment coefficient due to $W_0$ . . . . .	246



B.11 Comparison of state-space RFA model to frequency-domain aerodynamic model, hinge moment coefficient due to  $W_1$  . . . . . 247

B.12 Comparison of state-space RFA model to frequency-domain aerodynamic model, hinge moment coefficient due to  $D_0$  . . . . . 247

B.13 Comparison of state-space RFA model to frequency-domain aerodynamic model, hinge moment coefficient due to  $D_1$  . . . . . 248

# List of Tables

3.1	XV-15 Full-scale Test: Model Properties . . . . .	65
3.2	Boeing 222 Full-scale Test: Model Properties . . . . .	66
3.3	1/5-scale V-22 Model: Model Properties . . . . .	67
3.4	WRATS Model: Model Properties . . . . .	68
3.5	WRATS SASIP Model: Model Properties . . . . .	69
4.1	Design Parameters – Nominal Values for full-scale XV-15 semispan model	108
4.2	Constraints on Design Parameters . . . . .	109
4.3	Rotor Parameter Optimization Results . . . . .	109
4.4	Wing Parameter Optimization Results . . . . .	110
4.5	Concurrent Wing/Rotor Parameter Optimization Results . . . . .	110
B.1	RFA model curve-fit results . . . . .	241

# List of Symbols

$b$	Wing vertical bending mode
$c$	Wing chordwise bending mode, wing chord length
$c_{l\alpha}$	Lift curve slope
$I_b$	Moment of inertia of blade about gimbal
$I_\beta$	Moment of inertia of blade about flap hinge
$I_{\beta\alpha}$	Inertial coupling of blade flap and hub/gimbal motion: $I_{\beta\alpha} = \int_0^R mr(r - e)dr$
$I_\theta$	Blade sectional moment of inertia about pitch axis
$I_\zeta$	Moment of inertia of blade about lag hinge
$I_{\zeta\alpha}$	Inertial coupling of blade lag and hub/gimbal motion
$K_{Pq1}$	Wing beam-torsion coupling parameter
$K_{Pq2}$	Wing chord-torsion coupling parameter
$K_{PG}$	Pitch-gimbal coupling parameter
$K_{P\beta}$	Pitch-flap coupling parameter
$K_{P\zeta}$	Pitch-lag coupling parameter
$K_\beta$	Blade flap stiffness
$K_\zeta$	Blade lag stiffness
$k$	Reduced frequency of airfoil oscillation: ( $= \frac{\omega c}{V}$ )
$m$	Blade sectional mass
$R$	Rotor radius

$r$	Radial position on blade
$R_\beta, R_\zeta$	Structural flap-lag coupling parameters
$S_\beta$	First mass moment of inertia about flap hinge
$S_\zeta$	First mass moment of inertia about lag hinge
$t$	Wing torsion mode
$x, y, z$	Translational degrees of freedom of wing at hub attachment point
$\alpha_x, \alpha_y, \alpha_z$	Rotational degrees of freedom of wing at hub attachment point
$\beta$	Blade flapping degree of freedom
$\beta_G$	Gimbal degree of freedom
$\beta_P$	Rotor precone
$\delta$	Flaperon deflection
$\phi$	Blade rigid pitch degree of freedom
$\zeta$	Blade lead-lag degree of freedom
$v_\beta$	Non-dimensional rotating flap frequency: $v_\beta^2 = 1 + \frac{S_\beta}{I_\beta} \frac{e}{R-e} + \frac{K_{\beta\beta}}{I_\beta \Omega^2}$
$v_\zeta$	Non-dimensional rotating lag frequency: $v_\zeta^2 = \frac{S_\zeta}{I_\zeta} \frac{e}{R-e} + \frac{K_{\zeta\zeta}}{I_\zeta \Omega^2}$
$\psi_s$	Rotor azimuthal perturbation degree of freedom
$\Omega$	Rotor rotational speed
$\omega_{\beta 0}$	Non-rotating blade fundamental flap frequency
$\omega_{\zeta 0}$	Non-rotating blade fundamental lag frequency
$\omega_{\beta G 0}$	Non-rotating gimbal frequency
$\omega_\phi$	Non-rotating blade pitch frequency (due to control system stiffness)
$\omega_{q1}$	Wing vertical bending mode frequency
$\omega_{q2}$	Wing chordwise bending mode frequency
$\omega_p$	Wing torsion mode frequency
$( )^*$	$( )$ non-dimensionalized by $I_b$
$\dot{( )}$	$\frac{d( )}{dt}$
$\dot{( )}^*$	$\frac{d( )}{d\psi}$

# Dedication

This thesis is dedicated to my wife Carolyn and daughter Danielle. Their love and patience provided me the support necessary to see this work through to its conclusion.

# Acknowledgments

I must acknowledge my fellow Penn State Rotorcraft Center graduate students, for all the help and camaraderie they provided me over the years. I will always look back on my time at Penn State with fondness.

I would like to thank Dr. Mark Nixon of the U.S. Army Vehicle Technology Directorate, for his support of this research in the form of helpful technical discussions, assistance with obtaining input data, and especially for providing me the opportunity to participate in the 2002 wind tunnel test of the WRATS SASIP model. Participating in the test greatly enriched and complemented my own research experience. Thanks also to Dave Piatak, NASA Langley Research Center, and Tom Parham and Dr. Richard Bennett, Bell Helicopter Textron, Inc., for their advice and for their help providing me with WRATS model parameters. I am grateful to Rupinder Singh for his assistance in preparing some of the active control results presented here.

Thanks are also due to the members of my Doctoral Committee, Drs. Gandhi, Smith, Horn, and Rahn, for their time spent reviewing my research, and for their helpful comments and suggestions.

Finally, I would like to acknowledge the support and guidance I have received over the years from my advisor, Dr. Farhan Gandhi. It was his encouragement and enthusiasm for the subject that led me to the rotorcraft field as an undergraduate.

This research was funded by the NRTC under the Penn State Rotorcraft Center of Excellence program, with Dr. Yung Yu as technical monitor.

# Chapter 1

## Introduction

Tiltrotor aircraft combine the vertical take-off and landing capability of a helicopter with the speed and range of a conventional fixed-wing aircraft. After nearly fifty years of research and development, these unique flying vehicles are on the verge of full-scale production. The Bell/Boeing V-22 Osprey (Fig. 1.1) appears to have overcome its development problems and is ready to enter service with the U.S. armed forces. The Eagle Eye tiltrotor (Fig. 1.2), an unmanned aerial vehicle (UAV) developed by Bell, has been selected as a reconnaissance platform for the U.S. Coast Guard. The first tiltrotor designed for the civilian market has just recently entered flight test. Figure 1.3 is a picture of the first flight of the Bell-Agusta 609.

Despite their successful development, tiltrotors suffer from several aeroelastic and aeromechanical stability problems that must be overcome in order to achieve increased performance in future designs. In high speed airplane-mode flight, tiltrotors are susceptible to whirl flutter, an aeroelastic instability characterized by a coupling of rotor-generated aerodynamic forces and elastic wing modes. The conventional approach to ensuring adequate whirl flutter stability margins requires wing structures with very high torsional stiffness [3]. This stiffness requirement leads to rather thick wing sections, typically about a 23% thickness to chord ratio for current tiltrotor aircraft. The large aerodynamic drag associated with

such thick wing sections is an obstacle to achieving the higher cruise speeds envisioned for future tiltrotor aircraft. The conventional design approach will also not easily scale to larger vehicles, such as the Quad-Tiltrotor configuration currently being proposed by Bell Helicopters. The weight and loads penalties associated with high-stiffness wing structures and stiff-inplane rotors would be considerable for a large heavy-lift tiltrotor configuration. It is therefore desirable to explore alternative methods for providing the required aeroelastic stability margins.

Currently, all successful tiltrotor designs have featured stiff-inplane rotors, where the frequency of the first inplane blade bending mode is greater than the nominal rotor speed. Soft-inplane rotors, which are commonly used on conventional helicopters, are being considered for future tiltrotors [4]. Use of a soft-inplane rotor results in reduced dynamic blade loads (see Fig. 1.4), presenting the opportunity for reduced structural weight. Improving rotor performance by increasing the number of blades may also require a soft-inplane rotor design, since weight and geometry constraints make designing a stiff-inplane rotor with more than three blades difficult. A soft-inplane tiltrotor, however, is vulnerable to aeromechanical instabilities akin to helicopter ground or air resonance. Stiff-inplane rotors are inherently free from such instabilities. Before soft-inplane rotor designs may be used on future tiltrotor aircraft, a thorough understanding of their aeromechanical stability characteristics must be developed.

Due to the destructive nature of these instabilities, it is critical that tiltrotor designers ensure adequate aeroelastic and aeromechanical stability margins. To this end, accurate tiltrotor stability analyses are essential. The mechanism of tiltrotor whirl flutter instability has received considerable experimental and analytical attention. Perturbation aerodynamic forces generated on the rotor act on the wing/pylon support structure, exciting wing motions which in turn are fed back to the rotor. As airspeed increases, the magnitude of the destabilizing aerodynamic forces also increases, until an instability is encountered at some critical flutter speed. The complex interaction of rotor and wing degrees of freedom may be influenced by many different design parameters. Numerous studies have investigated



the influence of various rotor and wing design parameters on whirl flutter stability.

This chapter will present a historical overview of tiltrotor aeroelastic and aeromechanical stability research. Through wind tunnel and flight tests, an understanding of the underlying causes of instability, along with improved analytical modeling capabilities, has been developed. Important passive design parameters which can influence stability characteristics have been identified and studied. A survey of more recent efforts to further improve tiltrotor stability through the use of active control techniques will also be provided.

## **1.1 Overview of tiltrotor aeroelastic and aeromechanical stability research**

The potential for an instability involving pitching and yawing motions of a propeller-nacelle combination was first pointed out by Taylor and Browne [5] in a study of vibration isolation of aircraft engines. Nacelle pitch angles relative to the free stream cause angle-of-attack variations around the propeller disk, producing aerodynamic yawing moments on the propeller, while nacelle yaw angles similarly produce pitching moments. This creates the possibility for an unstable “backwards” (opposite the direction of propeller rotation) whirling motion of the propeller/nacelle combination. Taylor and Browne noted that for typical aircraft designs of the period (the late 1930’s), such an instability would not occur.

Twenty years later, with the advent of high-speed, thin-winged turboprop-powered aircraft, the theoretical stability problem noted by Taylor and Brown became a reality. On October 29, 1959, a Lockheed Electra, a turboprop-powered airliner (Fig. 1.5), broke up in mid-air, killing all aboard. A second Electra was lost a few months later, on March 17, 1960. Initial accident investigations by Lockheed and the Civil Aeronautics Board (precursor to today’s NTSB) could not determine a cause for the accidents. Lockheed and NASA researchers began an exhaustive investigation. Through analytical studies and wind tunnel testing at NASA Langley Research Center, propeller/nacelle whirl flutter was identified as

the probable cause of the accidents. It was determined that damage to the engine support structure of an outboard engine nacelle allowed a whirl mode instability which destabilized the wing vertical bending mode, causing failure of the wing structure. See Refs. 6 and 7 for more details of the Electra crash investigation.

The unexpected encounter with whirl flutter on the Electra sparked further research to better understand the design requirements to ensure adequate propeller/nacelle stability. In Ref. 8, Houbolt and Reed investigated the influence of various design parameters on whirl flutter stability. Their analytical studies were validated with wind tunnel tests of simple propeller models (Fig. 1.6). Nacelle support stiffness and damping were found to have the largest influence on stability. By independently varying the nacelle pitch and yaw stiffness, stability boundaries such as the plot shown in Fig. 1.7 were calculated. To ensure stability even with a reduction in pitch or yaw stiffness due to damage (as in the case of the Electra), the design pitch and yaw stiffness should be placed beyond the “peak” of the flutter stability boundary. Small amounts of pitch and yaw damping can greatly reduce the level of stiffness required to ensure stability. An increase in airspeed requires increased nacelle stiffness to maintain stability. An overview and summary of the problem of propeller whirl flutter instability is provided in Ref. 9.

At the same time research was being done on propeller/nacelle whirl flutter, there was increased interest in the related problem of whirl flutter stability for tiltrotors, as a result of flight test experience with the Bell XV-3 tiltrotor research aircraft. Reference 10 provides an excellent historical overview of early tiltrotor flight test efforts. Early experimental tiltrotor aircraft, such as the Transcendental Model 1-G (see Fig. 1.8) and Model 2 (Fig. 1.9), were used primarily to investigate hover performance and, in the case of the Model 1-G, to explore the conversion flight regime. Stability problems related to whirl flutter were first encountered during flight testing of the XV-3. In its initial configuration (Fig. 1.10), the XV-3 featured three-bladed articulated rotors. From its first hover test on August 11, 1955, the XV-3 was plagued with rotor dynamic instability problems which led to high vibration levels and difficulty controlling the aircraft. On October 25, 1956,

during flight tests to expand the conversion envelope, the XV-3 experienced a severe rotor instability resulting in a crash that seriously injured the pilot. A period of redesign and testing resulted in a new two-bladed, stiff-inplane, teetering rotor system for the XV-3 (Fig. 1.11). These rotor design changes, along with external struts to stiffen the wings, gave the XV-3 sufficient stability to perform the first full conversion of a tiltrotor from hover to airplane mode on December 18, 1958. Subsequent airplane mode flight testing revealed problems with transient blade flapping during maneuvers and poor longitudinal stability at high speed.

In 1962, the XV-3 was tested in the 40- by 80-foot wind tunnel at NASA Ames Research Center (Fig. 1.12) to investigate the effects of changes in pitch-flap coupling (often expressed in terms of a “ $\delta_3$  angle”) on transient rotor flapping and high speed airplane mode stability. Coupling blade pitch changes to blade flapping was already known to have a powerful influence on rotor flapping response. During the course of this test, a rotor/pylon instability very much like propeller/nacelle whirl flutter was encountered [11]. The instability manifested itself as a low frequency, high amplitude limit cycle oscillation, with the rotor and pylon precessing in the direction opposite rotor rotation.

The experimental data provided by XV-3 wind tunnel and flight tests provided researchers with the information required to gain an understanding of the underlying mechanism of whirl flutter in tiltrotor aircraft, and to develop the first rotor/pylon stability analyses. In Ref. 11, Hall shows that the principal destabilizing factor for rotor/pylon whirl flutter is rotor inplane forces generated by precession of the rotor disk in space. A four degree of freedom analytical model containing pylon pitch and yaw and rotor lateral and longitudinal flapping was developed which captures the fundamental physical behavior. Figure 1.13 from Ref. 11 illustrates the origin of the destabilizing inplane force. Consider a rotor/pylon system with a nose-up pitching rate ( $\dot{\phi}_x$  in Fig. 1.13). Unlike a conventional propeller which is rigidly attached to its shaft and thus constrained to follow all shaft motion, the rotor is free to flap relative to the shaft and maintain its orientation in space (assuming only a small influence due to root restraint or hinge offset). The control plane of the rotor (defined by

the orientation of the swashplate) follows the pylon, introducing cyclic pitch changes which produce an azimuthal variation in lift on the rotor ( $\Delta L$  in Fig. 1.13). The out-of-plane component of this lift ( $\Delta T_1$ ) produces a net moment on the rotor disk which precesses the rotor to follow the pylon motion. For a rotor operating in a high inflow environment, the perturbations in section lift also have large inplane components ( $\Delta H_1$ ). For high inflow, these inplane forces sum to produce a net inplane hub force which is in phase with pylon pitch rate (in this example). This inplane hub force constitutes a negative damping of pylon motion. The magnitude of the destabilizing force increases with airspeed, so at some critical speed it will overcome the inherent aerodynamic and structural damping in the rotor/pylon system, and cause an instability.

Reference 11 found that increased pylon stiffness and damping are generally stabilizing (as is the case for propeller/nacelle whirl flutter), and increased  $\delta_3$  coupling is destabilizing. In Ref. 12, Young and Lytwyn investigated the influence of blade flapping restraint on tiltrotor aeroelastic stability. By examining static and dynamic stability trends, an optimal flapping frequency between 1.1 and 1.2/rev was determined. In Ref. 13 however, Wernicke and Gaffey pointed out that other design considerations such as allowable blade loads may preclude taking advantage of this ideal flap frequency. Edenborough in Ref. 14 extended the basic four degree of freedom stability analysis to include vertical displacement of the pylon to represent the influence of wing vertical bending. Successful validation was achieved between the stability predictions of the analysis and data from a second wind tunnel test of the XV-3, conducted in 1966. The analytical and experimental results confirmed that increased pylon stiffness is stabilizing, increased  $\delta_3$  is destabilizing, and increased flapping restraint is stabilizing. Similar trends were observed in the experimental and analytical work done by DeLarm in Ref. 15. Gaffey investigated in great detail the influence of pitch-flap coupling on both stability and rotor flapping response in Ref. 16. He found that while both positive and negative values of  $\delta_3$  were effective for reducing flap response, negative  $\delta_3$  (blade flap-up, pitch-up coupling) was preferable for a stiff-inplane rotor operating in high inflow, because positive  $\delta_3$  results in a flap-lag blade instability. Kaza showed in

Ref. 17 that the steady state coning angle and flap damping may also have an influence on stability.

While this fundamental research was still ongoing, Bell became involved in the U.S. Army's Composite Aircraft Program. Started in 1965, this program sought to develop the technology for a vehicle with the hovering capability of a helicopter and the high cruise speed of a fixed-wing aircraft. In support of this program, Bell designed the Model 266 tiltrotor [18], using experience gained with the XV-3 and subsequent research. At the conclusion of the program, an aeroelastic model of the Model 266 was given to NASA Langley Research Center. This model was tested in the Langley Transonic Dynamics Tunnel as part of a joint NASA/Bell study of tiltrotor dynamics, stability, and loads. Reference 3 details the results of this study and describes some of the issues and trade-offs that must be considered in a practical tiltrotor design. Extensive analytical and experimental research efforts continued at NASA Langley into the early 1970's, using several different aeroelastic wind tunnel models. Details of these investigations are reported by Kvaternik in Refs. 19–21. These studies proved invaluable in developing the expertise required to develop future tiltrotor aircraft. The influence on whirl flutter stability of some parameters not considered in previous analyses was identified and reported. Wing aerodynamics were shown to provide a small stabilizing influence. Also, blade inplane flexibility was shown to have a significant effect on stability. For accurate whirl flutter stability predictions, blade lag and elastic wing motion must be considered in stability analyses. Development of the analytical model used during the course of these investigations was continued and in later years it became known as PASTA (Proprotor Aeroelastic STability Analysis). A historical overview of all the tiltrotor aeroelastic stability research performed at NASA Langley during this period is included in Ref. 22

Meanwhile in the early 1970's, NASA contracted with both Boeing and Bell to develop new tiltrotor research aircraft. The rotor designed for the Bell Model 301 proposal (Fig. 1.14) featured a stiff-inplane gimbaled hub, typical of previous Bell tiltrotor designs, while the Boeing Model 222 rotor (Fig. 1.15) was a hingeless, soft-inplane design. In sup-

port of these design efforts, full scale tests of both the Bell rotor (Ref. 23) and the Boeing rotor (Ref. 24) were conducted on a semispan wing mounted in the NASA Ames 40- by 80-foot wind tunnel. These tests collected substantial amounts of data on rotor performance, loads, and vibration, as well as rotor/pylon/wing stability. A summary of results and correlation of analysis with test for the Bell rotor are provided in Ref. 25, and for the Boeing rotor in Ref. 26. The success of these tests were key in reducing the risk associated with development and construction of an actual research aircraft. In 1973, the Bell Model 301 was selected for construction as the XV-15 (Fig. 1.16). The XV-15 has enjoyed a long and successful career in flight test and as a tiltrotor technology demonstrator [10]. Reference 27 provides a detailed description of the XV-15.

The Boeing Model 222 rotor was the first soft-inplane tiltrotor design to receive significant analytical and experimental attention. During testing in the Ames wind tunnel, this rotor experienced an air resonance instability involving coupling of the wing vertical bending mode with the rotor low-frequency cyclic lag mode [24]. The instability only occurred at low airspeeds (less than 140 knots) and high rotor speed (about 550 RPM, whereas nominal airplane mode rotor speed was 386 RPM). As airspeed increased, aerodynamic damping in the rotor lag modes increased, alleviating the instability. Even at nominal rotor speeds, the low-airspeed damping of the wing vertical bending mode was marginal, often less than 1% of critical damping.

In Ref. 2, Johnson developed a comprehensive tiltrotor analysis and validated it against experimental data from the Bell and Boeing full scale rotor tests at Ames. The analysis included both blade flap and lag degrees of freedom. Gimbal motion was modelled by assigning a value of flap stiffness to the cyclic flapping degrees of freedom lower than that used for the collective flap degree of freedom. Likewise, a windmilling rotor condition was approximated by setting the stiffness in the collective lag mode to zero. A modal representation of the wing was used, with modal frequencies and mode shapes selected to match test data. The analysis was later extended in Ref. 28 to include coupled blade bending modes, blade torsion, and non-axial flow (to model helicopter and conversion mode operation). In

Ref. 29, Johnson discusses the influence of these modeling refinements on stability prediction. The combination of rotor control system flexibility and blade bending flexibility outboard of the pitch bearing was shown to introduce a destabilizing pitch-lag coupling. A stiffer control system, reduced rotor pre-cone, and increased flexibility inboard of the pitch bearing all act to reduce this coupling. The magnitude of this coupling must be correctly modeled to achieve accurate predictions of stability boundaries. In Ref. 30, engine, transmission, and rotor speed governor dynamics were added. The principal influence of drivetrain dynamics is on the antisymmetric wing modes, where the interconnect shaft acts as a spring on rotor speed. The stability analysis developed by Johnson in Refs. 2, 28–30 formed the basis for the tiltrotor modeling capability in CAMRAD [31], a comprehensive rotorcraft analysis code.

Reference 32 discussed aeroelastic stability data collected from actual XV-15 flight test. Correlation of the data with analytical predictions was good. Johnson points out however in Ref. 33 that the test data was collected far from any stability boundary. Stability data obtained in the vicinity of a stability boundary would provide a better test of the predictive capability of a stability analysis. In an overview of recent developments in rotorcraft dynamics [34], Johnson mentions proprotor stability can be analyzed successfully, even using a simple rigid blade model for the rotor, provided effective pitch-flap, pitch-lag, and flap-lag couplings are properly specified. The importance of including corrections for compressibility effects in aerodynamic models is also discussed.

In the early 1980's Bell and Boeing teamed to propose a tiltrotor aircraft to meet the U.S. military's requirements under the J VX (Joint Services Vertical Lift Aircraft) program. The Bell/Boeing team were awarded the contract and began development of the V-22 Osprey. In 1984, a 1/5-scale aeroelastic model of the V-22 began wind tunnel tests in NASA Langley's Transonic Dynamics Tunnel [35]. Tests of the initial model configuration revealed unacceptably low stability boundaries. To improve aeroelastic stability, wing frequencies were adjusted to increase separation of the wing vertical and chordwise bending modes, and a new "coning hinge" rotor hub was designed. This hub featured flap flex-

ures inboard of the pitch bearing, to minimize the destabilizing pitch-lag coupling noted by Johnson in Ref. 29. Reference 36 used test data from the 1/5-scale V-22 model to examine the predictive capability of two tiltrotor stability analyses, CAMRAD and DYN4 (a proprietary Bell analysis, similar to PASTA). Initial correlation of both analyses with test data was poor. Improvements to DYN4's analysis of pitch-lag coupling, and improvements to CAMRAD's modeling of the coning hinge and airfoil tables led to much better correlation with test data for both analyses.

In the early 1990's, Nixon expanded UMARC, a comprehensive rotorcraft analysis developed at the University of Maryland [37], to provide a tiltrotor modeling capability to the code by allowing large shaft tilt angles and added additional degrees of freedom to the hub to model gimbal motion [1]. The resulting analysis has similar capabilities to CAMRAD, though blade and wing bending and torsion are modeled with finite elements, rather than using a modal approach. Srinivas and Chopra [38] performed extensive validation of UMARC's tiltrotor analysis capability, correlating with test data from XV-15 flight tests and from the 1/5-scale V-22 wind tunnel model. Predicted levels of wing modal damping compared well with the test data.

The 1/5-scale V-22 aeroelastic model developed for the V-22 development program has been the focus of considerable research efforts at NASA Langley in recent years (Fig. 1.17). Now known as WRATS (Wing and Rotor Aeroelastic Test System), the model has undergone considerable changes in configuration over the years to support various test efforts. Ref. 39 details the results of testing to re-establish baseline stability boundaries for the modified model, as well as a parametric investigation confirming the influence of several important parameters on stability. For a given operating condition, increased rotor speed, increased  $\delta_3$  angle, and reduced control system stiffness were all destabilizing. The destabilizing influence of compressibility was observed by testing the model in R-134a, a heavy gas medium that allowed the model to match full-scale tip Mach number. Analytical modeling of the WRATS model using a multi-body dynamics analysis is discussed in Refs. 40,41.

Recent experimental work using the WRATS model has turned to a study of soft-inplane



tiltrotor configurations. In Refs. 4, 42, results are given for hover-mode tests of a soft-inplane gimbaled tiltrotor. The rotor hub used in these tests was developed as part of an initial study of soft in-plane stability using the WRATS model, and is not representative of any proposed full-scale design. The model experienced an instability of the coupled wing-torsion-chord mode during testing in hover mode. No airplane-mode wind tunnel tests were conducted using this rotor hub. The model displayed some unexpected stability trends, such as an insensitivity of the instability to changes in lag damping.

The most recent WRATS test occurred in July and August, 2002. Details of this test are given in Ref. 43. A new four-bladed, semi-articulated, soft-inplane rotor design (Fig. 1.18) developed by Bell for future application to heavy-lift tiltrotors was tested in hover and in airplane mode at NASA Langley. In hover testing, the rotor was found to have adequate levels of damping over the range of rotor speeds tested. As was the case with the Boeing Model 222 soft-inplane rotor, however, very low wing vertical bending mode damping in airplane mode was a serious concern. Damping of this mode was so low that wind tunnel testing had to be performed in powered-mode, rather than with a windmilling rotor as is typically done. Running with a powered rotor improved the beam mode subcritical damping, but did not strongly influence stability boundaries. Measurements of dynamic loads during conversion revealed a significant reduction of rotor loads with the soft-inplane design, when compared to the baseline stiff-inplane WRATS hub.

## **1.2 Influence of passive design parameters on tiltrotor stability**

Throughout the body of research described in the previous section, an understanding of the influence of some of the more fundamental design parameters on tiltrotor aeroelastic stability was developed. Reference 3 provides a good summary of the trends that may be found reported in several early studies of tiltrotor aeroelastic stability. Reduced pitch-flap

coupling increases stability, though some amount of  $\delta_3$  is required to control rotor flapping. Increased wing torsional stiffness is stabilizing. In the normal design range, reduced wing vertical bending stiffness is slightly stabilizing, since it reduces the interaction between the between wing vertical bending and torsion motion. In the normal design range, changes in wing chordwise bending stiffness have little effect on stability. Increased blade flapping restraint and increased blade stiffness are generally stabilizing, but limits on weight and allowable loads preclude arbitrarily large increases in these parameters.

Other important design parameters which influence stability were identified by Johnson in Ref. 29, where a combination of control system flexibility and blade flexibility outboard of the pitch bearing was shown to introduce a strongly destabilizing pitch-lag coupling. Increased control system stiffness, the introduction of blade flexibility inboard of the pitch bearing, and reduced rotor pre-cone were all shown to have a stabilizing influence by reducing the magnitude of the pitch-lag coupling.

The reported influence of some of these fundamental parameters was analytically confirmed by Nixon in Ref. 44. Test data from a recent WRATS model test provided in Ref. 39 also agree with these stability trends.

Recent studies of the influence of passive design parameters have focused on the introduction of couplings in the wing and rotor systems in an attempt to improve stability by improving the damping of lightly damped modes. In Ref. 1, Nixon examined the influence of flatwise bending-twist couplings in the rotor blades. The couplings, obtained through composite tailoring, were shown to improve whirl flutter stability by introducing an effective positive pitch-lag coupling which offset the destabilizing pitch-lag coupling due to flexibility of the control system and blade. Nixon also examined the influence of extension-twist coupling on rotor performance in hover and cruise. While hover performance could be increased by as much as 7%, airplane mode stability was severely reduced.

Reference 45 considered the feasibility of designing a composite tailored wing for the V-22 with a thickness to chord ratio of 18%, versus 23% for the baseline V-22, while maintaining or exceeding baseline stability boundaries. Using realistic constraints on the design,

a configuration was developed which exceeded the baseline flutter speed by 10 knots with only a 1.2% increase in weight. The finalized design featured tailored skins which introduced a wing vertical bending-torsion coupling which favorably influenced stability of the wing vertical bending mode. In Ref. 46, a composite tailored wing for the WRATS model was designed, constructed, and tested. The composite tailored wing, though having a thinner cross-section than the baseline WRATS wing, showed an approximately 30 kt (58 kt full-scale) increase in flutter speed over the baseline, due to the beneficial vertical bending-torsion coupling. Chordwise bending-torsion coupling had little influence on stability of the chord mode.

A parametric study of the influence of aeroelastic couplings in the wing and rotor for a soft-inplane tiltrotor was conducted in Ref. 47. The Boeing Model 222 was used as a baseline configuration for this study. Values of vertical bending-torsion coupling were identified which stabilized the air resonance instability experienced by this rotor in low-speed airplane mode flight. These couplings were, however, destabilizing to whirl flutter. Similar conflicting requirements for whirl flutter and air resonance stability were reported for rotor pitch-flap and pitch-lag couplings.

A summary of the influence of aeroelastic tailoring on tiltrotor stability reported in the above studies may be found in Ref. 48. The influence of composite couplings in the wing and rotor on whirl flutter stability was also examined by Barkai and Rand in Ref. 49. For bending-twist coupling of the blades, qualitative agreement with Ref. 1 was reported. The beneficial influence of wing vertical bending-twist coupling was reported to be consistent with the findings in Ref. 45, but chordwise bending-twist coupling was reported to be very stabilizing, which is not consistent with previous studies.

Other studies have introduced couplings in the rotor system through methods other than composite tailoring. Reference 50 introduced kinematic couplings by adjusting control system geometry. Increased stability could be achieved by decreasing the length of the pitch horn, moving the pitch link-to-swashplate attachment point forward, or by raising the pitch horn cant angle above the plane of rotation. In Ref. 51, the influence of advanced geometry

blade tips on whirl flutter stability was examined using UMARC. Blade tip aft sweep and anhedral were found to be stabilizing, while taper was marginally destabilizing. References 52–55 investigated the influence of blade center of gravity (CG) and aerodynamic center (AC) offsets. Many combinations of CG and AC offsets at various radial locations were examined to identify a configuration which improved whirl flutter stability without significantly worsening pitch link loads. Rearward offsets of the AC and forward offsets of the CG near the blade tip were found to be most effective.

### **1.3 Application of active control to tiltrotor aircraft**

While passive design techniques, such as the introduction of composite couplings to the wing structure or pitch-flap and pitch-lag couplings to the rotor, can improve tiltrotor aeroelastic stability, there may be limits to this approach, particularly in the case of soft-inplane tiltrotors. For instance, Ref. 47 reported that for soft-inplane tiltrotors, combinations of couplings which alleviate air-resonance may be detrimental to whirl flutter stability. The few soft-inplane configurations that have been tested in a wind tunnel (see Refs. 24 and 43) have exhibited unacceptably low levels of wing vertical bending mode damping, which passive design changes alone may not be able to improve. Another alternative for alleviating these instabilities is the use of active controls. There have been several studies investigating the use of active controls on tiltrotor aircraft. Active control has been considered for purposes of gust alleviation (Ref. 56), reduction of blade loads (Ref. 57), and vibration reduction (Refs. 58 and 59), as well as aeroelastic and aeromechanical stability augmentation.

During the test of the Boeing Model 222 rotor in the NASA Ames 40- by 80-foot wind tunnel, Boeing researchers investigated the use of a simple feedback control system to increase damping of the poorly damped wing vertical bending mode [24]. An accelerometer mounted on the wingtip sensed excitations of the wing vertical bending mode. Active control inputs to the system were made through the swashplate. After an open loop study to

determine the best control gain and phase for the controller, closed loop tests were conducted. The controller was very successful at adding damping to the wing vertical bending mode.

In Ref. 56, Johnson analytically investigated the use of an optimal controller with an estimator, for reduction of tiltrotor gust response for both the Boeing and Bell full-scale rotors tested at NASA Ames in the early 1970's. The actuation strategies considered included active flaperons, swashplate inputs, and a combination of the two. Both flaperons and swashplate-based controllers were effective at improving proprotor gust response. Since the lowly-damped wing modes were an important part of the gust response, the controller acted to greatly increase the damping of the wing modes in order to reduce the response. Thus, while Ref. 56 did not explicitly consider the problem of aeroelastic instability, it did confirm that active control was a feasible technique for tiltrotor damping augmentation.

In Ref. 60, Nasu analytically investigated the use of feedback control to improve tiltrotor flutter stability. Velocity of the wing chordwise bending mode was selected as the sole feedback parameter, since the chord mode was the critical mode for the semispan tiltrotor model used in the study. Active control inputs were applied via longitudinal cyclic pitch. A brief parametric study was conducted to determine a controller gain that increased wing mode damping. No attempt was made to optimize the design of the active control system. In Ref. 61, van Aken expanded on Nasu's work. CAMRAD/JA was used to provide the tiltrotor analytical model. This model included many enhancements including full-span aircraft configuration, airframe rigid body modes, gimbal motion, blade pitch dynamics, and rotor speed perturbations. As in Ref. 60, a simple feedback control system was considered, where wing chordwise bending and torsional accelerations were used as feedback parameters on which active longitudinal cyclic pitch inputs were based. Again, no attempt was made to design an optimal control system. A parametric study was performed to develop a set of controller gains and a 15 knot increase in flutter speed was obtained. Reference 62 describes a similar investigation of the influence of active control on the whirl flutter stability of a proposed joined-wing variant of the XV-15.

In Ref. 63, Vorwald and Chopra used optimal control techniques to improve whirl flutter stability. A simple analytical model similar to Johnson's formulation in Ref. 2 was used. An LQR optimal controller with observer was formulated. Vertical velocity of the wingtip was measured, and the rest of the states were estimated by the observer (implemented as a Kalman-Bucy filter). Active control inputs were through rotor cyclic pitch. A 20% increase in predicted flutter speed was obtained for the full-scale XV-15 wind tunnel model. However, it should be noted that while the analytical model used in Ref. 63 captures the overall trends of aeroelastic behavior, accuracy of the resulting stability predictions suffered due to the lack of compressibility corrections to the blade aerodynamics and the lack of any representation of the influence of blade pitch dynamics.

Active control for tiltrotor vibration reduction was examined in Refs. 58 and 59. In both studies, an active control system known as MAVSS (Multipoint Adaptive Vibration Suppression System), designed by Bell, was used to reduce 1P and 3P vibrations on the WRATS model. Wing strain gauges and accelerometers installed in the engine nacelle measured system response. In Ref. 58, the MAVSS adaptive controller drove a wing flap-eron to reduce vibration, and in Ref. 59, the flap-eron was used in conjunction with HHC swashplate inputs. When the flap-eron alone was used, MAVSS was unable to simultaneously reduce wing beam, chord, and torsion responses. When MAVSS could simultaneously command wing flap-eron and HHC inputs through the swashplate, load reductions of 85% to 95% were achieved in all three wing modes.

More recently, a great deal of experimental work has been performed at NASA Langley Research Center and Bell Helicopters to evaluate the effectiveness of a modern adaptive control algorithm known as Generalized Predictive Control (GPC) for tiltrotor stability augmentation and vibration suppression. GPC is a digital time-domain multi-input, multi-output predictive control method [64]. System identification is carried out, and control inputs are calculated on-line from measured system input/output data. The user must specify certain controller parameters, such as the order of the system model, control weights, and prediction and control horizons (measures of how many time steps into the future sys-

tem outputs and control inputs are predicted). Experimental investigations [4, 42, 43, 65] have demonstrated the ability of a GPC-based controller to improve tiltrotor aeroelastic and aeromechanical stability. Reference 65 experimentally evaluated the ability of a GPC controller to improve airplane mode stability using the WRATS model. Strain gauge measurements of wing bending and torsion motion were used for feedback, and active control inputs were introduced through the swashplate. The GPC controller was found to be both robust and highly effective for increasing damping of the critical wing mode. However, the WRATS model with GPC controller was not operated at tunnel speeds above the open-loop stability boundary, so the increase in flutter speed due to active control was not experimentally determined. In Refs. 4 and 42, GPC successfully suppressed the hover mode instability experienced by the gimbaled soft-inplane rotor, using rotor cyclic pitch control inputs. In Ref. 43, GPC control of cyclic pitch inputs significantly improved the damping of the marginally stable vertical bending mode of the four-bladed, soft-inplane, semi-articulated rotor. The rotor was tested to 45 knots over the open-loop stability boundary, while still maintaining high levels of damping in all the modes. In addition to the experimental studies, some analytical work has been done to evaluate the influence of GPC on aeroelastic stability and gust response in forward flight, and on reduction of wing vibratory response in hover [66].

## 1.4 Summary

Tiltrotor whirl flutter instability has been the focus of considerable analytical and experimental research over the years. The fundamental cause of the instability, destabilizing inplane hub forces generated by the airloads required to precess the rotor, has been well understood for some time. Over time, continuing research has exposed the influence of various system parameters on whirl flutter stability. Given correct input parameters, modern tiltrotor stability analyses are able to give quite accurate stability predictions.

Compared to whirl flutter, the aeromechanical stability of soft-inplane tiltrotors has

received much less attention. In addition to the potential for ground or air resonance type instabilities in hover or low speed forward flight, the problem of marginal damping of wing vertical bending in airplane mode flight appears to be a common characteristic of soft-inplane tiltrotors. More research is required to better understand the aeroelastic and aeromechanical stability characteristics of soft-inplane tiltrotors.

Many different passive design parameters have been identified which have some influence on tiltrotor stability. Many studies have investigated the influence of these parameters, but no study has been performed which considers all or even most of these parameters in the same investigation. Such a study would allow relative comparisons of effectiveness to be made among the various design parameters, to truly identify the most influential. In addition to investigating the influence of changes in individual parameters, beneficial combinations of parameters could be identified through optimization techniques.

Active control appears to have great potential to improve tiltrotor aeroelastic stability. Soft-inplane tiltrotors in particular appear to be prime candidates for the application of active stability augmentation systems, due to inherently poor damping of the wing vertical bending mode. Active control has recently been demonstrated experimentally on soft-inplane tiltrotors [43], but as of yet very few analytical studies of active control for soft-inplane tiltrotor stability augmentation have appeared in the literature. Previous studies investigating tiltrotor active stability augmentation have largely focused on active control using inputs through the swashplate. Little attention has been paid to active control of a wing flaperon for tiltrotor aeroelastic stability augmentation. An actively controlled wing flaperon should be effective for increasing tiltrotor whirl flutter stability boundaries, due to the large control authority of the aerodynamic surface in high speed cruise.





Figure 1.1: The Bell/Boeing V-22 Osprey tiltrotor aircraft



Figure 1.2: The Bell Eagle Eye tiltrotor UAV



Figure 1.3: The Bell/Agusta BA-609 civilian tiltrotor

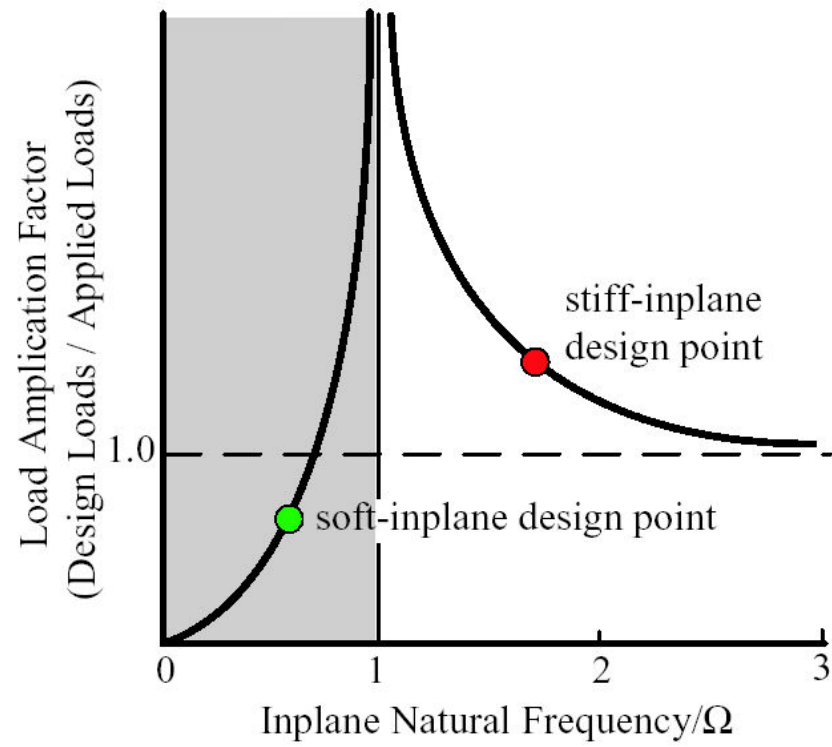


Figure 1.4: Effect of Lag Frequency on Hub Loads (from Ref. 4)



Figure 1.5: The Lockheed Electra turboprop airliner

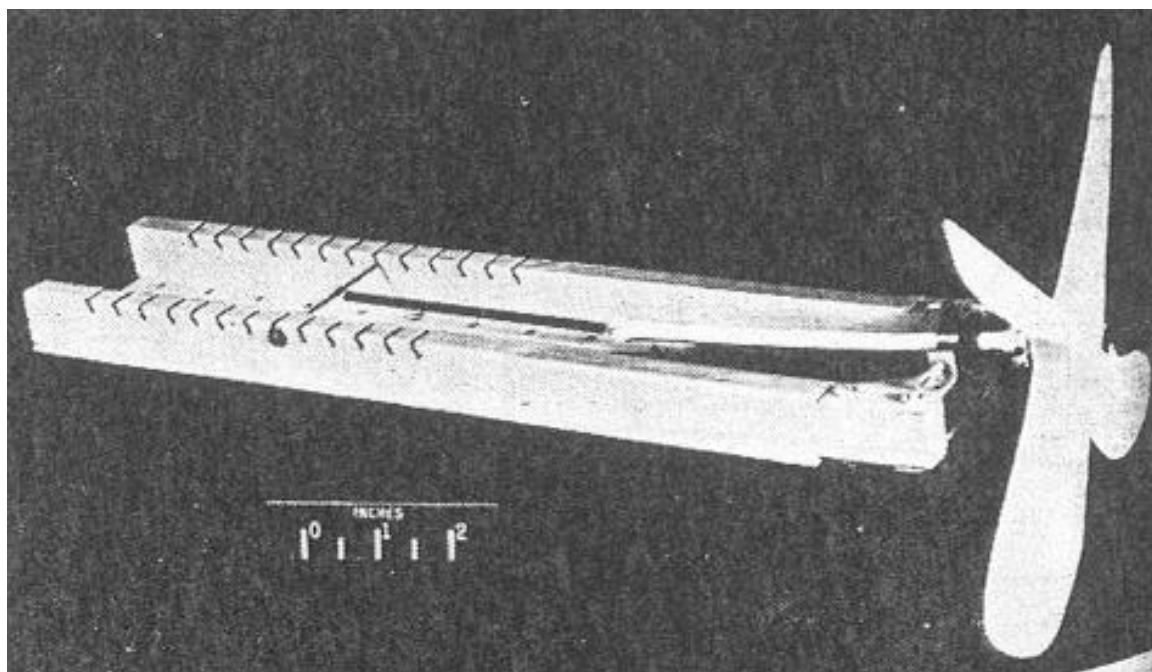


Figure 1.6: Simple propeller model used to validate analysis of Ref. 8

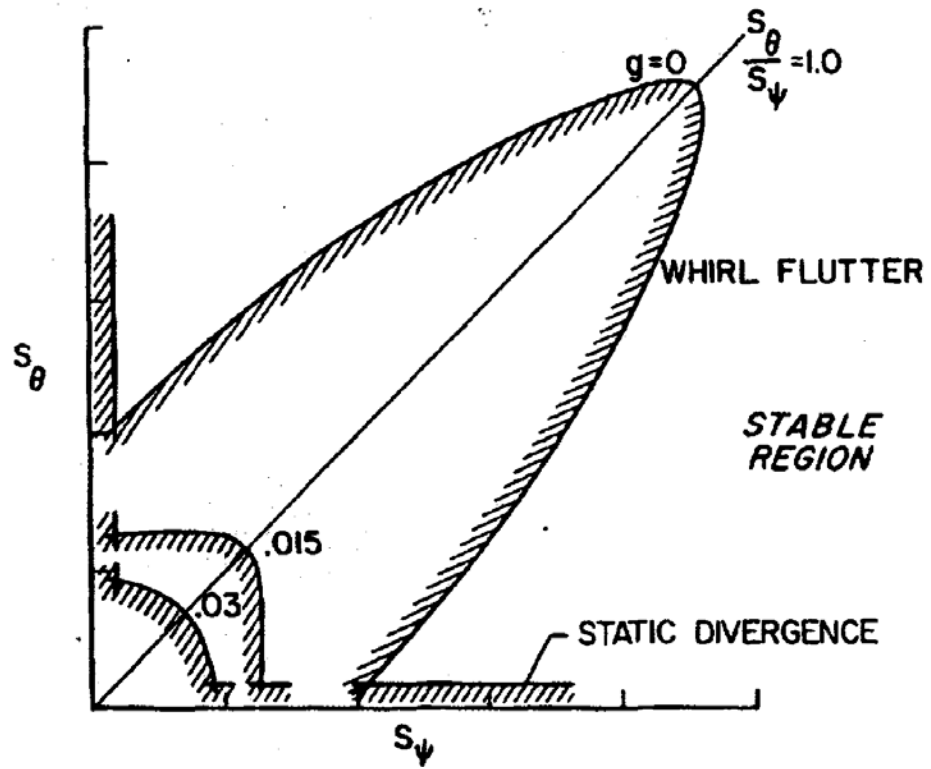


Figure 1.7: Pitch and Yaw Stiffness Required for Neutral Whirl Flutter Stability (from Ref. 7)

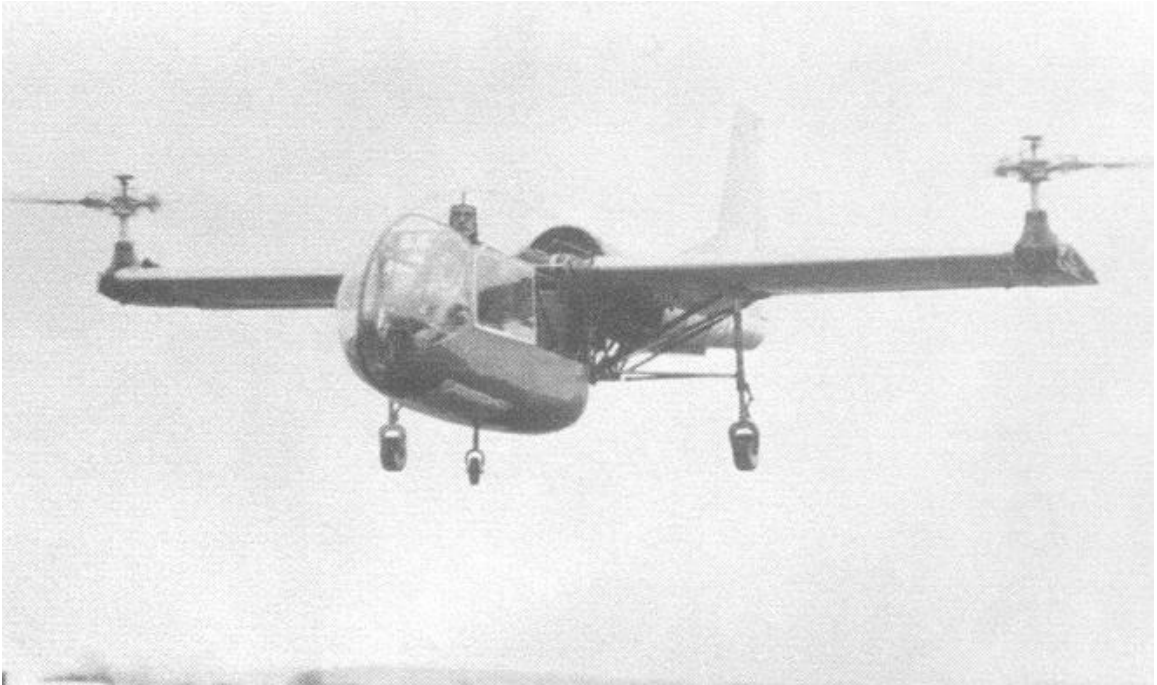


Figure 1.8: Transcendental Model 1-G (from Ref. 10)



Figure 1.9: Transcendental Model 2 (from Ref. 10)





Figure 1.10: First flight of Bell XV-3 tiltrotor research aircraft, August 11, 1955 (from Ref. 10)





Figure 1.11: Later configuration of XV-3 in airplane mode flight (from Ref. 10)

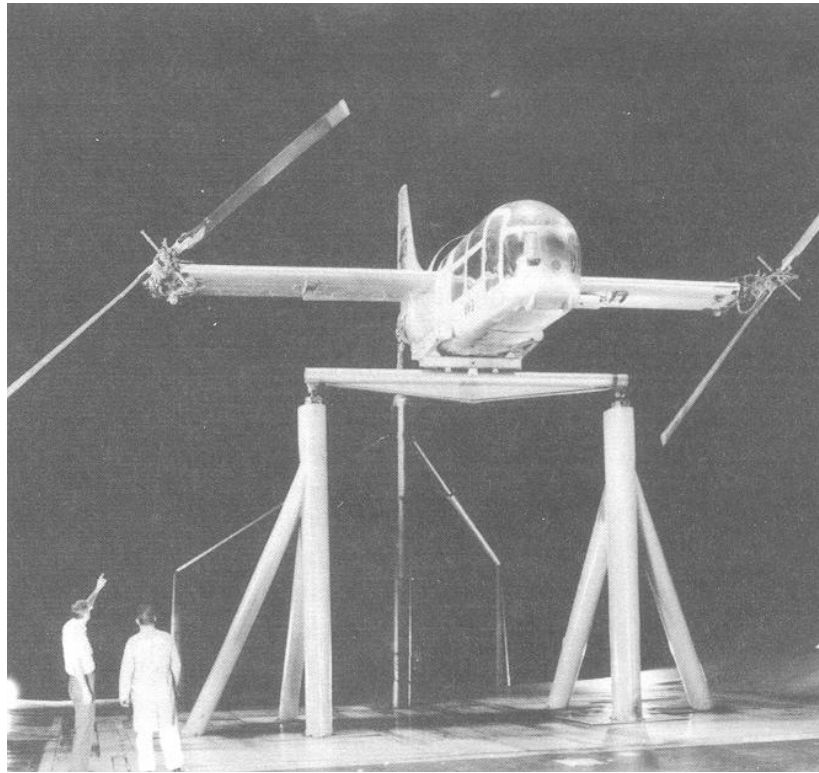


Figure 1.12: XV-3 in the NASA Ames Research Center 40- by 80- ft. wind tunnel (from Ref. 10)

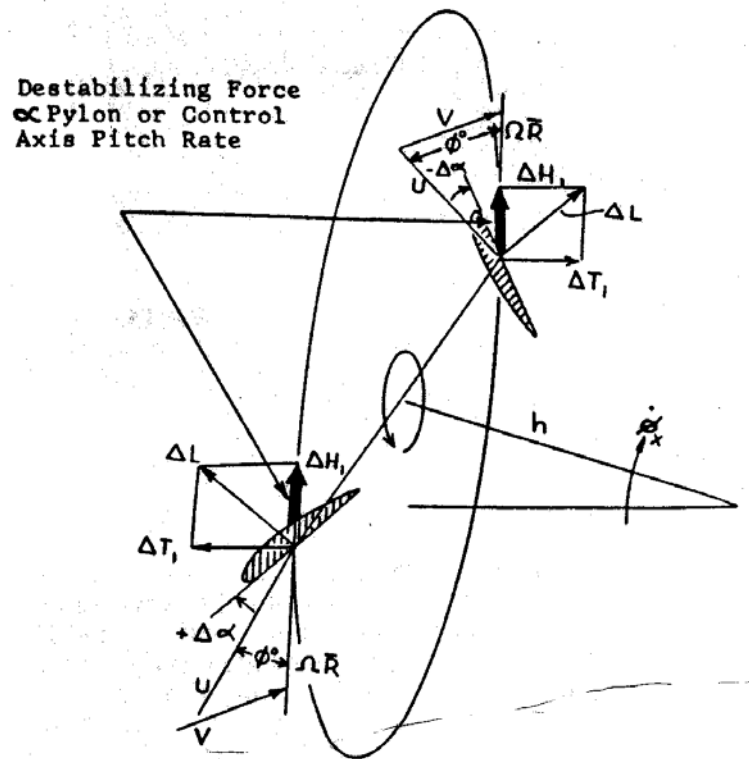


Figure 1.13: Proprotor Whirl Flutter: Origin of destabilizing aerodynamic force (from Ref. 11)



Figure 1.14: Bell Model 300 rotor in the Ames 40- by 80-ft wind tunnel (from Ref. 10)

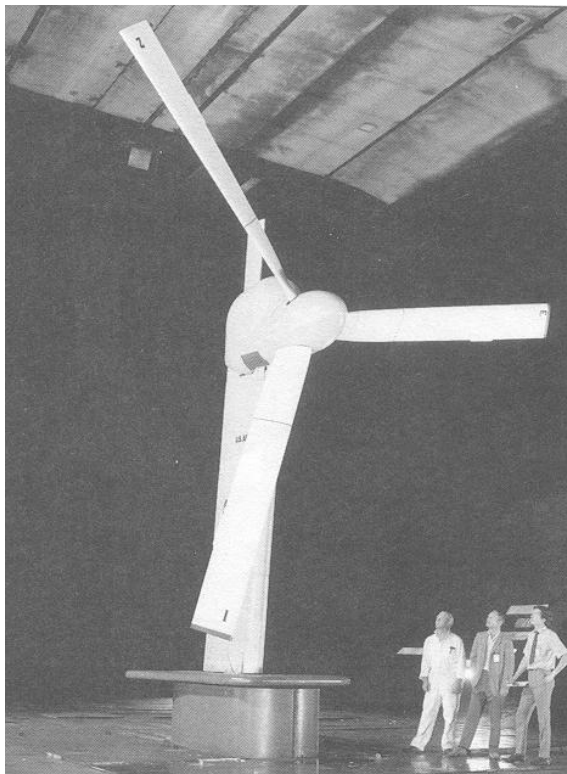


Figure 1.15: Boeing Model 222 rotor in the Ames 40- by 80-ft wind tunnel (from Ref. 10)



Figure 1.16: XV-15 Tiltrotor Research Aircraft in hover

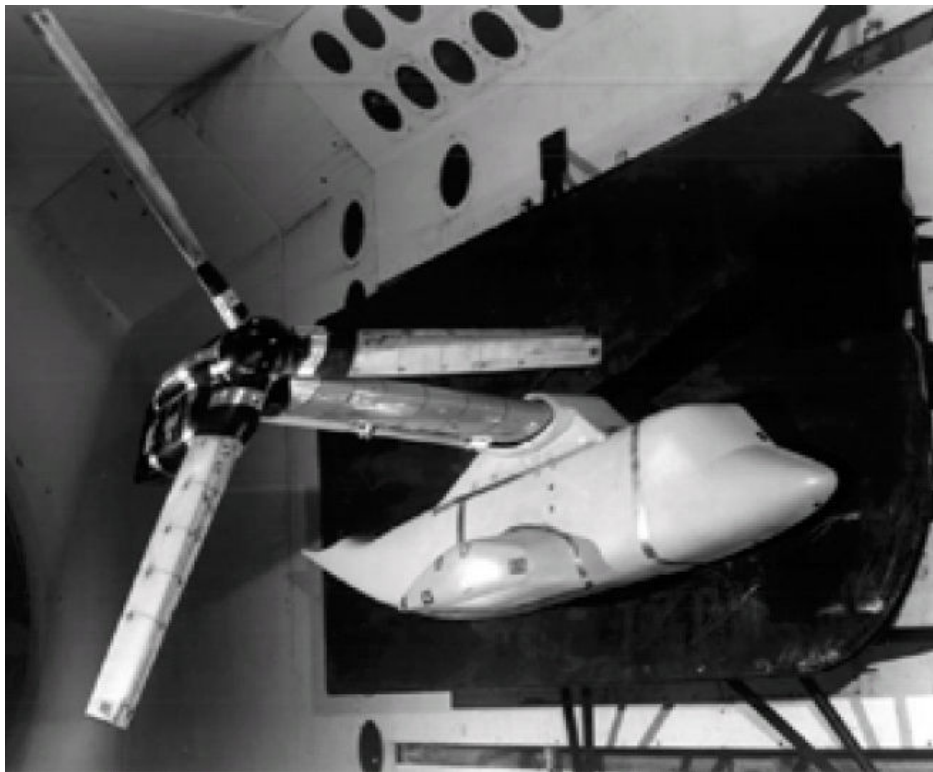


Figure 1.17: WRATS wind tunnel model in NASA Langley TDT (from Ref. 39)

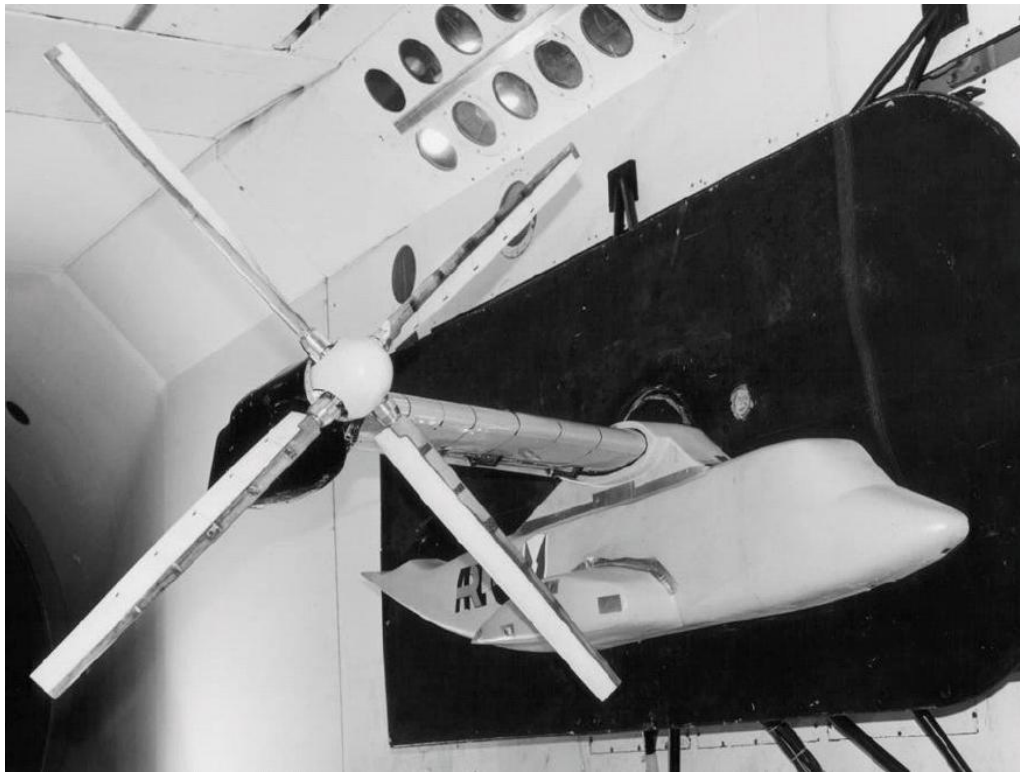


Figure 1.18: Bell semi-articulated soft-inplane rotor installed on WRATS model (from Ref. 43)



## **Chapter 2**

### **Objectives of Present Research**

The objective of this dissertation is to investigate various techniques to improve tiltrotor aeroelastic stability. A simple yet accurate stability analysis is developed and validated. Compared to more sophisticated comprehensive analyses, a simple model is easier to use as part of a larger analysis or as a plant model for control design, provided the model retains sufficient detail to provide accurate stability predictions. The analysis is then used to investigate both passive and active approaches to enhanced tiltrotor stability. The research effort may be divided into several sub-tasks, described below.

#### **2.1 Development of simple tiltrotor stability analysis**

Formulating a tiltrotor stability analysis is complicated by some of the design features unique to tiltrotor aircraft. The presence of a gimbaled hub and/or coning flexures at the blade root must be correctly modeled. To trim the rotor over a wide range of flight speeds, large changes in collective pitch are required. Blade fundamental flap and lag frequencies can vary considerably as a function of collective pitch, as blade flatwise bending near the root becomes more in-plane, and chordwise bending becomes more out-of-plane with increasing collective pitch. In addition, large values of collective pitch, highly twisted blades,

and the presence of blade flexibility outboard of the pitch bearing all act to aeroelastically couple blade flap, lag, and torsion motions.

Despite these difficulties, analytical models have been used successfully for many years to study the aeroelastic stability of tiltrotor aircraft. Even relatively simple models are able to capture fundamental stability characteristics. To accurately predict stability boundaries, however, an adequate representation of the effective rotor pitch-flap, pitch-lag, and flap-lag couplings is required [34]. Comprehensive analysis codes such as those described in Refs. 1, 28, 31 inherently capture these couplings by directly modeling the coupled elastic bending modes of the rotor blades. Existing rigid-blade tiltrotor stability analyses [2, 19, 67, 68] typically do not attempt to directly model these couplings. Rather, the variation of coupling parameters with trim collective pitch is explicitly input to the analysis in the form of tabular data. Variation of rotor flap and lag frequency with collective pitch is similarly treated. The tabular inputs describing rotor frequency and coupling parameters are obtained from more complex structural dynamics models of the rotor system or from experimental test data.

This treatment of rotor frequency and coupling variation is convenient for analysis of existing tiltrotor aircraft designs or for experimental models where the relevant parameters are readily available or may be directly measured. However, such an approach may not be well suited for the preliminary analysis of new configurations or for parametric design studies. Any change in model physical parameters (for example, blade flatwise bending stiffness) would require an entirely new table of input data be calculated or measured. A simple, stand-alone analysis producing accurate whirl flutter stability predictions by correctly modeling from first principles the physical origins of rotor frequency and coupling variations could prove useful in this situation. Once an acceptable design is identified using the simple analysis, more sophisticated tools could be employed to perform detailed structural modeling.

In the present study, a new whirl flutter aeroelastic stability analysis for tiltrotor aircraft is developed in which the blades are assumed to undergo rigid flap, lag, and torsion

rotations. This analysis does not rely on the existence of more complex models to provide variations in crucial input parameters with collective pitch or airspeed. Variation of blade flap and lag frequency, as well as effective pitch-flap, pitch-lag, and flap-lag couplings, are calculated from physical parameters, such as blade structural flap and lag stiffness distribution (inboard or outboard of pitch bearing), trim collective pitch setting, and rotor precone. By thus obtaining blade frequencies and coupling parameters from first principles, the formulation makes it possible to model configurations for which detailed structural design information does not yet exist or is unavailable.

## 2.2 Optimization of passive design parameters

The influence of variations in passive design parameters has received considerable attention in the literature. In the references cited previously, the various parameters under consideration in each study were typically varied *individually*. Differences in the analyses and model configurations between the various studies make comparisons of the relative effectiveness of all the design variables difficult. In addition, the effects of simultaneous variation of *multiple* design variables has not been explored. Since other design considerations besides aeroelastic stability (such as limits on allowable loads or rotor transient flapping) likely prevent the designer from fully exploiting the stabilizing influence of any one design parameter, the effects of changes in multiple parameters should be investigated. Small changes in several design parameters may be able to provide the required gains in stability while still respecting other design constraints. Furthermore, the effect of interactions between various design variables on tiltrotor aeroelastic stability has not been established. For instance, Ref. 69 showed that a combination of pitch-flap and pitch-lag couplings provided a greater increase in helicopter aeromechanical stability than the sum of the individual parameters' stabilizing influences. Similarly, there may be combinations of design parameters that prove beneficial for tiltrotor aeroelastic stability. When considering a large number of potential design variables, optimization techniques offer an efficient method to

identify potentially serendipitous combinations of parameters.

This study uses formal optimization techniques to identify combinations of design parameters which provide the greatest improvement in whirl flutter stability. In addition to the design parameters generally considered in the literature (such as wing/rotor stiffness properties or aeroelastic couplings), the analysis used in this investigation considers some design parameters which have not been examined in previous studies, such as the distribution of blade flexibility inboard and outboard of the pitch bearing. Stability trends of the various design parameters are identified through a parametric study, and formal optimization techniques used to determine a *unique combination* of parameters that maximizes tiltrotor whirl flutter stability. Constraints on the optimization are selected that prevent unrealistically large changes in the design parameters. The process of formulating a properly posed optimization problem in order to achieve the desired stability characteristics is also discussed. The influence of rotor and wing design parameters are first considered separately, after which concurrent optimization studies are conducted. Emphasis is placed on a physical interpretation of the optimization results, to better understand the means by which certain combinations of design variables improve stability.

## **2.3 Active control of wing flaperons for stability augmentation**

The active control strategies considered in previous studies for tiltrotor aeroelastic stability augmentation varied considerably in terms of sophistication of the controller, from simple unoptimized feedback controllers which served to demonstrate the feasibility of active control, to complex adaptive control systems. A full-state optimal controller would provide a useful benchmark for analytical investigations of tiltrotor active control, as the performance of such a controller would establish the maximum possible stability augmentation for a given system. It should be noted that the performance of the GPC controllers

used in the recent experimental tests at NASA Langley [4, 42, 43, 65] approaches that of an optimal controller as the prediction horizon of the predictive controller is increased. Thus, the relatively simple optimal controller can also indicate the maximum performance potential of the more complex adaptive controller.

This study evaluates the effectiveness of wing flaperon active control for alleviation of whirl flutter. The study seeks to establish how large an increase in flutter speed may be achieved while observing realistic limits on flaperon deflection. Both stiff- and soft-inplane tiltrotor configurations are examined, to develop an understanding of the influence of vehicle configuration on flaperon effectiveness. The importance of considering unsteady aerodynamic effects in stability analyses and in controller design is also examined. The study focuses on optimal control systems using full-state feedback. Feedback gains from the optimal controllers are examined to gain insight into the most important feedback paths that could be exploited by simpler reduced-order controllers.

# Chapter 3

## Description of Present Analysis

This chapter provides a brief description of the analytical model developed for the present research. Particular attention is paid to the modeling assumptions required in developing expressions to describe the effective pitch-flap, pitch-lag, and flap-lag coupling parameters and rotor frequency variation. Results from the present analysis are validated against experimental data and compared to results obtained from existing rigid blade analyses (which require external tabular inputs), and more complex elastic blade models. The influence of these modeling refinements on whirl flutter stability predictions is evaluated and discussed.

While this chapter focuses on the unique features of the present analysis, a more detailed description of the basic model formulation is contained in Appendix A.

### 3.1 Overview of formulation

The analytical model represents a proprotor with three or more blades, mounted on a semi-span, cantilevered wing structure. The point of attachment between the rotor hub and the wing/pylon system can undergo three displacements  $(x, y, z)$  and three rotations  $(\alpha_x, \alpha_y, \alpha_z)$ , as shown in Fig. 3.1. The mass, damping, and stiffness properties associated

with these degrees of freedom are derived from the wing/pylon structure. The rotor hub may be gimbaled, allowing cyclic flapping motion at the blade root ( $\beta_G$ ). In the fixed frame, this gimbal degree of freedom allows for longitudinal ( $\beta_{GC}$ ) and lateral ( $\beta_{GS}$ ) tilting of the rotor disk. Thus the rotating-frame gimbal flapping for the  $m^{\text{th}}$  blade is related to the fixed-frame gimbal degrees of freedom by

$$\beta_G^{(m)} = \beta_{GC} \cos \psi_m + \beta_{GS} \sin \psi_m \quad (3.1)$$

The blade is attached to the hub with some precone angle,  $\beta_P$ . Perturbation of rotor azimuthal position in the rotating frame ( $\psi_s$ ) is included, allowing a windmilling rotor condition to be modeled. Note that although a perturbation in azimuthal position is used in the formulation, only velocity and acceleration terms in  $\psi_s$  appear in the final equations. Thus the true degree of freedom is  $\dot{\psi}_s$ , a rotor speed perturbation. A spring-restrained offset flapping hinge represents the flap flexibility of the blade ( $\beta$ ), as well as the flexibility due to a coning hinge (if present). Blade in-plane flexibility ( $\zeta$ ) is accommodated by a spring-restrained offset lagging hinge. Figures 3.2 and 3.3 illustrate the blade out-of-plane and in-plane degrees of freedom. The model used to represent blade flap and lag flexibility, its distribution with respect to the pitch bearing, and its implications on system behavior, will be described in more detail in Section 3.3.1. Blade rigid pitch rotation as a result of control system flexibility ( $\phi$ ) is modeled by perturbations in blade pitch about an offset pitch bearing. Blade pitch dynamics will be discussed in detail in Section 3.3.3.

From the given model geometry, the position, velocity, and acceleration of a point on the rotor blade is written, and equations of motion for the rotor degrees of freedom are derived, along with the forces and moments acting at the rotor hub. Details of these derivations are provided in Appendix A.

### 3.1.1 Aerodynamics

The rotor aerodynamic model is based on quasi-steady blade element theory. The rotor is assumed to operate in purely axial flow, which is a reasonable assumption for a tiltrotor in the high-speed airplane mode flight condition. The aerodynamic model used in the present analysis is derived from the formulation developed in Ref. 2. Details of the model as implemented in the present analysis are given in Section A.6 of Appendix A. Aerodynamic forces and moments are expressed in terms of aerodynamic coefficients multiplying the perturbations in air velocity due to the rotor/hub degrees of freedom. These coefficients are functions of the steady tangential, perpendicular, and radial velocities seen by the blade, blade section pitch, and airfoil lift and drag coefficients, which are dependent on angle of attack and Mach number. For the general case of a rotor blade with arbitrary twist distribution and large values of collective pitch, small angle assumptions for local blade pitch and angle of attack are not necessarily appropriate. As a result, the aerodynamic coefficients are most conveniently determined via numerical integration over the length of the blade. In addition to the details provided in Appendix A, Ref. 2 provides a complete derivation and discussion of these aerodynamic coefficients. The major difference between the aerodynamic model in Ref. 2 and the present analysis lies in the expressions for perturbed perpendicular ( $\delta u_p$ ) and tangential ( $\delta u_t$ ) velocities, and perturbed blade pitch angle ( $\delta\theta$ ), due to the additional degrees of freedom used in the present analysis (Ref. 2 did not include separate degrees of freedom for both gimbal motion ( $\beta_G$ ) and blade flapping relative to the gimbal ( $\beta$ ), nor did it have a separate rotor shaft degree of freedom ( $\psi_s$ ) separate from collective lag motion ( $\zeta_0$ )). Expressions for the perturbation velocities, including the additional degrees of freedom considered in the present analysis, are provided below:

$$\begin{aligned} \delta u_t = & r(\dot{\alpha}_z + \dot{\psi}_s) - (r - e)\dot{\zeta} \\ & - (\dot{x} - V\dot{\alpha}_y) \sin \psi_m \\ & + (\dot{y} + V\dot{\alpha}_x) \cos \psi_m \end{aligned} \quad (3.2)$$



$$\begin{aligned} \delta u_p = & r\dot{\beta}_G + (r - e)\dot{\beta} + \dot{z} \\ & + r(\dot{\alpha}_x \sin \psi_m - \dot{\alpha}_y \cos \psi_m) \end{aligned} \quad (3.3)$$

$$\delta \theta = \phi - K_{PG}\beta_G - K_{P\beta}\beta - K_{P\zeta}\zeta \quad (3.4)$$

The coupling parameter  $K_{PG}$  (positive for gimbal flap-up, pitch-down) relates perturbation changes in blade pitch to perturbation gimbal motion  $\beta_G$ . This coupling is typically the result of rotor control system kinematics, and can be specified in terms of a “ $\delta_3$ ” angle through the relation  $K_{PG} = \tan \delta_3$ . The pitch-flap coupling parameter  $K_{P\beta}$  (positive for flap-up, pitch-down) and pitch-lag coupling parameter  $K_{P\zeta}$  (positive for lag-back, pitch-down) relate changes in blade pitch to blade flap and lag deflections. Potential sources of pitch-flap and pitch-lag coupling include composite tailoring [1, 49], advanced geometry blade tips [51], or blade CG and AC offsets [52]–[55]. In the present analysis, terms which describe the pitch-flap and pitch-lag couplings that arise due to blade flexibility outboard of the pitch bearing (described later) are included.

In Reference 2, Johnson notes that in the high inflow environment in which tiltrotors operate, the aerodynamic forces are dominated by terms proportional to the blade lift curve slope,  $c_{l\alpha}$ . Stability predictions obtained with a complete aerodynamic model were compared to results from a simpler aerodynamic model where airfoil drag and pitching moment coefficients were neglected and only the  $c_{l\alpha}$  terms were retained. The simpler model is attractive because it allows closed-form expressions for the aerodynamic coefficients to be derived, since the section angle of attack is no longer required. The results reported in Ref. 2 seemed to indicate that while lift curve slope terms do dominate the aerodynamic forces, a full representation of the blade aerodynamic properties is required to produce accurate stability predictions. However, the full aerodynamic model in Ref. 2 included Prandtl-Glauert compressibility corrections to the airfoil properties, while the  $c_{l\alpha}$ -only model did not. It is the compressibility correction which primarily accounts for the differences observed between the two aerodynamic models, rather than the more complete description of blade lift

and drag properties. In Ref. 34, Johnson notes the importance of compressibility for accurate whirl flutter stability predictions. Compressibility effects change the magnitude of the airfoil lift curve slope, thus directly influencing the magnitude of the aerodynamic forces which cause whirl flutter instability.

In the present analysis, aerodynamic coefficients may be calculated using either the full aerodynamic model, or with a simplified model which retains only terms proportional to  $c_{l\alpha}$ , the sectional lift-curve slope. This simplifying assumption has the advantage of allowing the aerodynamic coefficients to be evaluated analytically, rather than through numerical integration, but implicitly assumes that the blade pitch and twist distribution is such that the entire rotor blade is not stalled. Compressibility corrections may be applied to either aerodynamic model. The correlation results presented in this chapter were generated using only the  $c_{l\alpha}$  aerodynamic terms, with compressibility corrections applied. For the configurations considered in this study, both aerodynamic models produce nearly identical stability predictions, provided the same compressibility corrections are applied to each model.

### 3.1.2 Assembling rotor/wing equations

The rotor equations of motion are transformed to the non-rotating frame using a multi-blade coordinate transformation. The fixed-frame rotor-hub degrees of freedom are as follows:

$$\{q\} = [xyz \ \alpha_x \ \alpha_y \ \alpha_z \ \beta_0 \ \beta_{1C} \ \beta_{1S} \ \zeta_0 \ \zeta_{1C} \ \zeta_{1S} \ \phi_0 \ \phi_{1C} \ \phi_{1S} \ \psi_s \ \beta_{GC} \ \beta_{GS}]^T \quad (3.5)$$

The rotor equations, along with expressions for the hub forces and moments, are then coupled to a wing structural model, yielding a fully coupled set of rotor/wing equations. The present analysis is formulated generally, and may be coupled to a variety of wing models. The model may be a FEM representation of the wing structure, with a node defined

at the hub attachment point for assembly purposes. Appendix A contains details of the FEM wing model developed for this study. Alternatively, the wing may be represented by a set of normal modes, where effective mass, damping, and stiffness properties, as well as mode shapes, must be defined at the hub attachment point. In either case, the rotor equations are coupled to the wing model by a transformation of the hub attachment point degrees of freedom  $(x, y, z, \alpha_x, \alpha_y, \alpha_z)$  into the wing degrees of freedom, and by expressing the work done to the wing degrees of freedom in terms of the hub forces and moments.

An eigenanalysis is performed on the rotor/wing equations of motion to obtain the modal frequency and damping characteristics of the system.

## 3.2 Validation

The present analysis is validated against experimental data from three different semi-span tiltrotor configurations. The present results are also compared with stability predictions obtained from existing whirl flutter stability analyses, both rigid- and elastic-blade.

### 3.2.1 XV-15

Validation results are provided for a full-scale Bell XV-15 rotor, tested in a semi-span configuration in the NASA Ames 40- × 80-ft wind tunnel in 1970. Table 3.1 lists some of the important model parameters used in the present analysis (see Ref. 2 for a more complete listing of model properties). Figure 3.4 shows the damping of the wing vertical bending mode as a function of airspeed. The present rigid-blade analysis results are in close agreement with the elastic-blade results produced by Johnson's analysis [29] as well as with the predictions from an elastic-blade analysis by Nixon [1]. The predicted trends in damping below flutter speed are in good agreement, and all three analyses predict similar stability boundaries. Figures 3.5 and 3.6 show the same comparisons for wing chordwise bending and wing torsion modes, respectively. Though there is more scatter in the experimental

data in Figs. 3.5 and 3.6, the present analysis continues to provide stability predictions comparable to the more complex elastic blade analyses.

### **3.2.2 Boeing Model 222**

A full-scale rotor designed for the Boeing Model 222 tiltrotor was also tested at NASA Ames, in 1972. Unlike the stiff-inplane, gimbaled XV-15 rotor, the Model 222 rotor was a soft-inplane, hingeless design. Table 3.2 provides some of the parameters used to model the 222 in the present analysis (complete listing of rotor and wing properties may be found in Ref. 2). Figure 3.7 shows wing vertical bending mode damping versus airspeed. The present analysis agrees closely with the results from Johnson's elastic blade formulation from Ref. 29, and both analyses correlate well with experimental data from Ref. 2. Figures 3.8 and 3.9 compare damping predictions from the present analysis with the elastic blade results from Ref. 29 for the wing chordwise bending and torsion modes, respectively (experimental data for these modes was not available). Figure 3.8 shows excellent agreement between the two analyses for the chordwise bending mode. In Fig. 3.9, the peak damping in the wing torsion mode predicted using the present analysis is higher than that predicted by Johnson, but there is good agreement in prediction of the stability boundary for this mode.

### **3.2.3 1/5-scale V-22 aeroelastic model**

In Ref. 67, experimental data obtained from wind tunnel tests of a 1/5-scale V-22 semi-span model were used to validate the predictions from two different stability analyses: CAMRAD [31], an elastic blade analysis, and DYN4, a Bell Helicopter-developed rigid blade analysis. Detailed structural inputs to DYN4 are derived from the output of a Myklestad rotor analysis. The results from Ref. 67 are reproduced here, along with stability predictions from the present analysis. Table 3.3 gives the parameters used to model this rotor in the present analysis. Figure 3.10 shows the variation of wing vertical bending mode damping with airspeed. Though the predicted level of damping at velocities less than the

flutter speed varies in each analysis, the stability boundary predicted by the present analysis agrees quite well with the experimental data, as well as the CAMRAD and DYN4 predictions. Figure 3.11 shows the variation in wing chordwise bending mode damping. Here too, the present analysis is in close agreement with both experiment and the CAMRAD and DYN4 results.

### 3.2.4 WRATS model

The 1/5-scale V-22 semi-span model used for the tests described in Ref. 67 has undergone numerous changes in configuration (descriptions of which appear in Refs. 39, 70) which have altered the model's whirl flutter stability characteristics. Originally developed as part of the JVX (V-22) research and development program in the 1980's, the model, now known as the Wing and Rotor Aeroelastic Test System (WRATS), is in use as part of a joint NASA/Army/Bell Helicopter Textron, Inc. research program. Reference 39 provides experimental whirl flutter stability data for the WRATS model in its current configuration, but provides no analytical results for comparison purposes. Whirl flutter stability predictions for the WRATS model were generated using the present analysis, with the input data shown in Table 3.4. For comparison, PASTA 4.1, the latest publicly available version of PASTA [19], a rigid blade stability analysis developed at NASA Langley, was also run. Figures 3.12–3.15 show the comparison of the present analysis to PASTA predictions and to the experimental data from Ref. 39 for different rotor speeds and on- vs. off-downstop cases (Fig. 3.14 does not include PASTA results, since PASTA inputs for a rotor speed of 770 RPM were unavailable). Modelling of the on-downstop vs. off-downstop condition is accomplished through use of a modal representation of the wing and pylon, with different sets of experimentally obtained mode shapes for the two downstop states. The use of experimental mode shapes to represent the wing/pylon structure is described in more detail in Section A.9 of Appendix A. In this case, the same wing modal information is used by both PASTA and the present analysis, thus isolating any differences between the two analy-

ses to the rotor model. Agreement between the present analysis and PASTA predictions, as well as between the present analysis and experiment, varies considerably from case to case. In Fig. 3.12 (742 RPM, off-downstop case), the present analysis and PASTA are in good agreement, and both capture the experimental stability boundary. For the 888 RPM, off-downstop case in Fig. 3.13, the present analysis and PASTA are still in close agreement, but both somewhat over-predict the whirl flutter speed. At 770 RPM (on-downstop, Fig. 3.14), the present analysis underpredicts the experimental stability boundary. In Fig. 3.15 (888 RPM, on-downstop), the present analysis seems to capture the flutter speed well, while PASTA overpredicts the stability boundary.

There are several possible explanations for the poor correlation between results from the present analysis, PASTA, and the experimental data. One possibility is that the model parameters used as inputs to both analyses do not adequately represent the physical WRATS model. Alternatively, there may be some structural feature of the WRATS configuration which a simple rigid blade analysis is not able to adequately model. Comparison of the present results against those generated by an elastic blade analysis might provide additional insight into the correlation problem. Further investigation is not currently possible, since no elastic blade validation results for the stiff-inplane WRATS model have yet appeared in the literature.

### **3.2.5 WRATS Semi-Articulated, Soft-Inplane rotor model**

The basic WRATS wing-pylon system was used in the Summer of 2002 to test a new soft-inplane rotor design. The WRATS Semi-Articulated, Soft-Inplane (SASIP) rotor model was tested for whirl flutter stability in the NASA Langley Transonic Dynamics Tunnel. Reference 43 provides details of the SASIP rotor and a discussion of test results. Data from this wind tunnel test is being used to correlate two multi-body dynamics models of the WRATS SASIP configuration, using the multi-body dynamics codes DYMORE and MBDyn. References 71 and 72 discuss these correlation efforts. Figures 3.16 – 3.19 show

wing beam mode damping vs. airspeed predictions for the present analysis compared to predictions from the multi-body analyses (from Ref. 71) as well as actual test data. Input model parameters used by the present analysis to model the SASIP rotor are summarized in Table 3.5. Figure 3.16 shows wing beam damping vs. airspeed for an off-design rotor speed of 550 RPM (design airplane mode RPM for the SASIP rotor is 742 RPM) with the pylon locked on the downstop. While the available test data does not indicate the location of the stability boundary, the flutter speed predicted by the present analysis agrees closely with that predicted by DYMORE. At lower speeds, the present analysis slightly underpredicts the modal damping, while DYMORE overpredicts the damping level. Figure 3.17 shows the off-downstop case at 550 RPM. The test data indicates a flutter speed just above 90 knots, and DYMORE predicts this boundary well. The damping prediction from the present analysis generally agrees well with DYMORE and test data, but misses the slight bump in damping which occurs near 80 knots, and as a result underpredicts the flutter speed. Figure 3.18 shows the on-downstop case at the design cruise rotor speed, 742 RPM. There is considerable scatter in the experimental data, but a flutter speed of about 120 knots is clearly identifiable. DYMORE predicts the level of damping reasonably well, but does not capture the sharp reduction in damping at 120 knots. The present analysis consistently underpredicts the damping, and thus gives a very low flutter speed. The damping prediction from MBDyn is still lower than that from the present analysis. Similar trends are seen in Figure 3.19 for the off-downstop condition at 742 RPM. DYMORE matches the test data well, while both MBDyn and the present analysis underpredict the damping, with the present analysis being closer to the test data than MBDyn.

Correlation of the multi-body analyses with the SASIP test data is an ongoing effort at NASA Langley, and there is the potential for improvements in the predictive capabilities of all three analyses (DYMORE, MBDyn, and the present rigid-blade model) as additional data becomes available. At this time, the present analysis gives results that compare well with the state-of-the-art multi-body analyses, particularly at lower rotor speeds (Figs. 3.16 and 3.17).

### 3.3 Influence of unique model features

The present analysis incorporates several features unique among existing rigid blade stability analyses. A proper treatment of blade flexibility outboard of the pitch bearing correctly models the variation of blade flap and lag frequency with collective pitch. The analysis also retains separate gimbal and blade flapping degrees of freedom, providing a more physically based formulation than existing analyses. Expressions which account for the influence of blade flexibility outboard of the pitch bearing on blade pitch dynamics are also included. The influence of these model features on tiltrotor aeroelastic stability modeling is investigated below. Throughout this section, the full-scale XV-15 semi-span model tested at NASA Ames will be used to illustrate the influence of various model features.

#### 3.3.1 Structural flap-lag coupling

The presence of blade flexibility outboard of the pitch bearing allows the present analysis to predict the variation in blade frequencies with collective pitch. Furthermore, a model of blade stiffness which allows for flexibility outboard of the pitch bearing is essential in deriving expressions for the pitch-flap and pitch-lag couplings that result when blade flexibility is located outboard of the pitch bearing. The distribution of blade flexibility is represented in the present analysis by a structural flap-lag coupling (SFLC) model, which has been commonly used in helicopter rigid-blade stability analyses [73, 74]. In this formulation, blade flap and lag stiffness is modeled using a set of orthogonal “hub” springs ( $K_{\beta H}, K_{\zeta H}$ ) inboard of the pitch bearing, and orthogonal “blade” springs ( $K_{\beta B}, K_{\zeta B}$ ) outboard of the pitch bearing (see Fig. 3.20). The relative angle between the hub and blade springs ( $\bar{\theta}$ ) varies as the blade springs rotate with changes in collective pitch. This series of hub and blade springs may be equivalently described in terms of effective flap and lag flexural stiffnesses ( $K_{\beta}, K_{\zeta}$ ) and structural flap-lag coupling parameters ( $R_{\beta}, R_{\zeta}$ ) which define the distribution of flap and lag flexibility inboard and outboard of the pitch bearing.



$$K_\beta = \frac{K_{\beta H} K_{\beta B}}{K_{\beta H} + K_{\beta B}} \quad \text{and} \quad K_\zeta = \frac{K_{\zeta H} K_{\zeta B}}{K_{\zeta H} + K_{\zeta B}} \quad (3.6)$$

$$R_\beta = \frac{K_\beta}{K_{\beta B}} \quad \text{and} \quad R_\zeta = \frac{K_\zeta}{K_{\zeta B}} \quad (3.7)$$

In Eq. (3.7), a value of  $R_\beta = 0$  describes a blade where all the flap flexibility is located inboard of the pitch bearing, and  $R_\beta = 1$  represents a blade where all the flap flexibility is outboard of the pitch bearing. The distribution of lag flexibility varies similarly, but with parameter  $R_\zeta$ . See Ref. 74 for a detailed description of this formulation.

Note that the terms “flap” and “lag” in the above description may be somewhat misleading. At the high collective pitch settings required to trim the rotor in cruise, the blade “flap” and “lag” springs are rotated such that the primary source of stiffness for in-plane blade motion is actually  $K_\beta$  (assuming a rotor where most of the flexibility is located outboard of the pitch bearing). The “flap stiffness” in the SFLC formulation physically corresponds most closely to the blade flatwise bending stiffness, and “lag stiffness” corresponds to chordwise bending stiffness. For clarity, blade stiffness properties will henceforth be discussed in terms of flatwise and chordwise bending stiffnesses.

Using the definitions of blade stiffness given above, the elastic flap and lag restoring moments may be written as

$$\begin{aligned} \begin{Bmatrix} M_\beta \\ M_\zeta \end{Bmatrix} &= [K_{\text{eff}}] \begin{Bmatrix} \beta \\ \zeta \end{Bmatrix} \\ &= \begin{bmatrix} K_{\beta\beta} & K_{\beta\zeta} \\ K_{\beta\zeta} & K_{\zeta\zeta} \end{bmatrix} \begin{Bmatrix} \beta \\ \zeta \end{Bmatrix} \end{aligned} \quad (3.8)$$

where  $K_{\text{eff}}$  represents an effective stiffness matrix, the individual terms of which are defined as

$$\begin{aligned}
K_{\beta\beta} &= \frac{1}{\Delta} [K_{\beta} + (R_{\beta}K_{\zeta} - R_{\zeta}K_{\beta}) \sin^2 \bar{\theta}] \\
K_{\zeta\zeta} &= \frac{1}{\Delta} [K_{\zeta} - (R_{\beta}K_{\zeta} - R_{\zeta}K_{\beta}) \sin^2 \bar{\theta}] \\
K_{\beta\zeta} &= -\frac{1}{\Delta} (R_{\beta}K_{\zeta} - R_{\zeta}K_{\beta}) \cos \bar{\theta} \sin \bar{\theta}
\end{aligned} \tag{3.9}$$

and

$$\begin{aligned}
\Delta &= 1 + (2R_{\beta}R_{\zeta} - R_{\beta} - R_{\zeta}) \sin^2 \bar{\theta} \\
&+ \left[ R_{\zeta} (1 - R_{\zeta}) \frac{K_{\beta}}{K_{\zeta}} + R_{\beta} (1 - R_{\beta}) \frac{K_{\zeta}}{K_{\beta}} \right] \sin^2 \bar{\theta}
\end{aligned} \tag{3.10}$$

There are several important features to note about the above formulation. First, Eqs. (3.8–3.10) show that blade flap and lag stiffness is now a function of collective pitch. By selecting proper values of the fundamental blade flap and lag stiffnesses  $K_{\beta}$  and  $K_{\zeta}$ , and coupling parameters  $R_{\beta}$  and  $R_{\zeta}$  (or equivalently,  $K_{\beta H}$ ,  $K_{\zeta H}$ ,  $K_{\beta B}$ , and  $K_{\zeta B}$ ), the proper variation of blade flap and lag frequency with collective pitch may be modeled. Selection of appropriate values for the SFLC parameters is a relatively straightforward process. If blade inertias and approximate values for flap and lag frequency are defined, it is possible to manually select stiffness parameters that yield reasonable results. If the configuration being modeled contains a “coning hinge” or any sort of flexure inboard of the pitch bearing,  $R_{\beta}$  and/or  $R_{\zeta}$  should be set closer to 0; a blade which is rigidly attached to the hub inboard of the pitch bearing should have  $R_{\beta}$  and  $R_{\zeta}$  set to 1. Such a simple procedure for selecting the SFLC parameters would be adequate to define a generic baseline configuration for use in design trade studies or other parametric investigations. Alternatively, it is often desired to model an existing configuration with a high degree of accuracy. In this case, the SFLC parameters may be selected such that the resulting flap and lag frequencies fit, in a least-squares sense, the same tabular frequency data used as inputs to conventional rigid blade stability analyses. This parameter identification process need only be performed once off-line, and the SFLC parameters may then be used with no further reference to the tabular data. This was

the procedure used to define the SFLC parameters for the various tiltrotor configurations examined in this study.

Second, the off-diagonal terms of Eq. (3.8) serve to elastically couple blade flap and lag motion. In the output of the eigenanalysis, this coupling will create elastically coupled flap/lag blade modes. The magnitude of the off-diagonal terms is of approximately the same order as the on-diagonal terms, since  $\bar{\theta}$  may be a large angle due to the large values of collective pitch required to trim the rotor in high speed forward flight. The off-diagonal terms therefore contribute significantly to the total blade flap and lag elastic restoring moments, and will thus have a significant influence on blade flap and lag frequency. Other simple stability analyses do not model the elastic coupling of blade flap and lag motion, represented in the present analysis by the off-diagonal SFLC terms.

Figures 3.21–3.23 examine the influence of coupled blade flap and lag motion on wing mode damping. The baseline results are compared to a case where the off-diagonal terms from Eq. (3.8) are set to zero. In Fig. 3.21, there is a noticeable change in the character of wing vertical bending mode damping when the off-diagonal terms are removed. Figures 3.22 and 3.23 show smaller changes in stability characteristics for the wing chord and torsion modes. In each case, however, prediction of the whirl flutter stability boundary is affected, by as much as 40 knots. The majority of the changes seen in Figures 3.21–3.23 when eliminating the off-diagonal terms comes from the resulting shift in flap and lag frequencies. For instance, the peak in wing vertical bending mode damping in Fig. 3.21 is shifted to a higher forward speed when the off-diagonal terms are neglected; this is due to the frequencies of the low-frequency cyclic lag mode and the wing vertical bending mode crossing at a higher forward speed. If curve-fit flap and lag frequencies are used instead of the SFLC formulation from the present analysis, the profile of the resulting modal damping predictions (shown in Figs. 3.21–3.23) is closer to the baseline. There is still a noticeable difference in the calculated stability boundaries, however.

To model the variation of blade flap and lag frequencies with collective pitch, existing rigid blade stability analyses require the variation to be explicitly input to the analysis. Con-

sider the case of blade lag frequency, which for the XV-15 varies from as high as 1.8/rev at low speed (low collective pitch) to about 1.2/rev at high speed. In the PASTA analysis, the variation of frequency is input in the form of tabular data. In Ref. 1, a rigid blade stability analysis similar to the formulation in Ref. 2 was used to perform preliminary whirl flutter investigations. In this rigid blade analysis, Nixon modeled the variation in lag frequency by fitting a curve to experimental data. By contrast, the present analysis allows a portion of the blade flap and lag flexibility to be located outboard of the pitch bearing, thus directly modeling the physical mechanism behind the frequency variation. Figure 3.24 shows the resulting output eigenfrequency of the low frequency cyclic lag mode for the present analysis where the source of the frequency variation is directly modeled, and for a case where the present analysis has been modified to use Nixon's curve-fit frequency variation. The output frequency variation from the present SFLC formulation closely matches that of the curve-fit frequency case. This shows that if the effective flap and lag stiffness and the distribution of stiffness inboard and outboard of the pitch bearing is properly specified, then the present formulation is capable of correctly modeling rotor frequency variation as a result of changes in collective pitch, rather than requiring the variation in frequency as an input.

### **3.3.2 Gimbal/Blade flapping degrees of freedom**

In the derivation of the rigid blade model in Ref. 2 all blade out-of-plane motions are treated by one rotating-frame degree of freedom, the blade flap angle ( $\beta$ ). When the flap equation of motion is transformed to the fixed system, the cyclic and collective flapping modes are assigned different frequencies to account for the different root restraints in each case (the cyclic modes behave as if they are hinged at the root, due to the presence of the gimbal, while the collective mode is cantilevered at the root). Similarly, the PASTA analysis includes a rotor coning degree of freedom, as well as rotor (gimbal) longitudinal and lateral flapping degrees of freedom. The frequencies for the collective and cyclic flapping degrees of freedom are specified separately in the input to the analysis. This is essentially a *modal*

approach, where the stability analysis is simply a math model, and the frequency of each mode must be provided as an input to the analysis. Such an approach is different from the typical helicopter rigid blade stability analysis, where collective and cyclic flap frequencies are calculated from physical properties. For instance, the non-dimensional flap frequency for a helicopter is often defined as

$$v_{\beta}^2 = 1 + \frac{3}{2}\bar{e} + \frac{K_{\beta}}{I_{\beta}\Omega^2} \quad (3.11)$$

In an expression for flap frequency such as that given by Eq. (3.11), one cannot select a flap stiffness  $K_{\beta}$  which satisfies both the cyclic (gimbal) and collective (cantilever) boundary conditions. In reality, the gimbal motion and blade flapping represent two distinct physical degrees of freedom.

In the present analysis, separate gimbal ( $\beta_G$ ) and blade flapping ( $\beta$ ) degrees of freedom are retained. This allows a low-stiffness gimbal spring  $K_{\beta_G}$  to be specified, yielding a low-frequency cyclic flap mode (dominated by gimbal motion), while the higher flap stiffness of the blade produces a higher frequency coning mode. This approach means there is no need to assign separate frequencies to each mode (collective vs. cyclic). Rather, the correct frequencies for each mode are obtained as outputs of the physical model. Figure 3.25 shows the output eigenfrequencies for the low-frequency cyclic gimbal mode and rotor coning mode from the present analysis, and for the case where assigned frequencies are used as inputs, as in Ref. 2.

It may appear that the cyclic blade flapping degrees of freedom ( $\beta_{1c}, \beta_{1s}$ ) are redundant in the present analysis, since any cyclic flapping motion of the rotor should be accommodated by the lower stiffness gimbal motion ( $\beta_{Gc}, \beta_{Gs}$ ). Indeed, examination of the eigenvector associated with the low-frequency cyclic mode shown in Fig. 3.25 reveals that, although there is some contribution from other degrees of freedom, the gimbal degrees of freedom dominate, and the contributions from  $\beta_{1c}$  and  $\beta_{1s}$  are small. So the behavior of this mode, dominated by the gimbal motion, would not be greatly influenced by dropping the cyclic

blade flapping degrees of freedom.

Consider however the rotor low-frequency lag mode shown in Fig. 3.24. Physically, the reduction in lag mode frequency with increased forward speed (collective pitch) occurs due to the rotation of the blade structural axes (blade flatwise bending becomes more in-plane). In the present analysis, this frequency variation is modeled by allowing for blade flexibility outboard of the pitch bearing as described in the previous section. Since blade flap and lag motions are elastically coupled, dropping the rotor cyclic flap degrees of freedom from the analysis would make it impossible to predict from first principles the variation of lag frequency with collective pitch. In the present analysis, the cyclic flap and lag degrees of freedom couple to represent in effect the first cyclic blade bending mode of the rotor, the displacement of which has components both in-plane ( $\zeta_{1c}, \zeta_{1s}$ ) and out-of-plane ( $\beta_{1c}, \beta_{1s}$ ).

### 3.3.3 Modeling blade pitch-flap and pitch-lag coupling

The present analysis includes a blade rigid-pitch degree of freedom (perturbation in blade pitch due to control system flexibility). Reference 29 states that the primary influence of blade pitch dynamics on tiltrotor aeroelastic stability is to introduce a destabilizing pitch-lag coupling due to blade flexibility outboard of the pitch bearing. In the present analysis, the full pitch dynamic equations of motion may be retained, or effective pitch-flap and pitch-lag coupling parameters may be extracted from the pitch equations of motion, with the equations themselves dropped from the analysis. As was the case when modeling the variation of flap and lag frequency with collective pitch, the distribution of blade flexibility inboard and outboard of the pitch bearing plays an important role in determining the magnitude of these destabilizing pitch-flap and pitch-lag couplings.

Considering the model of blade stiffness described in the SFLC formulation above, the total blade flap and lag flexibility can be expressed as the sum of flap and lag flexibilities inboard and outboard of the pitch bearing:

$$[K_{\text{eff}}]^{-1} = [K_{\text{in}}]^{-1} + [K_{\text{out}}]^{-1} \quad (3.12)$$

As a result of this distribution of flap and lag flexibility, the total flap and lag displacement of the blade may be defined (assuming small rotations) as the sum of flap and lag displacements inboard and outboard of the pitch bearing:

$$\begin{Bmatrix} \beta \\ \zeta \end{Bmatrix} = \begin{Bmatrix} \beta_{\text{in}} \\ \zeta_{\text{in}} \end{Bmatrix} + \begin{Bmatrix} \beta_{\text{out}} \\ \zeta_{\text{out}} \end{Bmatrix} \quad (3.13)$$

When the blade undergoes flap and lag motions, the feather axis of the blade undergoes a rotation of  $\beta_{\text{in}}$  out-of-plane and  $\zeta_{\text{in}}$  in-plane. At the same time, the blade itself undergoes rotations of  $\beta_{\text{out}}$  and  $\zeta_{\text{out}}$  relative to the feather axis, as shown in Fig. 3.26. These motions must be considered when formulating the blade pitch equations of motion.

The flap and lag motions inboard of the pitch bearing ( $\beta_{\text{in}}, \zeta_{\text{in}}$ ) and the motions outboard of the pitch bearing ( $\beta_{\text{out}}, \zeta_{\text{out}}$ ) can be expressed as fractions of the total flap and lag angles ( $\beta, \zeta$ ). To begin, Eq. (3.13) is rewritten in terms of flap and lag flexibility multiplied by the applied flap and lag moments:

$$[K_{\text{eff}}]^{-1} \begin{Bmatrix} M_{\beta} \\ M_{\zeta} \end{Bmatrix} = \left[ [K_{\text{in}}]^{-1} + [K_{\text{out}}]^{-1} \right] \begin{Bmatrix} M_{\beta} \\ M_{\zeta} \end{Bmatrix} \quad (3.14)$$

Combining Eqs. (3.8) and (3.14) produces

$$\begin{aligned} [K_{\text{eff}}]^{-1} [K_{\text{eff}}] \begin{Bmatrix} \beta \\ \zeta \end{Bmatrix} = \\ [K_{\text{in}}]^{-1} [K_{\text{eff}}] \begin{Bmatrix} \beta \\ \zeta \end{Bmatrix} + [K_{\text{out}}]^{-1} [K_{\text{eff}}] \begin{Bmatrix} \beta \\ \zeta \end{Bmatrix} \end{aligned} \quad (3.15)$$

Comparing Eqs. (3.13) and (3.15), the following expressions for  $\beta_{\text{in}}, \zeta_{\text{in}}, \beta_{\text{out}}$ , and  $\zeta_{\text{out}}$  can be defined:

$$\begin{Bmatrix} \beta_{\text{in}} \\ \zeta_{\text{in}} \end{Bmatrix} = [K_{\text{in}}]^{-1} [K_{\text{eff}}] \begin{Bmatrix} \beta \\ \zeta \end{Bmatrix} = \begin{bmatrix} A & B \\ C & D \end{bmatrix} \begin{Bmatrix} \beta \\ \zeta \end{Bmatrix} \quad (3.16)$$

$$\begin{Bmatrix} \beta_{\text{out}} \\ \zeta_{\text{out}} \end{Bmatrix} = [K_{\text{out}}]^{-1} [K_{\text{eff}}] \begin{Bmatrix} \beta \\ \zeta \end{Bmatrix} = \begin{bmatrix} W & X \\ Y & Z \end{bmatrix} \begin{Bmatrix} \beta \\ \zeta \end{Bmatrix} \quad (3.17)$$

where

$$\begin{aligned} A &= \frac{1}{\Delta} \left[ 1 - R_{\beta} + \left( R_{\zeta} - \frac{K_{\zeta}}{K_{\beta}} R_{\beta} \right) (R_{\beta} - 1) \sin^2 \bar{\theta} \right] \\ B &= -\frac{1}{\Delta} \left( R_{\zeta} - \frac{K_{\zeta}}{K_{\beta}} R_{\beta} \right) (R_{\beta} - 1) \sin \bar{\theta} \cos \bar{\theta} \\ C &= \frac{1}{\Delta} \left( R_{\beta} - \frac{K_{\beta}}{K_{\zeta}} R_{\zeta} \right) (R_{\zeta} - 1) \sin \bar{\theta} \cos \bar{\theta} \\ D &= \frac{1}{\Delta} \left[ 1 - R_{\zeta} + \left( R_{\beta} - \frac{K_{\beta}}{K_{\zeta}} R_{\zeta} \right) (R_{\zeta} - 1) \sin^2 \bar{\theta} \right] \end{aligned} \quad (3.18)$$

and

$$\begin{aligned} W &= \frac{1}{\Delta} \left[ R_{\beta} + \left( R_{\beta} - \frac{K_{\beta}}{K_{\zeta}} R_{\zeta} \right) (R_{\zeta} - 1) \sin^2 \bar{\theta} \right] \\ X &= -B \\ Y &= -C \\ Z &= \frac{1}{\Delta} \left[ R_{\zeta} + \left( R_{\zeta} - \frac{K_{\zeta}}{K_{\beta}} R_{\beta} \right) (R_{\beta} - 1) \sin^2 \bar{\theta} \right] \end{aligned} \quad (3.19)$$

(The term  $\Delta$  in Eqs. (3.18) and (3.19) is given in Eq. (3.10).)

Equations (3.16–3.19) show that the relative amount of flap and lag motion inboard and outboard of the pitch bearing is determined by the fundamental blade flap and lag stiffnesses  $K_{\beta}$  and  $K_{\zeta}$ , by the SFLC parameters  $R_{\beta}$  and  $R_{\zeta}$ , and by the collective pitch setting.

Now consider the forces and moments on the blade which contribute to the blade pitch equation of motion. Figure 3.27 illustrates the forces acting on a representative section of the blade outboard of the pitch bearing. The figure is oriented such that the blade's feather



axis is directly out of the page. In addition to the terms which are part of the fundamental pitch dynamics ( $I_\theta \ddot{\phi}$ , the pitching moment due to the pitch inertia of the blade section, and  $dM_\phi^{\text{aero}}$ , the perturbation aerodynamic pitching moment acting on the section), there are in-plane aerodynamic and inertial forces ( $F_x$ ) acting on the blade which have a moment arm about the feather axis due to flapping outboard of the pitch bearing ( $\beta_{\text{out}}$ ), and out-of-plane forces ( $F_z$ ) with a moment arm due to lag deflection outboard of the pitch bearing ( $\zeta_{\text{out}}$ ). Radial forces on the blade ( $F_r$ ) also have a moment arm around the feather axis, as a result of the displacement of the feather axis, due to motion inboard of the pitch bearing (from  $\beta_G$  and  $\beta_{\text{in}}$  out-of-plane, and  $\psi_s$  and  $\zeta_{\text{in}}$  in-plane). Finally, there is also an elastic restoring moment at the root of the blade due to control system stiffness ( $K_\theta$ ). Integrating all of these terms along the length of the blade produces the blade pitch equation of motion:

$$M_\phi = \int_e^R \left[ \begin{aligned} & \left( \begin{array}{c} F_z^{\text{aero}} + F_z^{\text{inert}} \\ -F_r^{\text{inert}} (\beta_{\text{in}} + \beta_P + \beta_G) \end{array} \right) (r-e) \zeta_{\text{out}} \\ & - \left( \begin{array}{c} F_x^{\text{aero}} + F_x^{\text{inert}} \\ -F_r^{\text{inert}} (\zeta_{\text{in}} - \psi_s) \end{array} \right) (r-e) \beta_{\text{out}} \\ & + I_\theta \ddot{\phi} + dM_\phi^{\text{aero}} \end{aligned} \right] dr + K_\theta \phi = 0 \quad (3.20)$$

Consider Eq. (3.20) for the case where the blade pitch degree of freedom is dropped. The terms in the last line of Eq. (3.20) would vanish. However, there would still exist moments about the feather axis due to blade in-plane forces with a moment arm due to  $\beta_{\text{out}}$ , and blade out-of-plane forces with a moment arm due to  $\zeta_{\text{out}}$ . Comparing the remaining terms in Eq. (3.20) with the blade flap and lag equations of motion and Eq. (3.13), the pitching moment can be expressed in terms of the components of the elastic flap and lag restoring moments acting along the feather axis:

$$M_\phi = -M_\beta^{\text{elas}} \zeta_{\text{out}} + M_\zeta^{\text{elas}} \beta_{\text{out}} \quad (3.21)$$

Combining Eq. (3.21) with the definitions in Eqs. (3.8) and (3.17) yields

$$\begin{aligned} M_\phi = & - (K_{\beta\beta}\beta + K_{\beta\zeta}\zeta) (Y\beta + Z\zeta) \\ & + (K_{\beta\zeta}\beta + K_{\zeta\zeta}\zeta) (W\beta + X\zeta) \end{aligned} \quad (3.22)$$

The blade pitching moment is thus non-linear in flap and lag. This moment produces a pitch deflection due to flexibility of the control system:

$$\Delta\theta = -\frac{\Delta M_\phi}{K_\theta} \quad (3.23)$$

Linearizing about the steady-state flap and lag deflections  $\bar{\beta}_0$  and  $\bar{\zeta}_0$ , effective pitch-flap and pitch-lag coupling parameters can be defined as

$$\begin{aligned} K_{P\beta} &= -\frac{\partial\theta}{\partial\beta} \\ &= \frac{1}{K_\theta} \left[ \begin{array}{l} 2(YK_{\beta\beta} - WK_{\beta\zeta})\bar{\beta}_0 \\ +(ZK_{\beta\beta} - (X - Y)K_{\beta\zeta} - WK_{\zeta\zeta})\bar{\zeta}_0 \end{array} \right] \end{aligned} \quad (3.24)$$

$$\begin{aligned} K_{P\zeta} &= -\frac{\partial\theta}{\partial\zeta} \\ &= \frac{1}{K_\theta} \left[ \begin{array}{l} (ZK_{\beta\beta} - (X - Y)K_{\beta\zeta} - WK_{\zeta\zeta})\bar{\beta}_0 \\ +2(ZK_{\beta\zeta} - XK_{\zeta\zeta})\bar{\zeta}_0 \end{array} \right] \end{aligned} \quad (3.25)$$

The effective pitch-flap and pitch-lag couplings defined above have been derived following a procedure set out in Ref. 75, significantly expanded to account for the present structural flap-lag coupling formulation.

Note that the effective pitch-flap and pitch-lag coupling parameters both have contributions from the off-diagonal terms in the SFLC formulation. The expressions in Ref. 75 do not include these contributions. If the trim lag angle  $\bar{\zeta}_0$  is assumed negligible, the pitch-flap

coupling parameter  $K_{p\beta}$  (Eq. (3.24)) is purely a result of the presence of off-diagonal terms ( $Y$  and  $K_{\beta\zeta}$ ). Due to the large values of collective pitch present in a tiltrotor, these off-diagonal terms are not small. In the present analysis, the magnitude of  $K_{p\beta}$  is comparable to  $K_{p\zeta}$ . Figure 3.28 shows the variation of these coupling parameters as calculated in the present analysis for the XV-15 semi-span model.

Figures 3.29, 3.30 and 3.31 examine the influence of blade pitch modeling on whirl flutter stability. The results presented thus far for the present analysis did not include the blade pitch equations of motion, but did include the derived pitch-flap and pitch-lag coupling parameters. Comparing these results to those obtained from the present analysis with full pitch dynamics included, it is clear that the coupling parameters do capture the primary influence of blade pitch dynamics on whirl flutter stability. Removing both coupling parameters from the present analysis causes the predicted stability boundary to increase by over 100 knots. This is consistent with the observation, reported in Ref. 29 and elsewhere, that the primary influence of blade pitch dynamics is to effectively couple blade pitch and lag motions, causing a reduction in overall whirl flutter stability. In Ref. 29, Johnson estimates an effective pitch-lag coupling for the XV-15 semi-span model of about  $-0.3$ , based on results from his elastic blade analysis. Near this configuration's stability boundary (308 knots), the present analysis predicts a similar level of coupling ( $K_{p\zeta} = -0.29$ , see Fig. 3.28). In addition to this destabilizing pitch-lag coupling due to blade pitch dynamics (Eq. (3.25)), the present analysis also predicts the presence of a pitch-flap coupling (Eq. (3.24)). To examine the relative influence of these two coupling parameters, Figs. 3.29–3.31 include results for a case where  $K_{p\beta}$  is neglected, while still including  $K_{p\zeta}$ . Comparing this result to the baseline case and to the case where neither coupling was included shows that the pitch-lag coupling parameter is responsible for most of the decrease in flutter speed. The influence of the pitch-flap coupling parameter on flutter speed is not negligible however. Comparing the baseline results from the present analysis to the case where only  $K_{p\beta}$  was neglected shows a change in the stability boundary of about 20 knots. Together, the pitch-flap and pitch-lag coupling parameters are very destabilizing, and both must be correctly

accounted for in order to obtain accurate stability predictions.

Examining Eqs. (3.24) and (3.25), some of the important design parameters which influence the magnitude of these couplings can be identified. First, the couplings depend on the distribution of blade flexibility inboard and outboard of the pitch bearing. The distribution of blade flap and lag flexibility determines how much blade motion occurs outboard of the pitch bearing. Smaller values of the SFLC parameters  $R_\beta$  and  $R_\zeta$  will yield less flap and lag motion outboard of the pitch bearing, causing the terms  $W, X, Y$ , and  $Z$  to all decrease in magnitude, thus reducing the magnitude of the pitch-flap and pitch-lag couplings. If all the blade flexibility is inboard of the pitch bearing ( $R_\beta, R_\zeta = 0$ ), the pitch-flap and pitch-lag couplings in Eqs. (3.24) and (3.25) are eliminated. It is this observation that provides the motivation for the use of a flexured hub on the V-22. The hub flexure allows more trim elastic coning deflection to take place inboard of the blade pitch bearing, thus minimizing the undesirable coupling [39]. The XV-15 semi-span rotor tested at Ames did not have a hub flexure. As a result, its stability boundary was reduced greatly by the presence of the destabilizing couplings. Secondly, the magnitude of the destabilizing pitch-flap and pitch-lag couplings is proportional to rotor precone. In the case of ideal rotor precone, the trim coning deflection  $\bar{\beta}_0$  will be zero, eliminating the couplings ( $\bar{\zeta}_0$  is assumed negligible). For tiltrotors, precone is typically set for the hover condition, leading to higher than ideal precone in cruise. Finally, the couplings are inversely proportional to control system stiffness,  $K_\theta$ . Increased control system stiffness will also reduce the magnitude of the destabilizing couplings.

In the present analysis, the *total* pitch-flap and pitch-lag coupling can be represented as

$$K_{p\beta}^{\text{total}} = \tilde{K}_{p\beta} + \Delta K_{p\beta} \quad (3.26)$$

$$K_{p\zeta}^{\text{total}} = \tilde{K}_{p\zeta} + \Delta K_{p\zeta} \quad (3.27)$$

where the terms  $\Delta K_{p\beta}$  and  $\Delta K_{p\zeta}$  are additional design variables introduced to represent the

influence of other potential sources of pitch-flap and pitch-lag coupling in the rotor blades, such as composite tailoring, blade CG and AC offsets, or advanced blade tip shapes such as sweep and anhedral. The influence of these design parameters on whirl flutter stability stems largely from the coupling between blade bending and pitch that these parameters introduce. While the present analysis does not attempt to model these sources of pitch-flap and pitch-lag coupling in detail, the parameters  $\Delta K_{p\beta}$  and  $\Delta K_{p\zeta}$  may serve as a general representation of the couplings arising from any or all of these sources.

### 3.4 Summary

The tiltrotor stability analysis described in this chapter retains the simplicity of a rigid-blade model, while correctly accounting for the variations in blade frequency, as well as the flap-lag, pitch-flap, and pitch-lag couplings necessary for accurate whirl flutter stability prediction. The model shows good agreement with experimental data and more complex elastic blade analyses. Investigation of the influence of several features of the model revealed:

1. Including the distribution of blade flexibility inboard and outboard of the pitch bearing in the present analysis allows the variation of blade flap and lag frequencies with collective pitch to be modeled from first principles, instead of being treated as an input to the analysis, as in existing rigid-blade formulations.
2. Elastic coupling of blade flap and lag motion due to the off-diagonal structural flap-lag coupling terms in the present analysis contributes significantly to the blade flap and lag elastic restoring moments, and is important for correct evaluation of rotor flap and lag frequencies.
3. The present analysis retains a separate degree of freedom to represent each physical degree of freedom being modeled (e.g. gimbal vs. blade flapping). There is thus no

need to assign separate collective and cyclic modal frequencies. By having both a soft gimbal spring and a stiff blade flap spring, the analysis automatically produces a lower frequency cyclic flap mode and a higher frequency coning mode.

4. The present analysis accounts for blade pitch dynamics, including the effects of blade flexibility outboard of the pitch bearing on the pitch dynamics. Alternatively, expressions for effective pitch-flap and pitch-lag coupling parameters have been extracted from the pitch dynamics, and the pitch equations of motion may be dropped.
5. As has been reported previously, the primary influence of blade pitch dynamics on whirl flutter stability is a destabilizing coupling between blade pitch and blade elastic bending. Using the expressions for both pitch-flap and pitch-lag coupling derived from the blade pitch dynamics, the present formulation accurately predicts this destabilizing influence.
6. Increasing blade flexibility inboard of the pitch bearing, reducing rotor precone, and increasing control system stiffness will all reduce the magnitude of the destabilizing pitch-flap and pitch-lag couplings.

Table 3.1: XV-15 Full-scale Test: Model Properties

Number of blades, $N$	3
Radius, $R$	12.5 ft
Lock number, $\gamma$	3.83
Solidity, $\sigma$	0.089
Lift curve slope, $c_{l\alpha}$	5.7
Rotor rotational speed, $\Omega$	458 RPM
Pitch-gimbal coupling, $K_{PG}$	-0.268
Inertia Properties	
$I_b$	105 slug-ft <sup>2</sup>
$I_\beta$	81.8 slug-ft <sup>2</sup>
$I_{\beta\alpha}$	105 slug-ft <sup>2</sup>
$I_\zeta$	70.4 slug-ft <sup>2</sup>
$I_{\zeta\alpha}$	82.6 slug-ft <sup>2</sup>
$S_\beta$	10.2 slug-ft
$S_\zeta$	8.69 slug-ft
Blade Stiffness	
$\omega_{\beta 0}$	59.8 rad/sec
$\omega_{\zeta 0}$	103 rad/sec
$R_\beta$	1
$R_\zeta$	1

Table 3.2: Boeing 222 Full-scale Test: Model Properties

Number of blades, $N$	3
Radius, $R$	13 ft
Lock number, $\gamma$	4.06
Solidity, $\sigma$	0.115
Lift curve slope, $c_{l\alpha}$	5.7
Rotor rotational speed, $\Omega$	386 RPM
Pitch-gimbal coupling, $K_{PG}$	$N/A$
Inertia Properties	
$I_b$	150 slug-ft <sup>2</sup>
$I_\beta$	138 slug-ft <sup>2</sup>
$I_{\beta\alpha}$	143 slug-ft <sup>2</sup>
$I_\zeta$	129 slug-ft <sup>2</sup>
$I_{\zeta\alpha}$	138 slug-ft <sup>2</sup>
$S_\beta$	14.8 slug-ft
$S_\zeta$	12.6 slug-ft
Blade Stiffness	
$\omega_{\beta 0}$	16.8 rad/sec
$\omega_{\zeta 0}$	32.7 rad/sec
$R_\beta$	1
$R_\zeta$	1



Table 3.3: 1/5-scale V-22 Model: Model Properties

Number of blades, $N$	3
Radius, $R$	3.8 ft
Lock number, $\gamma$	5.34
Solidity, $\sigma$	0.105
Lift curve slope, $c_{l\alpha}$	5.9
Rotor rotational speed, $\Omega$	742–888 RPM
Pitch-gimbal coupling, $K_{PG}$	-0.268
Inertia Properties	
$I_b$	0.229 slug-ft <sup>2</sup>
$I_\beta$	0.179 slug-ft <sup>2</sup>
$I_{\beta\alpha}$	0.200 slug-ft <sup>2</sup>
$I_\zeta$	0.159 slug-ft <sup>2</sup>
$I_{\zeta\alpha}$	0.185 slug-ft <sup>2</sup>
$S_\beta$	0.0898 slug-ft
$S_\zeta$	0.0771 slug-ft
Blade Stiffness	
$\omega_{\beta 0}$	90 rad/sec
$\omega_{\zeta 0}$	134 rad/sec
$R_\beta$	1
$R_\zeta$	1

Table 3.4: WRATS Model: Model Properties

Number of blades, $N$	3
Radius, $R$	3.8 ft
Lock number, $\gamma$	5.34
Solidity, $\sigma$	0.105
Lift curve slope, $c_{l\alpha}$	5.9
Rotor rotational speed, $\Omega$	742–888 RPM
Pitch-gimbal coupling, $K_{PG}$	-0.268
Inertia Properties	
$I_b$	0.229 slug-ft <sup>2</sup>
$I_\beta$	0.179 slug-ft <sup>2</sup>
$I_{\beta\alpha}$	0.200 slug-ft <sup>2</sup>
$I_\zeta$	0.159 slug-ft <sup>2</sup>
$I_{\zeta\alpha}$	0.185 slug-ft <sup>2</sup>
$S_\beta$	0.0898 slug-ft
$S_\zeta$	0.0771 slug-ft
Blade Stiffness	
$\omega_{\beta 0}$	31.9 rad/sec
$\omega_{\zeta 0}$	134 rad/sec
$R_\beta$	0.10
$R_\zeta$	0.23

Table 3.5: WRATS SASIP Model: Model Properties

Number of blades, $N$	4
Radius, $R$	3.8 ft
Lock number, $\gamma$	6.19
Solidity, $\sigma$	0.105
Lift curve slope, $c_{l\alpha}$	5.9
Rotor rotational speed, $\Omega$	742–888 RPM
Pitch-flap coupling, $K_{P\beta}$	0.268
Pitch-lag coupling, $K_{P\zeta}$	0.158
Inertia Properties	
$I_b$	0.1492 slug-ft <sup>2</sup>
$I_\beta$	0.1263 slug-ft <sup>2</sup>
$I_{\beta\alpha}$	0.1367 slug-ft <sup>2</sup>
$I_\zeta$	0.0887 slug-ft <sup>2</sup>
$I_{\zeta\alpha}$	0.1095 slug-ft <sup>2</sup>
$S_\beta$	0.0680 slug-ft
$S_\zeta$	0.0380 slug-ft
Blade Stiffness	
$\omega_{\beta 0}$	0.511 rad/sec
$\omega_{\zeta 0}$	48.7 rad/sec
$R_\beta$	0
$R_\zeta$	0

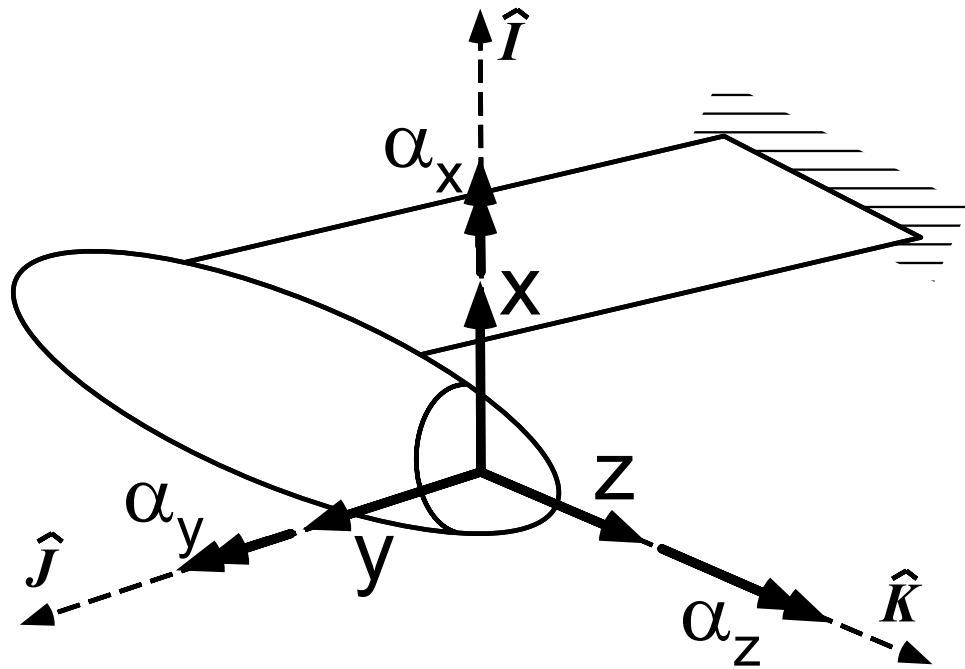


Figure 3.1: Degrees of freedom at hub attachment point

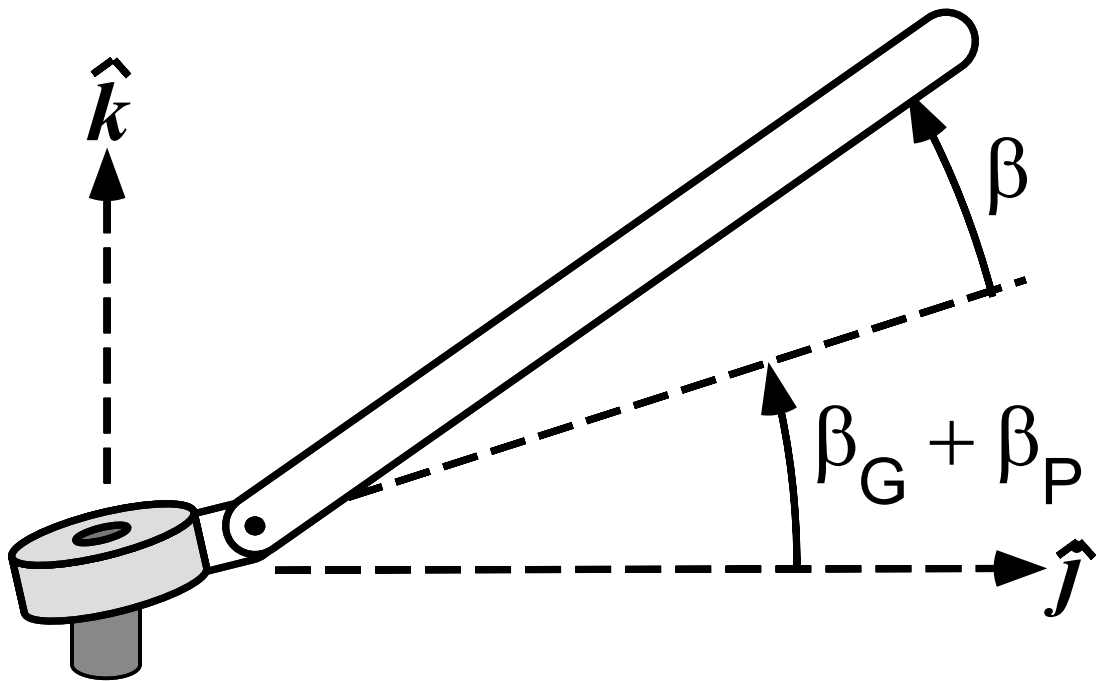


Figure 3.2: Gimbal and blade flapping degrees of freedom

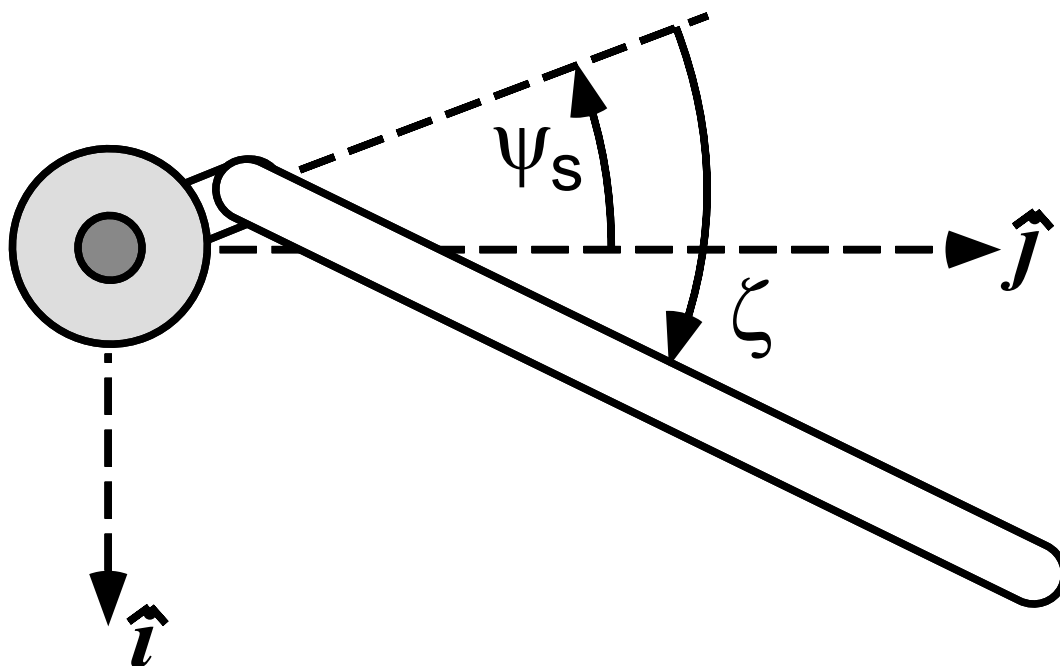


Figure 3.3: Rotor azimuthal position and blade lead-lag degrees of freedom

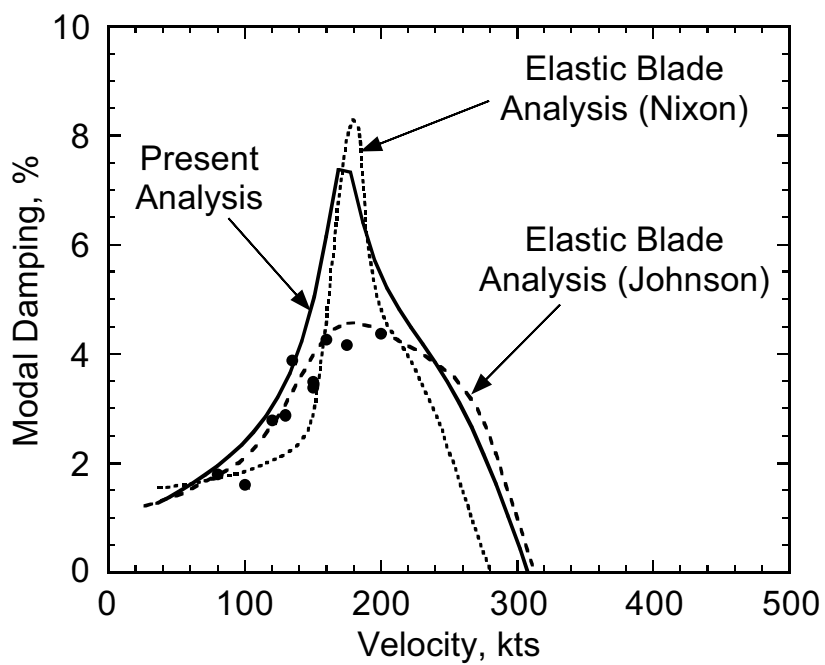


Figure 3.4: Semi-span XV-15 – Damping of wing vertical bending mode vs. airspeed

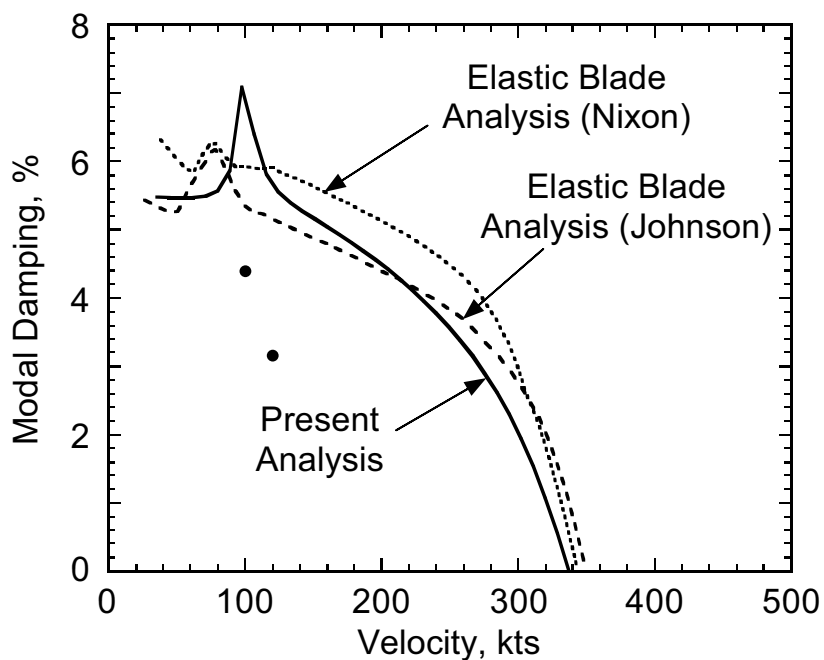


Figure 3.5: Semi-span XV-15 – Damping of wing chordwise bending mode vs. airspeed

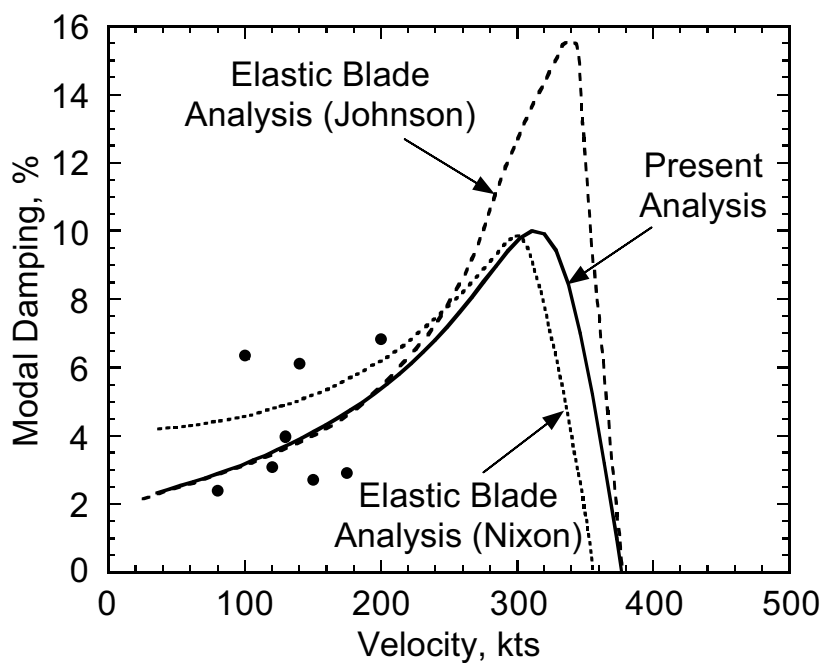


Figure 3.6: Semi-span XV-15 – Damping of wing torsion mode vs. airspeed

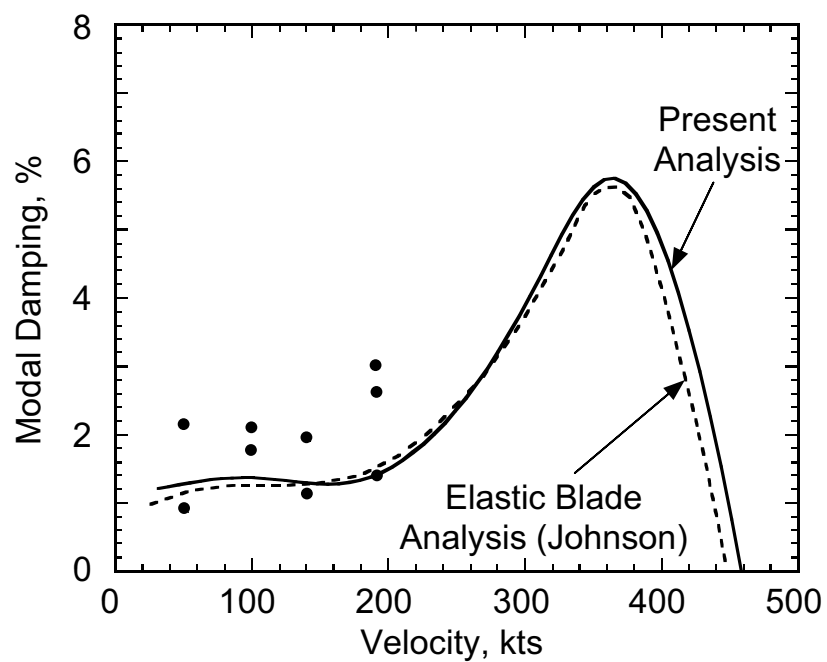


Figure 3.7: Boeing Model 222 – Damping of wing vertical bending mode vs. airspeed

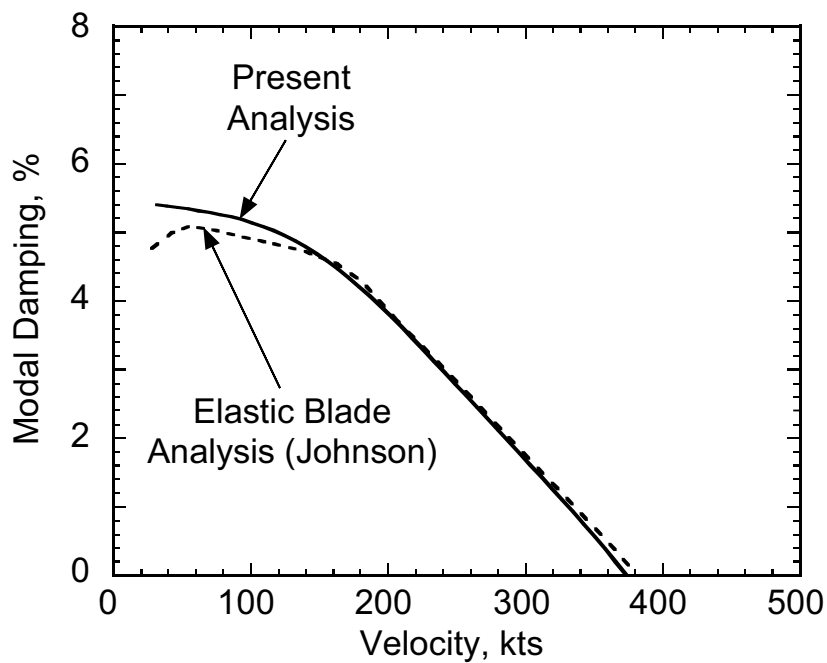


Figure 3.8: Boeing Model 222 – Damping of wing chordwise bending mode vs. airspeed

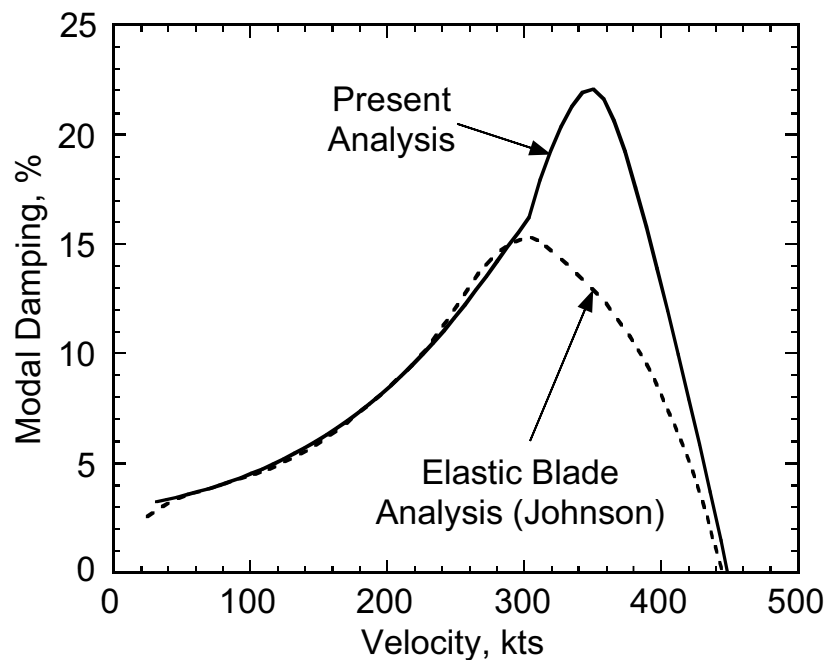


Figure 3.9: Boeing Model 222 – Damping of wing torsion mode vs. airspeed

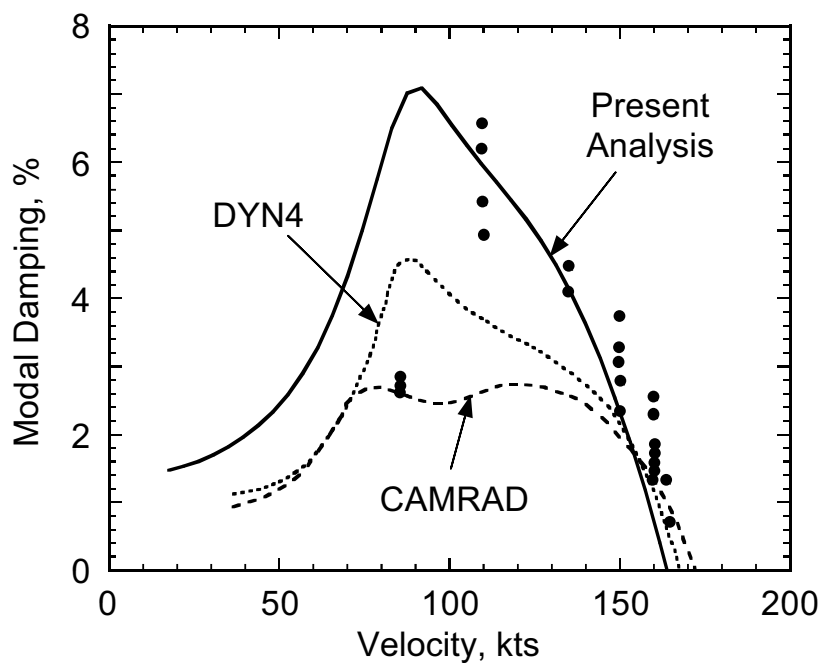


Figure 3.10: 1/5-scale V-22 model – Damping of wing vertical bending mode vs. airspeed (85% RPM, on-downstop, air)



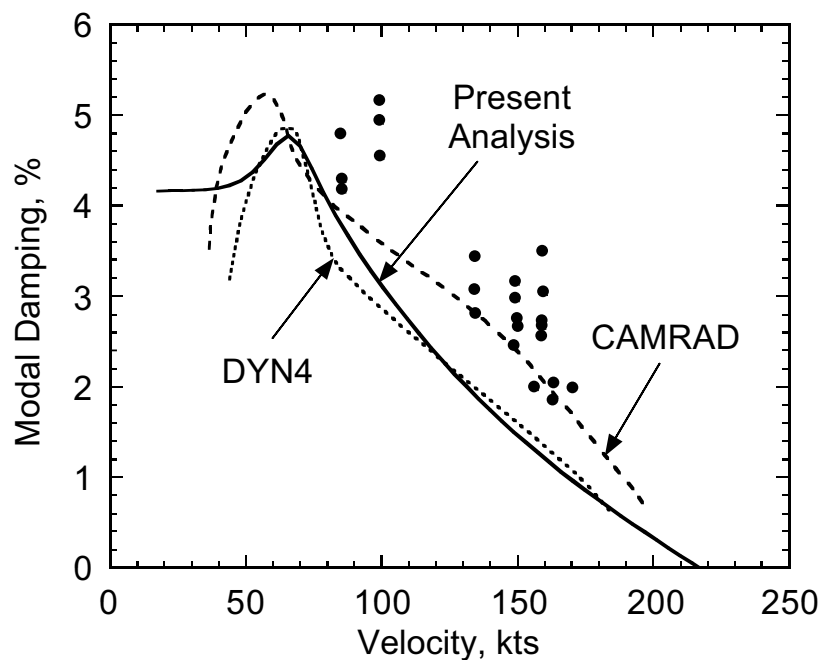


Figure 3.11: 1/5-scale V-22 model – Damping of wing chordwise bending mode vs. airspeed (85% RPM, on-downstop, air)

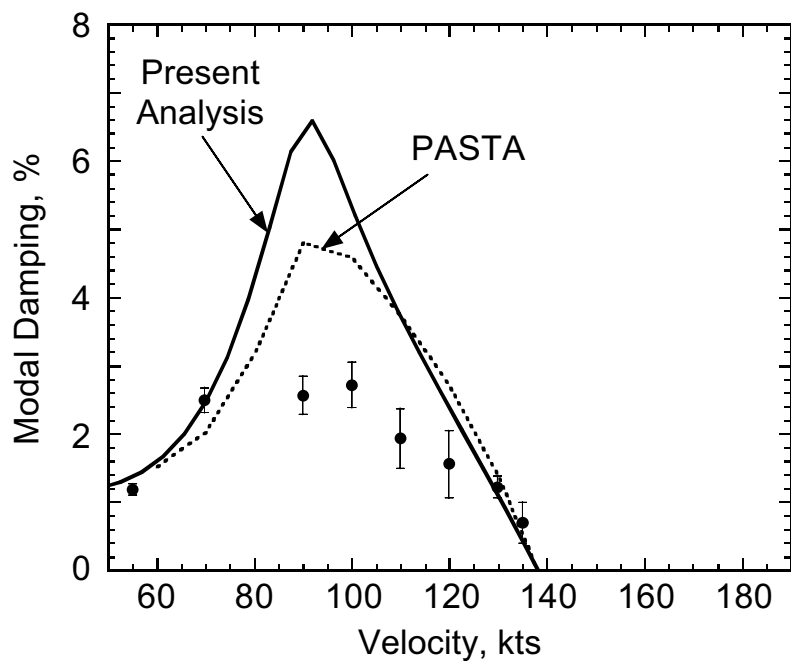


Figure 3.12: WRATS model – Damping of wing vertical bending mode vs. airspeed (742 RPM, off-downstop, air)

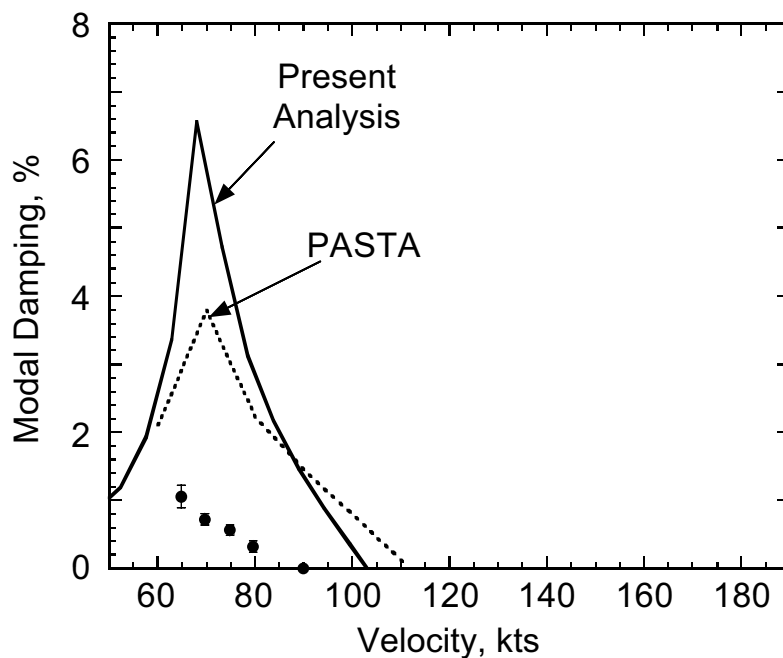


Figure 3.13: WRATS model – Damping of wing vertical bending mode vs. airspeed (888 RPM, off-downstop, air)

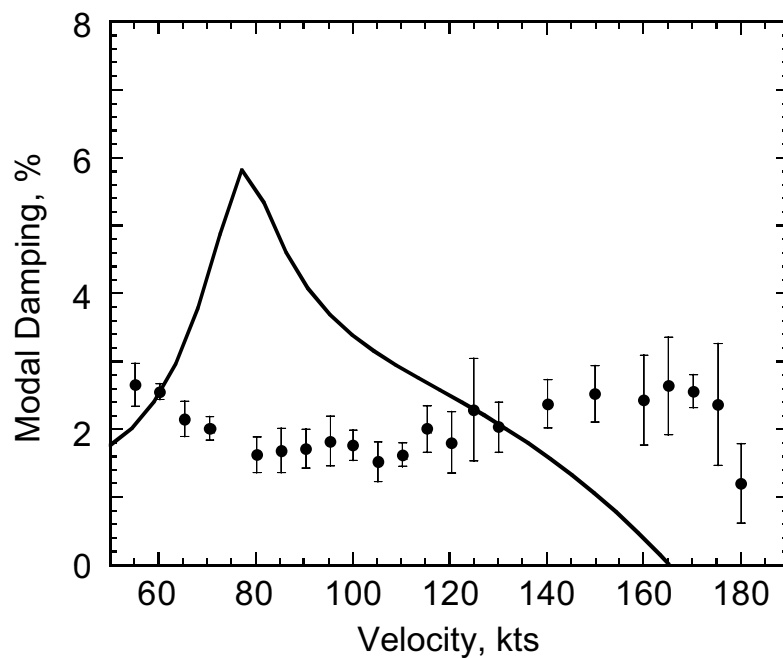


Figure 3.14: WRATS model – Damping of wing vertical bending mode vs. airspeed (770 RPM, on-downstop, air)

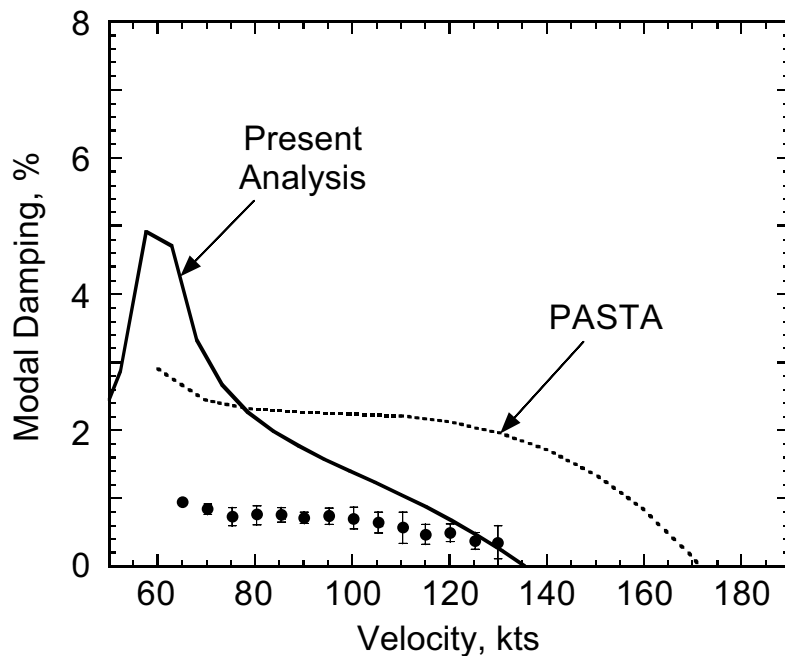


Figure 3.15: WRATS model – Damping of wing vertical bending mode vs. airspeed (888 RPM, on-downstop, air)

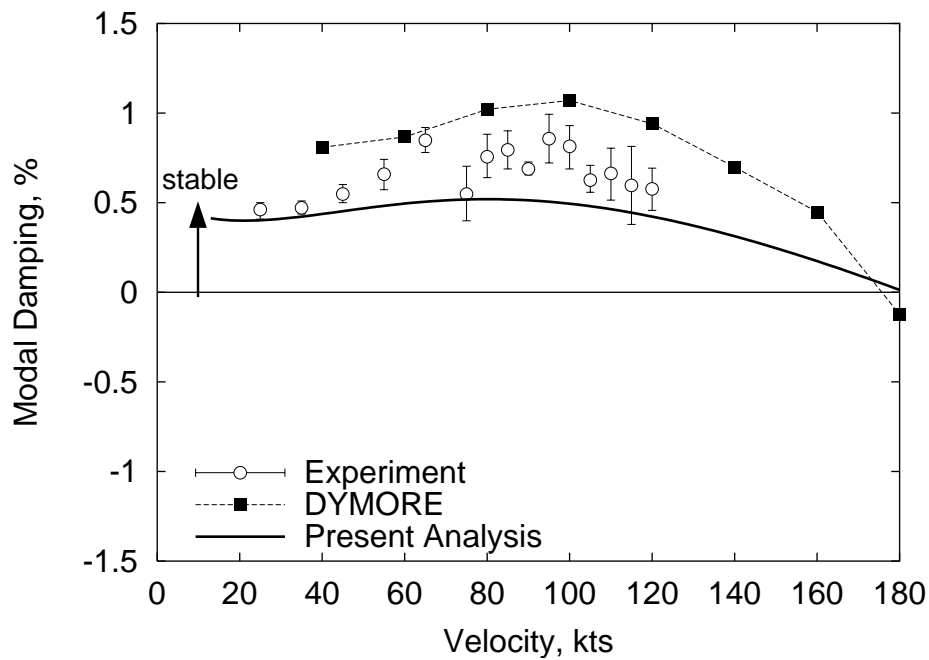


Figure 3.16: WRATS SASIP model – Damping of wing vertical bending mode vs. airspeed (550 RPM, on-downstop, air)

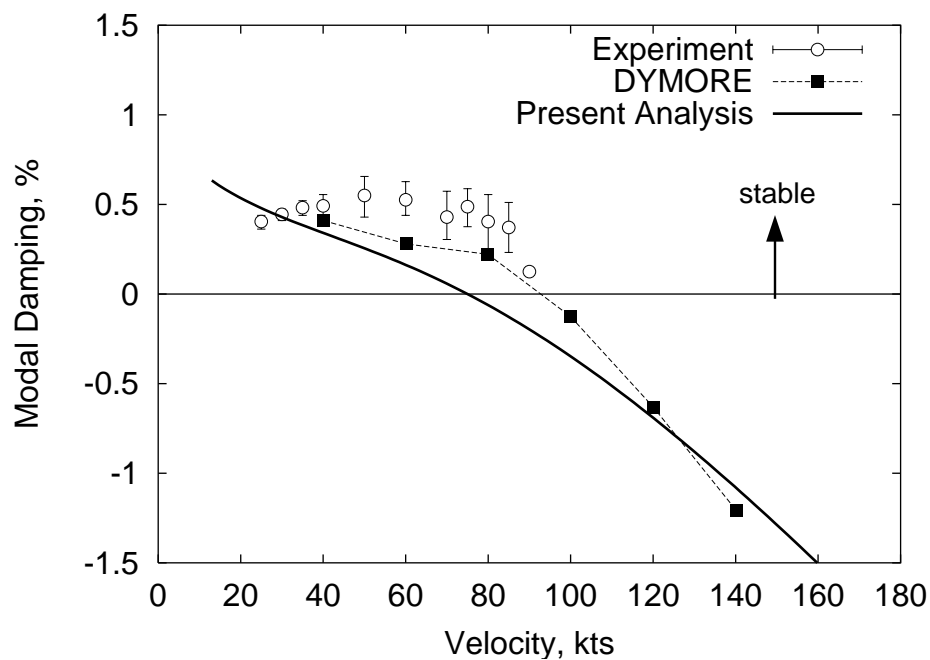


Figure 3.17: WRATS SASIP model – Damping of wing vertical bending mode vs. airspeed (550 RPM, off-downstop, air)

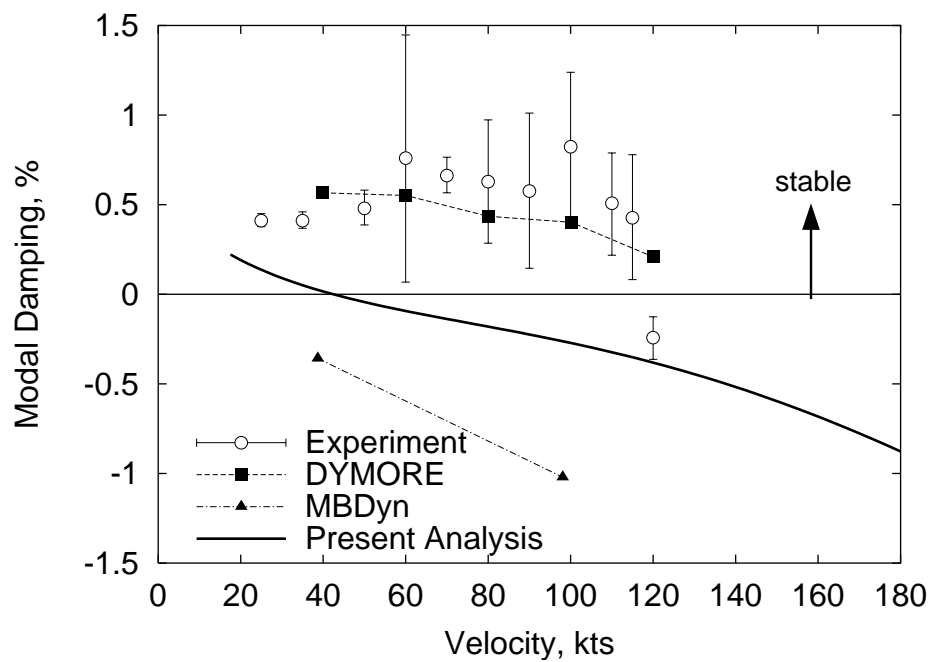


Figure 3.18: WRATS SASIP model – Damping of wing vertical bending mode vs. airspeed (742 RPM, on-downstop, air)

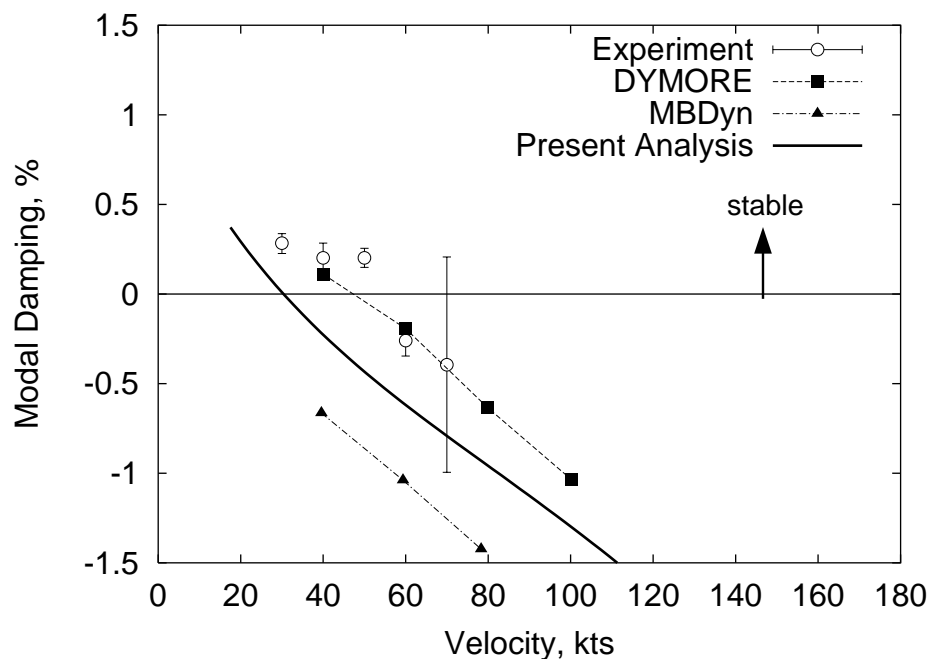


Figure 3.19: WRATS SASIP model – Damping of wing vertical bending mode vs. airspeed (742 RPM, off-downstop, air)

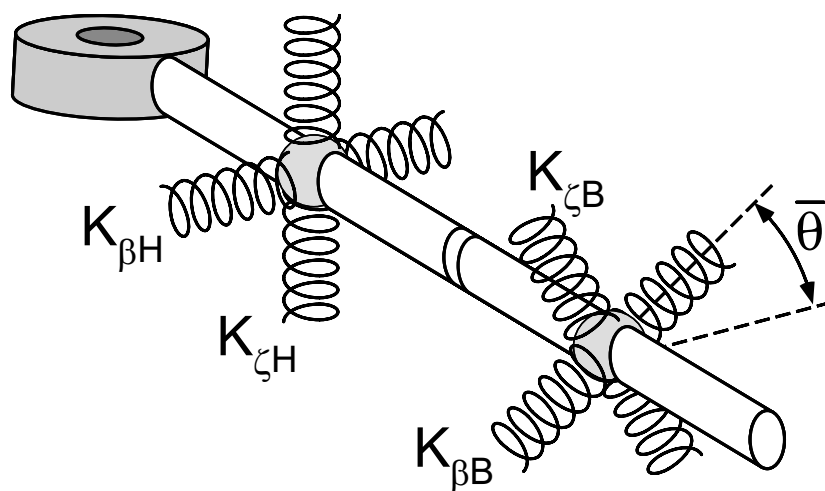


Figure 3.20: Arrangement of springs used to model blade Structural Flap Lag-Coupling (SFLC)

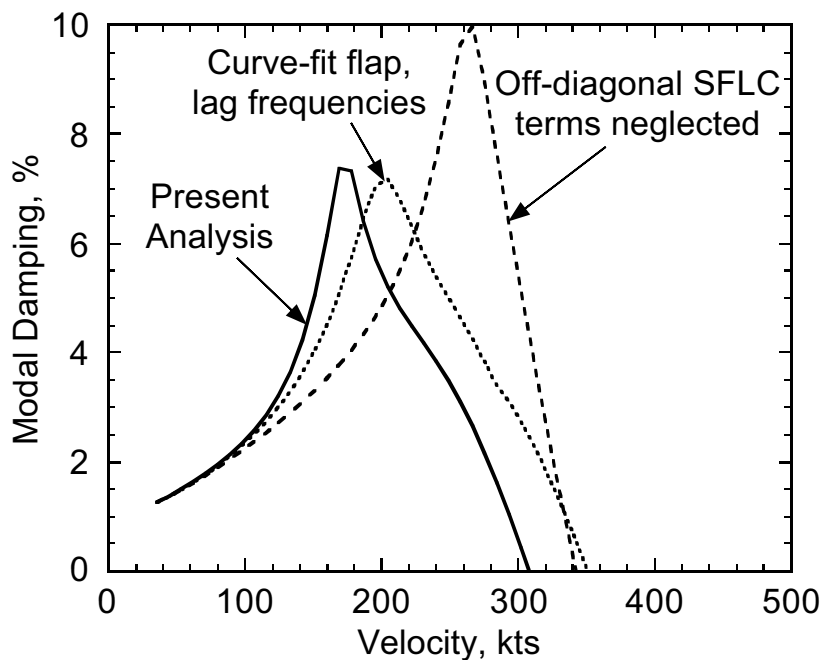


Figure 3.21: Influence of blade Structural Flap-Lag Coupling (SFLC) on damping of wing vertical bending mode

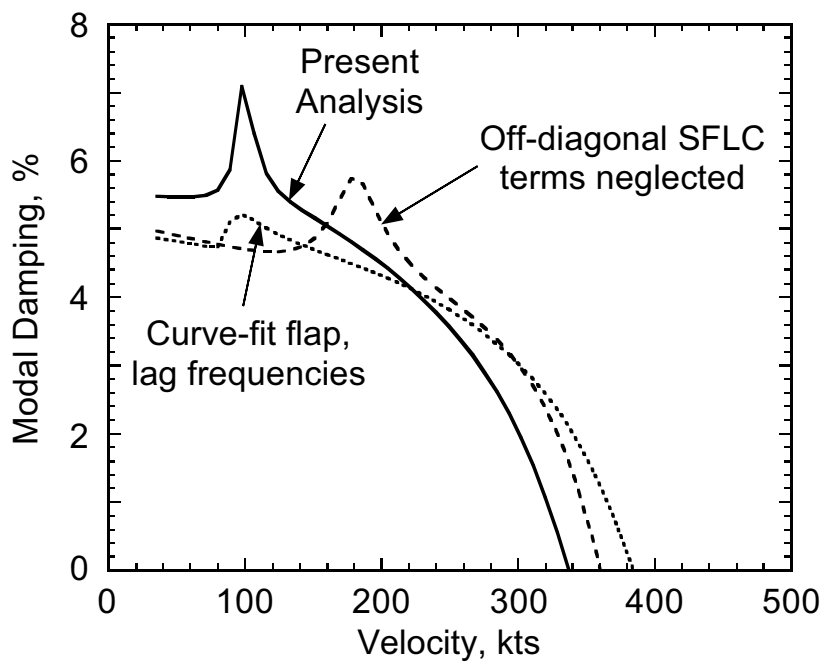


Figure 3.22: Influence of blade Structural Flap-Lag Coupling (SFLC) on damping of wing chordwise bending mode

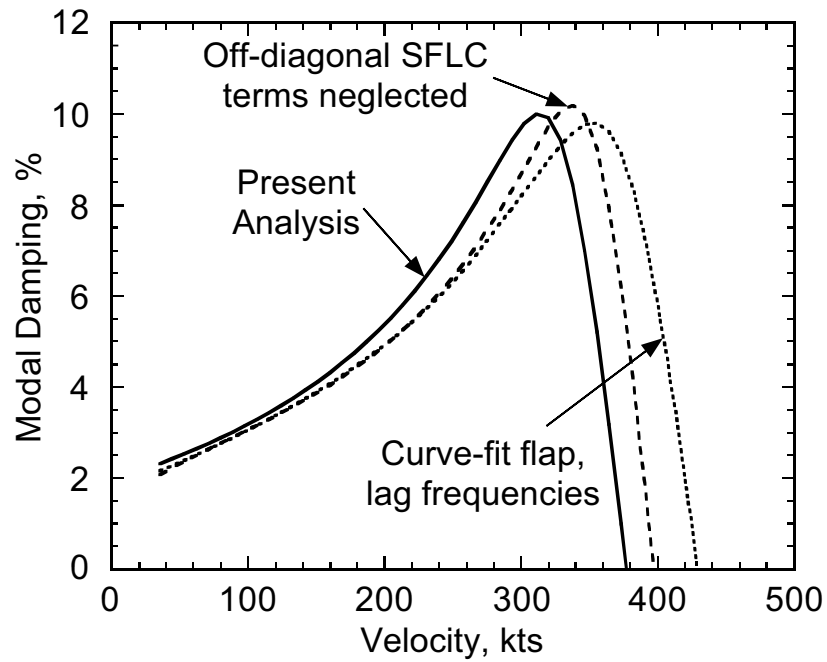


Figure 3.23: Influence of blade Structural Flap-Lag Coupling (SFLC) on damping of wing torsion mode

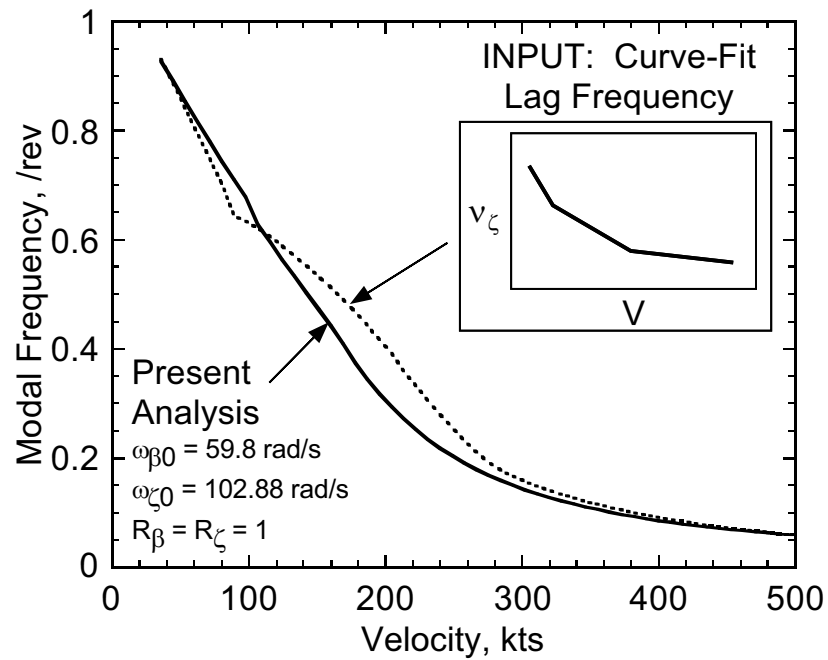


Figure 3.24: Variation of rotor low-frequency lag mode frequency (Curve-fit variation of lag frequency from the rigid blade analysis of Ref. 1)

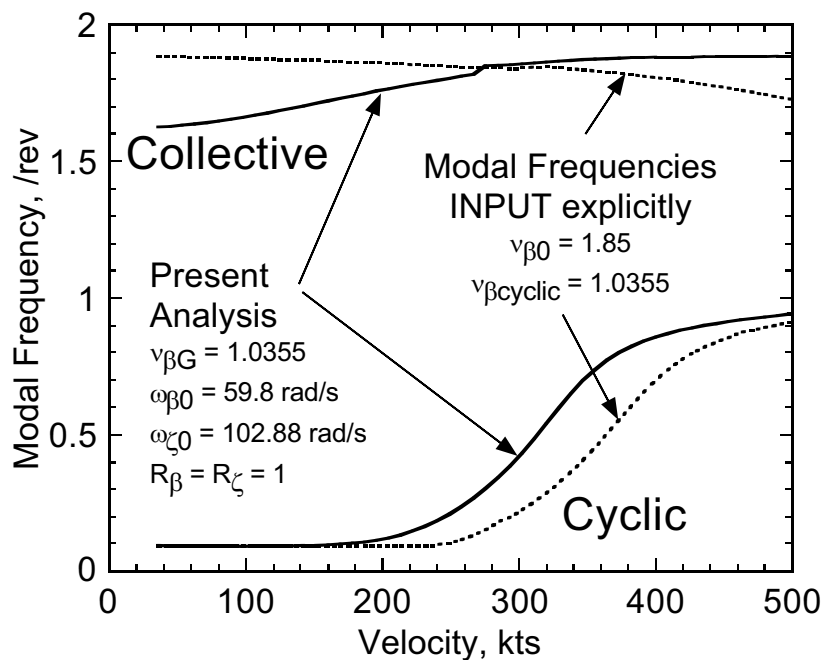


Figure 3.25: Variation of rotor cyclic and collective flap frequencies (Explicit cyclic and collective modal frequencies from Ref. 2)

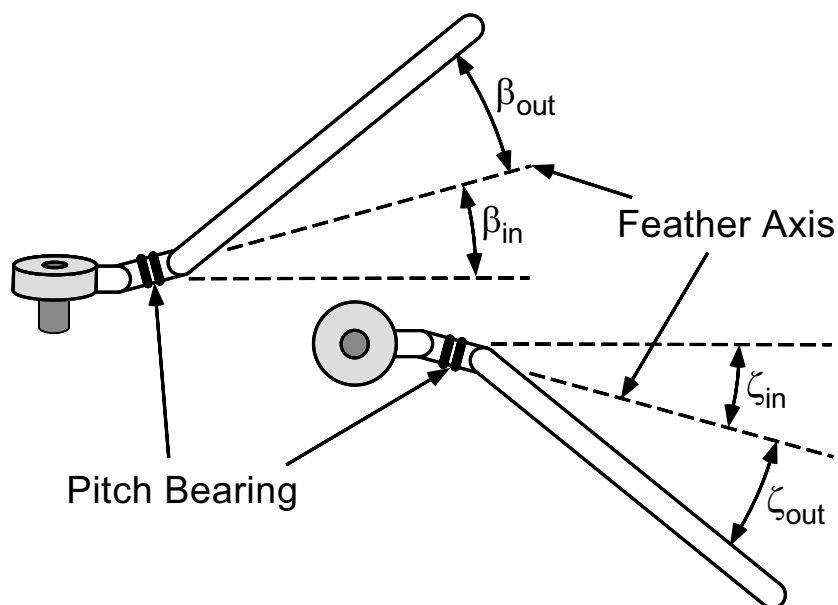


Figure 3.26: Blade flap and lag angles inboard and outboard of pitch bearing



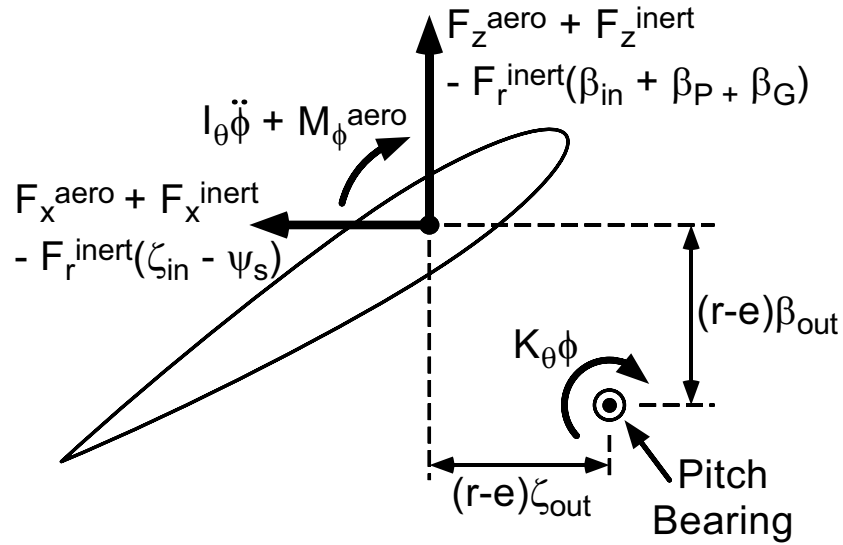


Figure 3.27: Definition of forces and moments contributing to blade pitch equation of motion

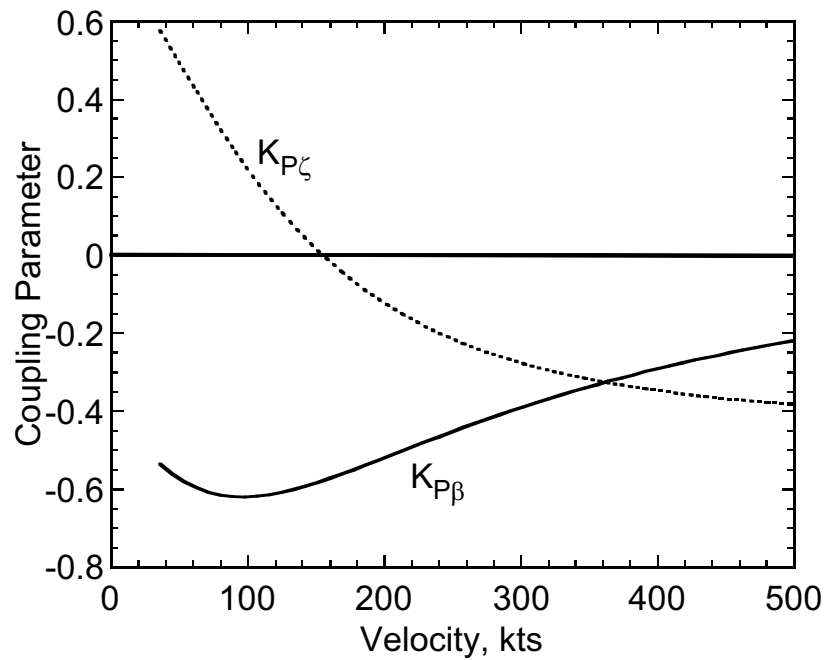


Figure 3.28: Variation of effective pitch-flap and pitch-lag coupling parameters

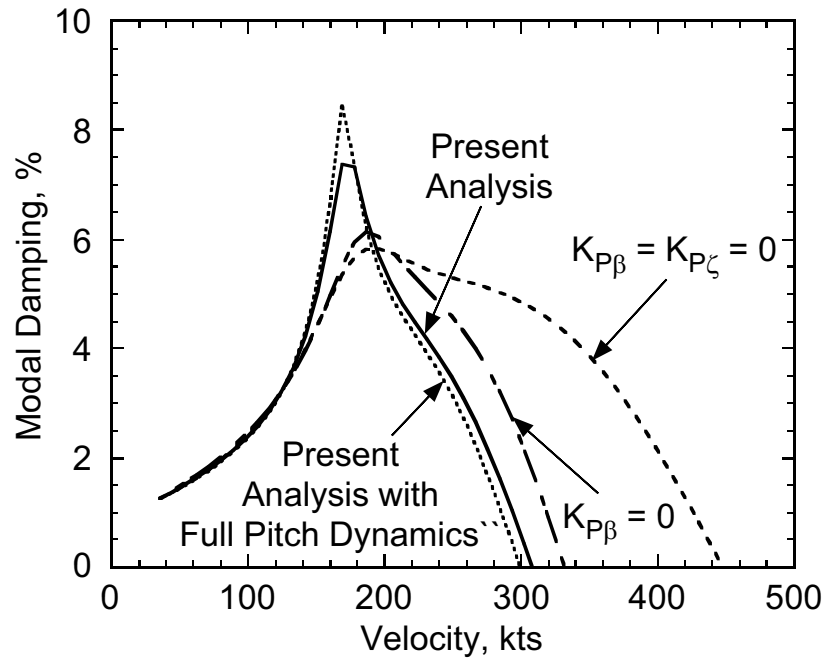


Figure 3.29: Influence of blade pitch modeling on damping of wing vertical bending mode

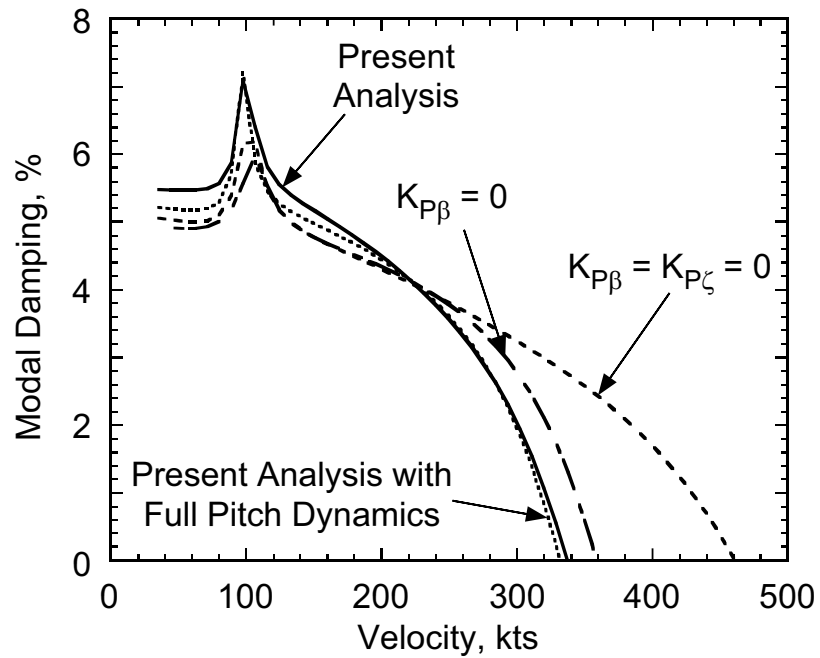


Figure 3.30: Influence of blade pitch modeling on damping of wing chordwise bending mode

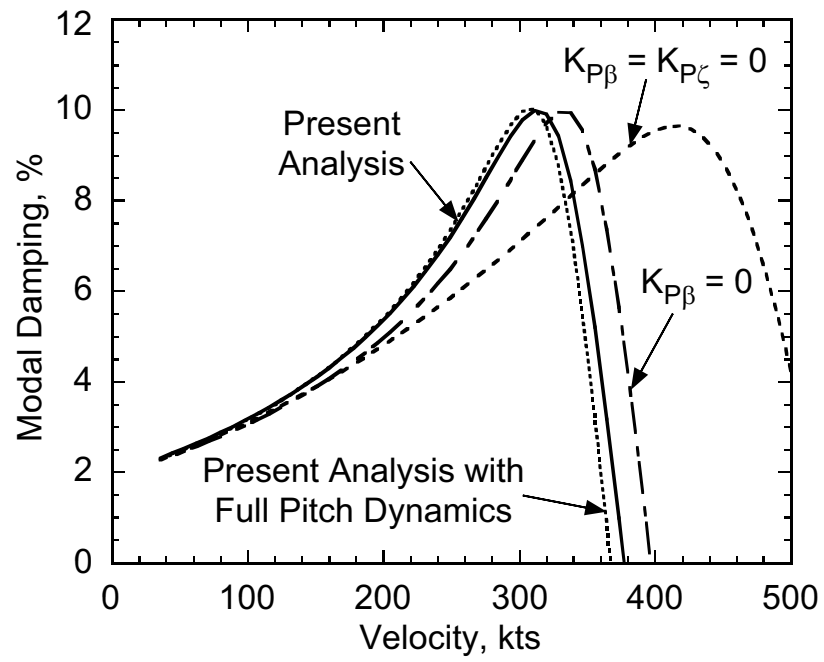


Figure 3.31: Influence of blade pitch modeling on damping of wing torsion mode

## Chapter 4

# Optimization of Rotor and Wing Design Parameters

The results of a computational study on the effects of various design parameters on tiltrotor whirl flutter characteristics are reported. First, effect of individual variations of rotor/wing design parameters are considered, including design variables such as the distribution of rotor flexibility inboard/outboard of the pitch bearing, which have not been previously addressed in the literature. The parametric studies are followed by use of formal design optimization techniques. When tight constraints are imposed on the design variables during the optimization process, the resulting optimal design is consistent with the trends observed in the parametric studies. The rotor parameters most influential in increasing the critical whirl-flutter speed are: pitch-flap and pitch-lag couplings, and distribution of flap flexibility inboard/outboard of the pitch bearing. When the constraints on the rotor design variables are relaxed, the resulting optimal designs differ from expectations based on trends observed in parametric studies. Of particular interest is the reduced sensitivity to the  $\delta_3$  angle (related to pitch-gimbal coupling). With large negative  $\delta_3$  values permissible, design of tiltrotors with four or more blades may be feasible. The most influential wing design parameters are wing vertical bending and torsion stiffness, and vertical bending-torsion

coupling. However, the rotor design parameters have a far greater stabilizing influence, as compared to the wing design parameters.

## 4.1 Wing model

The previous chapter provides an overview of the rotor model used in this investigation. The semi-span cantilevered wing model used in this chapter is based upon the model developed by Johnson in Ref. [2]. The wing is represented using only the first three structural modes: vertical bending ( $q_1$ ), chordwise bending ( $q_2$ ), and torsion ( $p$ ). The three wing modes are normalized such that unity values of  $q_1$ ,  $q_2$ , and  $p$  correspond to a wingtip vertical displacement of one rotor radius, a wingtip lateral displacement of one rotor radius, and a wingtip twist rotation of one radian, respectively. Offsets of the wing, pylon, and rotor centers of gravity relative to the wing elastic axis are considered which couple wing bending and torsion motion. In addition to these inertial couplings which are present in Johnson's original model, elastic coupling parameters have been added to the present analysis. These parameters represent wing elastic bending-torsion coupling due to composite tailoring of the wing structure. The modal wing model does not provide the level of structural detail necessary to relate the elastic coupling parameters to physical design parameters. The coupling parameters are nevertheless useful for determining general design requirements for improved aeroelastic stability, such as determining what sort of coupling should be introduced (bend-up/twist-down vs. bend-up/twist-up, for example). The vertical bending-torsion coupling parameter  $K_{Pq1}$  and chordwise bending-torsion coupling parameter  $K_{Pq2}$  are included in the wing structural stiffness matrix as off-diagonal coupling terms. The wing structural stiffness matrix can then be written as:

$$\begin{bmatrix} K_{q1} & 0 & K_{Pq1} \\ 0 & K_{q2} & K_{Pq2} \\ K_{Pq1} & K_{Pq2} & K_p \end{bmatrix} \quad (4.1)$$

where  $K_{q1}$ ,  $K_{q2}$ ,  $K_p$ , are the fundamental stiffnesses associated with the wing modes.

## 4.2 Parametric study

Before beginning formal optimization studies, a parametric study is conducted. The study provides an understanding of the influence of individual design variables on whirl flutter stability. The tiltrotor configuration used is the full-scale XV-15 semi-span model. Table 3.1 lists some of the important model parameters used in the present analysis (see Ref. 2 for a more complete listing of model properties).

### 4.2.1 Influence of individual rotor design parameters

The rotor design parameters considered in this investigation are: (1) blade flatwise bending stiffness, in terms of the non-rotating natural frequency  $\omega_{\beta 0}$ , (2) blade chordwise bending stiffness, in terms of the non-rotating natural frequency  $\omega_{\zeta 0}$ , (3) gimbal spring stiffness, denoted by  $\omega_{\beta G 0}$ , the non-rotating gimbal frequency, (4) pitch-gimbal coupling, expressed as a “ $\delta_3$ ” angle, (5) blade pitch-flap coupling parameter,  $\Delta K_{p\beta}$ , which is added to  $\tilde{K}_{p\beta}$  (Eq. (3.24)) to obtain the total pitch-flap coupling, (6) blade pitch-lag coupling parameter  $\Delta K_{p\zeta}$ , which is added to  $\tilde{K}_{p\zeta}$  (Eq. (3.25)) to obtain the total pitch-lag coupling, (7) distribution of blade flatwise bending flexibility,  $R_\beta$ , and (8) chordwise bending flexibility,  $R_\zeta$  (inboard/outboard of the pitch bearing), and (9) control system stiffness, expressed in terms of the frequency  $\omega_\phi$ . The nominal value for each of these design variables for the baseline configuration are given in Table 4.1.

Changes in some of the rotor design parameters considered in this study influence the magnitudes of  $\tilde{K}_{p\beta}$  and  $\tilde{K}_{p\zeta}$ , the pitch-flap and pitch-lag couplings due to blade flexibility distribution given by Eqs. (3.24) and (3.25). These couplings have a powerful influence on whirl flutter stability (compare Figs. 4.1 and 4.2), and it is useful to identify whether the primary impact on whirl flutter from a change in a given parameter is due to a direct

influence on the system dynamics (such as through a change in modal characteristics), or from its effect on the magnitude of pitch-flap and pitch-lag coupling. Thus the influence of each design variable on overall whirl flutter stability can be better understood.

Figures 4.4–4.14 show the influence of the various rotor design variables on the critical whirl flutter speed. The influence of the various design variables may be summarized as follows:

1. Altering the blade flatwise and chordwise bending stiffness properties can influence stability two ways. The change in blade stiffness will affect the variation of rotor frequencies with collective pitch, influencing the interaction between rotor and wing modes. In addition, a change in blade stiffness affects the magnitude of the destabilizing pitch-flap and pitch-lag couplings given in Eqs. (3.24) and (3.25). In the case of increased flatwise bending stiffness (Fig. 4.4), the stabilizing influence comes mainly through the change in rotor frequencies. Increased flatwise bending stiffness increases the frequency of the rotor lag modes. The shift in low-frequency cyclic lag mode frequency in particular changes the interaction of that mode with the wing modes, increasing damping in the wing modes. Increased flatwise bending stiffness slightly reduces the magnitude of  $\tilde{K}_{p\zeta}$ , but also slightly increases the magnitude of  $\tilde{K}_{p\beta}$ , so the net influence of the changes in pitch-flap and pitch-lag coupling is negligible. If the influence of changes in blade flatwise bending stiffness on flutter speed was examined while holding  $\tilde{K}_{p\beta}$  and  $\tilde{K}_{p\zeta}$  to their baseline values, the results would be almost exactly the same as shown in Fig. 4.4.

For reduced chordwise bending stiffness (Fig. 4.5), the increased stability comes almost entirely through a decrease in the magnitude of  $\tilde{K}_{p\zeta}$ . Negative pitch-lag coupling as calculated by Eq. (3.25) is reduced by a third at high speeds, from about -0.3 to -0.2, while the pitch-flap coupling from Eq. (3.24) remains virtually unchanged. Figure 4.6 illustrates the reduction in  $\tilde{K}_{p\zeta}$  as a result of reduced chordwise bending stiffness. If  $\tilde{K}_{p\beta}$  and  $\tilde{K}_{p\zeta}$  are held to the baseline values shown in Fig. 4.3, changes in

blade chordwise bending stiffness have almost no influence on flutter speed.

The stabilizing influence shown in Fig. 4.5 comes from a reduction in magnitude of the effective pitch-flap and pitch-lag couplings (Eqs. (3.24) and (3.25)) as a result of the reduction in lag stiffness. Figure 4.6 shows pitch-lag coupling reduced by about a third as a result of reduced lag stiffness.

2. Increased gimbal spring stiffness has only a slight beneficial influence on flutter speed. In Ref. 1, changes in cyclic flap frequency (equivalent to gimbal natural frequency in the present analysis) had a somewhat larger effect on stability than in the present analysis. However, the range of frequency variation considered in Ref. 1 (0.9–2.5/rev) is much larger than in the present analysis and is unlikely to be attainable in practice. Reference 13 points out that although increased flapping restraint can be stabilizing, design constraints on allowable blade loads place an upper limit on flap restraint stiffness which may preclude taking advantage of this parameter to increase aeroelastic stability. In the present analysis, a variation in  $\Delta\omega_{\beta G0}$  of  $\pm 100\%$  corresponds to a rotating frequency variation of 1–1.07/rev. Since the XV-15's gimbal spring is composed of a relatively soft elastomeric material, changes in stiffness required to achieve a  $\pm 100\%$  change in  $\Delta\omega_{\beta G0}$  are feasible.
3. The  $\delta_3$  angle (Fig. 4.8) gives rise to a coupling between blade pitch and gimbal flapping, and has a strong influence on aeroelastic stability. The baseline value of  $\delta_3$  for the XV-15 is  $-15^\circ$ . In Fig. 4.8, we can see that more negative values of  $\delta_3$  are very destabilizing. The maximum increase in flutter speed occurs as  $\delta_3$  approaches  $0^\circ$ , followed by a sharp decrease in flutter speed for positive  $\delta_3$  angles, as a flap/lag instability is encountered. These results are consistent with the descriptions in Ref. 16 and elsewhere of the influence of  $\delta_3$  on stiff-inplane proprotor stability.

The baseline  $\delta_3$  angle of  $-15^\circ$  represents a trade-off between conflicting design requirements, as described in Ref. 3. Larger (more negative) values of  $\delta_3$  are desirable



to minimize transient blade flapping response, while a  $\delta_3$  angle close to zero is beneficial for aeroelastic stability. Furthermore, due to geometric constraints, it is difficult to design a control mechanism with a  $\delta_3$  angle close to zero, especially for gimbaled rotors which have effectively zero flapping hinge-offset. For these reasons, it may be difficult to exploit reduced  $\delta_3$  angles to improve tiltrotor aeroelastic stability, and it may in fact be desirable to identify design configurations which allow for larger negative values of  $\delta_3$  while still maintaining adequate stability boundaries.

4. The design variables  $\Delta K_{p\beta}$  in Fig. 4.9 and  $\Delta K_{p\zeta}$  in Fig. 4.10 refer to an additional value of pitch-flap and pitch-lag coupling, respectively, that are added to the couplings due to blade flexibility distribution,  $\tilde{K}_{p\beta}$  and  $\tilde{K}_{p\zeta}$ , to obtain the total values of blade pitch-flap and pitch-lag coupling. Positive values of additional pitch-flap (Fig. 4.9) and pitch-lag (Fig. 4.10) couplings are both stabilizing. Positive pitch-lag coupling has a particularly strong stabilizing influence. This is consistent with the findings reported in Refs. 1 and 49, where composite couplings that produced lag-back, pitch-down motions in the blade were stabilizing.

It should be noted in Fig. 4.10 that the stabilizing influence of  $\Delta K_{p\zeta}$  becomes particularly strong as the parameter reaches values near +0.3. At high airspeeds near the flutter boundary, the baseline level of pitch-lag coupling due to blade flexibility distribution calculated in Eq. (3.25) is approximately -0.3 (see Fig. 4.3). The critical flutter speed in Fig. 4.10 increases most sharply when the positive pitch-lag coupling from  $\Delta K_{p\zeta}$  completely offsets the negative contribution from  $\tilde{K}_{p\zeta}$ . Thus, the important criteria to ensure a beneficial influence on aeroelastic stability is that the *total* level of pitch-lag coupling (amount of coupling from Eq. (3.25) plus any pitch-lag coupling contribution from other sources) in the rotor be positive (lag-back, pitch-down).

5. The influence of blade flexibility distribution inboard and outboard of the pitch bearing is examined in Figs. 4.11 and 4.13. As was the case for blade stiffness, changes in blade flexibility distribution may influence stability by directly changing the vari-

ation of blade frequencies with collective pitch, or by effecting the magnitude of  $\tilde{K}_{p\beta}$  and  $\tilde{K}_{p\zeta}$ , the pitch-flap and pitch-lag couplings due to blade flexibility distribution. Figure 4.11 shows that  $R_\beta$ , the distribution of blade flatwise bending flexibility, is a powerful parameter. As the flap flexibility inboard of the pitch bearing increases (the parameter  $R_\beta$  becomes smaller), the amount of pitch-flap and pitch-lag coupling from Eqs. (3.24) and (3.25) is reduced sharply (as shown in Fig. 4.12), increasing the flutter speed. It is this observation that provides the motivation for the use of a flexured hub on the V-22. The hub's coning flexure allows more trim elastic coning deflection to take place inboard of the blade pitch bearing, thus minimizing the undesirable coupling, as reported in Ref. 76. Moving some of the blade flatwise bending flexibility inboard of the pitch bearing also influences the variation of rotor lag frequency with collective pitch. Figure 4.11 shows that even if  $\tilde{K}_{p\beta}$  and  $\tilde{K}_{p\zeta}$  are held to their baseline values, increased flap flexibility inboard of the pitch bearing still has some stabilizing influence. As was the case for increased blade flatwise bending stiffness, this stability increase is due to a change in the nature of the interaction of the rotor low-frequency cyclic lag mode with the wing modes. The total influence of changes in the parameter  $R_\beta$  on whirl flutter stability is thus a result of both rotor frequency changes and a reduction in the destabilizing pitch-flap and pitch-lag couplings.

Increased blade chordwise flexibility inboard of the pitch bearing (Fig. 4.13) has a slightly destabilizing influence on stability. Reducing the parameter  $R_\zeta$  from its baseline value of 1 causes a stabilizing positive increase in  $\tilde{K}_{p\zeta}$ , but also a destabilizing negative change in  $\tilde{K}_{p\beta}$ . The net influence of these changes in pitch-flap and pitch-lag couplings on stability is negligible. The primary source of the slightly destabilizing effect of increased chordwise flexibility inboard of the pitch bearing is through a change in the variation of rotor frequencies with collective pitch. Holding  $\tilde{K}_{p\beta}$  and  $\tilde{K}_{p\zeta}$  to their baseline values has little effect on the influence of  $R_\zeta$  on stability.

6. The influence of control system stiffness (Fig. 4.14) on whirl flutter stability is due to its effect on the magnitude of  $\tilde{K}_{p\beta}$  and  $\tilde{K}_{p\zeta}$  (Eqs. (3.24) and (3.25)). As the control system stiffness increases, flutter speed also increases, since a stiffer control system reduces the destabilizing couplings due to blade flexibility distribution. This is consistent with observations in Refs. 29 and 76. If  $\tilde{K}_{p\beta}$  and  $\tilde{K}_{p\zeta}$  are held fixed to their baseline values, changes in control system stiffness have no influence on the predicted stability boundary.

#### 4.2.2 Influence of individual wing design parameters

The wing design parameters considered in the present study are (1) wing vertical bending stiffness ( $K_{q1}$ ), (2) chordwise bending stiffness ( $K_{q2}$ ), (3) torsional stiffness ( $K_p$ ), (4) vertical bending-torsion coupling ( $K_{pq1}$ ), and (5) chordwise bending-torsion coupling ( $K_{pq2}$ ). The bending-torsion coupling represented by the parameters  $K_{pq1}$  and  $K_{pq2}$  may come from several sources, including composite tailoring of the wing structure, wing sweep, or mass offsets of the wing or rotor/nacelle structure, relative to the wing elastic axis. The findings of a parametric study of the influence of these wing stiffness and coupling parameters on whirl flutter stability may be summarized as follows:

1. Reduced vertical bending stiffness increases the stability of the wing vertical bending mode, while slightly destabilizing the chordwise bending and torsion modes. Figure 4.15 shows how changes in the wing vertical bending stiffness influence flutter speed. This observation is consistent with the results reported in Refs. 3, 1, and 77. While decreased wing stiffness is generally destabilizing for whirl flutter, decreased vertical bending stiffness increases the frequency separation between the vertical bending mode and torsion mode, reducing the amount of coupling between wing vertical bending and torsion motion. This interpretation of the influence of reduced vertical bending stiffness is confirmed by examination of the eigenvectors produced by the stability analysis. For typical tiltrotor configurations, wing vertical bending and tor-

sion motions are inertially coupled through the mass of the rotor and nacelle which is offset from the wing elastic axis. When the separation between wing vertical bending and torsion mode frequencies is increased, there is less pitching motion of the nacelle in the wing vertical bending mode, which reduces the amount of blade flapping and thus reduces the destabilizing rotor aerodynamic forces acting on the wing. Figure 4.15 shows that if the natural frequency of the vertical bending mode is reduced by about 17%, the mode is completely stabilized.

2. Figure 4.16 shows that reduced wing torsional stiffness is destabilizing, particularly in the case of the vertical bending mode. This is again due to the fact that reduced torsional stiffness reduces the frequency separation between the vertical bending mode and torsion mode and increases the coupling between wing vertical bending and torsion motion. Figure 4.16 illustrates the need for the very thick, torsionally stiff wings in current tiltrotor designs. Even a modest reduction in wing torsional stiffness from the baseline value results in an unacceptable decrease in flutter speed. Increased torsional stiffness, on the other hand, is not a desirable design solution, since increasing the torsional stiffness would require even thicker wing sections, increasing aerodynamic drag, or increased structural weight.
3. The analysis shows very little sensitivity to changes in wing chordwise bending stiffness, as shown in Figure 4.17. This is consistent with Ref. 3, where changes in wing chordwise stiffness within the typical design range had little influence on flutter speed.
4. Figure 4.18 illustrates the influence of wing vertical bending-torsion coupling. Positive values of the coupling parameter  $K_{Pq1}$  (which in the present analysis denotes a wing bend up/twist nose down coupling) improve the flutter speed of the critical vertical bending mode, and are only slightly destabilizing for the other modes, yielding an overall increase in flutter speed. This additional elastic coupling introduced

in the wing opposes the inherent inertial coupling due to the offset mass of the rotor and nacelle at the wing tip. Thus the overall coupling of wing vertical bending and torsion motion is reduced, as was the case for reduced vertical bending stiffness. The beneficial influence of vertical bending-torsion coupling in the wing has been reported in Refs. 48, 45, 49.

5. Wing chordwise bending-torsion coupling (Fig. 4.19) has virtually no influence on flutter speed boundaries for the baseline wing/rotor configuration. Negative values of the coupling parameter  $K_{Pq2}$  do slightly improve the sub-critical damping of the wing chordwise bending mode, however. References 48 and 45 do not note any stability benefits from wing chordwise bending-torsion coupling. In Ref. 49 however, chordwise bending-torsion coupling was reported to be strongly stabilizing for tiltrotor whirl flutter. The source of the discrepancy between these studies and the reported influence of chordwise bending-torsion coupling in Ref. 49 is unclear. It is possible that differences in the tiltrotor configuration used to perform the study are responsible for the discrepancy. The wing chordwise bending and torsion motions were reported to be coupled in Ref. 49, while the configuration used in the present analysis shows little coupling of these motions.

### 4.3 Parametric optimization

After developing an understanding of the influence of the individual design parameters on whirl-flutter stability, formal optimization techniques are used to identify combinations of these design variables that improve the vehicle's whirl-flutter stability characteristics.

A gradient-based algorithm is used to perform the parametric optimization. This routine attempts to minimize a user-defined objective function  $F(D_j)$ , where  $D_j$  is the vector of design parameters considered in the optimization. The optimizer calculates sensitivity gradients,  $\partial F / \partial D_j$ , numerically by individually perturbing each design variable. Based on

these gradients, a steepest-descent search direction is determined, and a new combination of design variables is selected. This procedure is repeated until the objective function reaches a minimum value (i.e. when  $\partial F / \partial D_j = 0$ ), or the design variables have reached their user-specified limits. For the purposes of this optimization study, three sets of constraints on the design parameters are considered: relaxed, moderate, and tight constraints. In an actual tiltrotor design, constraints based on considerations such as weight, allowable loads, handling qualities, and transient rotor flapping would prevent the designer from making arbitrarily large changes in the design parameters in order to improve aeroelastic stability. A small change in any one design parameter may not provide sufficient stability gains. The tight set of constraints is formulated to examine what increases in stability may be obtained through relatively modest changes to many design variables simultaneously. The moderate and relaxed sets of constraints further show what additional gains in stability are possible if larger changes to the design parameters are permitted by the overall design constraints. The three sets of constraints on the design parameters are given in Table 4.2. Nominal values for each design parameter (corresponding to the XV-15 full-scale semi-span model) are provided in Table 4.1.

Since the optimization uses a gradient-based approach, the optimizer may return a locally optimal solution, instead of the global optimum. To avoid this problem, the optimization was repeatedly performed, with random initial starting points. Different “optimized” solutions were returned for some initial conditions, indicating that local minima do exist in the design space. Performing the optimization repeatedly allowed locally optimal solutions to be discarded in favor of globally optimized configurations.

### **4.3.1 Selection of objective function**

In order to obtain a satisfactory design solution from the optimization, the objective function  $F(D_j)$  must be well-posed. Selection of a proper objective function can often be a trial-and-error process, where several candidate functions are tested before a function is

identified which most effectively achieves the intended goal of the optimization. The goal of the optimization in general is to increase the whirl flutter stability boundary. Additionally, it is desirable to avoid “cliff-type” instabilities, where the transition from a stable to an unstable condition occurs rapidly over a very small speed range. The objective functions in the present study are not explicitly formulated to avoid these sharp instabilities. Rather, the rate at which damping decreases with forward speed is qualitatively examined when evaluating the suitability of each proposed design configuration.

Initial efforts to improve whirl flutter stability by formulating an objective function that sought to improve damping of the wing vertical bending mode (the critical flutter mode of the baseline configuration) were unsuccessful. Combinations of design parameters which increased damping in the selected mode were often strongly destabilizing for some other mode. To achieve satisfactory design solutions, the optimization must be formulated to improve the damping of the *least-damped* mode, whichever mode that may be. Thus, for each iteration of the optimization, the critical mode must be re-identified, since changes to the design parameters in the course of the optimization may cause different modes to become critical. Furthermore, attempts to improve whirl flutter stability by formulating an objective function to increase damping at some given velocity produced unacceptable design configurations. Performing the optimization at only one airspeed tended to produce designs that displayed sharp decreases in stability just beyond the optimization speed. In addition, in some cases the damping of several modes at low speed was degraded from the baseline configuration. While most of this reduction in damping occurred at or below the speed where a tiltrotor would begin the transition to helicopter mode, it is not generally desirable to achieve increased damping at high speeds at the expense of reduced damping at lower speeds.

To address these issues, and produce significant stability margins over a range of flight speeds, a *moving point* optimization is conceived. The objective function is written as

$$\text{maximize } F(D_j) = \zeta_{\min}|_{V=200 \rightarrow 500 \text{ kts}} \quad (4.2)$$

Over an airspeed range from 200 to 500 knots, the optimizer attempts to maximize the damping at the point of least damping within that range. As the design variables are adjusted in each iteration of the optimization, this point may shift to a different airspeed. Thus for each iteration of the optimization, the airspeed corresponding to the point of minimum damping must first be identified. The search for the airspeed at which damping is lowest can be formulated as a minimization problem (Find the airspeed  $V$  such that  $\zeta_{\min}$  is at a minimum), and placed within the main optimization loop. The same gradient-based optimization routine used to determine optimal combinations of the design variables can then also be used to locate the airspeed at which the optimization is to occur. This two-stage optimization process is illustrated in Fig. 4.20.

For each iteration, using the current set of rotor design variables, the optimizer first determines the airspeed  $V$  at which the damping is lowest. An iteration of the optimization is then performed at that airspeed  $V$  obtained from the inner loop optimization. Sensitivity gradients for each of the design variables are calculated at the current design point and the design variables are updated, yielding a new configuration which is tested for optimality. If the design is not yet optimal, the optimization procedure is repeated, first re-identifying the airspeed where damping is minimum for the new configuration. Such an optimization algorithm was used in Ref. 69 to optimize rotor design variables to alleviate helicopter ground resonance. See Ref. 69 for further discussion of the algorithm.

The upper and lower limits of the speed range over which the optimizer seeks to improve damping were selected after experimenting with several different values. The lower bound of 200 knots was set low enough to ensure that the optimized configuration would not trade off damping at low speed for gains in stability at higher speeds closer to the flutter boundary, but not so low that the optimizer is trying to increase the damping of modes that are inherently lightly damped at very low speeds. The upper limit of 500 knots was set well above the maximum speed of conventional tiltrotor aircraft. This ensures that any sharp “cliff-type” instabilities will only occur well above the tiltrotor’s maximum speed.



### 4.3.2 Optimization of rotor parameters

A moving point optimization attempting to maximize damping over an airspeed range from 200 to 500 knots was performed, using each of the three previously defined sets of bounds on the design parameters. Table 4.3 provides the resulting values of the optimized design parameters.

The damping characteristics of the configuration optimized with tight constraints are shown in Fig. 4.21. Note that for this optimization, each design parameter has reached either its upper or lower limit. Comparing the optimized design to the parametric study results shows that each parameter follows the stabilizing trend identified in the parametric study. Even though only small changes to the baseline configuration are allowed by the tight bounds on the design parameters, the optimized configuration was still able to substantially improve the flutter speed by about 130 knots, from 310 to 440 knots.

The influence of each design parameter on the final configuration is examined by individually setting each parameter in turn to its baseline value and examining the resulting stability prediction. Using this procedure, it was determined that the majority of the increase in damping over the baseline is produced by the change in the parameters  $\Delta K_{p\beta}$ ,  $\Delta K_{p\zeta}$ , and  $R_\beta$ . Leaving these parameters set to the optimal values given in the first column of Table 4.3 and returning the others to their baseline values yielded a configuration with a flutter speed of 409 knots, still almost a 100 knot increase over the baseline.

Figure 4.22 shows the damping characteristics of the configuration optimized with the intermediate set of constraints. As was the case when optimizing with the tight bounds, each design parameter has reached either its upper or lower limit. The values of each parameter are again consistent with the stability trends identified in the parametric study, with the exception of blade chordwise bending stiffness ( $\Delta\omega_{\zeta_0}$ ), which changed from its lower limit value for the tight constraint case to its upper limit in this case. Manually changing  $\Delta\omega_{\zeta_0}$  from the optimized value results in reduced damping in the wing chordwise bending mode, the critical (least-damped) mode for this optimized configuration. The reduction in

damping is small, however. The sensitivity of modal damping to changes in  $\Delta\omega_{\zeta_0}$  is very low for this configuration; large changes in  $\Delta\omega_{\zeta_0}$  have little effect on stability. The change in trend for the optimal value of  $\Delta\omega_{\zeta_0}$  shows that, as the bounds on the design variables are relaxed, the stabilizing influence of the optimized combination of variables begin to differ from the trends identified through parametric examination of each individual variable.

The greater freedom allowed by the intermediate bounds allows for an optimized configuration that stabilizes the system up to 500 knots, with damping levels of at least 3.2% over that range. Examining the contribution of each design parameter to the overall increase in stability reveals that, in addition to  $\Delta K_{p\beta}$ ,  $\Delta K_{p\zeta}$ , and  $R_\beta$ , the  $\delta_3$  angle also provides an important contribution. For the tight set of bounds, the upper limit on  $\delta_3$  was set to its baseline value of  $-15^\circ$ . The intermediate constraints allowed  $\delta_3$  to increase to  $0^\circ$ , providing a stabilizing influence on the wing modes, as shown in the parametric study. It should be noted however that this optimal value of  $\delta_3$  may not be achievable, due to geometric constraints and blade transient flapping considerations. Retaining only the optimized values of  $\Delta K_{p\beta}$ ,  $\Delta K_{p\zeta}$ ,  $R_\beta$ , and  $\delta_3$  yielded a configuration which still remained stable to 500 knots, with at least 2.7% damping from 200 to 500 knots.

Figure 4.23 shows that the configuration obtained using the relaxed bounds is stable to 500 knots, with at least 4.8% critical damping from 200 to 500 knots. The optimized parameter values are given in the last column of Table 4.3. While some of the design parameters in the optimized configuration have continued following the parametric study trends to their allowable limits, some have not. Both flatwise ( $\Delta\omega_{\beta_0}$ ) and chordwise ( $\Delta\omega_{\zeta_0}$ ) blade bending stiffness parameters have reversed trends from the intermediate constraint results. In the case of  $\Delta\omega_{\zeta_0}$ , the optimized configuration remains relatively insensitive to changes in this parameter. For  $\Delta\omega_{\beta_0}$ , stability of the optimized configuration is sensitive to parameter changes. Moving  $\Delta\omega_{\beta_0}$  to a more positive value (following the stability trend identified in the parametric study) results in noticeable reductions in both beam and chord mode stability. The marked change in behavior for this parameter may be explained by noting that for the optimized configuration, blade flatwise flexibility is now nearly equally

distributed inboard and outboard of the pitch bearing (determined by the value of parameter  $R_\beta$ ). This is a substantial change from the baseline, where the blade flexibility was entirely outboard of the pitch bearing. The change in configuration brought about by the optimized combination of variables is substantial enough that the baseline stability trends are of little value in predicting the stabilizing effects of changes in individual parameters.

Also notable in the relaxed-bounds optimized configuration is the change in  $\delta_3$ , which reaches its lower bound of  $-45^\circ$ . This is a surprising result because, as discussed previously, large values of  $\delta_3$  typically result in reduced aeroelastic stability. Achieving adequate stability margins with large values of  $\delta_3$  is highly desirable, as allowing large values of  $\delta_3$  eases some of the geometric constraints that presently hinder the design of tiltrotors with more than three blades per rotor. As was the case for  $\Delta\omega_{\beta 0}$  and  $\Delta\omega_{\zeta 0}$ , the optimized combination of parameters has changed the configuration enough that the baseline stability trends for changes in  $\delta_3$  no longer apply. In fact, the optimized configuration is relatively insensitive to changes in  $\delta_3$ , such that a change in  $\delta_3$  from the optimized value of  $-45^\circ$  to the baseline  $-15^\circ$  results in a reduction in chord mode damping at 500 knots from about 5% to 3.5%, and no reduction in critical flutter speed (over the range of airspeeds analyzed).

The distribution of blade flatwise bending stiffness inboard and outboard of the pitch bearing ( $R_\beta$ ) stayed near the value it reached during the intermediate constraint optimization, moving only from 0.5 to about 0.4. The parametric study results showed that flutter speed was maximized for values of  $R_\beta$  near 0.5, while further reductions in  $R_\beta$  had little effect on flutter speed. For the configuration optimized with relaxed bounds, changes in the other design variables have shifted this maximum slightly, resulting in an optimal value of  $R_\beta$  around 0.4. This shift in blade flexibility has a large influence on the pitch-flap and pitch-lag couplings given by Eqs. (3.24) and (3.25). Reduced  $R_\beta$  greatly reduces the negative pitch-lag coupling due to pitch dynamics, as shown in Fig. 4.24, which compares the variation of  $\tilde{K}_{p\beta}$  and  $\tilde{K}_{p\zeta}$  with airspeed for the baseline configuration and the configuration optimized with the relaxed constraints.

For all three rotor optimization cases considered, the design parameters which have

the most influence on stability while still showing consistent sensitivity trends (regardless of the level of constraint) are additional positive blade pitch-flap and pitch-lag coupling (positive  $\Delta K_{p\beta}$  and  $\Delta K_{p\zeta}$ ) and increased blade flatwise bending flexibility inboard of the pitch bearing ( $R_\beta < 1$ ). It should be noted that more recent tiltrotor designs than the XV-15 rotor used in this study already have a value of  $R_\beta$  less than one due to the presence of a coning flexure, as used in the V-22 rotor hub. The primary influence of all three of these design parameters is to cause a net positive change in the *total* pitch-flap and pitch-lag couplings (Eqs. (3.26) and (3.27)) by reducing (in the case of  $R_\beta$ ) or offsetting (by positive  $\Delta K_{p\beta}$  and  $\Delta K_{p\zeta}$ ) the negative pitch-flap and pitch-lag couplings due to the distribution of blade flexibility.

The results of this rotor parameter optimization study indicate that whirl flutter stability can be improved substantially by achieving positive total pitch-flap and pitch-lag couplings. Sufficiently large changes in other design parameters, if permitted by other design constraints, allow for further improvements in stability and also may permit larger values of  $\delta_3$  coupling, facilitating the design of advanced rotor configurations.

### 4.3.3 Optimization of wing parameters

The optimization process is repeated, this time considering only the wing stiffness and coupling parameters as design variables. Initial attempts at improving stability through optimization using the objective function in Eq. (4.2) did not produce satisfactory results. The problem is illustrated in Fig. 4.25, which shows the damping of the wing modes for the baseline configuration. The figure shows that the vertical bending mode is the critical mode, becoming unstable at 310 knots. At speeds above 400 knots, however, all three wing modes are unstable and both the chordwise bending and torsion modes are more unstable than the vertical bending mode. An optimization process seeking to satisfy the objective function of Eq. (4.2) will first seek a configuration that increases damping at the point of lowest damping in the speed range under consideration. For the baseline configuration shown in

Fig. 4.25, the optimization would seek to increase the damping of the torsion mode at high speed. Unfortunately, as shown in the wing parametric study results (Figs. 4.15–4.19), changes in the wing design parameters do not significantly improve wing chord or torsion mode stability, so the optimization is unable to proceed. The optimization never even gets around to attempting to improve damping of the critical vertical bending mode.

To obtain favorable configurations of wing design parameters, the objective function must be restricted to operate only in regions where the design parameters are effective at increasing the damping of the critical mode. This is achieved by reducing the upper bound on the range of airspeeds considered in the optimization from 500 knots to 300 knots. Therefore, the objective function used to optimize the wing design parameters is now:

$$\text{maximize } F(D_j) = \zeta_{\min}|_{V=200 \rightarrow 300 \text{ kts}} \quad (4.3)$$

Optimized combinations of the wing design parameters obtained by using the objective function in Eq. (4.3) and the three different sets of constraints (Table 4.2) are shown in Table 4.4.

Figure 4.26 shows the damping characteristics of the configuration obtained using the tight constraints on the design variables. Table 4.4 shows that each design parameter has reached a limit imposed on it by the tight constraints, and the optimized values are in agreement with the stability trends identified in the parametric study. Using this optimized configuration, the stability boundary of the critical vertical bending mode is increased from 310 to 340 knots. This increase in flutter speed is due almost entirely to the influence of the design parameters  $\Delta\omega_{q1}$ ,  $\Delta\omega_p$ , and  $K_{Pq1}$ . As was observed in the parametric study, increased frequency separation between the wing vertical bending and torsion modes (such as is provided by decreased  $\omega_{q1}$  and increased  $\omega_p$ ) and positive vertical bending-torsion coupling improve the stability of the vertical bending mode. The other two design parameters,  $\Delta\omega_{q2}$  and  $K_{Pq2}$ , have a much smaller influence on the overall damping, providing only a very slight increase in damping.

The stability characteristics of the configuration optimized with the intermediate set of constraints are shown in Fig. 4.27. Comparing the performance of this design to that of the tightly-constrained optimized configuration (Fig. 4.26) reveals that the vertical bending mode is further stabilized, actually becoming stable over the entire speed range considered in this study. There is however only a marginal gain in actual flutter speed relative to the design using tight constraints, since the chordwise bending mode is now the critical mode, and the wing design parameters are unable to significantly improve the damping of that mode.

Examining the values (given in Table 4.4) of the design parameters obtained using the intermediate set of constraints shows that all of the variables follow the same trends seen in the parametric study and reach either an upper or lower bound, except for the chordwise bending-torsion coupling parameter,  $K_{Pq2}$ . This is due to the fact that positive  $K_{Pq2}$  slightly increases vertical bending mode damping, while slightly reducing chordwise bending mode damping. For the optimized configuration obtained using tight variables, over the speed range considered by the optimization (200 to 300 knots), the vertical bending mode damping is always lower than the chordwise bending mode damping. For the configuration using intermediate constraints, near 300 knots the damping of the vertical and chordwise bending modes are nearly equal. Thus if the value of  $K_{Pq2}$  is either increased or decreased, the damping of one of the two modes would be decreased. It should be noted however that the additional damping provided by  $K_{Pq2}$  is very small.

Optimization of Eq. (4.3) using the relaxed constraints yields a configuration with damping characteristics shown in Fig. 4.28. As was the case for the configuration optimized using the intermediate constraints, relaxing the constraints allows for further gains in vertical bending mode damping, but flutter speed is unchanged, since the chord mode stability boundary is not strongly influenced by any of the wing design parameters. As shown in Table 4.4, the parameters  $\Delta\omega_{q1}$ ,  $\Delta\omega_{q2}$ , and  $K_{Pq1}$  continue to follow the trends shown in the parametric study. Compared to the previous wing optimization results, the change in torsion frequency,  $\Delta\omega_p$ , and the chordwise bending-torsion coupling parameter  $K_{Pq2}$  have

now changed sign. This is again due to the fact that these parameters have conflicting influences on damping of the vertical and chordwise bending modes. The optimization process balances these effects on damping of the two modes, increasing the damping of both of them as much as possible. It should be noted that the change in damping levels as a result of changes in these two parameters is quite small. Figure 4.28 shows that over most of the speed range considered by the optimization, the level of damping in the vertical and chordwise bending modes is the same.

The results presented in this study of wing design optimization show that there is an upper limit on the stability gains that can be achieved by changes in the wing design parameters. Modest changes in the wing vertical bending and torsion mode stiffnesses ( $\Delta\omega_{q1}$  and  $\Delta\omega_p$ ) and wing vertical bending-torsion coupling ( $K_{Pq1}$ ) improve the stability of the critical wing vertical bending mode. However, none of the wing design parameters are able to significantly influence stability of the wing chordwise bending and torsion modes. Once the vertical bending mode is sufficiently stabilized such that chordwise bending becomes the critical mode, larger changes in wing design parameters are ineffective in further increasing the critical whirl flutter speed.

#### **4.3.4 Concurrent wing/rotor optimization**

An optimization is performed which considers both rotor and wing design parameters simultaneously. Because of the much greater influence of the rotor parameters on damping, the concurrent wing/rotor optimization study is restricted to the tight set of constraints. Equation (4.2) is used as the objective function. Table 4.5 lists the design configuration resulting from this optimization. Figure 4.29 shows the damping characteristics of the design. The optimized configuration has a stability boundary of 435 knots, a 125 knot increase over the baseline. For comparison, optimizing rotor parameters alone using the tight constraints produced a flutter speed of 440 knots, and using the wing parameters alone yielded a 340 knot flutter speed.

The fact that the concurrent optimization produces a design with a lower flutter speed than optimization of the rotor parameters alone indicates there is a problem with the concurrent optimization as it is originally posed. As was the case for the wing parameter optimization, performing the concurrent optimization from 200 to 500 knots causes the optimizer to select values for the wing design parameters that are (slightly) beneficial to the wing chord and torsion modes at high speed, but do not provide as great a benefit to the critical vertical bending mode as is possible. However, it is not desirable to use the objective function used for the wing optimization study (Eq. (4.3)) for the concurrent optimization, because reducing the upper limit of the speed range under consideration will prevent the optimization from taking full advantage of the rotor design parameters.

To perform a useful concurrent optimization, a new objective function is formulated. Instead of attempting to increase damping at a certain speed or over a range of speeds, the objective function is formulated to maximize the flutter speed of the system, the speed at which the first instability is encountered. The objective function is thus written as:

$$\text{maximize } F(D_j) = V_{\text{flutter}} \quad (4.4)$$

where  $V_{\text{flutter}}$  is the airspeed at which the damping of any system mode goes to zero. It should be noted that the objective function in Eq. (4.4) would not be suitable for an optimization performed using the intermediate or relaxed constraints on rotor parameters, since the rotor parameters would then be powerful enough to drive the critical flutter speed beyond the upper limit on airspeed considered in the study. Once the upper limit on airspeed was reached, the optimization would make no effort to improve stability by increasing the subcritical damping, as is the case when optimizing using Eq. (4.2).

The results of a concurrent wing/rotor parameter optimization using Eq. (4.4) as the objective function are also provided in Table 4.5. Figure 4.30 shows the stability characteristics of this configuration. The optimization to maximize flutter speed produced a design with a flutter speed of 450 knots, a 140 knot increase over the baseline configu-



ration. The values of the optimized rotor design parameters are the same as the values obtained when optimizing rotor parameters alone. The wing parameters  $\Delta\omega_{q1}$  and  $K_{Pq2}$  differ from the values they take when wing parameters are optimized alone. This again has to do with a difference in which mode is critical between the wing-only optimization and the concurrent optimization. It is interesting to note that the concurrently optimized design (Fig. 4.30) only slightly outperforms the design obtained by optimizing only the rotor parameters (Fig. 4.21). This demonstrates how much more potential is available for improving stability through the rotor variables than through the wing parameters. Optimizations performed with more relaxed constraints on the wing parameters did not produce configurations that significantly improved on the stability of the configurations given in Table 4.5.

For all configurations in this study that were optimized using the tight constraints on design parameters, the parameters which had the greatest influence on improving whirl flutter stability are: the blade pitch-flap and pitch-lag coupling parameters ( $\Delta K_{p\beta}$  and  $\Delta K_{p\zeta}$ ), the distribution of blade flatwise bending stiffness ( $R_\beta$ ), change in wing vertical bending and torsion stiffness ( $\Delta\omega_{q1}$  and  $\Delta\omega_p$ ), and wing vertical bending-torsion coupling ( $K_{Pq1}$ ). A tightly constrained optimization using the objective function in Eq. (4.4) was performed using only these key parameters as design variables. Table 4.5 provides the resulting optimized values of these design parameters. Figure 4.31 shows that the damping characteristics using only the key parameters is quite similar to the case shown in Fig. 4.30, where all design parameters were considered. The flutter speed attained through modest changes in only the key parameters is 425 knots, still 115 knots above the baseline stability boundary.

Table 4.1: Design Parameters – Nominal Values for full-scale XV-15 semispan model

$\omega_{\beta 0}$	59.8 rad/sec (1.3 /rev)
$\omega_{\zeta 0}$	103 rad/sec (2.2 /rev)
$\omega_{\beta G 0}$	9.04 rad/sec (0.19 /rev)
$\delta_3$	$-15^\circ$
$\Delta K_{P\beta}$	0
$\Delta K_{P\zeta}$	0
$R_\beta$	1
$R_\zeta$	1
$\omega_\phi$	225 rad/sec (4.7 /rev)
$\omega_{q1}$	19.9 rad/sec (0.42 /rev)
$\omega_{q2}$	32.2 rad/sec (0.67 /rev)
$\omega_p$	67.4 rad/sec (1.4 /rev)
$K_{Pq1}$	0
$K_{Pq2}$	0

Table 4.2: Constraints on Design Parameters

	Tight Constraints	Intermediate Constraints	Relaxed Constraints
	(Lower Bound/Upper Bound)		
$\Delta\omega_{\beta 0}$	-5%/+5%	-10%/+10%	-20%/+20%
$\Delta\omega_{\zeta 0}$	-5%/+5%	-10%/+10%	-20%/+20%
$\Delta\omega_{\beta G 0}$	-25%/+25%	-50%/+50%	-100%/+100%
$\delta_3$	-15°/-45°	0°/-45°	+15°/-45°
$\Delta K_{P\beta}$	-0.1/0.1	-0.3/0.3	-0.6/0.6
$\Delta K_{P\zeta}$	-0.1/0.1	-0.3/0.3	-0.6/0.6
$R_\beta$	0.8/1	0.5/1	0/1
$R_\zeta$	0.8/1	0.5/1	0/1
$\Delta\omega_\phi$	-5%/+5%	-10%/+10%	-20%/+20%
$\Delta\omega_{q1}$	-5%/+5%	-10%/+10%	-20%/+20%
$\Delta\omega_{q2}$	-5%/+5%	-10%/+10%	-20%/+20%
$\Delta\omega_p$	-5%/+5%	-10%/+10%	-20%/+20%
$K_{Pq1}$	-0.1/0.1	-0.3/0.3	-0.6/0.6
$K_{Pq2}$	-0.1/0.1	-0.3/0.3	-0.6/0.6

Table 4.3: Rotor Parameter Optimization Results

	Tight Constraints	Intermediate Constraints	Relaxed Constraints
$\Delta\omega_{\beta 0}$	+5%	+10%	-14.0%
$\Delta\omega_{\zeta 0}$	-5%	+10%	-9.03%
$\Delta\omega_{\beta G 0}$	+25%	+50%	+99.2%
$\delta_3$	-15°	0°	-45°
$\Delta K_{P\beta}$	0.1	0.3	0.6
$\Delta K_{P\zeta}$	0.1	0.3	0.6
$R_\beta$	0.8	0.5	0.408
$R_\zeta$	1	1	0.972
$\Delta\omega_\phi$	+5%	+10%	+20%

Table 4.4: Wing Parameter Optimization Results

	Tight Constraints	Intermediate Constraints	Relaxed Constraints
$\Delta\omega_{q1}$	-5%	-10%	-20%
$\Delta\omega_{q2}$	+5%	+10%	+20%
$\Delta\omega_p$	+5%	+10%	-11.2%
$K_{Pq1}$	0.1	0.3	0.572
$K_{Pq2}$	0.1	0.0714	-0.6

Table 4.5: Concurrent Wing/Rotor Parameter Optimization Results

	Maximize Damping	Maximize Flutter Speed	
	All Design Parameters	All Design Parameters	Only Key Parameters
$\Delta\omega_{\beta 0}$	+5%	+5%	0% ( <i>fixed</i> )
$\Delta\omega_{\zeta 0}$	-5%	-5%	0% ( <i>fixed</i> )
$\Delta\omega_{\beta G 0}$	+25%	+25%	0% ( <i>fixed</i> )
$\delta_3$	-15°	-15°	-15° ( <i>fixed</i> )
$\Delta K_{P\beta}$	0.1	0.1	0.1
$\Delta K_{P\zeta}$	0.1	0.1	0.1
$R_\beta$	0.8	0.8	0.8
$R_\zeta$	1	1	1 ( <i>fixed</i> )
$\Delta\omega_\phi$	+5%	+5%	0% ( <i>fixed</i> )
$\Delta\omega_{q1}$	+3.68%	+2.07%	+0.104%
$\Delta\omega_{q2}$	-5%	+5%	0% ( <i>fixed</i> )
$\Delta\omega_p$	+5%	+5%	+5%
$K_{Pq1}$	0.1	0.1	0.1
$K_{Pq2}$	-0.1	-0.1	0 ( <i>fixed</i> )

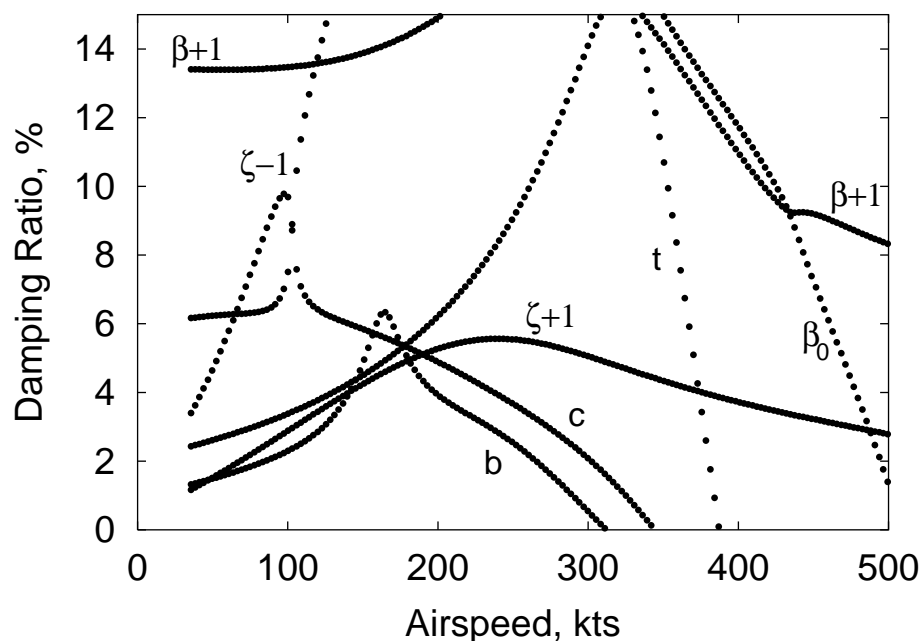


Figure 4.1: Modal damping of baseline system (b: wing beam mode, c: wing chord mode, t: wing torsion mode,  $\beta_0$ : rotor coning mode,  $\zeta - 1, \zeta + 1$ : cyclic lag modes,  $\beta - 1, \beta + 1$ : cyclic flap (gimbal) modes)

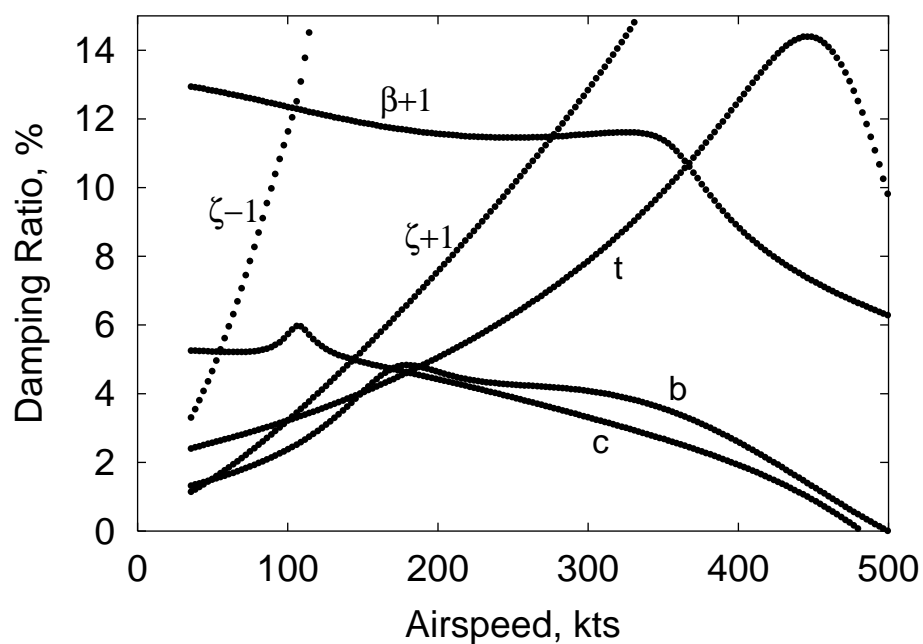


Figure 4.2: Modal Damping of Baseline System, no couplings due to pitch dynamics

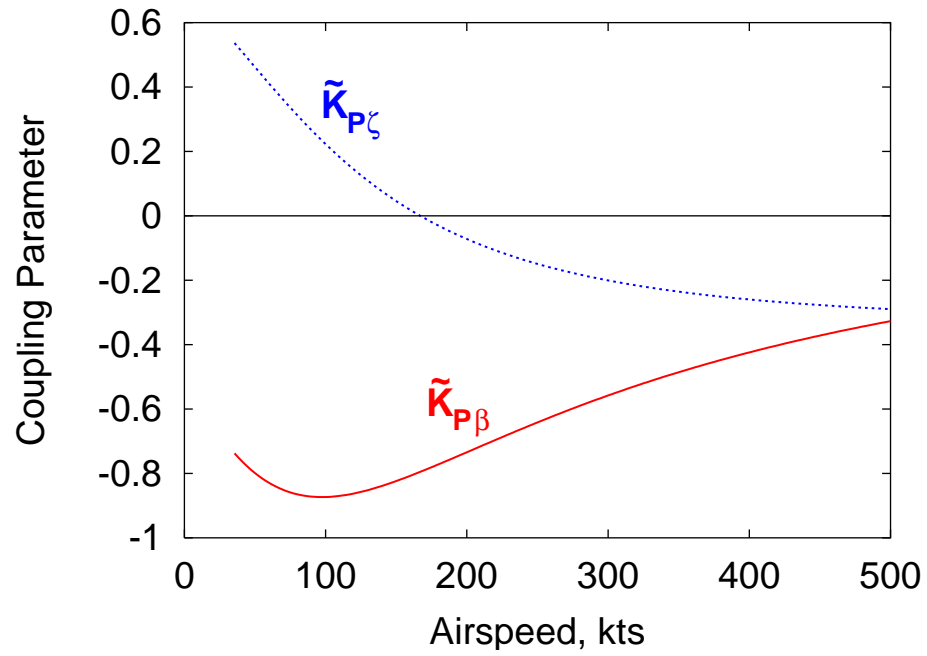


Figure 4.3: Variation of pitch-flap and pitch-lag coupling parameters (due to flexibility outboard of the pitch bearing) for baseline system

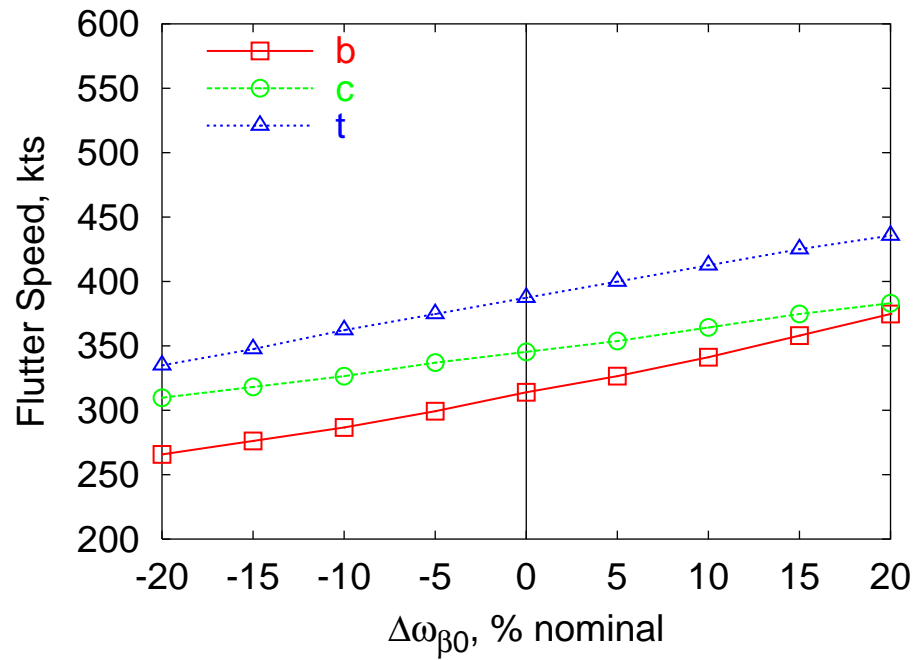


Figure 4.4: Influence of blade flatwise bending stiffness on flutter speed

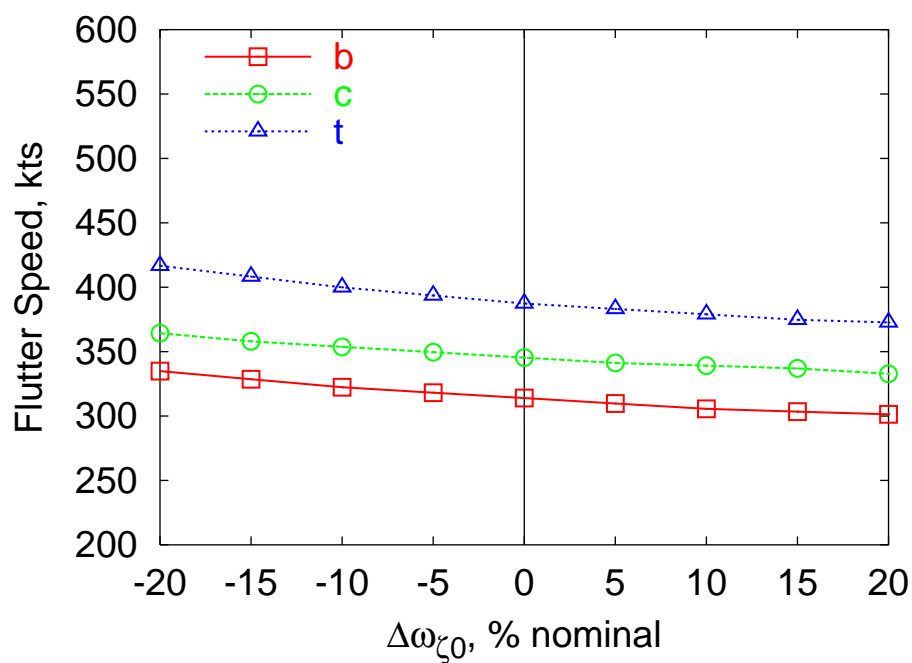


Figure 4.5: Influence of blade chordwise bending stiffness on flutter speed

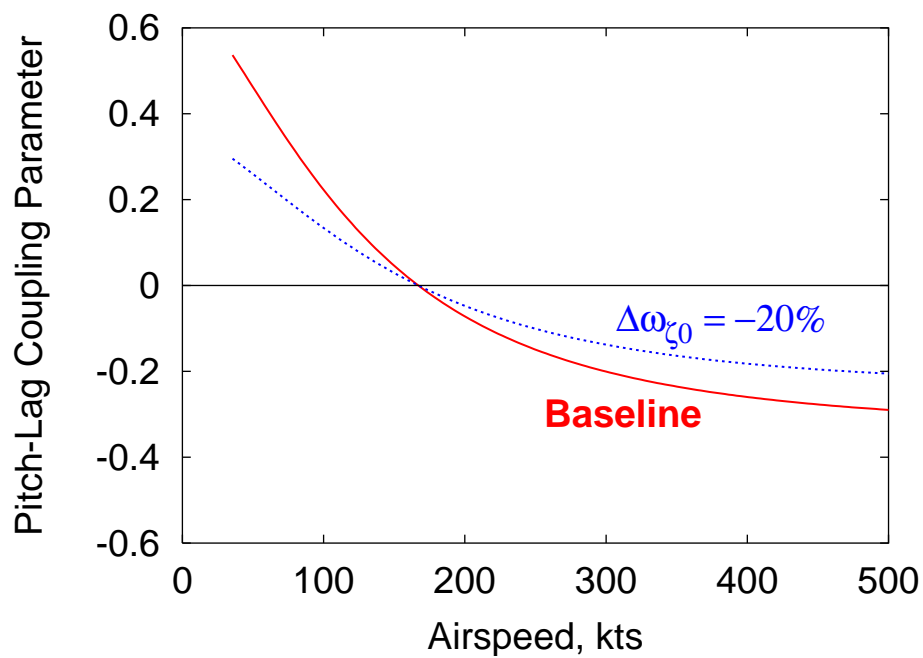


Figure 4.6: Effect of reduced chordwise bending stiffness on pitch-lag coupling due to blade flexibility distribution  $\tilde{K}_{P\zeta}$  (Eq. (3.25))

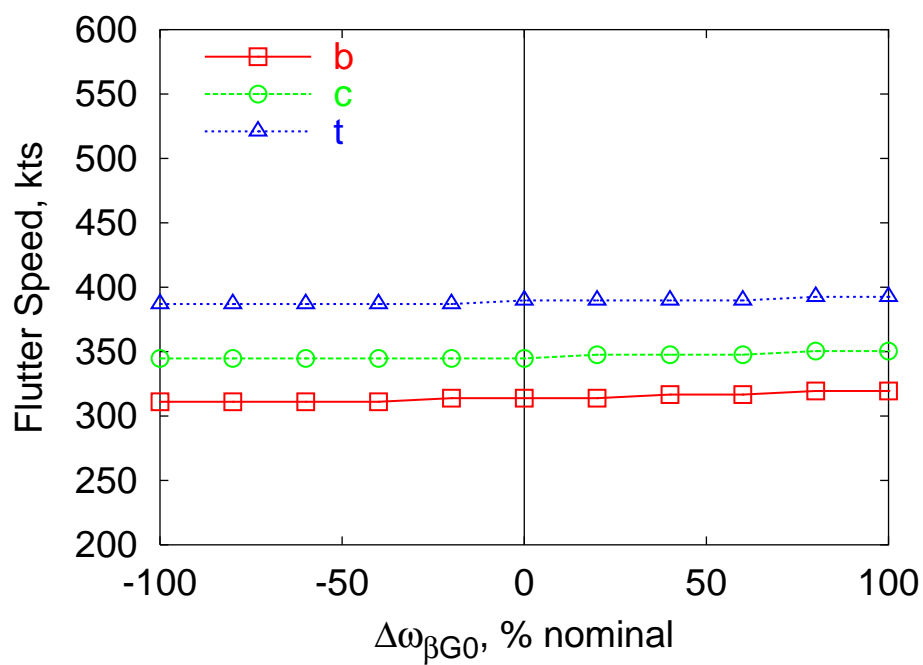


Figure 4.7: Influence of gimbal spring stiffness on flutter speed

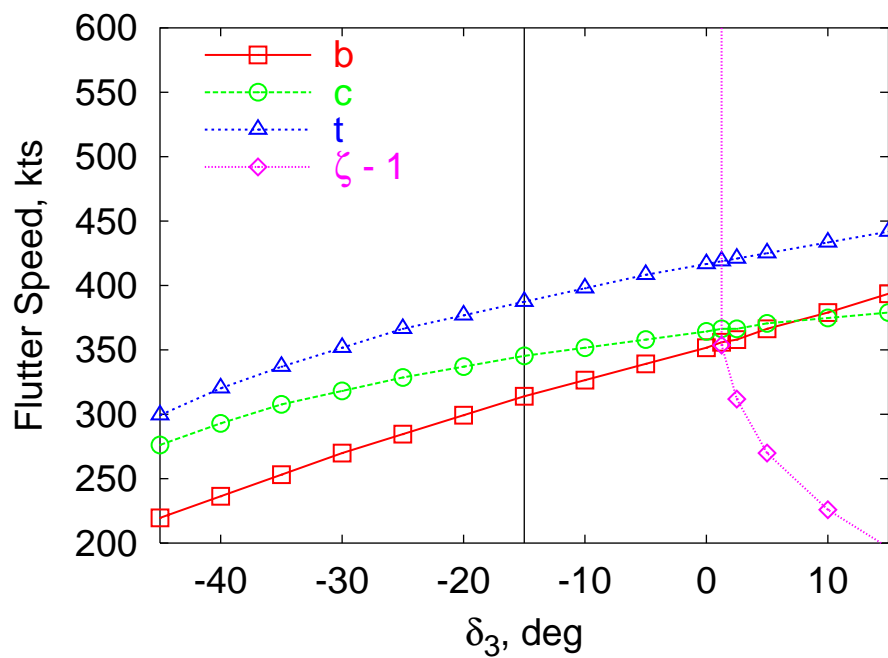


Figure 4.8: Influence of  $\delta_3$  angle (pitch-gimbal coupling) on flutter speed (Baseline  $\delta_3 = 15^\circ$ )



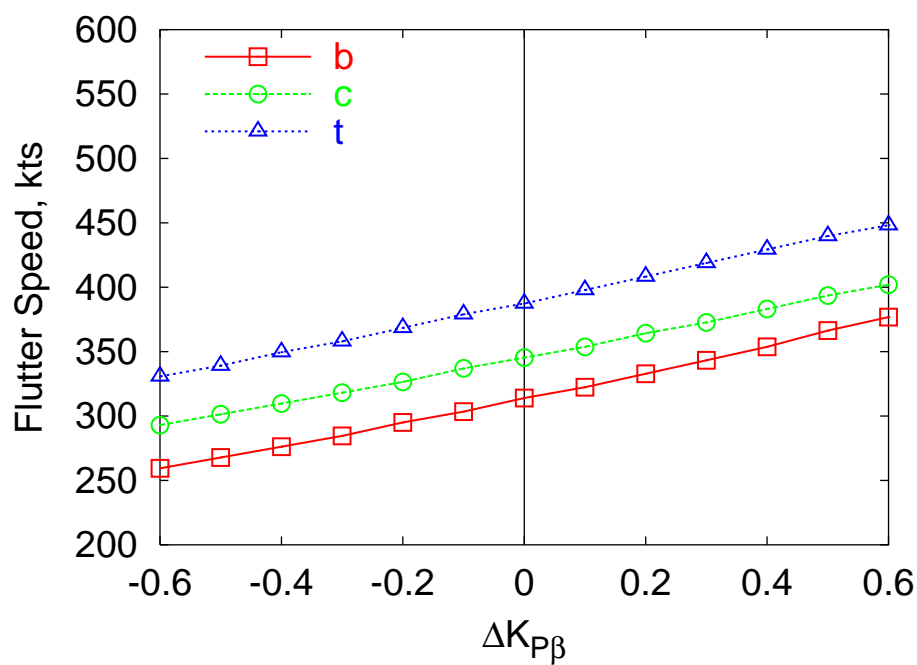


Figure 4.9: Influence of additional pitch-flap coupling on flutter speed

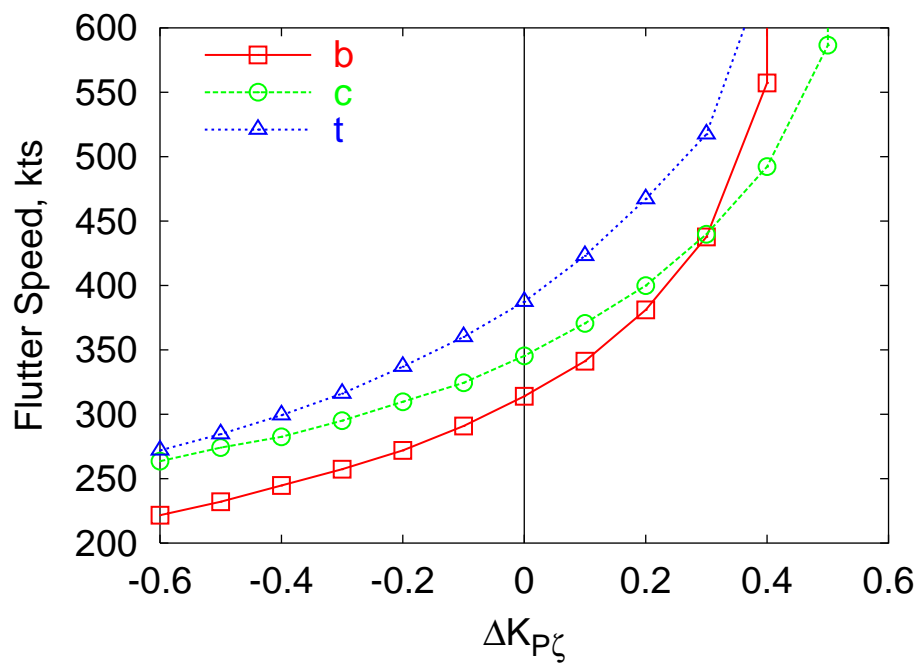


Figure 4.10: Influence of additional pitch-lag coupling on flutter speed

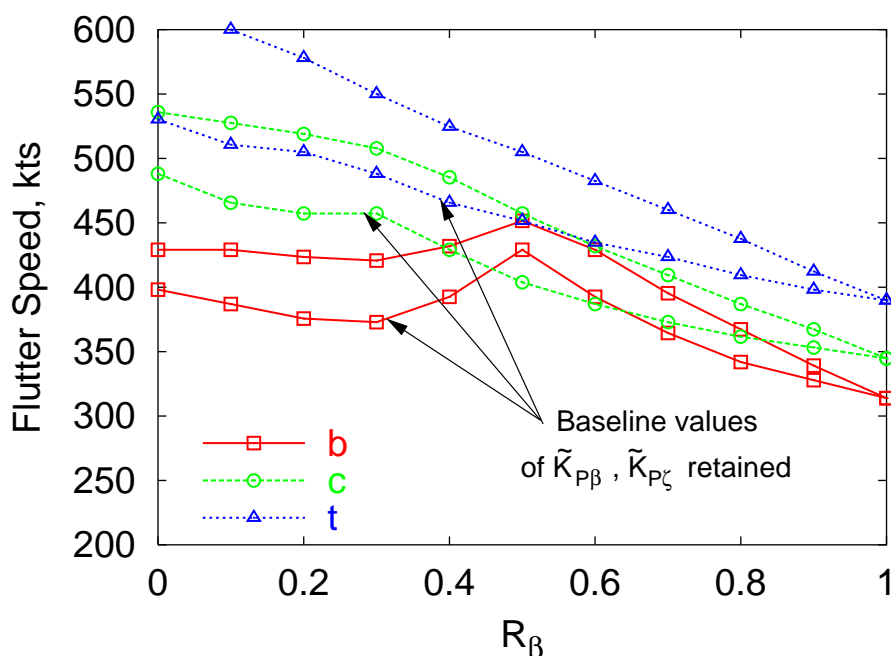


Figure 4.11: Influence of distribution of blade flatwise bending flexibility on flutter speed (Baseline  $R_\beta = 1$ )

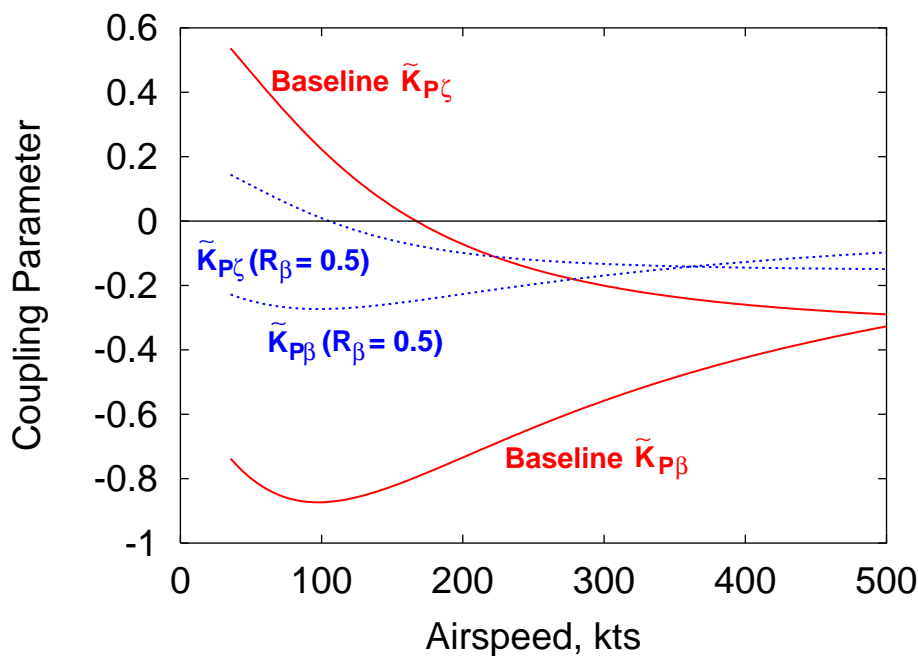


Figure 4.12: Influence of reduced  $R_\beta$  on couplings due to blade flexibility distribution (Baseline  $R_\beta = 1$ )

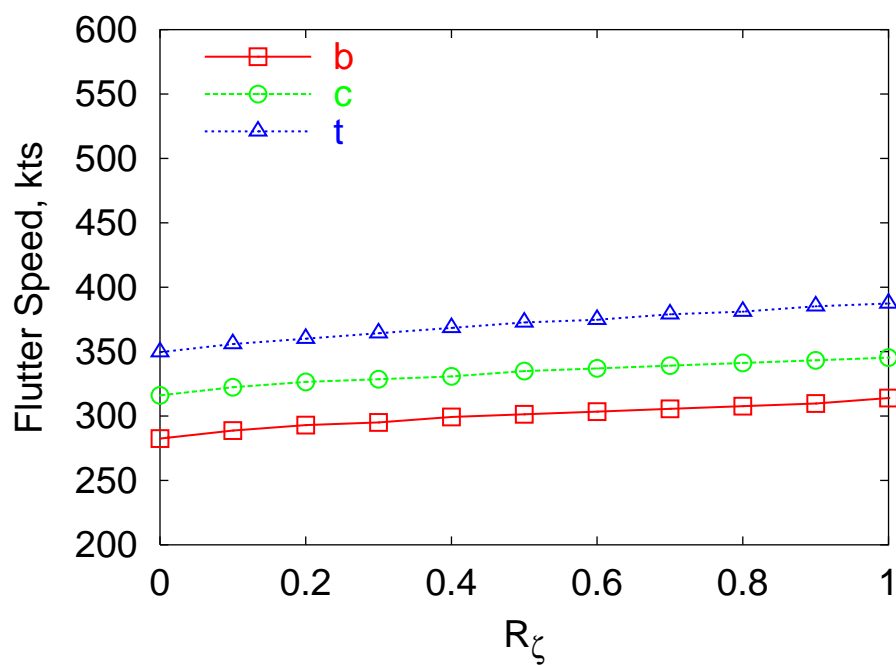


Figure 4.13: Influence of distribution of blade chordwise bending flexibility on flutter speed (Baseline  $R_\zeta = 1$ )

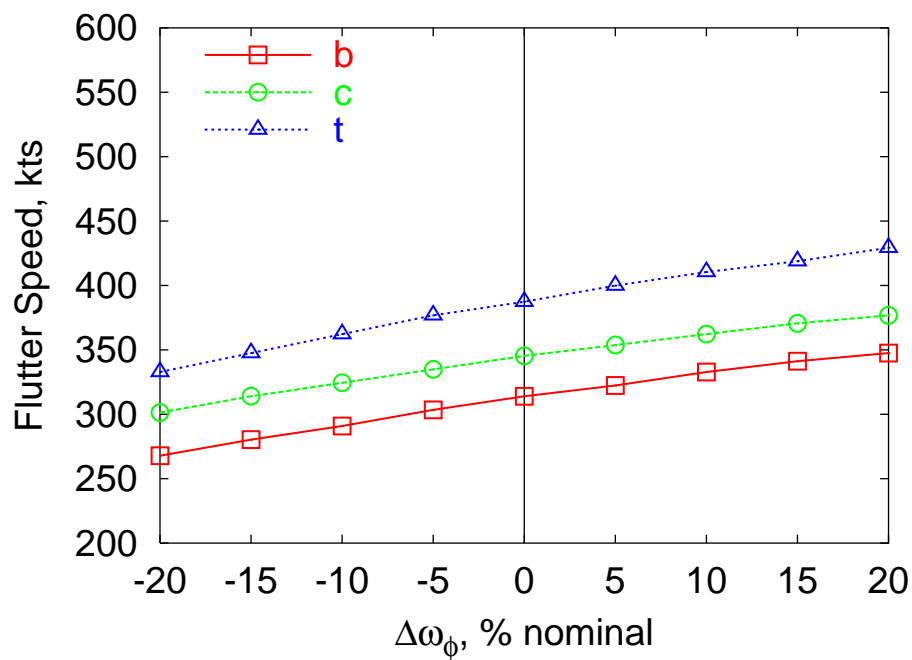


Figure 4.14: Influence of control system stiffness on flutter speed

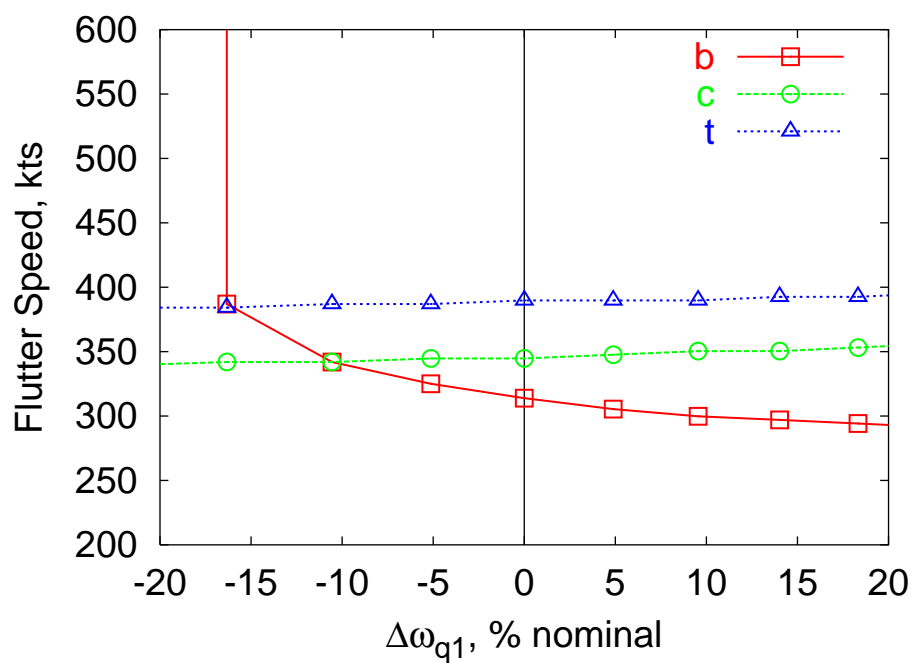


Figure 4.15: Influence of wing vertical bending stiffness on flutter speed

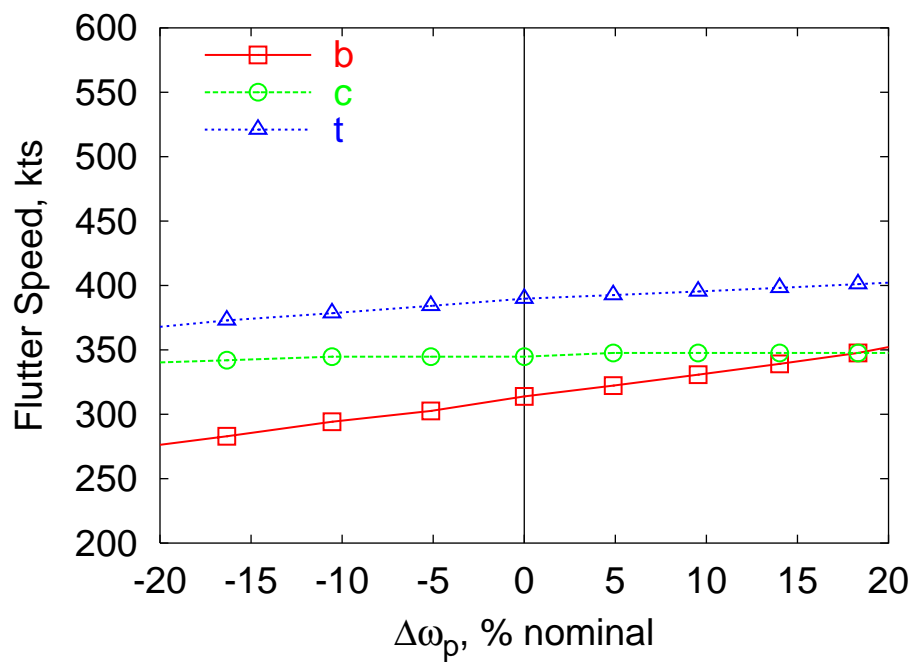


Figure 4.16: Influence of wing torsional stiffness on flutter speed

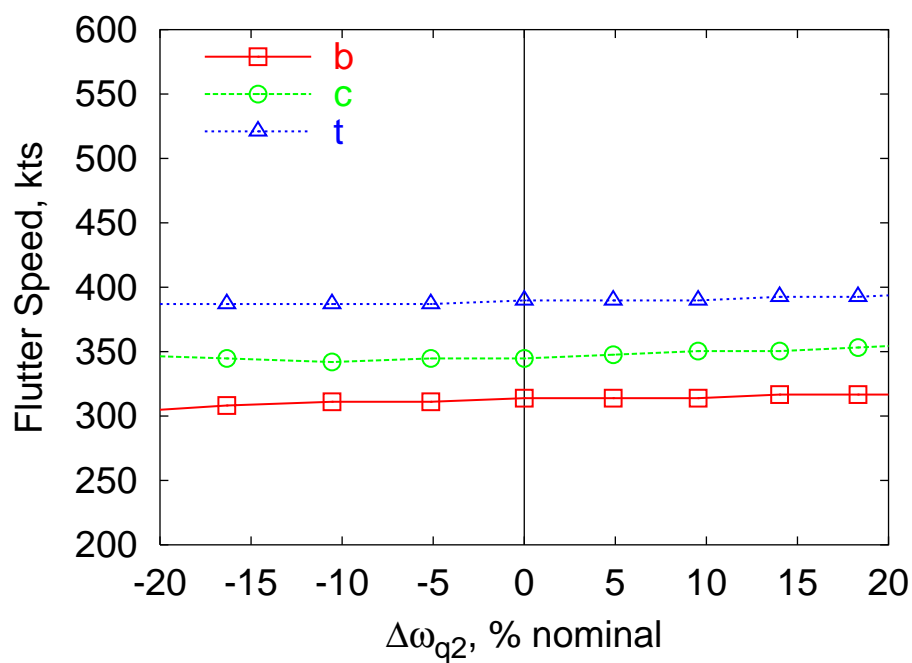


Figure 4.17: Influence of wing chordwise bending stiffness on flutter speed

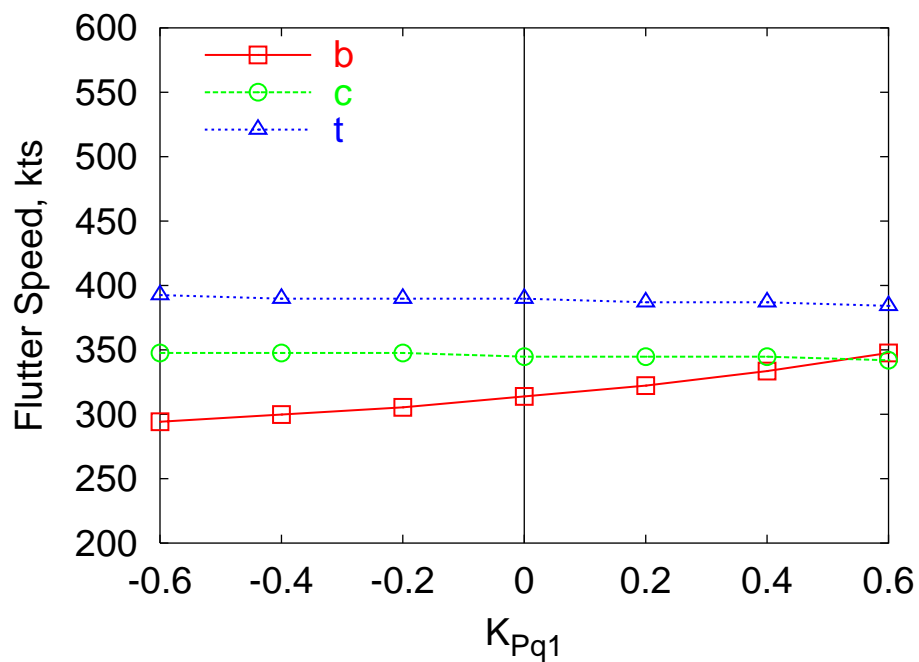


Figure 4.18: Influence of wing vertical bending-torsion coupling on flutter speed

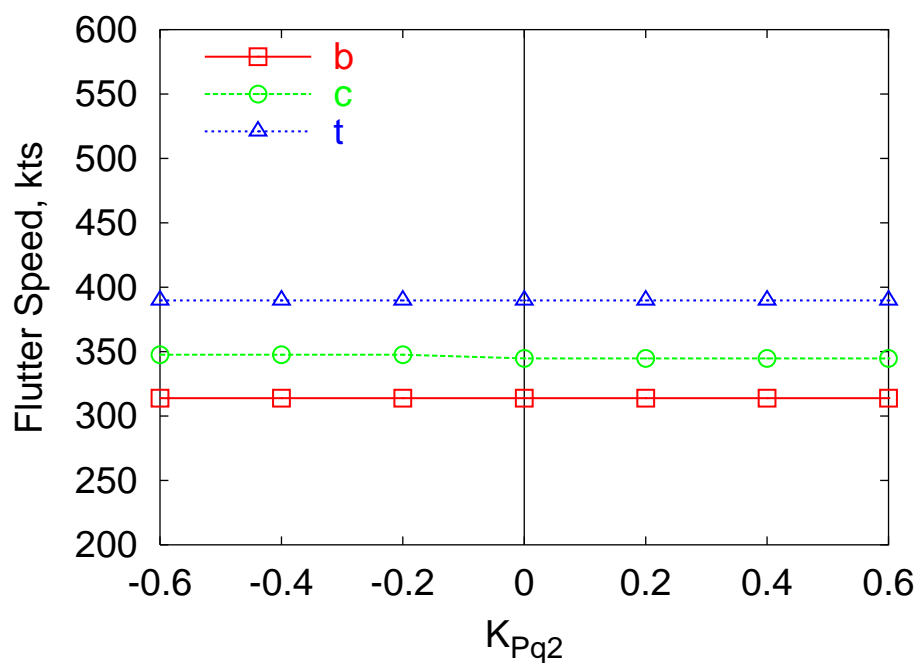


Figure 4.19: Influence of wing chordwise bending-torsion coupling on flutter speed

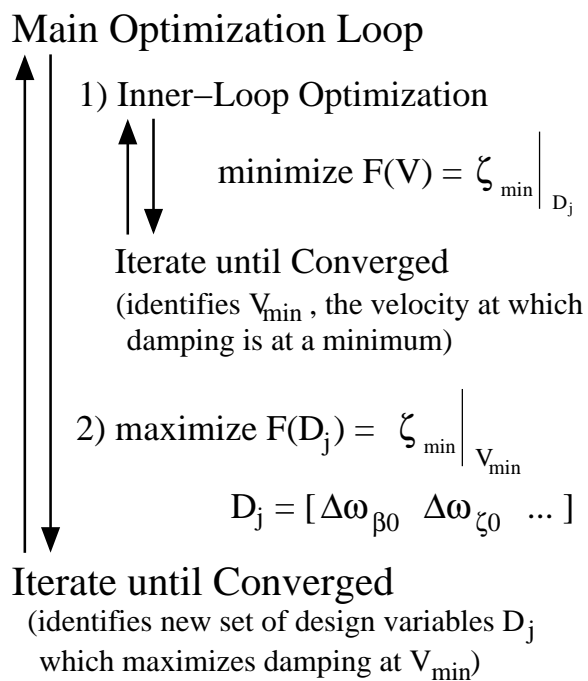


Figure 4.20: Illustration of two-stage optimization algorithm

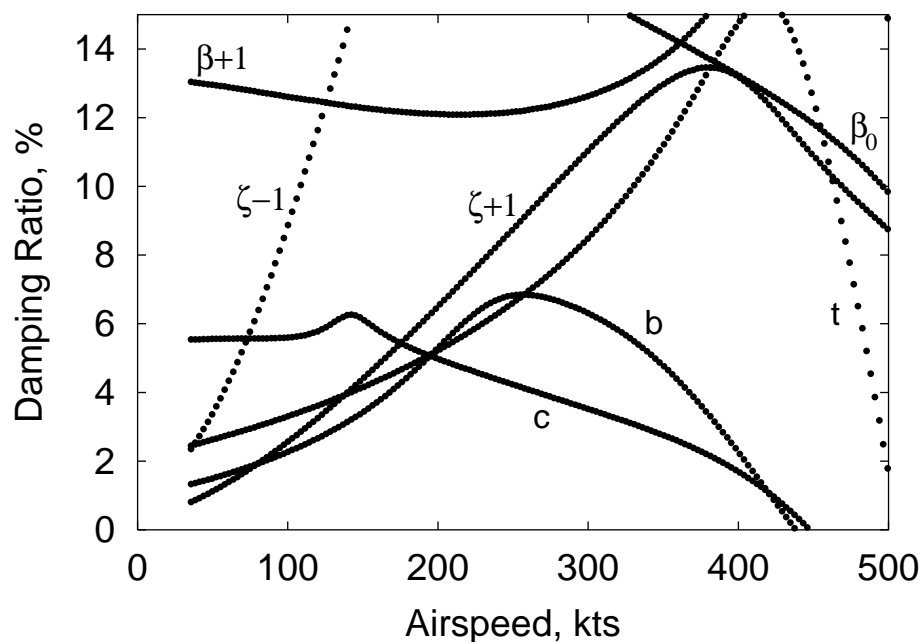


Figure 4.21: Rotor Optimization: Maximize damping from 200 to 500 kts (tight constraints)

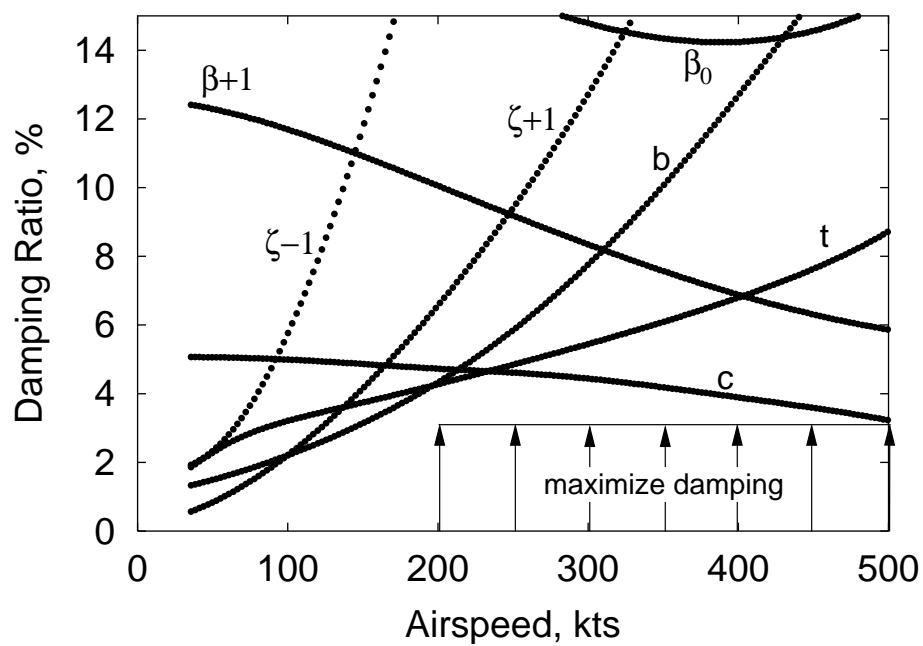


Figure 4.22: Rotor Optimization: Maximize damping from 200 to 500 kts (medium constraints)

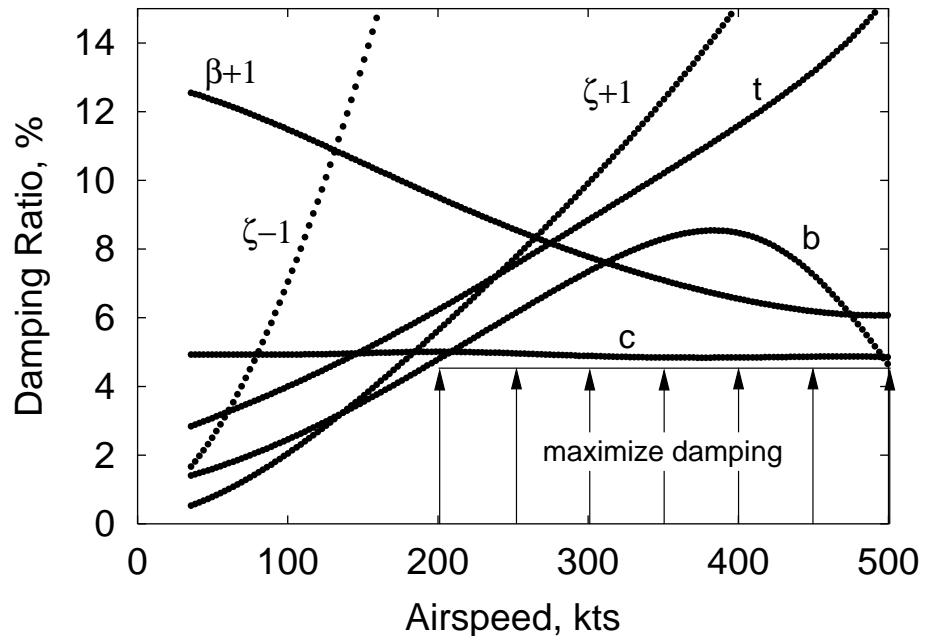


Figure 4.23: Rotor Optimization: Maximize damping from 200 to 500 kts (relaxed constraints)

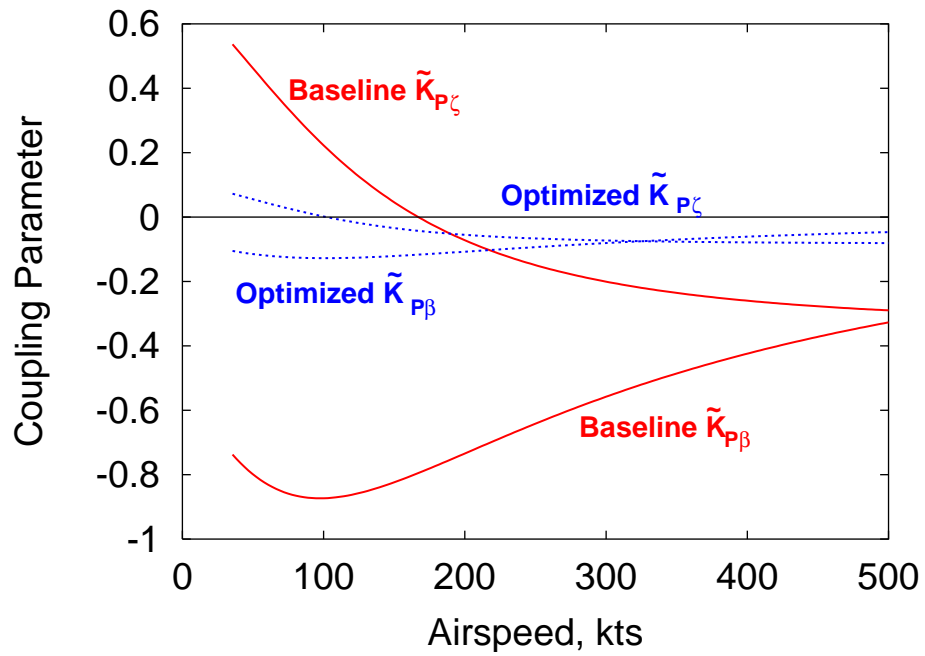


Figure 4.24: Rotor Optimization: Variation of pitch-flap and pitch-lag couplings due to distribution of blade flexibility



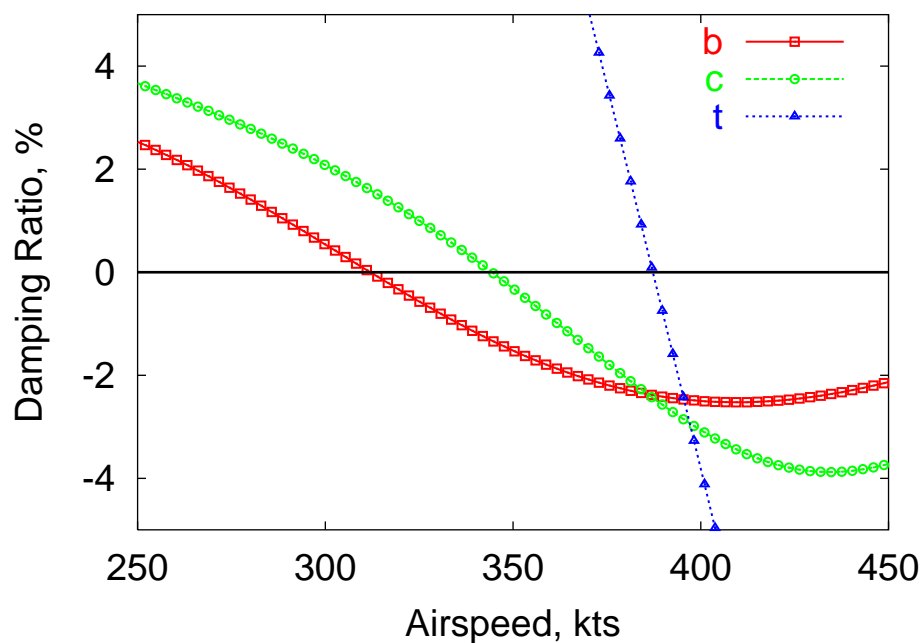


Figure 4.25: Wing design optimization: Optimization unable to improve beam mode damping, due to chord mode and torsion mode instabilities at high speeds

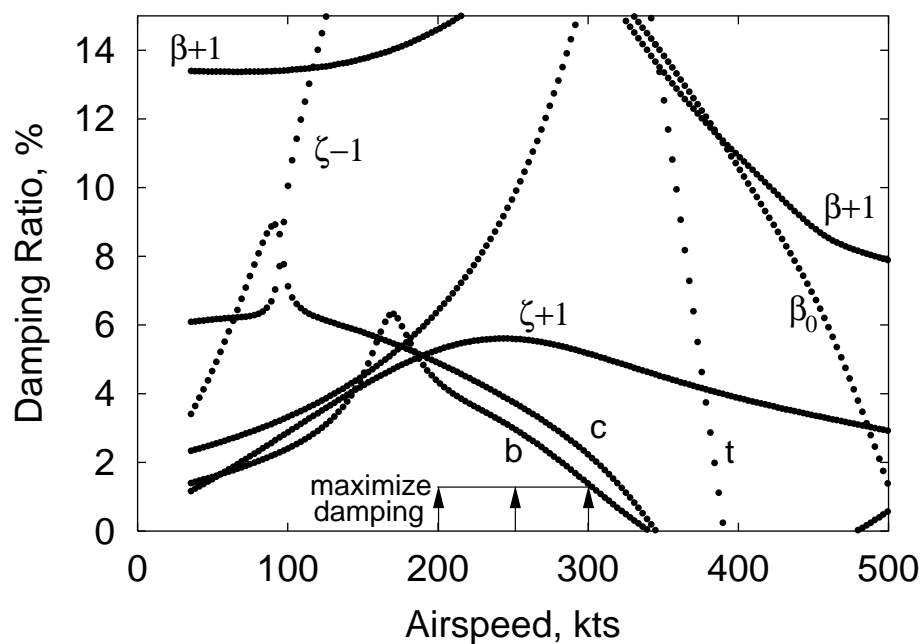


Figure 4.26: Wing Optimization: Maximize damping from 200 to 300 kts (tight constraints)

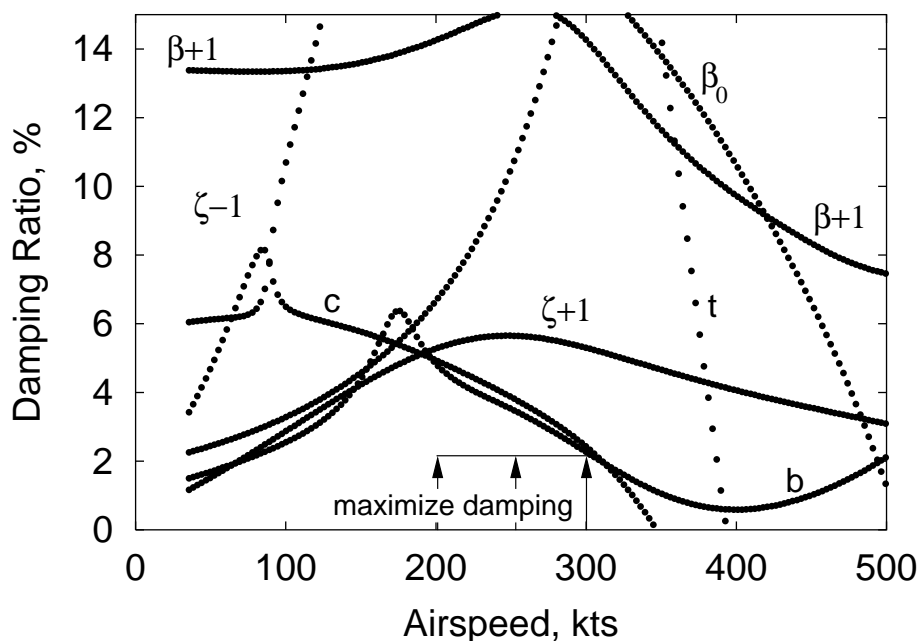


Figure 4.27: Wing Optimization: Maximize damping from 200 to 300 kts (medium constraints)

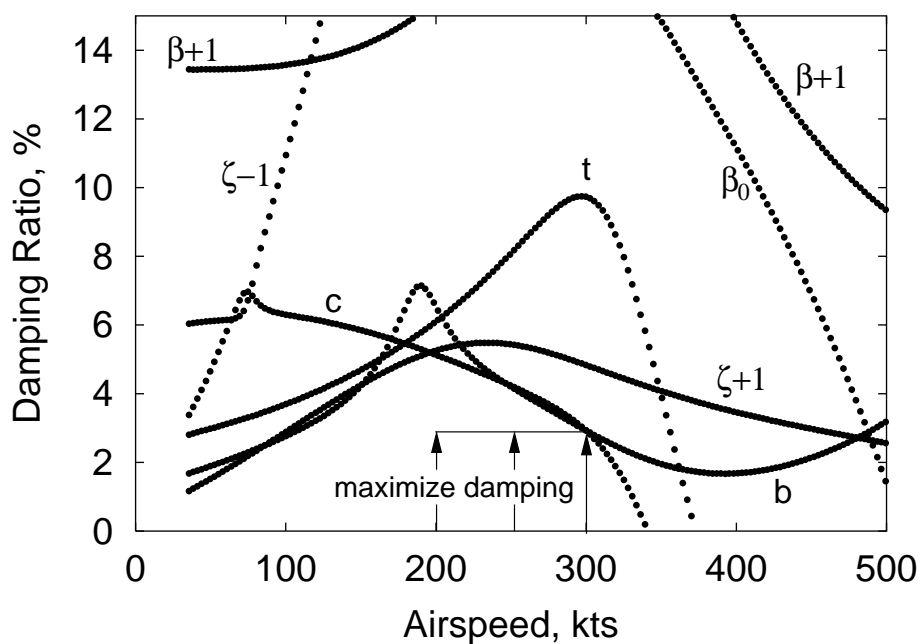


Figure 4.28: Wing Optimization: Maximize damping from 200 to 300 kts (relaxed constraints)

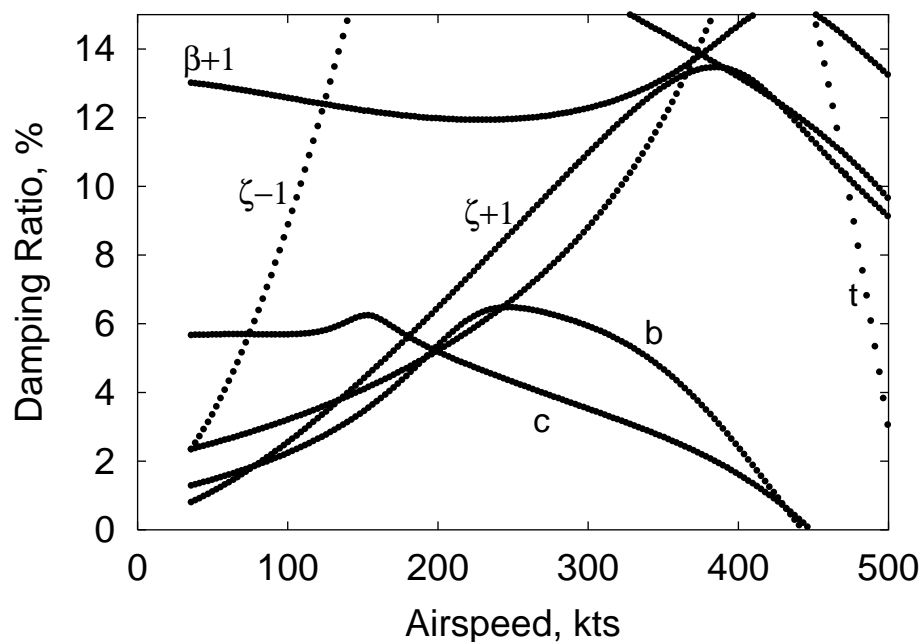


Figure 4.29: Concurrent Wing/Rotor Optimization: Maximize damping from 200 to 500 kts (tight constraints)

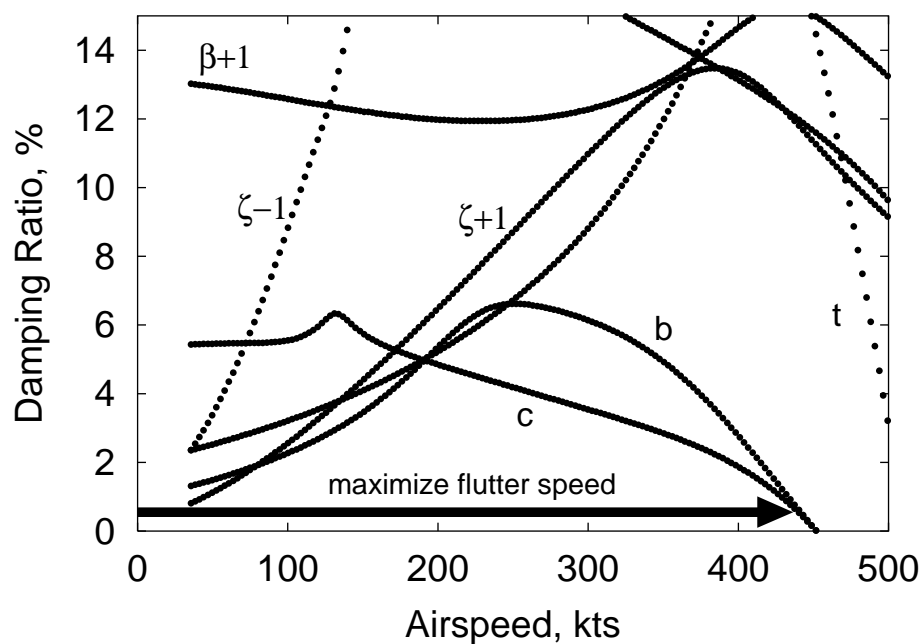


Figure 4.30: Concurrent Wing/Rotor Optimization: Maximize critical flutter speed (tight constraints)

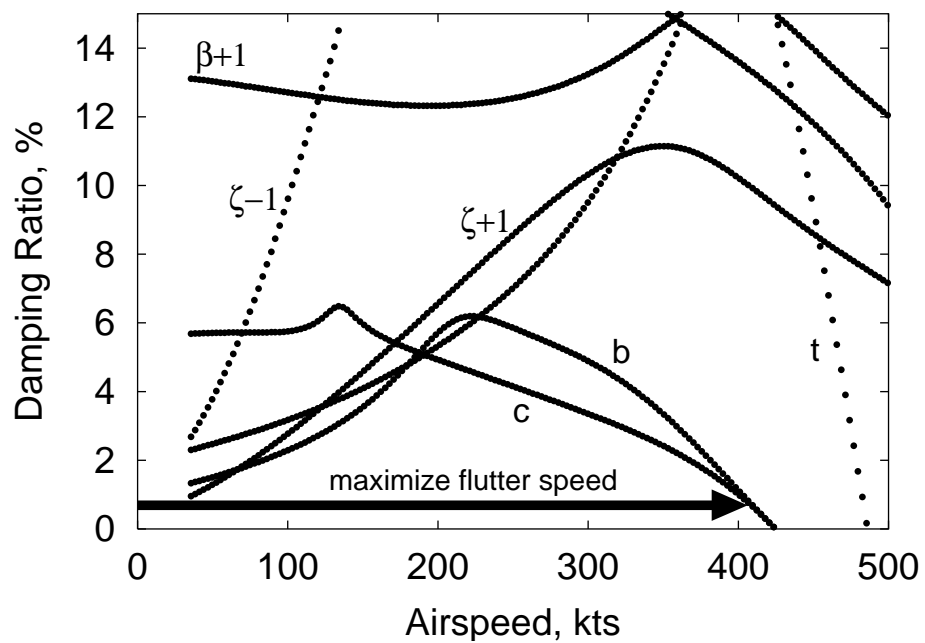


Figure 4.31: Concurrent Wing/Rotor Optimization: Maximize critical flutter speed (tight constraints, key parameters only)

## **Chapter 5**

# **Active Control of Wing Flaperons for Stability Augmentation**

This chapter presents the results of a study of the effectiveness of wing flaperon active control for alleviation of tiltrotor whirl flutter. Control systems that increase whirl flutter speed and wing mode sub-critical damping are designed while observing realistic limits on flaperon deflection. Both stiff- and soft-inplane tiltrotor configurations are examined, to develop an understanding of the influence of vehicle configuration on flaperon effectiveness. The importance of considering unsteady aerodynamic effects in stability analyses and in controller design is also examined. Controller designs considered include airspeed-scheduled optimal controllers based on full-state feedback, constant-gain full-state feedback controllers derived from the optimal controllers, and single-state feedback systems. The dominant feedback parameters in the optimal control systems are identified and examined to gain insight into the most important feedback paths that could be exploited by simpler reduced-order controllers. Feedback of wing vertical and chordwise bending modes are identified as the most powerful parameters, with wing vertical bending rate feedback being particularly beneficial. Wing vertical bending mode rate feedback substantially increases damping of the wing vertical bending mode, which is often poorly damped

in soft-inplane tiltrotor configurations.

## 5.1 Flaperon active control formulation

Active control inputs to the system are through wing flaperon deflection ( $\delta$ ). In the present study, the flaperon is sized to approximately match the XV-15's flaperon, with a chord equal to 25% of the total wing chord, and a span covering the outer 50% of the wing. Aerodynamic forces and moments generated by flaperon motion are in general functions of flaperon displacement, rate, and acceleration. Thus the rotor/wing equations of motion, including the forcing terms due to flaperon motion, may be written as:

$$[M]\ddot{\mathbf{q}} + [C]\dot{\mathbf{q}} + [K]\mathbf{q} = [D_2]\ddot{\delta} + [D_1]\dot{\delta} + [D_0]\delta \quad (5.1)$$

where  $\mathbf{q}$  is the vector of wing and rotor degrees of freedom. The matrix  $[D_2]$  may include terms due to flap inertial effects, while  $[D_1]$  and  $[D_0]$  contain aerodynamic terms. Forces proportional to flap rate may appear even for quasi-steady aerodynamic models. For instance, if the flap aerodynamic model were based upon a quasi-steady simplification of Theodorsen's unsteady aerodynamic model [78], the contribution to airfoil section lift from the flap would be:

$$\Delta l = \frac{1}{2}\rho V^2 c \left( 2T_{10}\delta + \frac{c}{2V}T_{11}\dot{\delta} \right) \quad (5.2)$$

where  $T_{10}$  and  $T_{11}$  are simply geometric constants related to the ratio of flap chord length to overall airfoil chord length, and are defined by Theodorsen in Ref. 78. An aerodynamic model that also includes unsteady effects would have additional terms proportional to flap displacement and rate.

For control system design and analysis, it is convenient to express the system in the familiar first-order form  $\dot{x} = Ax + Bu$ . If forces and moments proportional to flaperon rate and acceleration were to be neglected, the system could easily be placed in such a form,

using flaperon deflection  $\delta$  as the control variable  $u$ . A more rigorous approach, which retains the aerodynamic loads proportional to flaperon rate and acceleration, is used in the present study. The control variable used is the flaperon acceleration  $\delta^{**}$ . In a practical implementation of this control system using actual hardware, the controller would have to determine the hinge moment applied to the flaperon by an (unspecified) actuation system to achieve the desired flap acceleration. The present study does not consider the dynamics associated with the actuation system and as a result, the formulation can be simplified to treat acceleration as the control parameter directly:

$$u = \delta^{**} \quad (5.3)$$

By formulating the control system to prescribe flaperon acceleration, and including flaperon angular displacement and rate in an augmented state vector (along with the wing and rotor degrees of freedom), the complete system can be expressed in the desired first-order form:

$$\begin{Bmatrix} \ddot{\mathbf{q}} \\ \ddot{\delta} \\ \dot{\mathbf{q}} \\ \dot{\delta} \end{Bmatrix} = \begin{bmatrix} -M^{-1}C & M^{-1}D_1 & -M^{-1}K & M^{-1}D_0 \\ 0 & 0 & 0 & 0 \\ I & 0 & 0 & 0 \\ 0 & 1 & 0 & 0 \end{bmatrix} \begin{Bmatrix} \dot{\mathbf{q}} \\ \dot{\delta} \\ \mathbf{q} \\ \delta \end{Bmatrix} + \begin{bmatrix} M^{-1}D_2 \\ 1 \\ 0 \\ 0 \end{bmatrix} \delta^{**} \quad (5.4)$$

Flaperon acceleration is determined by the feedback control law:

$$\delta^{**} = -[G] \begin{Bmatrix} \dot{\mathbf{q}} \\ \dot{\delta} \\ \mathbf{q} \\ \delta \end{Bmatrix} \quad (5.5)$$

where  $[G]$  is the set of control gains to be determined by the controller design process.

Incorporation of unsteady aerodynamic forces will add additional terms and states to

the system in Eq. 5.4. Formulation of the model including unsteady effects is discussed briefly in Section 5.1.2 and in greater detail in Appendix B.

### 5.1.1 Limits on control gains

An important issue when evaluating the effectiveness of an active control scheme is the question of control gain limits. A given set of controller gains may be able to completely eliminate whirl flutter, but if the resulting control inputs command flap motions which greatly exceed the practical limits of flap deflection, the design is not feasible. To obtain an approximate estimate of control gain limits for the results presented here, some assumptions are made about maximum allowable flap deflection and about the magnitude of perturbations experienced by the wing modes. Flap deflection available to the active controller is assumed to be  $\pm 6^\circ$ . The  $6^\circ$  limit on flap deflection was selected based on practical considerations of aircraft control and actuator capability. In Ref. 27, the limits on flaperon deflection for the XV-15 operating in airplane mode are given as  $\pm 15^\circ$ . In Ref. 58, active control of the flaperon on the WRATS semi-span model was examined experimentally for vibration suppression. In that test, the flaperon was driven up to  $\pm 4^\circ$  of deflection, but at a higher frequency (3/rev) than is required for stability augmentation. Therefore  $6^\circ$  was selected as an aggressive but not unrealistic target for maximum flap deflection for this study.

Another important parameter in determining limits on control gains is the level of perturbation experienced by the system. In a linear feedback control system of the form  $u = -Kx$ , for a fixed maximum control input  $u$ , the magnitude of controller gains  $K$  for which the controller input does not exceed prescribed limits are reduced as the level of disturbance  $x$  is increased. For an actual control design intended for practical implementation, a worst-case disturbance condition must be identified, and controller gains limited to prevent the control input from exceeding the prescribed limits, even for these worst-case conditions. As an approximation, the following perturbations are considered for the



semispan tiltrotor model as the critical conditions used to limit controller gains: (1) wing vertical bending mode excitation, with wingtip vertical displacement of 2.5% of the rotor radius, (2) wing chordwise bending mode excitation, with a wingtip displacement of 1% rotor radius in the chordwise direction, and (3) wing torsion mode excitation, with  $1^\circ$  of twist at the wingtip. The controller gains used in the present study are chosen such that, given any one of the above disturbance conditions, the resulting flap deflections will not exceed the maximum  $\pm 6^\circ$  limit.

While the assumed disturbance conditions used in the present study could be considered somewhat artificial (excitation of a single mode to a known maximum level of perturbation), it should be noted that these disturbance conditions closely resemble the excitations typically applied to tiltrotor models undergoing aeroelastic testing in a wind tunnel. Reference 39 describes how the WRATS semi-span tiltrotor model is excited during whirl flutter testing through “stick stirs”, oscillatory blade pitch changes introduced through the swashplate at a wing mode natural frequency. The stick stir continues until a sufficient excitation amplitude of the wing mode is achieved, whereupon the excitation is removed, and the free response of the model is measured to obtain modal frequency and damping data. If the active flaperon control laws developed in the present study were implemented on a model undergoing similar testing, the limits imposed on controller gains would ensure that typical test excitations would not result in excessive flaperon commanded deflections.

### **5.1.2 Wing unsteady aerodynamic modeling**

In the initial model formulation, the wing aerodynamics were based on a quasi-steady aerodynamic model. Since the actively controlled flaperon is capable of generating large oscillatory aerodynamic loads on the wing, the appropriateness of this simple aerodynamic model should be investigated. To this end, an unsteady aerodynamic model was added to the wing. By comparing the results obtained using each of these models, the influence of unsteady aerodynamics on performance of the actively controlled flaperon and on controller

design can be evaluated to determine whether or not the quasi-steady aerodynamic model is adequate. This section describes the general approach used to incorporate an unsteady aerodynamic model for the wing and flaperon in the present analysis. Appendix B provides more specific implementation details.

To incorporate unsteady aerodynamics into the present tiltrotor wing model in a manner amenable to stability analysis and controller design, the aerodynamic model must be formulated in the time domain. A Rational Function Approximation (RFA) approach is used in the present study to generate a state-space, time domain aerodynamic model from oscillatory response data (airfoil lift and pitching moment about the quarter-chord and moments about the flap hinge, due to airfoil pitching and plunging and flap motions). The RFA technique has been commonly used in fixed-wing aeroelastic analysis. In Ref. 79, an RFA aerodynamic model was extended to account for unsteady freestream and Mach number effects and was successfully applied to a helicopter rotor with trailing-edge flaps. The RFA aerodynamic model used in the present study generally follows the formulation given in Ref. 79. A brief description of the present formulation is provided below.

Consider the aerodynamic loads on an airfoil section, expressed in the Laplace domain:

$$\mathbf{F}(\bar{s}) = \mathbf{Q}(\bar{s})\mathbf{H}(\bar{s}) \quad (5.6)$$

where  $\mathbf{F}(\bar{s})$  is a vector of generalized loads (in this case, sectional lift, pitching moment, and hinge moment),  $\mathbf{H}(\bar{s})$  is a vector of generalized motions (due to pitch, plunge, and flap deflection and rate), and  $\mathbf{Q}(\bar{s})$  is an aerodynamic transfer matrix, which determines the magnitude and phase of the aerodynamic loads generated by the airfoil motions. The term  $\bar{s}$  here denotes a reduced Laplace variable, normalized by freestream velocity  $U$  and airfoil semi-chord  $b$  (this is analogous to the reduced frequency parameter  $k$  often used in frequency-domain unsteady aerodynamic analysis). The reduced Laplace variable is defined as:

$$\bar{s} = \frac{sb}{U} \quad (5.7)$$

In the frequency domain,  $\mathbf{Q}(\bar{s})$  is readily obtained from tabulated oscillatory response data, but this frequency response data can not be directly applied to a time domain formulation.

The frequency domain oscillatory response data can be used to develop a time domain unsteady aerodynamic model, however, using the Rational Function Approximation approach. The transfer matrix  $\mathbf{Q}(\bar{s})$  is approximated by a rational function  $\tilde{\mathbf{Q}}(\bar{s})$ , assumed to be of the form:

$$\tilde{\mathbf{Q}}(\bar{s}) = \mathbf{C}_0 + \mathbf{C}_1\bar{s} + \sum_{n=1}^{n_L} \frac{\bar{s}}{\bar{s} + \gamma_n} \mathbf{C}_{n+1} \quad (5.8)$$

In Eq. (5.8),  $\mathbf{C}_0$  represents the quasi-steady aerodynamic contribution. Since a finite response is desired as the frequency of oscillation increases,  $\mathbf{C}_1$  is constrained to be zero. The final summation term in Eq. (5.8) represents  $n_L$  aerodynamic lag terms, with poles  $\gamma_n$  which lie on the negative real axis.

The approximate function  $\tilde{\mathbf{Q}}(\bar{s})$  is then adjusted to achieve the best fit, in a least squares sense, to the tabulated data in  $\mathbf{Q}(\bar{s})$  by choosing appropriate values for the elements of the matrices  $\mathbf{C}_{n+1}$ . The location of the poles  $\gamma_n$  are selected through an optimization process which seeks to minimize the fitting error between  $\mathbf{Q}(\bar{s})$  and  $\tilde{\mathbf{Q}}(\bar{s})$ . This fitting process takes place in the frequency domain ( $\bar{s} = i\frac{\omega b}{U} = ik$ ). Details of the implementation of the fitting process are provided in Appendix B.

By choosing a rational expression for the form of the approximate model in the Laplace domain, the model can be easily transformed to the time domain. For convenience, the summation term in Eq. (5.8) can be re-written using matrix notation, with the rational function taking the following form:

$$\tilde{\mathbf{Q}}(\bar{s}) = \mathbf{C}_0 + \mathbf{C}_1\bar{s} + \mathbf{D}(\mathbf{I}\bar{s} - \mathbf{R})^{-1} \mathbf{E}\bar{s} \quad (5.9)$$

where the matrices  $\mathbf{D}$ ,  $\mathbf{R}$ , and  $\mathbf{E}$  are defined as

$$\mathbf{D} = [\mathbf{I} \quad \mathbf{I} \quad \cdots \quad \mathbf{I}] \quad (5.10)$$

$$\mathbf{R} = - \begin{bmatrix} \gamma_1 \mathbf{I} & & & \\ & \gamma_2 \mathbf{I} & & \\ & & \ddots & \\ & & & \gamma_{n_L} \mathbf{I} \end{bmatrix} \quad (5.11)$$

$$\mathbf{E} = \begin{bmatrix} \mathbf{C}_2 \\ \mathbf{C}_3 \\ \vdots \\ \mathbf{C}_{n_L+1} \end{bmatrix} \quad (5.12)$$

Substituting the rational function approximation of the aerodynamic transfer matrix in Eq. (5.9) into Eq. (5.6), and defining a vector of aerodynamic states  $\mathbf{X}(\bar{s})$  as

$$\mathbf{X}(\bar{s}) = (\mathbf{I}\bar{s} - \mathbf{R})^{-1} \mathbf{E}\bar{s}\mathbf{H}(\bar{s}) \quad (5.13)$$

yields the following expression for the aerodynamic loads in the Laplace domain:

$$\mathbf{F}(\bar{s}) = \mathbf{C}_0\mathbf{H}(\bar{s}) + \mathbf{C}_1\bar{s}\mathbf{H}(\bar{s}) + \mathbf{D}\mathbf{X}(\bar{s}) \quad (5.14)$$

Equations (5.13) and (5.14) are then transformed from the reduced Laplace domain ( $\bar{s}$ ) to the time domain, resulting in the following expressions:

$$\dot{\mathbf{x}}(t) = \frac{U}{b}\mathbf{R}\mathbf{x}(t) + \mathbf{E}\dot{\mathbf{h}}(t) \quad (5.15)$$

$$\mathbf{f}(t) = \mathbf{C}_0\mathbf{h}(t) + \mathbf{C}_1\frac{b}{U}\dot{\mathbf{h}}(t) + \mathbf{D}\mathbf{x}(t) \quad (5.16)$$

Equation (5.16) gives the aerodynamic forces and moments on a 2-D airfoil section as a function of both the generalized airfoil motions  $\mathbf{h}(t)$  (pitch, plunge, and flap deflection and rate) and the aerodynamic states  $\mathbf{x}(t)$ . The aerodynamic states, governed by Eq. (5.15), are in turn influenced by airfoil motion.

Equations (5.15) and (5.16) provide the unsteady aerodynamic loading on an airfoil section. The total aerodynamic load on the wing is determined by evaluating Eqs. (5.15) and (5.16) at several spanwise locations, then numerically integrating these sectional loads across the entire span of the wing. The unsteady airloads are added to the system equations of motion given in Eq. (5.4). A detailed description of the integration of the unsteady aerodynamic model with the FEM wing model is provided in Appendix B. For the unsteady results presented in this paper, the 2-D unsteady airloads (lift, pitching moment, and hinge moment) are evaluated at 4 spanwise locations, with 5 aerodynamic lag poles at each location ( $n_L = 5$ ). This results in a total of 60 aerodynamic states (4 locations  $\times$  5 poles  $\times$  3 airloads – lift, pitching moment and hinge moment), which must be computed simultaneously with the system equations of motion.

## 5.2 Optimal Control Results

In this section, active flaperon control systems are designed to alleviate whirl flutter. Two different rotor configurations, the gimbaled stiff-inplane XV-15 semispan model [23] and the hingeless soft-inplane Boeing Model 222 semispan model [24], are considered. Key model parameters are given in Table 3.1 for the XV-15, and in Table 3.2 for the model 222. Optimal linear quadratic controllers are designed in which controller gains are selected to minimize the following quadratic cost function:

$$J = \int_0^{\infty} \left( \mathbf{q}_A^T [Q] \mathbf{q}_A + R \delta^{**2} \right) dt \quad (5.17)$$

where  $\mathbf{q}_A$  represents the augmented state vector in Eq. 5.4. If the unsteady aerodynamic

model is included in the analysis, this augmented state vector also includes all of the aerodynamic lag states  $\mathbf{x}$ . The matrix  $[Q]$  contains the weights placed on disturbance of each state variable. It is a diagonal matrix, with the on-diagonal entries corresponding to rotor and wing displacements set to one, and all other entries (corresponding to rates, flaperon displacement, and (if present) aerodynamic lag states) set to zero. The value of the weight on control effort (the parameter  $R$  in Eq. (5.17)) is manually adjusted to allow the largest possible increase in flutter speed, while respecting the limits on flap actuation previously discussed.

The optimal control results presented in this section are generated using a quasi-steady aerodynamic model for the wing and flaperon aerodynamics. The effect of including unsteady aerodynamic effects will be examined in Section 5.3.

### 5.2.1 XV-15

Figure 5.1 shows the baseline (uncontrolled) modal damping characteristics vs. air-speed for the full-scale XV-15 semispan wind tunnel model, generated using a quasi-steady model of wing aerodynamics. The wing vertical bending mode is the critical mode for this wing/rotor configuration, becoming unstable at 330 knots. It should be noted that the differences between the damping predictions shown in Fig. 5.1 and results presented in previous chapters (Figs. 3.4–3.6 and Fig. 4.1) are due to differences in the wing model used to generate the results. In previous chapters, the wing was modelled using an assumed-mode approach, originally developed by Johnson in Ref. 2. The addition of a flaperon necessitated the development of a new wing model. A finite element-based wing model, including a flaperon, was developed and used for the results in this chapter. Details of the FEM wing formulation are provided in Appendix A.

Performance of an optimal flaperon controller for the XV-15 is shown in Fig. 5.2. The optimal control system is able to improve damping for the wing modes, with wing vertical bending mode damping being particularly enhanced. The stability boundary is increased by

approximately 145 knots, from 330 knots for the baseline (Fig. 5.1) to nearly 475 knots for the controlled system, where the rotor coning mode ( $\beta_0$ ) reaches zero damping. However, the practical airspeed limit for this configuration is 420 knots, above which the required control inputs exceed the  $6^\circ$  limit imposed on flaperon deflection. This still represents a significant 90 knot increase in flutter speed over the baseline. Increasing the weight on control effort in Eq. (5.17) would reduce flaperon deflection, but this would also result in decreased damping augmentation in the wing modes. In particular, decreased damping in the wing chord mode near 380 knots would prevent safe operation above that speed.

Figure 5.3 shows the variation of controller gains with airspeed for the optimal flaperon control designed for the XV-15. Below about 400 knots, Fig. 5.3 shows that most of the feedback gains are near zero. The few non-zero gains, labeled on the figure, are on feedback of wing vertical bending mode rate ( $\dot{b}$ ) and displacement ( $b$ ), and wing chordwise bending mode rate ( $\dot{c}$ ) and displacement ( $c$ ). Of these modes, the gain on vertical bending rate feedback is the largest. Above about 400 knots, the controller gains and therefore the flap deflections required to provide stability increase rapidly, causing a sharp increase in the magnitude of the feedback gains which drive flaperon deflection. The increasingly large controller gains ultimately drive the flaperon to its deflection limit at 420 knots.

### 5.2.2 Model 222

The baseline modal damping vs. airspeed behavior for the uncontrolled full-scale Model 222 wind tunnel model using quasi-steady wing aerodynamics is shown in Fig. 5.4. For this configuration, the wing chordwise bending mode is the critical mode, whereas for the XV-15 model, the vertical bending mode was critical. The baseline Model 222 chordwise bending mode becomes unstable at 390 knots. It should be noted that the wing vertical bending mode, while not the critical mode for whirl flutter stability, does exhibit low damping levels, particularly below 200 knots.

The stability characteristics of the Model 222 with an optimal controller are shown in

Fig. 5.5. The stability boundary is increased by about 20 knots over the baseline (Fig. 5.4), from 390 to just over 410 knots, where the rotor progressing flap mode ( $\beta + 1$ ) reaches zero damping. Commanded flaperon deflections below this speed are within the imposed limits. Increasing flaperon deflection by reducing the weight on control effort in the optimal control cost function in Eq. (5.17) does not improve the damping of the now-critical rotor mode (unless the weight is reduced to the point that unreasonably large flaperon deflections are commanded). Besides the modest increase in flutter speed, the large increase in wing vertical bending mode damping, also seen in the XV-15, is particularly noteworthy for this configuration. The low inherent damping in the wing vertical bending mode of soft-inplane tiltrotors is significantly improved by the actively controlled flaperon.

Figure 5.6 shows the variation of controller gains with airspeed for the Model 222. Note that the general behavior of the gains is similar to the gains obtained for the XV-15 (compare Figs. 5.3 and 5.6). At speeds below the stability boundary, the only significant gains are those associated with feedbacks of the wing vertical and chordwise bending modes. Vertical bending mode rate feedback again has the largest gain in this speed range. At high airspeeds, the magnitude of all feedback gains begins to increase rapidly, as was the case for the XV-15.

### 5.3 Influence of Unsteady Aerodynamics

The results presented to this point have all been generated using a quasi-steady wing aerodynamic model. The influence of unsteady aerodynamic effects on flaperon active control is now examined using the RFA unsteady aerodynamic model described in Section 5.1.2.

Figure 5.7 shows the baseline damping characteristics for the XV-15, with unsteady wing aerodynamic effects included in the analysis. Careful comparison of Fig. 5.7 with Fig. 5.1 shows only small decreases in peak damping of the wing modes when unsteady effects are included. This is consistent with observations in Ref. 80, where a Peters/He



finite state wake model was applied to a tiltrotor wing. The nearly insignificant effect of wing unsteady aerodynamic effects on stability for the baseline (uncontrolled) case is due to the relatively small effect wing aerodynamic forces have on aeroelastic stability. Wing perturbation lift, drag, and pitching moments are much smaller than the perturbation forces and moments from the rotor acting on the wing.

Introducing the flaperon control system permits the controlled generation of larger wing aerodynamic forces. Nevertheless, Fig. 5.8 shows that including wing unsteady aerodynamic effects still results in only a slight reduction in wing damping levels achieved when flaperon active control is applied (compare with Fig. 5.2). The optimal control gains applied to the system in Fig. 5.8 are calculated while including the unsteady aerodynamic effects in the model. Figure 5.9 shows the variation of these controller gains with airspeed for the unsteady aerodynamics case. Though there are some differences in the values of the gains, the overall behavior of the gains is similar to the quasi-steady case.

A better understanding of the influence of unsteady aerodynamics on the behavior of the flaperon control system can be gained by examining the time history of flaperon deflection in response to a disturbance. Figure 5.10 shows the time history of flaperon deflection and vertical displacement of the wing tip due to an initial displacement of the wing vertical bending mode to the assumed maximum displacement of 2.5% of the rotor radius at the wing tip, at an airspeed of 350 knots (20 knots above the baseline flutter speed). Only quasi-steady aerodynamic effects are included in the simulation results shown in Fig. 5.10. The feedback gains shown in Fig. 5.3 are used. The well-damped behavior of the vertical bending mode with the flaperon control system active is apparent. In a given cycle of oscillation, the peak flaperon deflection occurs about 75 milliseconds after the peak wingtip displacement. At the frequency of oscillation (3.03 Hz), this corresponds to a phase delay of  $82^\circ$  between peak wingtip displacement and peak flap deflection. Figure 5.11 shows time history data for the same case, but with the unsteady aerodynamic model included in the analysis, and the feedback gains designed using the unsteady aerodynamic model (Fig. 5.9). The time history of the wing vertical bending motion is nearly identical between the two

cases (quasi-steady vs. unsteady aerodynamics), and the flaperon motion is very similar as well. There is a small difference in the phasing between wingtip and flaperon motion, however. In Fig. 5.11, there is only a 63 millisecond delay between peak wingtip displacement peak flaperon deflection. This corresponds to a phase delay of  $69^\circ$ . So the phase of the flaperon motion when unsteady aerodynamics are included in the analysis leads the flaperon motion when only quasi-steady aerodynamics are considered by  $13^\circ$ . Not coincidentally, this is very close to the phase delay predicted by Theordorsen for the reduced frequency corresponding to vertical bending mode frequency at this airspeed. So the design of the optimal control gains when unsteady aerodynamics are included compensated for the aerodynamic phase lag by changing the phase of the flap motion.

The influence of wing unsteady aerodynamics on the Model 222 is similar to that seen for the XV-15. Modal damping in the wing modes is slightly reduced for the baseline system (Fig. 5.12) and for the system with active flaperon control (Fig. 5.13). The optimal gains derived with the unsteady aerodynamics model active (Fig. 5.14) are similar in behavior, but not exactly the same as, the gains obtained using only quasi-steady aerodynamics. The primary difference is again a change in the phase relationship of the displacement-feedback and rate-feedback gains, to account for the phase loss due to unsteady aerodynamic effects.

The importance of including wing unsteady aerodynamics when designing flaperon control systems is further examined by looking at the stability characteristics obtained when a controller designed using the quasi-steady wing aerodynamic model is run with the unsteady aerodynamics model active. Figure 5.15 shows the damping characteristics in this case for the XV-15, and Figure 5.16 shows the corresponding data for the Model 222. In both cases, there is a noticeable reduction in damping at high speed when compared to Figs. 5.8 and 5.13, respectively, which show damping vs. airspeed when the controllers were designed with unsteady aerodynamic effects included. It should be noted that most of the differences in damping observed when running with the two different sets of gains occur at airspeeds above the stability boundary, and are of no practical consequence. Since the

modal damping results obtained from either aerodynamic model are similar in the airspeed range of interest, regardless of which aerodynamic model is used to design the controller, it is concluded that the simple quasi-steady wing aerodynamic model is adequate to explore the basic performance of flaperon control. To obtain the greatest benefit from the flaperon control system however, the control gains should be designed with the highest-fidelity aerodynamic model available.

## 5.4 Full-State Constant Gain Controller

The optimal control results presented above featured controller gains which vary with airspeed. For each airspeed considered, a new set of gains is obtained by minimizing the cost function in Eq. (5.17) at that airspeed. A control system with constant controller gains is generally preferred to a more complex gain-scheduled control system. Figure 5.17 shows the damping characteristics of the semi-span XV-15 model with a full-state constant gain controller, using the controller gains calculated as optimal at 380 knots. Figure 5.18 shows the stability of the Model 222 using a constant gain controller with the gains that were optimal at 380 knots. The data in both Figures 5.17 and 5.18 were generated using the quasi-steady aerodynamic model. For both configurations, the improvements in flutter speed and vertical bending mode damping are still maintained using the single set of control gains (as opposed to gain scheduling). Comparison of the constant gain results in Figs. 5.17 and 5.18 with the gain-scheduled optimal control results in Figs. 5.2 and 5.5 show that damping at speeds below the stability boundary is actually greater for the constant gain case. This is because the control gains used at low speeds for the constant gain case are larger than those used at those speeds by the optimal controller. As a result, flaperon actuation at low speeds is somewhat greater than for the optimally designed case. Despite the larger flaperon deflections, the constant gain designs are still within the imposed actuation limits.

## 5.5 Effect of Rotor Speed on Flaperon Control

All the active control results discussed to this point have been generated with the rotor operating at the design airplane mode rotational speed (458 RPM for the XV-15, 386 RPM for the Model 222). In operation, tiltrotor aircraft must transition from this lower rotational speed in airplane mode to a higher rotational speed for conversion and hover mode (565 RPM for the XV-15, 551 RPM for the Model 222). It is therefore desirable to ensure the flaperon control system, designed at one rotor speed, provides adequate stability over the range of rotor speeds encountered in operation. Allowable changes in whirl flutter stability as a function of rotor speed is a vehicle-specific design requirement. To examine the effect of rotor speed on flaperon control for this study, constant-gain controllers are developed that maintain a fixed minimum flutter speed, regardless of rotor speed.

Figure 5.19 shows the modal damping versus airspeed for the baseline uncontrolled XV-15, operating at the hover mode rotor speed. Comparing Fig. 5.19 to the airplane mode rotor speed case in Fig. 5.1 shows that increased rotor speed lowers wing beam and torsion mode damping, resulting in a reduction in the critical beam mode flutter speed, while wing chord mode sub-critical damping is actually improved slightly. Figure 5.20 shows modal damping versus rotor speed at 380 knots for the uncontrolled XV-15. At this airspeed, the wing chord mode is neutrally stable and nearly insensitive to changes in rotor speed, the beam mode is unstable for all rotor speeds considered, and the torsion mode damping varies considerably with rotor speed, becoming unstable above 510 RPM.

In Fig. 5.17 the constant gain control designed at 380 knots and 458 RPM was shown to provide whirl flutter stability up to 400 knots at 458 RPM. Figure 5.21 shows modal damping versus airspeed at 565 RPM (the hover rotor speed) for the same constant gain controller. At the higher rotor speed, the controller still provides a significant improvement in damping and flutter speed over the uncontrolled case (Fig. 5.19). The critical flutter speed of 360 knots is still less than the 458 RPM case shown in Fig. 5.17. Figure 5.22 shows damping versus rotor speed at 380 knots for the XV-15 with constant gain controller. The

wing beam and chord mode are both stable for all rotor speeds considered (the beam mode damping has increased so much that it is not shown in the scale of Fig. 5.22). Increasing rotor speed is still strongly destabilizing to the torsion mode however, with the torsion mode becoming unstable at 380 knots and 520 RPM.

In an attempt to provide flutter stability at 380 knots, regardless of rotor speed, an optimal controller was designed at 380 knots and 565 RPM (the hover rotor speed). Figure 5.23 shows modal damping versus airspeed at 565 RPM for the XV-15 with the new constant gain controller. Compared to the constant gain controller designed at 380 knots and 458 RPM, the new constant gain controller improves flutter speed at 565 RPM to 390 knots from 360 knots (Fig. 5.21). At the airplane mode rotor speed, Fig. 5.24 shows that the new constant gain controller maintains a flutter speed of 390 knots, which is only slightly less than the 400 knots achieved by the constant gain controller designed at 458 RPM (Fig. 5.17). Figure 5.25 shows that the constant gain controller designed at 380 knots and 565 RPM provides stability at 380 knots for all rotor speeds considered.

Figure 5.26 shows modal damping vs. airspeed for the Model 222 at its hover rotor speed of 551 RPM, using the constant gain controller designed at 380 knots and 386 RPM. For the Model 222, the constant gain controller designed at the airplane mode rotor speed still provides adequate stability at the hover rotor speed, with a flutter speed of 400 knots. Comparing Fig. 5.18 to Fig. 5.26 shows that increasing rotor speed decreases wing beam and torsion mode damping while increasing chord mode damping, just as was seen for the XV-15 in Figs. 5.1 and 5.19. Since the chord mode is the critical flutter mode for the 222 at the cruise rotor speed, increasing the rotor speed does not result in the large reduction in flutter speed that was seen in the XV-15, where the beam mode was critical.

## **5.6 Investigation of Key Feedback Parameters**

Examination of the controller gains obtained for both the XV-15 and Model 222 revealed that the gains on a few key feedback parameters are typically much larger than the

others. Wing vertical bending and chordwise bending feedback (position and rate) dominate the optimal control solutions below the speed where controller gains rapidly increase and the flaperon reaches its deflection limits.

The influence of feedback of each of these states (vertical bending rate and position, and chordwise bending rate and position) on flutter speed is examined individually to determine the effectiveness of these parameters for use in simple output feedback control systems. Results are provided here only for the XV-15, as the Model 222 shows similar trends. The following comments and discussion apply equally to both configurations, except where noted.

Figure 5.27 shows the influence on wing vertical bending rate feedback on flutter speed. The figure plots the speed at which each mode goes unstable as a function of vertical bending rate feedback gain. The range of gains shown in the figure is limited to the range for which the resulting flaperon motion does not exceed the deflection limits. Figure 5.27 shows that vertical bending rate feedback is able to completely stabilize the wing vertical bending mode, even for very small feedback gains. This increase in flutter speed is caused by a large increase in vertical bending mode damping, resulting in the mode becoming stable over the entire range of airspeeds considered. This large increase in damping is also seen in the full-state optimal control results discussed previously, and this is due to the presence of vertical bending rate feedback in the optimal control gains. The influence of feeding back vertical bending rate alone is largely restricted to this increase in vertical bending mode damping—there is little influence on the stability of the other wing modes. For the XV-15, the large increase in vertical bending mode damping produces a significant increase in critical flutter speed (about 50 knots), since the vertical bending mode is the critical flutter mode in the baseline configuration. For the Model 222, the chordwise bending mode is the critical mode, and it remains largely unaffected by feedback of vertical bending rate. However, the increased vertical bending mode damping associated with feedback of vertical bending rate is still beneficial for the Model 222, since the baseline vertical bending mode damping is poor for this configuration.

As is the case for feedback of vertical bending rate, feedback of vertical bending displacement (Fig. 5.28) improves the flutter speed of the vertical bending mode while having relatively little influence on the other modes. Forces generated by the flaperon driven with vertical bending displacement feedback act as a negative spring on the vertical bending mode. This reduces the frequency of the vertical bending mode, and increases the frequency separation between the vertical bending and torsion modes. Increased separation of these two modal frequencies is identified in Refs. 3 and 1 as having a stabilizing effect on whirl flutter. Stability of the vertical bending mode is not as sensitive to displacement feedback as it is to rate feedback, however. Larger flaperon deflections are required to achieve a given level of stability augmentation when the flaperon is driven with displacement feedback. So for single-state feedback applications, vertical bending rate feedback is the preferable option.

Negative values of wing chordwise bending rate feedback gain (Fig. 5.29) are beneficial to chordwise bending mode stability, while reducing the stability of the vertical bending mode. The opposite trends in stability of the vertical and chordwise bending modes with chordwise bending rate feedback limit the effectiveness of this gain for independently increasing flutter speed. For the XV-15, Fig. 5.29 shows that a positive value of wing chordwise bending rate feedback gain can provide a modest increase in flutter speed (about 25 knots). For the Model 222, with the chordwise bending mode as the critical whirl flutter mode, a negative value of chordwise bending rate feedback gain is more beneficial.

Chordwise bending displacement feedback (Fig. 5.30) shows a similar trend to what was observed with chordwise rate feedback. In both cases, the trend of chordwise bending mode stability with gain value runs opposite to that of the vertical bending mode. So depending on which wing mode is critical for a given aircraft design, either positive or negative feedback may be the most beneficial.

The influence of any one of the feedback parameters considered here is largely limited to changing the stability of one or two modes. Depending on which mode is the critical mode for a given aircraft configuration, feedback of different states may be the most

appropriate for a single-state feedback controller application. Wing vertical bending rate feedback may be attractive for any configuration however, because of the large increase it provides in vertical bending mode damping. In the case of the Model 222, for example, it may be much more desirable to improve the vertical bending mode damping at low speed than to increase the whirl flutter speed, which at 390 knots is already much higher than that of the XV-15.



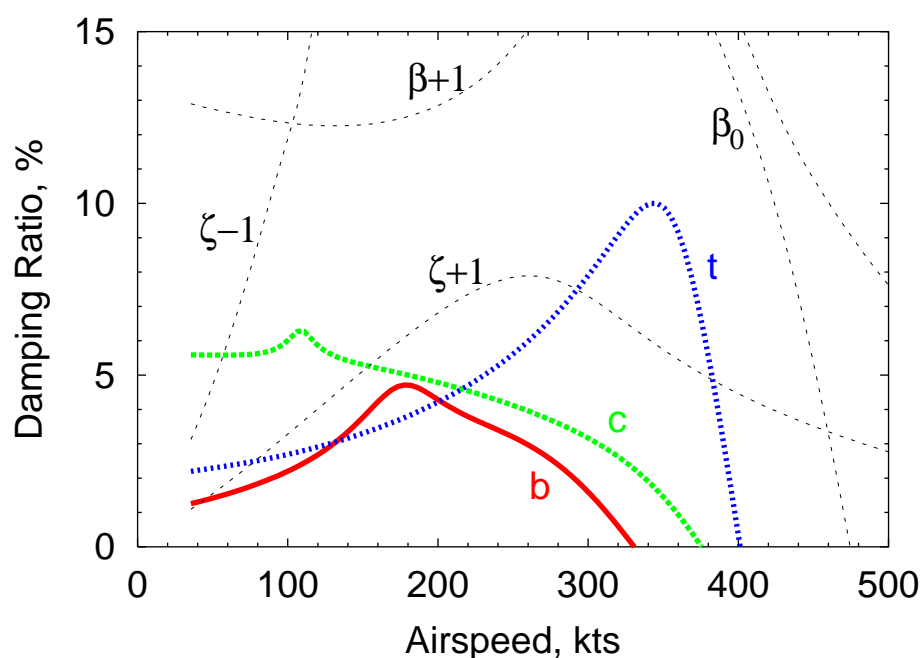


Figure 5.1: XV-15: Modal damping vs. airspeed for uncontrolled system (b: wing beam mode, c: wing chord mode, t: wing torsion mode,  $\beta_0$ : rotor coning mode,  $\zeta - 1$ ,  $\zeta + 1$ : cyclic lag modes,  $\beta + 1$ : cyclic flap (gimbal) mode)

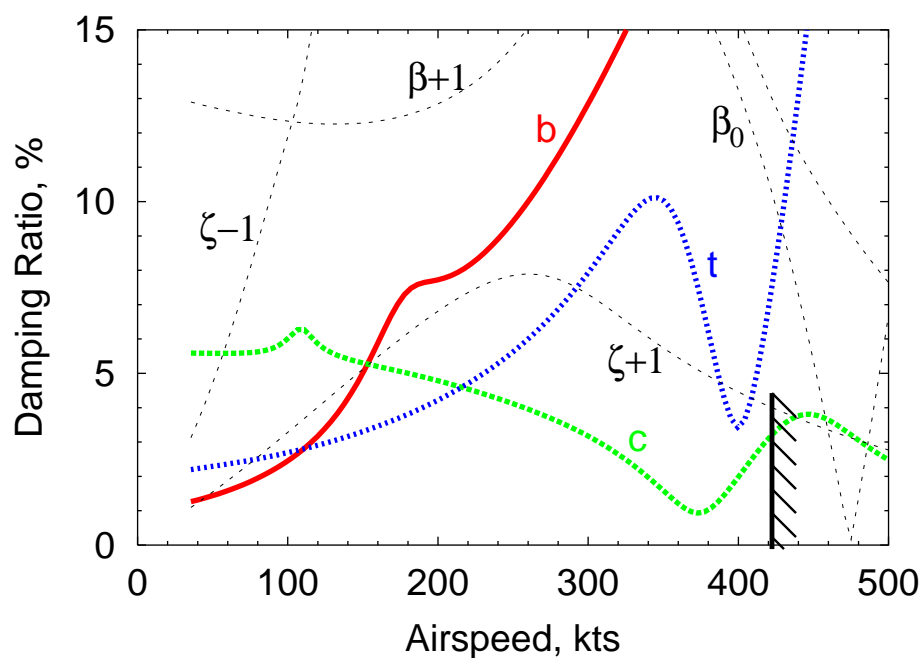


Figure 5.2: XV-15: Modal damping vs. airspeed with optimal wing flaperon control (flaperon deflection limit reached at 420 kts).

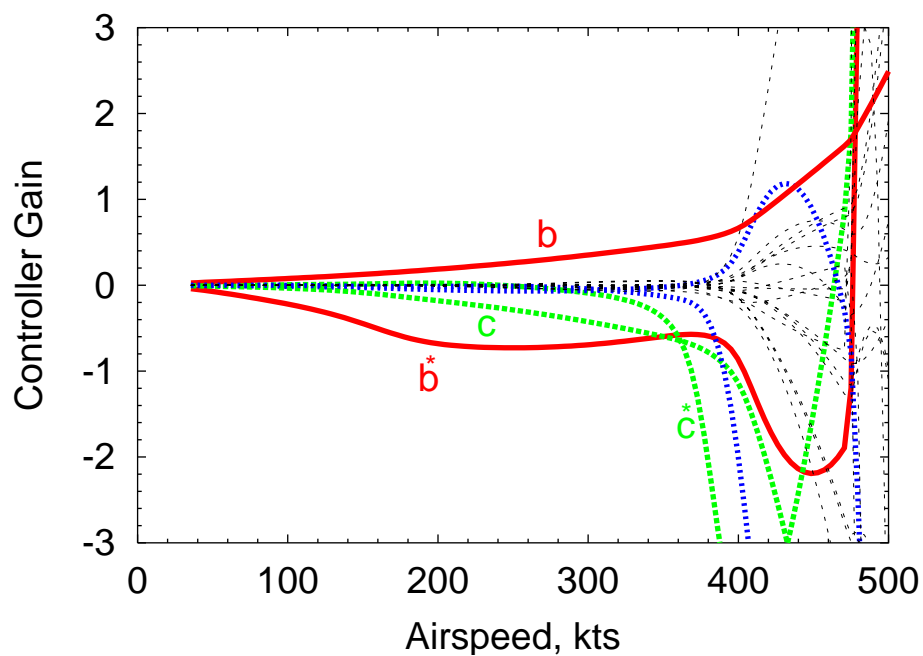


Figure 5.3: XV-15: LQR optimal controller gains

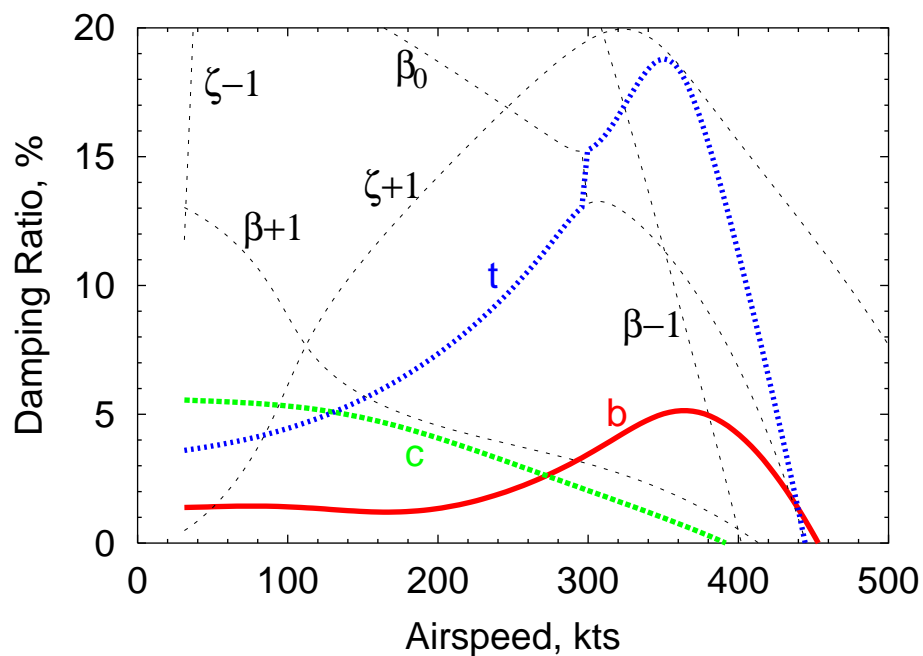


Figure 5.4: Model 222: Modal damping vs. airspeed for uncontrolled system (b: wing beam mode, c: wing chord mode, t: wing torsion mode,  $\beta_0$ : rotor coning mode,  $\zeta - 1, \zeta + 1$ : cyclic lag modes,  $\beta - 1, \beta + 1$ : cyclic flap modes)

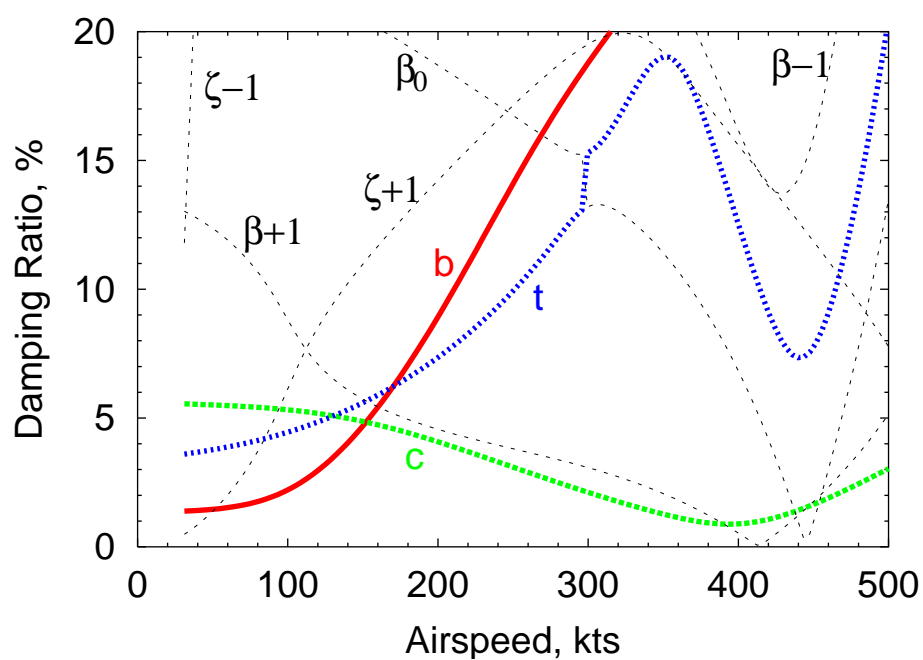


Figure 5.5: Model 222: Modal damping vs. airspeed with optimal wing flaperon control ( $\beta + 1$  mode reaches zero damping at 412 kts.)

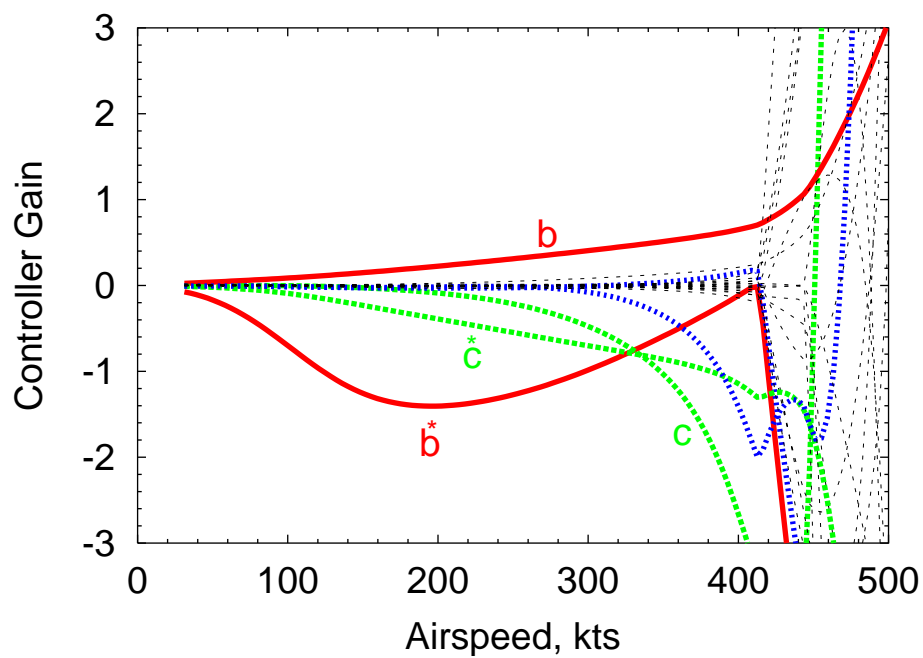


Figure 5.6: Model 222: LQR optimal controller gains

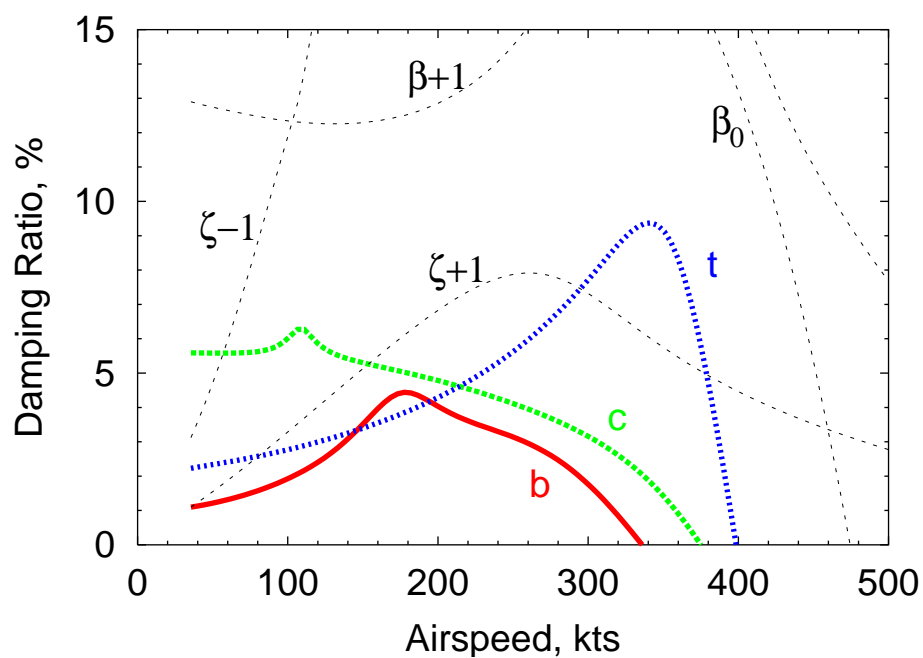


Figure 5.7: XV-15: Modal damping vs. airspeed for uncontrolled system, including unsteady aerodynamic model

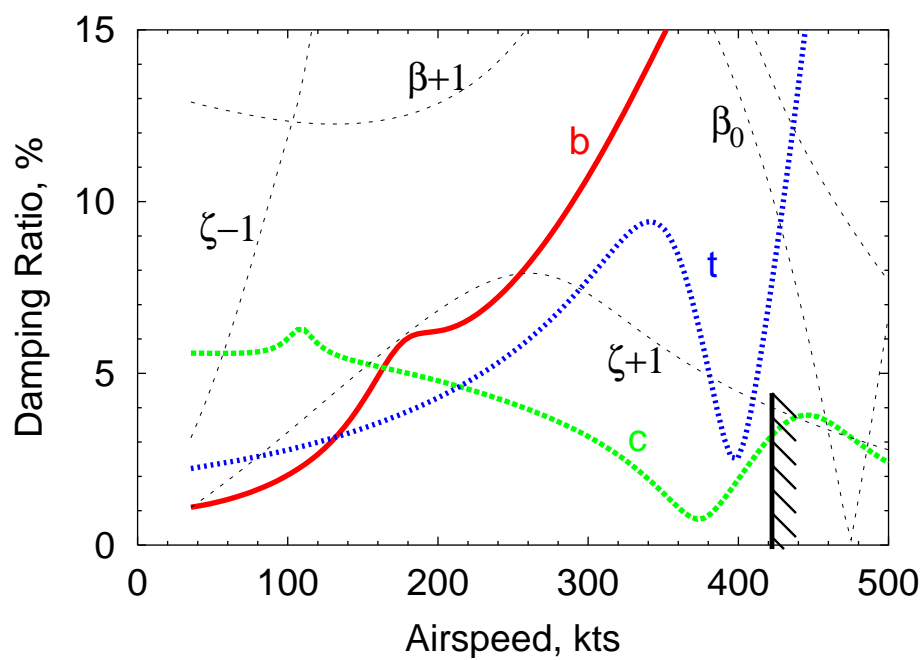


Figure 5.8: XV-15: Modal damping vs. airspeed with optimal wing flaperon control and unsteady aerodynamics (flaperon deflection limit reached at 420 kts).

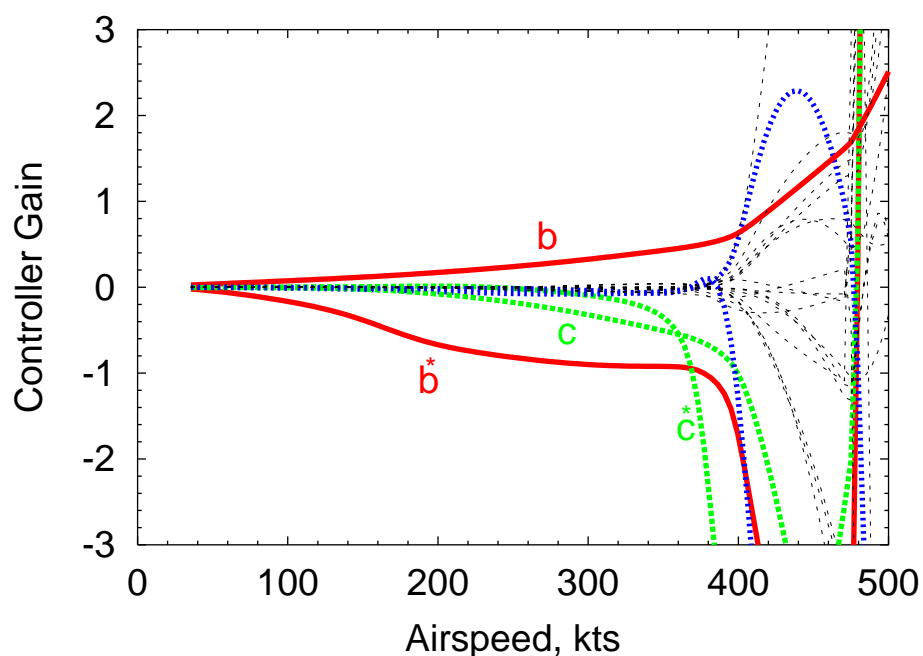


Figure 5.9: XV-15: LQR optimal controller gains when unsteady aerodynamic effects are included

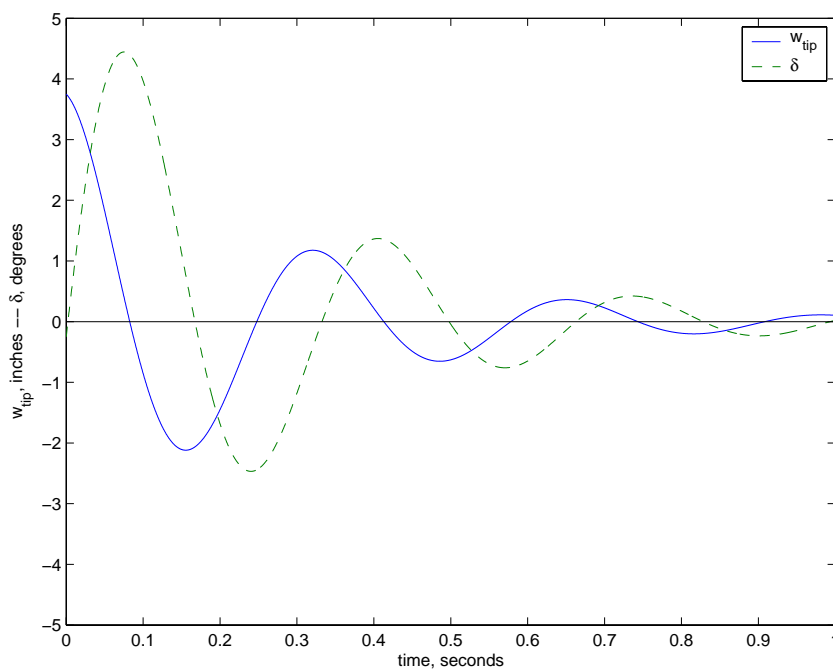


Figure 5.10: XV-15: Time history of wingtip vertical displacement and flaperon deflection, response to initial disturbance of wing vertical bending mode, quasi-steady aerodynamic model, airspeed = 350 knots

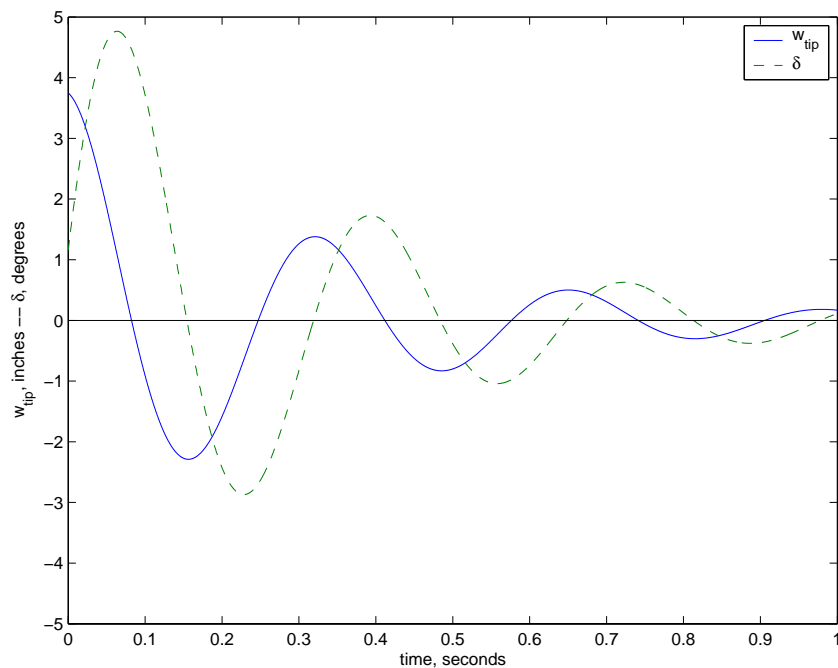


Figure 5.11: XV-15: Time history of wingtip vertical displacement and flaperon deflection, response to initial disturbance of wing vertical bending mode, unsteady aerodynamic effects included, airspeed = 350 knots

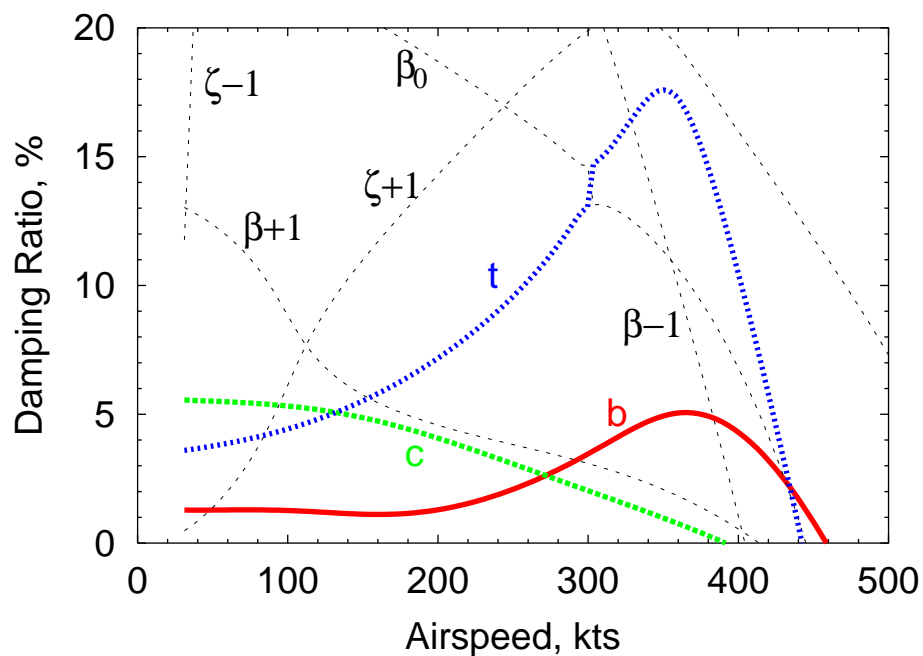


Figure 5.12: Model 222: Modal damping vs. airspeed for uncontrolled system, including unsteady aerodynamic model

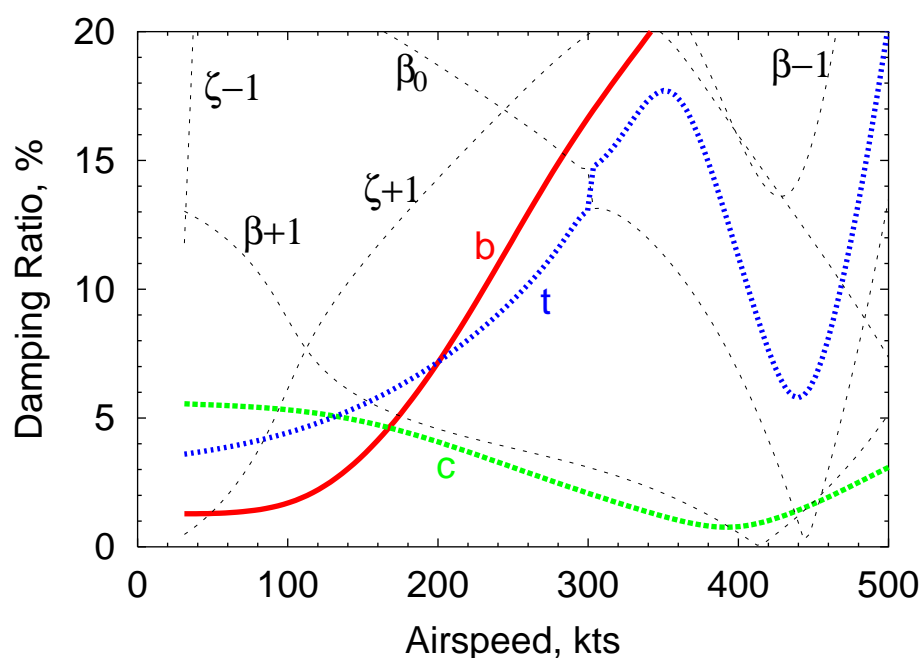


Figure 5.13: Model 222: Modal damping vs. airspeed with optimal wing flaperon control and unsteady aerodynamics ( $\beta + 1$  mode reaches zero damping at 412 kts.)

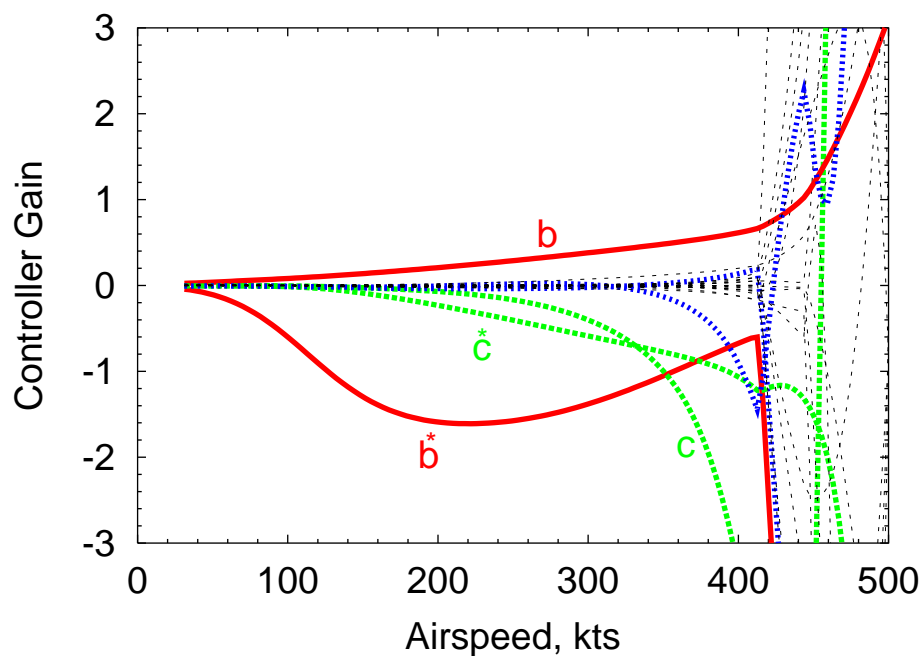


Figure 5.14: Model 222: LQR optimal controller gains when unsteady aerodynamic effects are included

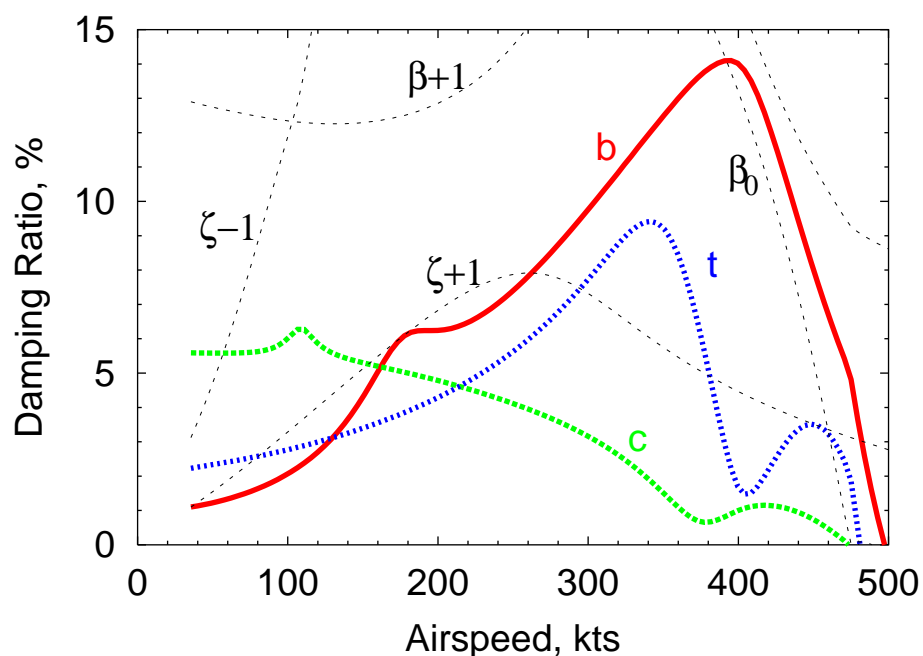


Figure 5.15: XV-15: Modal damping vs. airspeed for wing flaperon control with unsteady aerodynamics, controller gains obtained using quasi-steady aero model

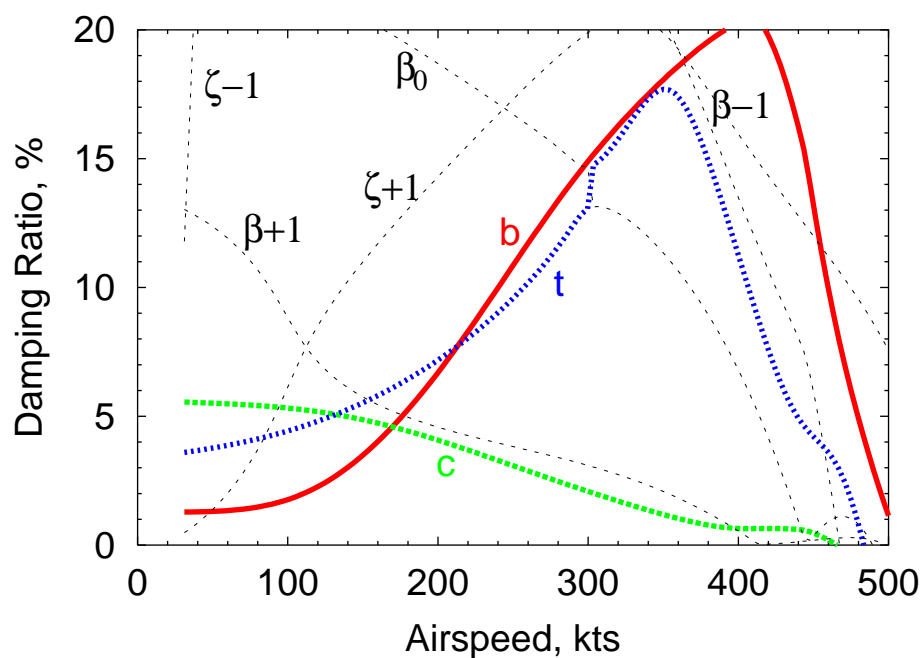


Figure 5.16: Model 222: Modal damping vs. airspeed for wing flaperon control with unsteady aerodynamics, controller gains obtained using quasi-steady aero model



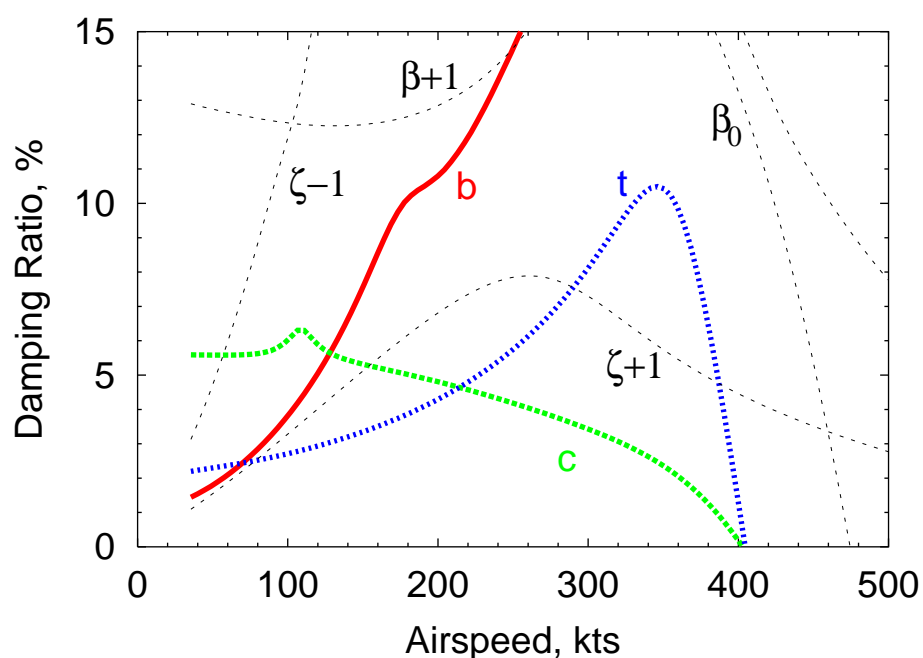


Figure 5.17: XV-15: Modal damping vs. airspeed for wing flaperon actuation with constant gains (optimally determined at 380 kts and 458 RPM) – rotor speed = 458 RPM (cruise)

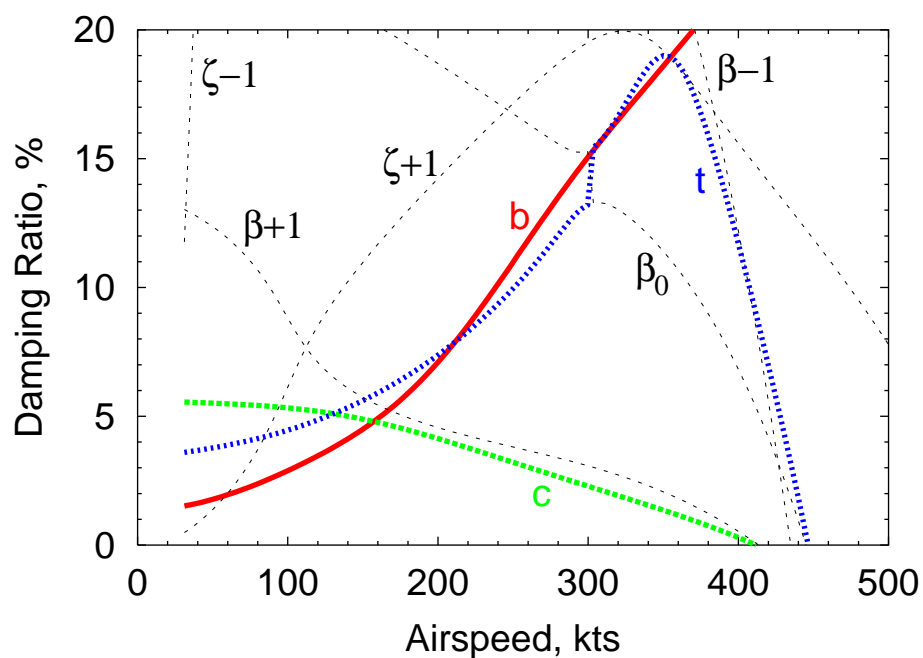


Figure 5.18: Model 222: Modal damping vs. airspeed for wing flaperon actuation with constant gains (optimally determined at 380 kts and 386 RPM) – rotor speed = 386 RPM (cruise)

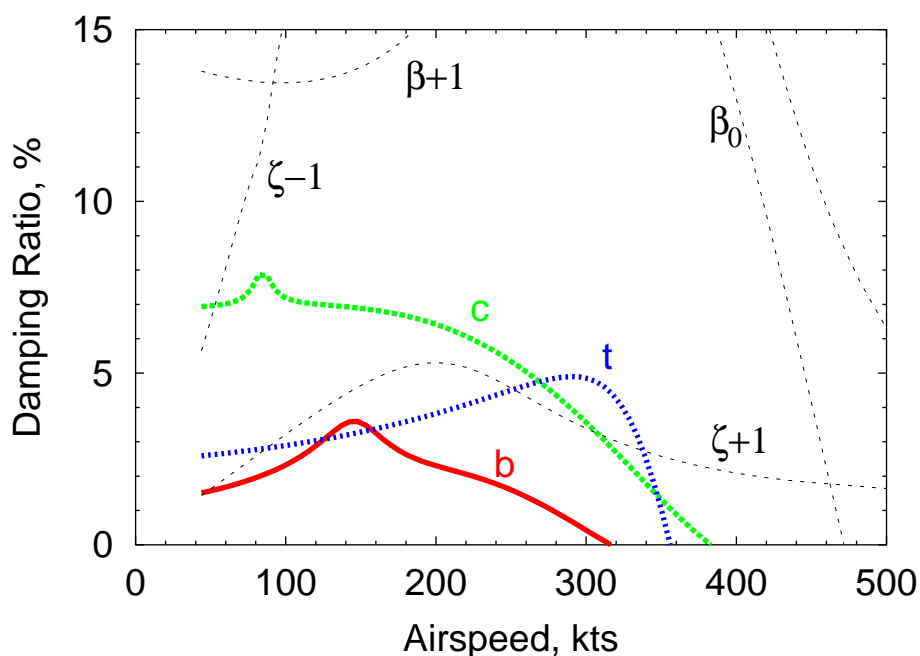


Figure 5.19: XV-15: Modal damping vs. airspeed for uncontrolled system – rotor speed = 565 RPM (hover)

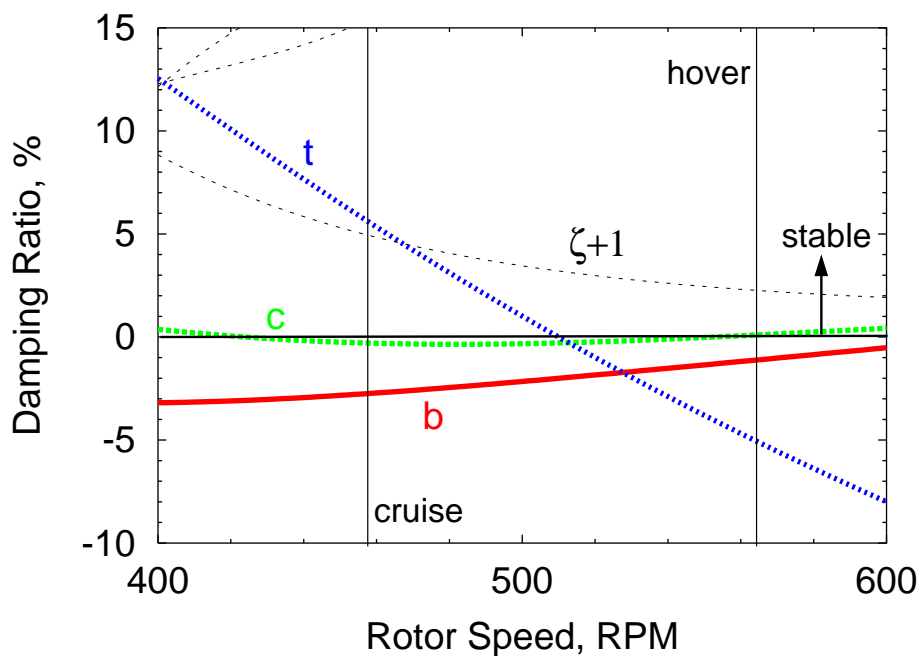


Figure 5.20: XV-15: Modal damping vs. rotor speed for uncontrolled system – airspeed = 380 kts

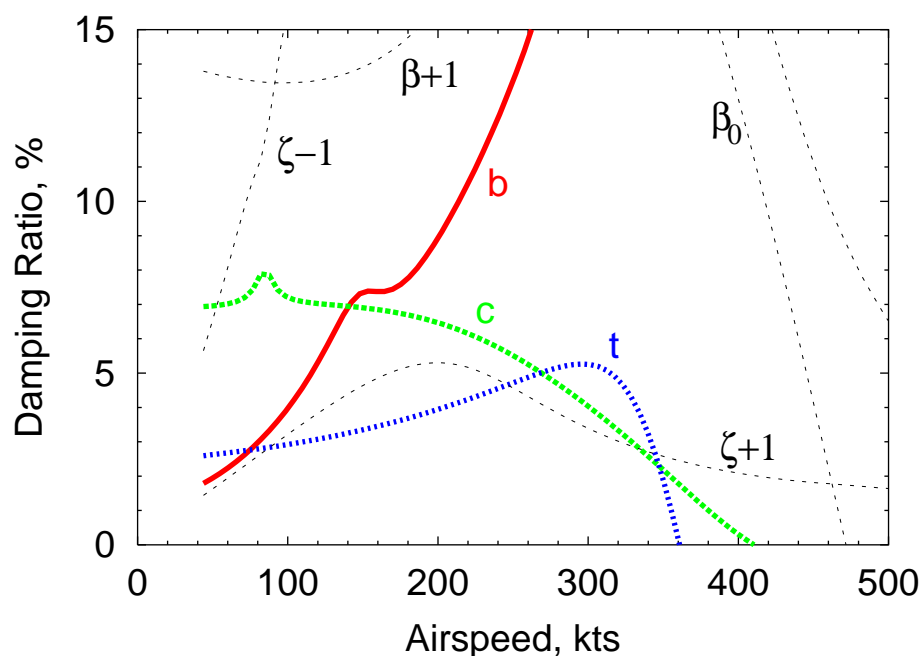


Figure 5.21: XV-15: Modal damping vs. airspeed for wing flaperon actuation with constant gains (optimally determined at 380 kts and 458 RPM) – rotor speed = 565 RPM (hover)

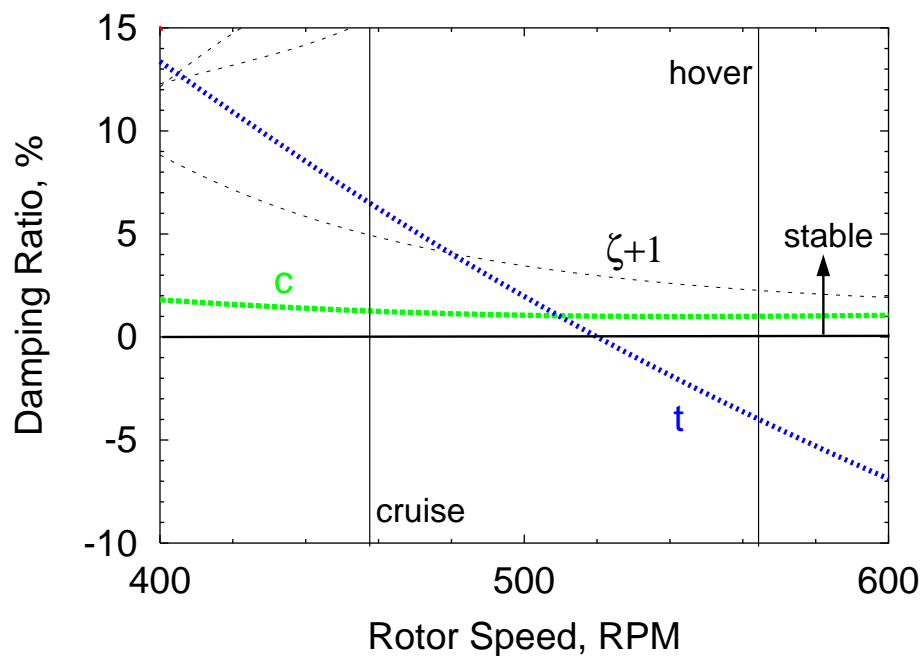


Figure 5.22: XV-15: Modal damping vs. rotor speed for wing flaperon actuation with constant gains (optimally determined at 380 kts and 458 RPM) – airspeed = 380 kts

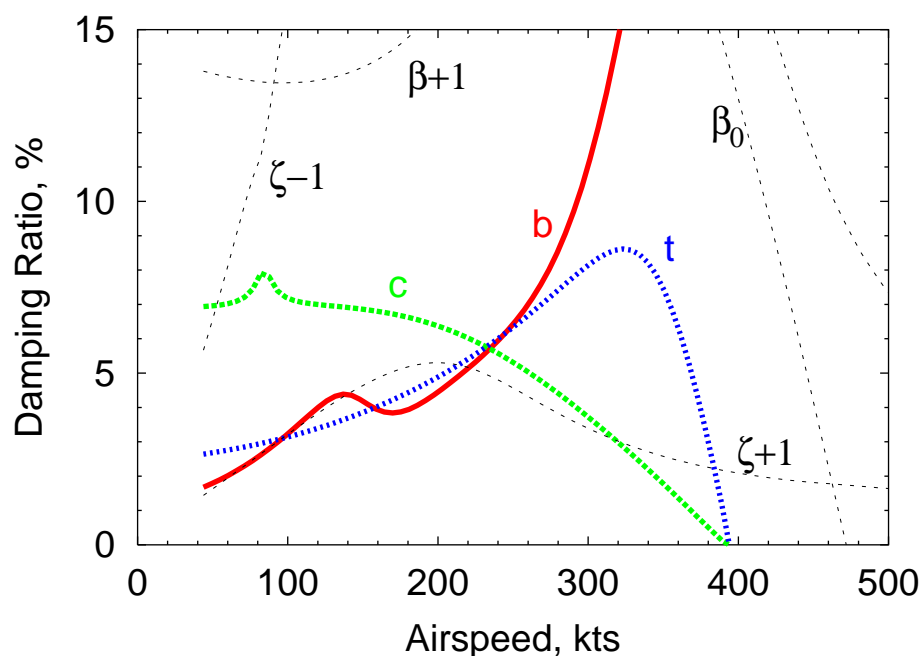


Figure 5.23: XV-15: Modal damping vs. airspeed for wing flaperon actuation with constant gains (optimally determined at 380 kts and 565 RPM) – rotor speed = 565 RPM (hover)

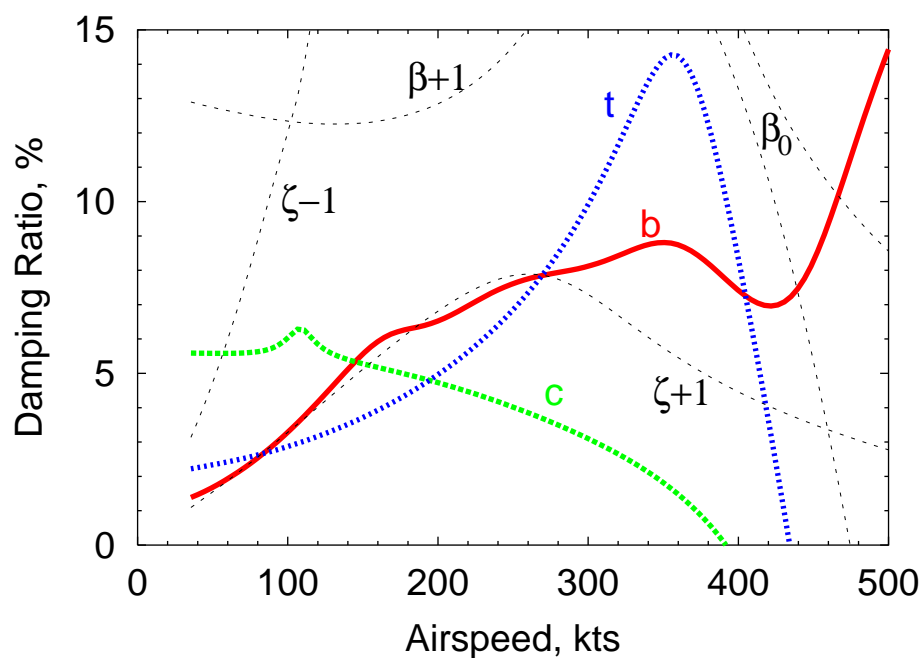


Figure 5.24: XV-15: Modal damping vs. airspeed for wing flaperon actuation with constant gains (optimally determined at 380 kts and 565 RPM) – rotor speed = 458 RPM (cruise)

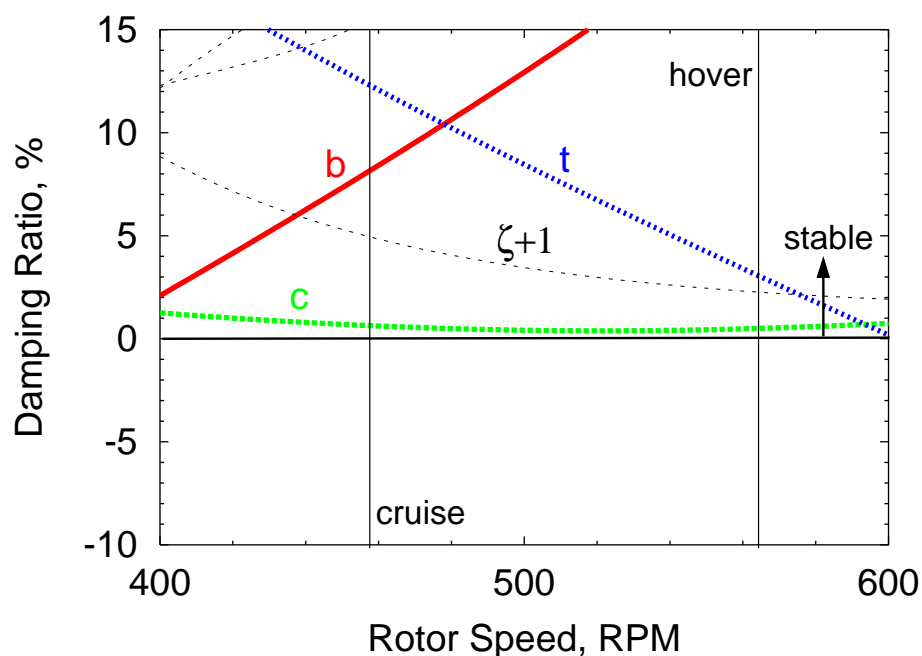


Figure 5.25: XV-15: Modal damping vs. rotor speed for wing flaperon actuation with constant gains (optimally determined at 380 kts and 565 RPM) – airspeed = 380 kts

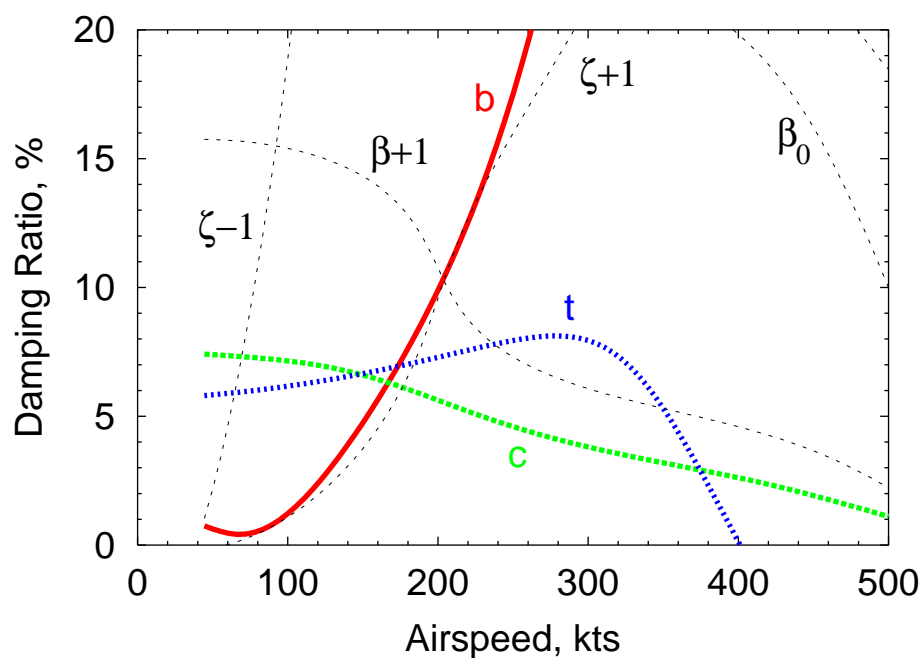


Figure 5.26: Model 222: Modal damping vs. airspeed for wing flaperon actuation with constant gains (optimally determined at 380 kts and 386 RPM) – rotor speed = 551 RPM (hover)

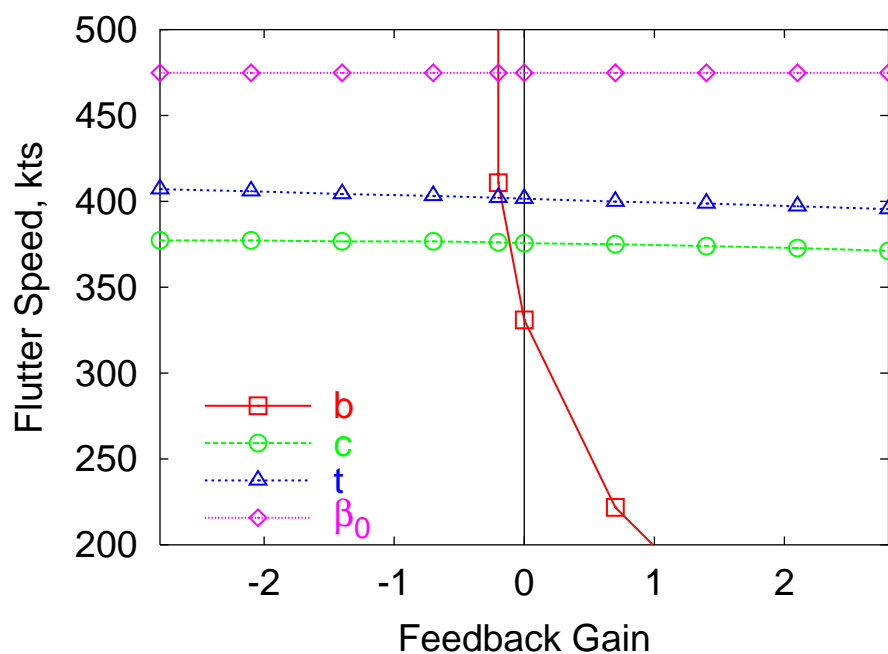


Figure 5.27: XV-15: Influence of rate feedback of wing vertical bending motion on flutter speed

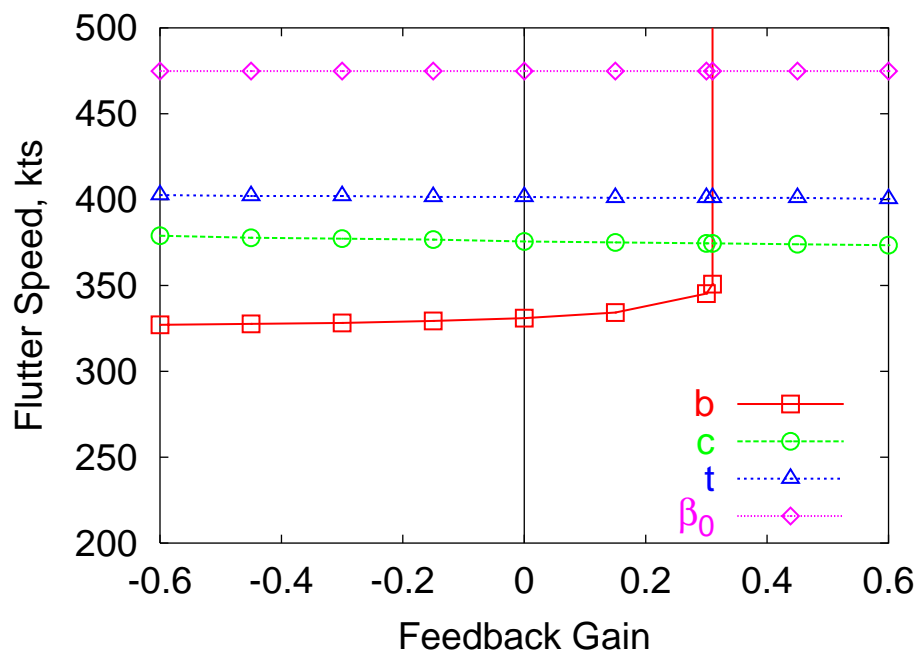


Figure 5.28: XV-15: Influence of position feedback of wing vertical bending motion on flutter speed

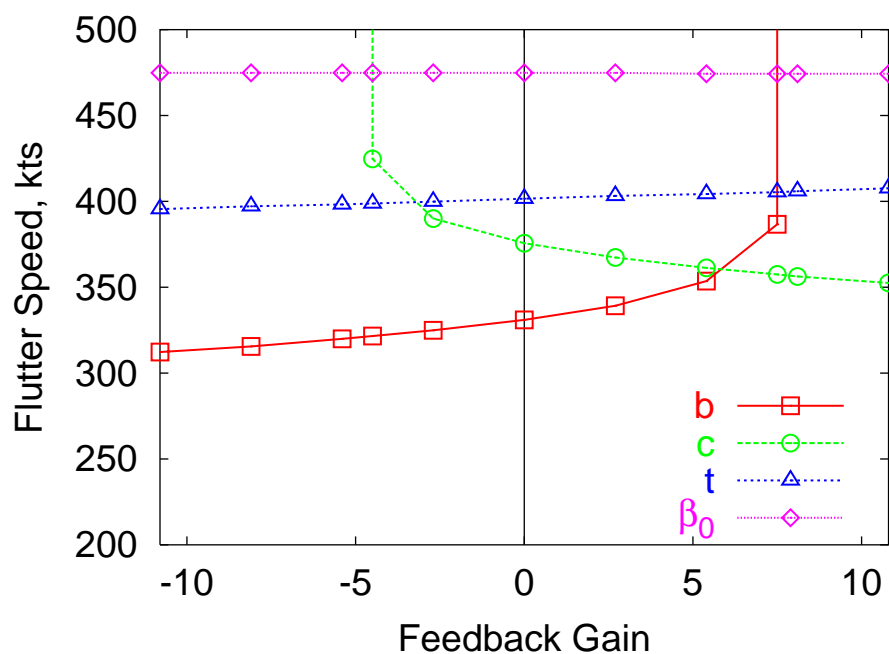


Figure 5.29: XV-15: Influence of rate feedback of wing chordwise bending motion on flutter speed

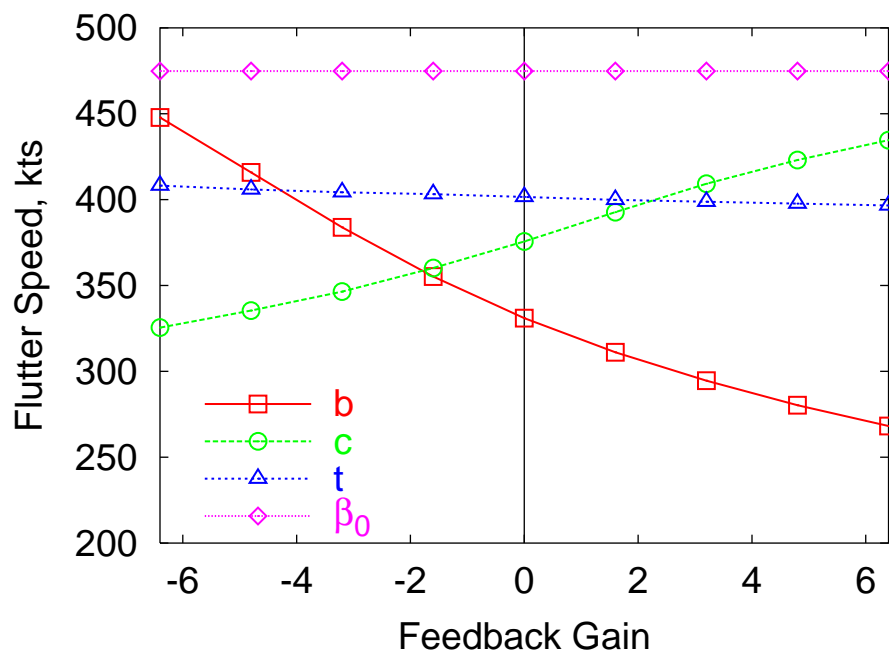


Figure 5.30: XV-15: Influence of position feedback of wing chordwise bending motion on flutter speed

# Chapter 6

## Conclusions

Active and passive techniques for tiltrotor stability augmentation have been explored. To perform these investigations, a whirl flutter stability analysis was developed that retains the simplicity of a rigid blade model, while incorporating sufficient structural detail to correctly model the important rotor characteristics (frequency variation with collective pitch, blade flexibility outboard of the pitch bearing, and the associated pitch-flap and pitch-lag couplings) necessary for accurate whirl flutter stability prediction. While more sophisticated elastic blade and multi-body analyses can provide an even greater level of modeling detail, the present analysis is better suited for use within larger analyses. For instance, the present whirl flutter stability analysis was easily used as a plant model for design of optimal controllers during the wing flaperon active control study. Likewise, the stability analysis was used to evaluate objective functions while performing passive design optimization. The additional computational time required by more complex models make them less attractive for such purposes.

Both passive design optimization and active control of wing flaperons were effective at improving tiltrotor whirl flutter stability. Both approaches should be considered when designing future high-speed tiltrotor aircraft. Findings from the design optimization and active control studies, and recommendations for future research directions, are discussed



below.

## 6.1 Optimization of rotor and wing design parameters

An analytical investigation of the influence of various rotor and wing design parameters on tiltrotor whirl flutter stability was conducted. The parameters were all examined using the same analysis and same baseline tiltrotor configuration, to allow for comparison of the relative effectiveness of each parameter. In addition to investigating the influence of each parameter individually (as in previous studies), numerical optimization techniques were utilized to identify combinations of the design parameters which could significantly improve tiltrotor whirl flutter stability. Relatively tight constraints on the design parameters were applied, in recognition of the fact that considerations other than aeroelastic stability preclude large changes in many of the parameters. Relaxed constraints on the design parameters, on the other hand, were also considered to evaluate the possible improvement in stability if significant changes to the baseline design were permissible, or for new designs being considered.

The findings of this optimization study may be summarized as follows:

1. When only small changes are allowed in rotor design parameters, the parameters which have the greatest influence on flutter speed are the additional pitch-flap and pitch-lag coupling parameters ( $\Delta K_{p\beta}$  and  $\Delta K_{p\zeta}$ ) and the distribution of blade flap flexibility inboard of the pitch bearing ( $R_\beta$ ). These parameters act to increase stability primarily by either offsetting (positive  $\Delta K_{p\beta}$  and  $\Delta K_{p\zeta}$ ) or reducing ( $R_\beta < 1$ ) the magnitude of the destabilizing couplings which arise due to blade flexibility outboard of the pitch bearing ( $\tilde{K}_{p\beta}$  and  $\tilde{K}_{p\zeta}$ ). Stability may be maximized by ensuring that the *total* pitch-flap and pitch-lag couplings are positive.
2. For cases with tight constraints on design parameters, the optimization process produces generally intuitive results. The configurations obtained through formal opti-

mization with tight constraints are consistent with the stability trends identified by individually varying each design parameter.

3. As the bounds on the design parameters are relaxed, additional gains in stability are achieved. The parameters that are most influential under tight constraints continue to follow the parametric study trends, while new trends emerge for other parameters. The optimal combination of design parameters obtained using relaxed constraints may not follow the baseline parametric stability trends, since more relaxed constraints allow the optimized configuration to differ markedly from the baseline.
4. If large enough changes in other design parameters are permitted, the destabilizing trend for large negative  $\delta_3$  angles (where  $\tan \delta_3$  is the pitch-gimbal coupling) may be reversed. For the configuration obtained through optimization of rotor parameters with relaxed constraints, stability of the optimized configuration showed very low sensitivity to changes in  $\delta_3$ . This gives the designer flexibility to select  $\delta_3$  angles that satisfy other design requirements, making the design of advanced rotors with large  $\delta_3$  angles feasible.
5. The wing design parameters which have the greatest influence on flutter speed are the wing vertical bending and torsion stiffness, and vertical bending-torsion coupling. Reduced vertical bending stiffness, increased torsional stiffness, and positive vertical bending-torsion coupling (bend-up, twist nose-down) all act to reduce the amount of nacelle pitching motion present in the wing vertical bending mode, which is the critical mode for the present model.
6. Flutter speed shows a much stronger sensitivity to changes in the rotor parameters than the wing parameters. Optimization of wing parameters using the relaxed set of constraints produces a design that increases flutter speed by about 50 knots, while optimizing the rotor parameters using the tight constraints on the design variable yields a 130 knot increase in flutter speed.

7. Because the ability of the wing design parameters to improve flutter speed is much less than that of the rotor parameters, attempts at concurrent optimization of rotor and wing parameters yield only small improvements in flutter speed compared to optimization using only the rotor variables.
8. The optimization procedures described in this study can successfully identify combinations of design parameters that increase whirl flutter stability. The optimal designs require only modest changes in the key rotor and wing design parameters in order to significantly increase flutter speed. Such changes may be possible while still respecting other design constraints.

## 6.2 Active control of wing flaperons

Active control of a wing flaperon was shown to improve tilt rotor whirl flutter stability margins, and also improve the sub-critical damping of poorly damped wing modes. The influence of unsteady aerodynamic effects on flaperon control performance and design were investigated. Full-state constant gain feedback control systems showed stability augmentation levels similar to the full gain-scheduled optimal controllers, at the expense of higher flaperon deflections at low to moderate speeds. Several candidate feedback parameters for simpler single-state control systems have been identified. The results of this investigation of tiltrotor whirl flutter stability augmentation using wing flaperon actuation may be summarized as follows:

1. Wing flaperon actuation has the potential to significantly increase flutter speed. The ability of the control system to increase flutter speed is ultimately dependent on details of a given aircraft configuration, such as which wing mode is the critical mode, and the stability characteristics of the rotor modes.
2. The full-state feedback optimal controller is effective for increasing stability. Below the stability boundary, the dominant gains in the optimal gain matrices are those

associated with wing vertical bending and chordwise bending feedback, with wing vertical bending rate feedback having the largest gain.

3. In addition to improving whirl flutter stability boundaries for both stiff- and soft-inplane tiltrotor configurations, active control through the wing flaperon significantly increased wing vertical bending mode damping, which is particularly beneficial for soft-inplane configurations, where this mode is typically lightly damped.
4. Including unsteady wing aerodynamic effects was shown to have some influence on predicted damping levels and on optimal controller design, but did not significantly change the results when compared to simpler quasi-steady aerodynamic models.
5. Optimal gains calculated at high speed provide increased damping at low speed as well, making constant-gain simplifications to the optimally-designed controllers possible. The larger flap deflections at low speed associated with the constant gain controller could be alleviated by only activating the stability augmentation at high speeds (above 300 kts, for instance).
6. Increasing rotor speed decreases the stability of the wing beam and torsion modes, while having a slight positive effect on the wing chord mode. The rotor speed at which a controller should be designed to provide stability over a range of rotor speeds depends on the particular vehicle configuration. For the XV-15, where the wing beam mode is the critical flutter mode, a constant gain active controller designed at the helicopter mode rotor speed provided stability regardless of rotor speed. For the Model 222, where the chord mode is critical, a controller designed at the lower airplane mode rotor speed provided adequate stability up to the hover mode rotor speed.
7. Performance of a simple single-state feedback controller is limited since in general the stabilizing influence is restricted to one mode. In some cases, the simple feedback control system is still able to achieve appreciable increases in stability (as much as 50

knots). The large increases in vertical bending mode damping seen in the full-state optimal control results can also be obtained through feedback of vertical bending rate alone. For some tiltrotor configurations, a simple single-state feedback controller may provide adequate performance.

8. For tiltrotor configurations with wing modes that have closely-spaced flutter speeds, a single-state feedback controller will not provide significant increases in aeroelastic stability, since the single-state feedback controller can only improve the stability of one of the two modes. As a result, the critical flutter speed will not change significantly. For such configurations, a multi-state feedback control system is required.

## **6.3 Recommendations for future work**

Continuing research, continuing this investigation of active and passive techniques for improving tiltrotor whirl flutter stability, could be pursued in the following areas:

### **6.3.1 Model Correlation**

The full-scale XV-15 semispan model served as the primary vehicle configuration for both the passive design optimization and active control studies. The XV-15 model was selected for this purpose because of the large amount of available information (model parameters, test data) with which to perform model correlation. Good correlation between the present analysis and test data was achieved for the XV-15 model, giving increased confidence in the results of subsequent analytical investigations. Efforts to achieve similar levels of correlation for the WRATS wind tunnel model, for both the stiff- and soft-inplane rotor configurations, are still underway.

The XV-15 rotor is an old design, and of limited interest to designers of future tiltrotor configurations. Analytical investigations using more recent rotor designs, such as the WRATS rotor models, would be of greater value. Correlation with WRATS wind tunnel

data is still an ongoing process, and should be continued to provide a new standard baseline configuration for future studies, to replace the XV-15 model. Achieving good correlation with the WRATS SASIP rotor in particular would be beneficial for investigations into the aeromechanical stability of soft-inplane tiltrotors.

### **6.3.2 Passive Design Optimization**

The investigation of passive design optimization to improve whirl flutter stability showed that modest changes in several key design parameters can have a significant influence on tiltrotor aeroelastic stability. The results from this investigation could be used to guide more detailed design optimization efforts. For example, the present study showed that for small allowable changes in the baseline configuration, flutter speed was most sensitive to changes in rotor aeroelastic coupling parameters. Based on this result, more detailed design optimization work could be focused on the beneficial tailoring of rotor pitch-flap, pitch-lag, and flap-lag couplings through a variety of techniques (blade geometry, hub/control system kinematics, composite tailoring, CG offsets, sweep, anhedral). The guidance provided by the simple optimization analysis would allow time and effort to be expended in detailed design optimization where it is most likely to have a positive effect on stability. The detailed design effort would require a more sophisticated structural model of the rotor blades and hub than the present analysis provides.

### **6.3.3 Active Control**

The flaperon active control study in this thesis assumed a control system with zero computational delays, and perfect sensors and actuators. Consider the time history data presented in Figs. 5.10 and 5.11. Near the beginning of these runs, the control system is commanding peak flap deflections near 5 degrees, at a frequency of just over 3 Hz. This translates to a flaperon actuation rate of 95 degrees per second. While the bandwidth necessary to meet these control input requirements may be achievable with model-scale actuation

systems, it may prove difficult to achieve with full-scale hydro-mechanical actuators. The effects of actuator dynamics and rate limits on system stability should be considered in future active control investigations. In addition to more representative actuator models, the representation of system disturbances could also be defined. The assumed disturbance amplitudes used in this study are representative of test conditions during wind tunnel whirl flutter stability testing, but are not adequate for design of a flight-worthy control system. Simultaneous excitation of multiple modes has not been considered, for example. Furthermore, more realistic estimates of expected disturbances (from an atmospheric gust model, for example) would also help to identify actuator bandwidth requirements.

Flaperon active control, as considered in this study, could be compared with a swashplate-based actuation approach. The two control strategies could be compared to determine which approach is more effective for increasing flutter speed. Practical considerations, such as differences in power requirements for the two techniques, and ease of integration with the vehicle's flight control system, could also be explored.

Although the present active control study focused on full-state feedback controllers, the results indicated that at least for some tiltrotor configurations, reduced-state feedback systems based on measurements of a few (or one) wing states can improve tiltrotor whirl flutter stability. These results were obtained for a flaperon control system. Similar investigations of reduced-state feedback control could be performed for swashplate-based active control to determine whether simple controllers are possible. To identify the feedback gains for a reduced-state system that provide the greatest increase in stability, formal optimization techniques similar to those used in this study for passive design optimization could be used.

The robustness of each active control system should also be examined. While the present study has indicated that reduced-state feedback control may be adequate to achieve increased stability for some tiltrotor configurations, it is possible that these simple controllers will not retain their effectiveness in the presence of sensor noise (for instance), or when operating at an off-design condition.

### **6.3.4 Active–Passive Hybrid Optimization**

Reference 81 explored the possibility of simultaneous structural optimization and active controller design to reduce vibration for a rotor with trailing edge flaps. This hybrid approach was found to be more effective at reducing vibration than designing an active controller for a fixed structural configuration. A similar technique could be applied to a simultaneous structural design optimization and active controller design to improve tiltrotor whirl flutter stability. It is expected that the hybrid approach would result in reduced control inputs required to achieve a given level of stability, when compared to an active control system designed for a fixed structural design.



# Bibliography

- [1] Nixon, M. W., *Aeroelastic Response and Stability of Tiltrotors with Elastically-Coupled Composite Rotor Blades*, Ph.D. thesis, University of Maryland, 1993.
- [2] Johnson, W., “Dynamics of Tilting Proprotor Aircraft in Cruise Flight,” NASA TN D-7677, May, 1974.
- [3] Gaffey, T. M., Yen, J. G., and Kvaternik, R. G., “Analysis and Model Tests of the Proprotor Dynamics of a Tilt-Proprotor VTOL Aircraft,” Presented at the Air Force V/STOL Technology and Planning Conference, Las Vegas, Nevada, September 23–25, 1969.
- [4] Nixon, M. W., Langston, C. W., Singleton, J. D., Piatak, D. J., Kvaternik, R. G., Corso, L. M., and Brown, R., “Aeroelastic Stability Of A Soft-Inplane Gimballed Tiltrotor Model In Hover,” Proceedings of the 42nd AIAA/ASME/ASCE/AHS/ASC Structures, Structural Dynamics, and Materials Conference, Seattle, Washington, April 16–19, 2001.
- [5] Taylor, E. S. and Browne, K. A., “Vibration Isolation of Aircraft Power Plants,” *Journal of the Aeronautical Sciences*, vol. 6, no. 2, December 1938, pp. 43–49.
- [6] Donham, R. E. and Watts, G. A., “The First Case of Whirl Flutter,” in H. I. Flomenhoft, (ed.) *The Revolution in Structural Dynamics*, chap. 10, Dynaflo Press, Palm Beach Gardens, FL, 1997, pp. 98–109.
- [7] Donham, R. E. and Watts, G. A., “Lessons Learned from Fixed and Rotary Wing Dynamic and Aeroelastic Encounters,” Proceedings of the 41st AIAA/ASME/ASCE/AHS/ASC Structures, Structural Dynamics, and Materials Conference, Atlanta, GA, April 3–6, 2000.
- [8] Houbolt, J. C. and Reed III, W. H., “Propeller-Nacelle Whirl Flutter,” *Journal of the Aerospace Sciences*, vol. 29, no. 3, March 1962, pp. 333–346.
- [9] Reed III, W. H., “Propeller-Rotor Whirl Flutter: A State-Of-The-Art Review,” *Journal of Sound and Vibration*, vol. 4, no. 3, April 1966, pp. 526–544.

- [10] Maisel, M. D., Giulianetti, D. J., and Dugan, D. C., "The History of the XV-15 Tilt Rotor Research Aircraft from Concept to Flight," NASA SP-2000-4517, Monographs in Aerospace History #17, 2000.
- [11] Hall, Jr., W. E., "Prop-Rotor Stability at High Advance Ratios," *Journal of the American Helicopter Society*, vol. 11, no. 2, April 1966, pp. 11–26.
- [12] Young, M. I. and Lytwyn, R. T., "The Influence of Blade Flapping Restraint on the Dynamic Stability of Low Disk Loading Propeller-Rotors," *Journal of the American Helicopter Society*, vol. 12, no. 4, October 1967, pp. 38–54.
- [13] Wernicke, K. G. and Gaffey, T. M., "Review and Discussion of 'The Influence of Blade Flapping Restraint on the Dynamic Stability of Low Disk Loading Propeller-Rotors'," *Journal of the American Helicopter Society*, vol. 12, no. 4, October 1967, pp. 55–60.
- [14] Edenborough, H. K., "Investigation of Tilt-Rotor VTOL Aircraft Rotor-Pylon Stability," *Journal of Aircraft*, vol. 5, no. 6, March-April 1968, pp. 97–105.
- [15] Delarm, D. L. N., "Whirl Flutter and Divergence Aspects of Tilt-Wing and Tilt-Rotor Aircraft," Presented at the Air Force V/STOL Technology and Planning Conference, Las Vegas, Nevada, September 23–25, 1969.
- [16] Gaffey, T. M., "The Effect of Positive Pitch-flap Coupling (Negative  $\delta_3$ ) on Rotor Blade Motion Stability and Flapping," *Journal of the American Helicopter Society*, vol. 14, no. 2, April 1969, pp. 49–67.
- [17] Kaza, K. R. V., "Effect of Steady State Coning Angle and Damping on Whirl Flutter Stability," *Journal of Aircraft*, vol. 10, no. 11, November 1973, pp. 664–669.
- [18] Wernicke, K. G., "Tilt Proprotor Composite Aircraft, Design State of the Art," *Journal of the American Helicopter Society*, vol. 14, no. 2, April 1969, pp. 10–25.
- [19] Kvaternik, R. G., *Studies in Tilt-Rotor VTOL Aircraft Aeroelasticity*, Ph.D. thesis, Case Western Reserve University, 1973.
- [20] Kvaternik, R. G., "Experimental and Analytical Studies in Tilt-Rotor Aeroelasticity," Presented at the AHS/NASA Ames Specialists' Meeting on Rotorcraft Dynamics, February 13-15, 1974.
- [21] Kvaternik, R. G., "A Review of Some Tilt-Rotor Aeroelastic Research at NASA-Langley," *Journal of Aircraft*, vol. 13, no. 5, May 1976, pp. 357–363.
- [22] Yeager, Jr., W. T. and Kvaternik, R. G., "Contributions of the Langley Transonic Dynamics Tunnel to Rotorcraft Technology and Development," AIAA Dynamics Specialists Conference, Atlanta, GA, April 5–6, 2000.

- [23] Anon., "Advancement of Proprotor Technology Task II – Wind-Tunnel Test Results," NASA CR 114363, Bell Helicopter Co., Sept. 1971.
- [24] Magee, J. P. and Alexander, H. R., "Wind Tunnel Tests of a Full Scale Hingeless Prop/Rotor Designed for the Boeing Model 222 Tilt Rotor Aircraft," NASA CR 114664, Boeing Vertol Co., Oct. 1973.
- [25] Wernicke, K. G. and Edenborough, H. K., "Full-Scale Proprotor Development," *Journal of the American Helicopter Society*, vol. 17, no. 1, January 1972, pp. 31–40.
- [26] Alexander, H. R., Hengen, L. M., and Weiberg, J. A., "Aeroelastic-Stability Characteristics of a V/STOL Tilt-Rotor Aircraft with Hingeless Blades: Correlation of Analysis and Test," *Journal of the American Helicopter Society*, vol. 20, no. 2, April 1975, pp. 12–22.
- [27] Maisel, M., "Tilt Rotor Research Aircraft Familiarization Document," NASA TM X-62,407, January, 1975.
- [28] Johnson, W., "Analytical Model for Tilting Proprotor Aircraft Dynamics, Including Blade Torsion and Coupled Bending Modes, and Conversion Mode Operation," NASA TM X-62,369, May, 1974.
- [29] Johnson, W., "Analytical Modeling Requirements for Tilting Proprotor Aircraft Dynamics," NASA TN D-8013, July, 1975.
- [30] Johnson, W., "The Influence of Engine/Transmission/Governor on Tilting Proprotor Aircraft Dynamics," NASA TM X-62,455, June, 1975.
- [31] Johnson, W., *A Comprehensive Analytical Model of Rotorcraft Aerodynamics and Dynamics*, Johnson Aeronautics, Palo Alto, CA, 1988.
- [32] Bilger, J. M., Marr, R. L., and Zahedi, A., "Results of Structural Dynamic Testing of the XV-15 Tilt Rotor Research Aircraft," *Journal of the American Helicopter Society*, vol. 27, no. 2, April 1982, pp. 58–65.
- [33] Johnson, W., "An Assessment of the Capability To Calculate Tilting Prop-Rotor Aircraft Performance, Loads, and Stability," NASA TP 2291, March, 1984.
- [34] Johnson, W., "Recent Developments in the Dynamics of Advanced Rotor Systems," NASA TM 86669, March, 1985.
- [35] Settle, T. B. and Kidd, D. L., "Evolution and Test History of the V-22 0.2-Scale Aeroelastic Model," Presented at the American Helicopter Society National Specialists' Meeting on Rotorcraft Dynamics, Arlington, Texas, November 1989.

- [36] Popelka, D., Sheffler, M., and Bilger, J., “Correlation of Stability Test Results and Analysis for the 1/5-Scale V-22 Aeroelastic Model,” .
- [37] Anon., “University of Maryland Advanced Rotor Code (UMARC) Theory Manual,” Center for Rotorcraft Education and Research, University of Maryland, College Park, MD, July 1994.
- [38] Srinivas, V. and Chopra, I., “Validation of a Comprehensive Aeroelastic Analysis for Tiltrotor Aircraft,” *Journal of the American Helicopter Society*, vol. 43, no. 4, October 1998, pp. 333–341.
- [39] Piatak, D. J., Kvaternik, R. G., Nixon, M. W., Langston, C. W., Singleton, J. D., Bennett, R. L., and Brown, R. K., “A Parametric Investigation of Whirl-Flutter Stability on the WRATS Tiltrotor Model,” *Journal of the American Helicopter Society*, vol. 47, no. 2, April 2002, pp. 134–144.
- [40] Ghiringhelli, G. L., Masarati, P., Mantegazza, P., and Nixon, M. W., “Multi-Body Analysis of a Tiltrotor Configuration,” Presented at the 7th Conference on Nonlinear Vibration, Stability, and Dynamics of Structures, Virginia Polytechnic Institute and State University, Blacksburg, VA, July 26–30, 1998.
- [41] Ghiringhelli, G. L., Masarati, P., Mantegazza, P., and Nixon, M. W., “Multi-Body Analysis of the 1/5 Scale Wind Tunnel Model of the V-22 Tiltrotor,” Proceedings of the 55th Annual AHS Forum, Montreal, Canada, May 25–27, 1999.
- [42] Nixon, M. W., Langston, C. W., Singleton, J. D., Piatak, D. J., Kvaternik, R. G., Corso, L. M., and Brown, R. K., “Technical Note: Hover Test of a Soft-Inplane Gimballled Tiltrotor Model,” *Journal of the American Helicopter Society*, vol. 48, no. 1, January 2003, pp. 63–66.
- [43] Nixon, M. W., Langston, C. W., Singleton, J. D., Piatak, D. J., Kvaternik, R. G., Corso, L. M., and Brown, R. K., “Aeroelastic Stability of a Four-Bladed Semi-Articulated Soft-Inplane Tiltrotor Model,” Proceedings of the 59th Annual AHS Forum, Phoenix, Arizona, May 6–8, 2003.
- [44] Nixon, M. W., “Parametric Studies for Tiltrotor Aeroelastic Stability in High-Speed Flight,” *Journal of the American Helicopter Society*, vol. 38, no. 4, October 1993, pp. 71–79.
- [45] Popelka, D. A., Lindsay, D., Parham, Jr., T., Berry, V., and Baker, D. J., “Results of an Aeroelastic Tailoring Study for a Composite Tiltrotor Wing,” *Journal of the American Helicopter Society*, vol. 42, no. 2, April 1997, pp. 126–136.

- [46] Corso, L. M., Popelka, D. A., and Nixon, M. W., "Design, Analysis, and Test of a Composite Tailored Tiltrotor Wing," *Journal of the American Helicopter Society*, vol. 45, no. 3, July 2000.
- [47] Howard, A. K. T., *The Aeromechanical Stability of Soft-Inplane Tiltrotors*, Ph.D. thesis, The Pennsylvania State University, 2001.
- [48] Nixon, M. W., Piatak, D. J., Corso, L. M., and Popelka, D. A., "Aeroelastic Tailoring for Stability Augmentation and Performance Enhancement of Tiltrotor Aircraft," Proceedings of the 55th Annual AHS Forum, Montreal, Canada, May 25–27, 1999.
- [49] Barkai, S. M. and Rand, O., "The Influence of Composite Induced Couplings on Tiltrotor Whirl Flutter Stability," *Journal of the American Helicopter Society*, vol. 43, no. 2, April 1998, pp. 133–145.
- [50] Moore, M. J., Yablonski, M. J., Mathew, B., and Liu, J., "High Speed Tiltrotors: Dynamics Methodology," Proceedings of the 49th Annual AHS Forum, St. Louis, MO, May 19–21, 1993.
- [51] Srinivas, V., Chopra, I., and Nixon, M., "Aeroelastic Analysis of Advanced Geometry Tiltrotor Aircraft," *Journal of the American Helicopter Society*, vol. 43, no. 3, July 1998, pp. 212–221.
- [52] Acree, Jr., C. W., Peyran, R. J., and Johnson, W., "Rotor Design for Whirl Flutter: An Examination of Options for Improving Tiltrotor Aeroelastic Stability Margins," Proceedings of the 55th Annual AHS Forum, Montreal, Canada, May 25–27, 1999.
- [53] Acree, Jr., C. W., Peyran, R. J., and Johnson, W., "Improving Tiltrotor Whirl-Mode Stability with Rotor Design Variables," Proceedings of the 26th European Rotorcraft Forum, The Hague, The Netherlands, September 2000.
- [54] Acree, Jr., C. W., "Effects of Rotor Design Variations on Tiltrotor Whirl-Mode Stability," Tiltrotor/Runway Independent Aircraft Specialists' Meeting of the American Helicopter Society, Arlington, TX, March 20–21, 2001.
- [55] Acree, Jr., C. W., "Rotor Design Options for Improving V-22 Whirl-Mode Stability," Proceedings of the 58th Annual AHS Forum, Montreal, Canada, June 11–13, 2002.
- [56] Johnson, W., "Optimal Control Alleviation of Tilting Proprotor Gust Response," *Journal of Aircraft*, vol. 14, no. 3, March 1977, pp. 301–308.
- [57] Miller, D. G. and Ham, N. D., "Active Control of Tilt-Rotor Blade In-Plane Loads During Manuevers," Proceedings of the Fourteenth European Rotorcraft Forum, Milan, Italy, September 1988.

- [58] Settle, T. B. and Nixon, M. W., "MAVSS Control of an Active Flaperon for Tiltrotor Vibration Reduction," Proceedings of the 53rd Annual AHS Forum, Virginia Beach, Virginia, April 29 – May 1, 1997.
- [59] Nixon, M. W., Kvaternik, R. G., and Settle, T. B., "Tiltrotor Vibration Reduction Through Higher Harmonic Control," Proceedings of the 53rd Annual AHS Forum, Virginia Beach, Virginia, April 29 – May 1, 1997.
- [60] Nasu, K.-i., "Tilt-Rotor Flutter Control in Cruise Flight," NASA TM 88315, December, 1986.
- [61] van Aken, J. M., "Alleviation of Whirl-Flutter on Tilt-Rotor Aircraft Using Active Controls," Proceedings of the 47th Annual AHS Forum, Phoenix, AZ, May 6–8, 1991.
- [62] van Aken, J. M., "Alleviation of Whirl-Flutter on a Joined-Wing Tilt-Rotor Aircraft Configuration Using Active Controls," Presented at the International Specialists' Meeting on Rotorcraft Basic Research of the American Helicopter Society, Atlanta, Georgia, March 25–27, 1991.
- [63] Vorwald, J. G. and Chopra, I., "Stabilizing Pylon Whirl Flutter on a Tilt-Rotor Aircraft," Proceedings of the 32nd AIAA/ASME/ASCE/AHS/ASC Structures, Structural Dynamics, and Materials Conference, Baltimore, MD, April 8–10, 1991.
- [64] Kvaternik, R. G., "Exploratory Studies in Generalized Predictive Control for Active Aeroelastic Control of Tiltrotor Aircraft," NASA TM-2000-210552.
- [65] Kvaternik, R. G., Piatak, D. J., Nixon, M. W., Langston, C. W., Singleton, J. D., Bennett, R. L., and Brown, R. K., "An Experimental Evaluation of Generalized Predictive Control for Tiltrotor Aeroelastic Stability Augmentation in Airplane Mode of Flight," Proceedings of the 57th Annual AHS Forum, Washington, DC, May 9–11, 2001.
- [66] Ghiringhelli, G. L., Masarati, P., Mantegazza, P., and Nixon, M. W., "Multi-Body Analysis of an Active Control for a Tiltrotor," Presented at the CEAS/AIAA/ICASE/NASA LaRC International Forum on Aeroelasticity and Structural Dynamics, Williamsburg, VA, June 22–25, 1999.
- [67] Popelka, D., Sheffler, M., and Bilger, J., "Correlation of Test and Analysis for the 1/5-Scale V-22 Aeroelastic Model," *Journal of the American Helicopter Society*, vol. 32, no. 2, April 1987, pp. 21–33.
- [68] Parham, Jr., T. C., Chao, D., and Zwillenberg, P., "Tiltrotor Aeroservoelastic Design Methodology at BHTI," Proceedings of the 45th Annual AHS Forum, Boston, MA, May 22–24, 1989.

- [69] Hathaway, E. and Gandhi, F., “Concurrently Optimized Aeroelastic Couplings and Rotor Stiffness for Alleviation of Helicopter Aeromechanical Instability,” *Journal of Aircraft*, vol. 38, no. 1, January–February 2001, pp. 69–80.
- [70] Settle, T. B. and Kidd, D. L., “Evolution and Test History of the V-22 0.2-Scale Aeroelastic Model,” *Journal of the American Helicopter Society*, vol. 37, no. 1, January 1992, pp. 31–45.
- [71] Masarati, P., Quaranta, Piatak, D. J., Quaranta, G., and Singleton, J. D., “Further Results of Soft-Inplane Tiltrotor Aeromechanics Investigation Using Two Multibody Analyses,” Proceedings of the 60th Annual AHS Forum, Baltimore, Maryland, June 8–10, 2004.
- [72] Shen, J., Singleton, J. D., Piatak, D. J., and Bauchau, O. A., “Multibody Dynamics Simulation and Experimental Investigation of a Model-Scale Tiltrotor,” Proceedings of the 61st Annual AHS Forum, Grapevine, Texas, June 1–3, 2005.
- [73] Ormiston, R. A. and Hodges, D. H., “Linear Flap-Lag Dynamics of Hingeless Helicopter Rotor Blades in Hover,” *Journal of the American Helicopter Society*, vol. 17, no. 2, April 1972, pp. 2–14.
- [74] Gandhi, F. and Hathaway, E., “Optimized Aeroelastic Couplings for Alleviation of Helicopter Ground Resonance,” *Journal of Aircraft*, vol. 35, no. 4, July–August 1998, pp. 582–590.
- [75] Johnson, W., *Helicopter Theory*, Dover Publications, Inc., New York, 1994, pp. 408–411.
- [76] Piatak, D. J., Kvaternik, R. G., Nixon, M. W., Langston, C. W., Singleton, J. D., Bennett, R. L., and Brown, R. K., “A Wind-Tunnel Parametric Investigation of Tiltrotor Whirl-Flutter Stability Boundaries,” Proceedings of the 57th Annual AHS Forum, Washington, DC, May 9–11, 2001.
- [77] Wang, J. M., Jones, C. T., and Nixon, M. W., “A Variable Diameter Short Haul Civil Tiltrotor,” Proceedings of the 55th Annual AHS Forum, Montreal, Canada, May 25–27, 1999.
- [78] Theodorsen, T., “General Theory of Aerodynamic Instability and the Mechanism of Flutter,” NACA Report No. 496, 1935.
- [79] Myrtle, T. F., *Development of an Improved Aeroelastic Model for the Investigation of Vibration Reduction in Helicopter Rotors Using Trailing Edge Flaps*, Ph.D. thesis, University of California, Los Angeles, 1998.

- [80] Stettner, M., Schrage, D. P., and Peters, D. A., "Application of a State-Space Wake Model to Tiltrotor Wing Unsteady Aerodynamics," Presented at the American Helicopter Society Aeromechanics Specialists Conference, San Francisco, CA, January 19–21, 1994.
- [81] Zhang, J., *Active-Passive Hybrid Optimization of Rotor Blades with Trailing Edge Flaps*, Ph.D. thesis, The Pennsylvania State University, 2001.



# Appendix A

## Analytical Model

### A.1 Degrees of Freedom

The analytical model described below represents a proprotor with three or more blades, mounted on a semi-span, cantilevered wing structure. The point of attachment between the rotor hub and the wing/pylon system can undergo three displacements  $(x, y, z)$  and three rotations  $(\alpha_x, \alpha_y, \alpha_z)$ , as shown in Fig. 3.1. The mass, damping, and stiffness properties associated with these degrees of freedom are derived from the wing/pylon structure. The rotor hub may be gimbaled, allowing cyclic flapping motion at the blade root ( $\beta_G$ ). In the fixed frame, this gimbal degree of freedom allows for longitudinal ( $\beta_{Gc}$ ) and lateral ( $\beta_{Gs}$ ) tilting of the rotor disk. Thus the rotating-frame gimbal flapping for the  $m^{\text{th}}$  blade is related to the fixed-frame gimbal degrees of freedom by

$$\beta_G^{(m)} = \beta_{Gc} \cos \psi_m + \beta_{Gs} \sin \psi_m \quad (\text{A.1})$$

The blade is attached to the hub with some precone angle,  $\beta_p$ . Perturbation of rotor azimuthal position in the rotating frame ( $\psi_s$ ) is included, allowing a windmilling rotor condition to be modeled. Note that although a perturbation in azimuthal position is used in the formulation, only velocity and acceleration terms in  $\psi_s$  appear in the final equations.

Thus the true degree of freedom is  $\psi_s$ , a rotor speed perturbation. A spring-restrained offset flapping hinge represents the flap flexibility of the blade ( $\beta$ ), as well as the flexibility due to a coning hinge (if present). Blade in-plane flexibility ( $\zeta$ ) is accommodated by a spring-restrained offset lagging hinge. Figures 3.2 and 3.3 illustrate the blade out-of-plane and in-plane degrees of freedom. The model used to represent blade flap and lag flexibility, its distribution with respect to the pitch bearing, and its implications on system behavior, was discussed in detail in Chapter 3. Blade rigid pitch motion as a result of control system flexibility ( $\phi$ ) is modeled by perturbations in blade pitch about an offset pitch bearing. The importance of accurately capturing the effects of blade pitching motion for accurate whirl flutter stability prediction was also discussed in Chapter 3

## A.2 Acceleration of a Point on the Blade

With the degree-of-freedom definitions given above, the position of a point on the rotor blade, located a distance  $r$  from the center of rotation, may be expressed in the rotating frame (the “ $b$ ” coordinate system, defined by the unit vectors  $(\hat{i}, \hat{j}, \hat{k})$  as shown in Figs. 3.2 and 3.3), with respect to the hub attachment point (the position of which in turn is defined in the non-rotating “ $h$ ” coordinate system defined by the unit vectors  $(\hat{I}, \hat{J}, \hat{K})$  shown in Fig. 3.1). Thus,

$$\underline{r}_{b/h} = [(r - e)\zeta - r\psi_s]\hat{i} + r\hat{j} + [(r - e)\beta + r(\beta_G + \beta_P)]\hat{k} \quad (\text{A.2})$$

The angular velocity of the rotating frame with respect to the hub attachment point is

$$\underline{\omega}_{b/h} = \Omega\hat{k} \quad (\text{A.3})$$

Taking successive time derivatives of the position vector gives the velocity and acceleration of a point on the blade, with respect to the hub attachment point:

$$\underline{v}_{b/h} = \left[ (r-e)\dot{\zeta} - r\dot{\psi}_s - \Omega r \right] \hat{i} + \left[ \Omega(r-e)\zeta - \Omega r\psi_s \right] \hat{j} + \left[ (r-e)\dot{\beta} + r\dot{\beta}_G \right] \hat{k} \quad (\text{A.4})$$

$$\begin{aligned} \underline{a}_{b/h} = & \left[ (r-e) \left( \ddot{\zeta} - \Omega^2 \zeta \right) - r \left( \ddot{\psi}_s - \Omega^2 \psi_s \right) + 2\Omega(r-e)(\beta_P + \bar{\beta}_0)\dot{\beta} \right] \hat{i} \quad (\text{A.5}) \\ & + \left[ 2\Omega(r-e)\dot{\zeta} - 2\Omega r\dot{\psi}_s - \Omega^2 r \right] \hat{j} + \left[ (r-e)\ddot{\beta} + r\ddot{\beta}_G \right] \hat{k} \end{aligned}$$

In Eq. (A.5), the term  $\bar{\beta}_0$  represents the trim blade coning deflection from the undeformed state. The total coning angle is then  $(\beta_P + \bar{\beta}_0)$ .

Equation (A.5) gives the acceleration of the blade with respect to the hub attachment point. To calculate the inertial forces and moments acting on the blade, the acceleration with respect to an inertial reference frame is required. The acceleration, angular velocity, and angular acceleration of the hub attachment point is given in the fixed frame  $(\hat{I}, \hat{J}, \hat{K})$  as

$$\underline{a}_h = \ddot{x}\hat{I} + \ddot{y}\hat{J} + \ddot{z}\hat{K} \quad (\text{A.6})$$

$$\underline{\omega}_h = \dot{\alpha}_x\hat{I} + \dot{\alpha}_y\hat{J} + \dot{\alpha}_z\hat{K} \quad (\text{A.7})$$

$$\underline{\alpha}_h = \ddot{\alpha}_x\hat{I} + \ddot{\alpha}_y\hat{J} + \ddot{\alpha}_z\hat{K} \quad (\text{A.8})$$

In the rotating frame, these hub motions become

$$\underline{a}_h = (\ddot{x} \sin \psi_m - \ddot{y} \cos \psi_m) \hat{i} + (\ddot{x} \cos \psi_m + \ddot{y} \sin \psi_m) \hat{j} + \ddot{z} \hat{k} \quad (\text{A.9})$$

$$\underline{\omega}_h = (\dot{\alpha}_x \sin \psi_m - \dot{\alpha}_y \cos \psi_m) \hat{i} + (\dot{\alpha}_x \cos \psi_m + \dot{\alpha}_y \sin \psi_m) \hat{j} + \dot{\alpha}_z \hat{k} \quad (\text{A.10})$$

$$\underline{\alpha}_h = (\ddot{\alpha}_x \sin \psi_m - \ddot{\alpha}_y \cos \psi_m) \hat{i} + (\ddot{\alpha}_x \cos \psi_m + \ddot{\alpha}_y \sin \psi_m) \hat{j} + \ddot{\alpha}_z \hat{k} \quad (\text{A.11})$$

The total acceleration of a point on the blade with respect to the inertial frame can now be calculated, using the following formula:

$$\underline{a} = \underline{a}_h + \underline{a}_{b/h} + 2\underline{\omega}_h \times \underline{v}_{b/h} + \underline{\omega}_h \times \left( \underline{\omega}_h \times \underline{r}_{b/h} \right) + \underline{\alpha}_h \times \underline{r}_{b/h} \quad (\text{A.12})$$

Evaluating Eq. (A.12), and eliminating certain higher-order terms yields

$$\begin{aligned}
\underline{a} = & \left[ \begin{array}{l} \ddot{x} \sin \psi_m - \ddot{y} \cos \psi_m - r \ddot{\alpha}_z - r (\ddot{\psi}_s - \Omega^2 \psi_s) + (r-e) (\ddot{\zeta} - \Omega^2 \zeta) \\ + 2\Omega(r-e)(\beta_P + \bar{\beta}_0) \dot{\beta} \end{array} \right] \hat{i} \\
& + \left[ \ddot{x} \cos \psi_m + \ddot{y} \sin \psi_m - \Omega^2 r - 2\Omega r \dot{\alpha}_z - 2\Omega r \dot{\psi}_s + 2\Omega(r-e) \dot{\zeta} \right] \hat{j} \\
& + \left[ (r \ddot{\alpha}_x + 2\Omega r \dot{\alpha}_y) \sin \psi_m - (r \ddot{\alpha}_y - 2\Omega r \dot{\alpha}_x) \cos \psi_m + \ddot{z} + r \ddot{\beta}_G + (r-e) \ddot{\beta} \right] \hat{k}
\end{aligned} \quad (\text{A.13})$$

## A.3 Rotor Equations of Motion

### A.3.1 Blade flapping equations

The expression for the acceleration of a point on the blade given in Eq. (A.13) is used to derive the inertial forces and moments in the rotor equations of motion, as well as the forces and moments acting on the hub. The blade flap equation of motion is obtained by summing the inertial and elastic moments about the blade flap hinge, and setting the resulting expression equal to the aerodynamic moments about the flap hinge. Referring to Fig. 3.2 and Eq. (A.13), this equation can be written as

$$\int_e^R \left[ m(\underline{a} \cdot \hat{k})(r-e) - m(\underline{a} \cdot \hat{j})(r-e)(\beta + \beta_P + \beta_G) \right] dr + M_\beta^{\text{elas}} = M_\beta^{\text{aero}} \quad (\text{A.14})$$

The aerodynamic flap moments on the right hand side of Eq. (A.14) will be provided in greater detail in a later section. Evaluating the integral in Eq. (A.14) to find the total inertial flap moment on the blade, and non-dimensionalizing the resulting equation by  $I_b \Omega^2$  gives

$$\begin{aligned}
& \left[ I_{\beta\alpha}^* (\overset{**}{\alpha}_x + 2 \overset{*}{\alpha}_y) - S_\beta^* (\beta_P + \bar{\beta}_0) \overset{**}{y} \right] \sin \psi - \left[ I_{\beta\alpha}^* (\overset{**}{\alpha}_y - 2 \overset{*}{\alpha}_x) + S_\beta^* (\beta_P + \bar{\beta}_0) \overset{**}{x} \right] \cos \psi \\
& + S_\beta^* \overset{**}{z} + I_{\beta\alpha}^* (\overset{**}{\beta}_G + \beta_G) + I_\beta^* (\overset{**}{\beta} + v_\beta^2 \beta) + 2I_{\beta\alpha}^* (\beta_P + \bar{\beta}_0) (\overset{*}{\alpha}_z + \overset{*}{\psi}_s) \\
& - 2I_\beta^* (\beta_P + \bar{\beta}_0) \overset{*}{\zeta} + \frac{K_{\beta\zeta}}{I_b \Omega^2} \zeta = \frac{M_\beta^{\text{aero}}}{I_b \Omega^2}
\end{aligned} \quad (\text{A.15})$$

In writing Eq. (A.15), the following definitions have been applied:

$$\bar{x} = \frac{x}{R}, \quad \bar{y} = \frac{y}{R}, \quad \bar{z} = \frac{z}{R} \quad (\text{A.16})$$

$$I_b = \int_0^R mr^2 dr \quad (\text{A.17})$$

$$I_{\beta\alpha}^* = \frac{1}{I_b} \int_e^R mr\eta_\beta dr \quad (\text{A.18})$$

$$I_\beta^* = \frac{1}{I_b} \int_e^R m\eta_\beta^2 dr \quad (\text{A.19})$$

$$S_\beta^* = \frac{R-e}{I_b} \int_e^R m\eta_\beta dr \quad (\text{A.20})$$

$$M_\beta^{\text{elas}} = K_{\beta\beta}\beta + K_{\beta\zeta}\zeta \quad (\text{A.21})$$

$$v_\beta^2 = 1 + \frac{e}{R-e} \frac{S_\beta^*}{I_\beta^*} + \frac{K_{\beta\beta}}{I_b\Omega^2} \quad (\text{A.22})$$

The term  $\eta_\beta$  represents the blade flapping mode shape. For the present rigid blade analysis, the mode shape is simply  $(r - e)$ . Equation (A.15) is the blade flap equation of motion in the rotating frame. Applying the multi-blade coordinate transformation to Eq. (A.15) produces the collective, longitudinal cyclic, and lateral cyclic rotor flap equations of motion:

$\beta_0$ :

$$\begin{aligned} S_\beta^* \bar{z}^{**} + I_\beta^* \left( \beta_0^{**} + v_\beta^2 \beta_0 \right) + 2I_{\beta\alpha}^* (\beta_P + \bar{\beta}_0) \left( \dot{\alpha}_z^* + \dot{\psi}_s^* \right) - 2I_\beta^* (\beta_P + \bar{\beta}_0) \dot{\zeta}_0^* \\ + \frac{K_{\beta\zeta}}{I_b \Omega^2} \zeta_0 = \frac{M_{\beta_0}^{\text{aero}}}{I_b \Omega^2} \end{aligned} \quad (\text{A.23})$$

$\beta_{1c}$ :

$$\begin{aligned} -I_{\beta\alpha}^* \left( \dot{\alpha}_y^{**} - 2 \dot{\alpha}_x^* \right) - S_\beta^* (\beta_P + \bar{\beta}_0) \bar{x}^{**} + I_{\beta\alpha}^* \left( \dot{\beta}_{Gc}^{**} + 2 \dot{\beta}_{Gs}^* \right) \\ + I_\beta^* \left( \beta_{1c}^{**} + 2 \dot{\beta}_{1s}^* + (v_\beta^2 - 1) \beta_{1c} \right) - 2I_\beta^* (\beta_P + \bar{\beta}_0) \left( \dot{\zeta}_{1c}^* + \zeta_{1s} \right) \\ + \frac{K_{\beta\zeta}}{I_b \Omega^2} \zeta_{1c} = \frac{M_{\beta_{1c}}^{\text{aero}}}{I_b \Omega^2} \end{aligned} \quad (\text{A.24})$$

$\beta_{1s}$ :

$$\begin{aligned} I_{\beta\alpha}^* \left( \dot{\alpha}_x^* + 2 \dot{\alpha}_y^{**} \right) - S_\beta^* (\beta_P + \bar{\beta}_0) \bar{y}^{**} + I_{\beta\alpha}^* \left( \dot{\beta}_{Gs}^{**} - 2 \dot{\beta}_{Gc}^* \right) \\ + I_\beta^* \left( \beta_{1s}^{**} - 2 \dot{\beta}_{1c}^* + (v_\beta^2 - 1) \beta_{1s} \right) - 2I_\beta^* (\beta_P + \bar{\beta}_0) \left( \dot{\zeta}_{1s}^* - \zeta_{1c} \right) \\ + \frac{K_{\beta\zeta}}{I_b \Omega^2} \zeta_{1s} = \frac{M_{\beta_{1s}}^{\text{aero}}}{I_b \Omega^2} \end{aligned} \quad (\text{A.25})$$

### A.3.2 Blade lead-lag equations

The blade lead-lag equation of motion is obtained by taking moments about the lag hinge.

$$\int_e^R \left[ m(\underline{a} \cdot \hat{i})(r-e) - m(\underline{a} \cdot \hat{j})(r-e)(\zeta - \psi_s) \right] dr + M_\zeta^{\text{elas}} = M_\zeta^{\text{aero}} \quad (\text{A.26})$$

Evaluating the integral in Eq. (A.26), and non-dimensionalizing the resulting expressions by  $I_b \Omega^2$  gives

$$\begin{aligned}
& S_{\zeta}^* \left( \bar{x}^{**} \sin \psi - \bar{y}^{**} \cos \psi \right) - I_{\zeta\alpha}^* \bar{\alpha}_z^{**} - I_{\zeta\alpha}^* \bar{\psi}_s^{**} + I_{\zeta}^* \left( \bar{\zeta}^{**} + v_{\zeta}^2 \bar{\zeta} \right) \\
& + 2I_{\beta}^* (\beta_P + \bar{\beta}_0) \bar{\beta}^* + \frac{K_{\beta\zeta}}{I_b \Omega^2} \beta = \frac{M_{\zeta}^{\text{aero}}}{I_b \Omega^2}
\end{aligned} \tag{A.27}$$

The definitions in Eq. (A.16) have again been applied, along with the following definitions, where  $\eta_{\zeta}$  is the blade lead-lag mode shape:

$$I_{\zeta\alpha}^* = \frac{1}{I_b} \int_e^R m r \eta_{\zeta} dr \tag{A.28}$$

$$I_{\zeta}^* = \frac{1}{I_b} \int_e^R m \eta_{\zeta}^2 dr \tag{A.29}$$

$$S_{\zeta}^* = \frac{R-e}{I_b} \int_e^R m \eta_{\zeta} dr \tag{A.30}$$

$$M_{\zeta}^{\text{elas}} = K_{\beta\zeta} \beta + K_{\zeta\zeta} \zeta \tag{A.31}$$

$$v_{\zeta}^2 = \frac{e}{R-e} \frac{S_{\zeta}^*}{I_{\zeta}^*} + \frac{K_{\zeta\zeta}}{I_b \Omega^2} \tag{A.32}$$

Applying the multi-blade coordinate transform to Eq. (A.27) yields the fixed-system collective and cyclic lead-lag equations of motion.

$$\begin{aligned}
\underline{\underline{\zeta_0}} : \\
& -I_{\zeta\alpha}^* \ddot{\alpha}_z - I_{\zeta\alpha}^* \ddot{\psi}_s + I_{\zeta}^* \left( \zeta_0^{**} + v_{\zeta}^2 \zeta_0 \right) + 2I_{\beta}^* (\beta_P + \bar{\beta}_0) \dot{\beta}_0 \\
& + \frac{K_{\beta\zeta}}{I_b \Omega^2} \beta_0 = \frac{M_{\zeta_0}^{\text{aero}}}{I_b \Omega^2}
\end{aligned} \tag{A.33}$$

$$\begin{aligned}
\underline{\underline{\zeta_{1c}}} : \\
& -S_{\zeta}^* \ddot{y} + I_{\zeta}^* \left( \zeta_{1c}^{**} + 2 \zeta_{1s}^* + (v_{\zeta}^2 - 1) \zeta_{1c} \right) + 2I_{\beta}^* (\beta_P + \bar{\beta}_0) \left( \dot{\beta}_{1c} + \beta_{1s} \right) \\
& + \frac{K_{\beta\zeta}}{I_b \Omega^2} \beta_{1c} = \frac{M_{\zeta_{1c}}^{\text{aero}}}{I_b \Omega^2}
\end{aligned} \tag{A.34}$$

$$\begin{aligned}
\underline{\underline{\zeta_{1s}}} : \\
& S_{\zeta}^* \ddot{x} + I_{\zeta}^* \left( \zeta_{1s}^{**} - 2 \zeta_{1c}^* + (v_{\zeta}^2 - 1) \zeta_{1s} \right) + 2I_{\beta}^* (\beta_P + \bar{\beta}_0) \left( \dot{\beta}_{1s} - \beta_{1c} \right) \\
& + \frac{K_{\beta\zeta}}{I_b \Omega^2} \beta_{1s} = \frac{M_{\zeta_{1s}}^{\text{aero}}}{I_b \Omega^2}
\end{aligned} \tag{A.35}$$

## A.4 Blade Root Loads – Inertial Contribution

Blade root shears and moments are obtained by integrating the aerodynamic and inertial forces over the length of the blade to determine the reaction at the blade root. The inertial contributions to the blade root loads are given below– the aerodynamic contributions will be presented in a later section.

Vertical shear force:



$$\begin{aligned}
S_z^{\text{inert}} &= \int_0^R -m (\underline{a} \cdot \hat{k}) dr \\
&= -\left(S_\beta^* + \bar{e}M^*\right) \left[ \left(\overset{**}{\alpha}_x + 2 \overset{*}{\alpha}_y\right) \sin \psi - \left(\overset{**}{\alpha}_y - 2 \overset{*}{\alpha}_x\right) \cos \psi \right] \\
&\quad -M^* \overset{**}{z} - \left(S_\beta^* + \bar{e}M^*\right) \overset{**}{\beta}_G - S_\beta^* \overset{**}{\beta}
\end{aligned} \tag{A.36}$$

Inplane shear force:

$$\begin{aligned}
S_x^{\text{inert}} &= \int_0^R -m (\underline{a} \cdot \hat{i}) dr \\
&= -M^* \left( \overset{**}{x} \sin \psi - \overset{**}{y} \cos \psi \right) + \left(S_\zeta^* + \bar{e}M^*\right) \overset{**}{\alpha}_z \\
&\quad + \left(S_\zeta^* + \bar{e}M^*\right) \left( \overset{**}{\psi}_s - \psi_s \right) - S_\zeta^* \left( \overset{**}{\zeta} - \zeta \right) - 2S_\beta^* (\beta_P + \bar{\beta}_0) \overset{*}{\beta}
\end{aligned} \tag{A.37}$$

Radial shear force:

$$\begin{aligned}
S_r^{\text{inert}} &= \int_0^R -m (\underline{a} \cdot \hat{j}) dr \\
&= -M^* \left( \overset{**}{x} \cos \psi + \overset{**}{y} \sin \psi \right) + 2 \left(S_\zeta^* + \bar{e}M^*\right) \overset{*}{\alpha}_z \\
&\quad + 2 \left(S_\zeta^* + \bar{e}M^*\right) \overset{*}{\psi}_s - 2S_\zeta^* \overset{*}{\zeta}
\end{aligned} \tag{A.38}$$

## A.5 Rotor Hub Loads – Inertial Components

The blade root shears and moments are summed over all the blades to obtain expressions for the rotor hub forces and moments.

Thrust force:

$$T^{\text{inert}} = \sum_{k=1}^{N_b} S_z^{(k)} \tag{A.39}$$

$$T^{\text{inert}} = \frac{N_b}{2} \left[ -2M^* \overset{\star\star}{z} - 2S_\beta^* \overset{\star\star}{\beta}_0 \right] \quad (\text{A.40})$$

H-force:

$$H^{\text{inert}} = \sum_{k=1}^{N_b} \left( S_r^{(k)} \cos \psi^{(k)} + S_x^{(k)} \sin \psi^{(k)} \right) \quad (\text{A.41})$$

$$H^{\text{inert}} = \frac{N_b}{2} \left[ -2M^* \overset{\star\star}{x} - S_\zeta^* \overset{\star\star}{\zeta}_{1s} - 2S_\beta^* (\beta_P + \bar{\beta}_0) \left( \overset{\star}{\beta}_{1s} - \beta_{1c} \right) \right] \quad (\text{A.42})$$

Y-force:

$$Y^{\text{inert}} = \sum_{k=1}^{N_b} \left( S_r^{(k)} \sin \psi^{(k)} - S_x^{(k)} \cos \psi^{(k)} \right) \quad (\text{A.43})$$

$$Y^{\text{inert}} = \frac{N_b}{2} \left[ -2M^* \overset{\star\star}{y} + S_\zeta^* \overset{\star\star}{\zeta}_{1c} + 2S_\beta^* (\beta_P + \bar{\beta}_0) \left( \overset{\star}{\beta}_{1c} + \beta_{1s} \right) \right] \quad (\text{A.44})$$

Torque:

$$Q^{\text{inert}} = \sum_{k=1}^{N_b} \left[ M_\zeta^{\text{inert}} + \bar{e} S_x^{\text{inert}} \right]^{(k)} \quad (\text{A.45})$$

$$Q^{\text{inert}} = \frac{N_b}{2} \left[ 2I_0^* \overset{\star\star}{\alpha}_z + 2I_0^* \overset{\star\star}{\psi}_s - 2I_{\zeta\alpha}^* \overset{\star\star}{\zeta}_0 - 4I_{\beta\alpha}^* (\beta_P + \bar{\beta}_0) \overset{\star}{\beta}_0 \right] \quad (\text{A.46})$$

Yawing Moment:

$$M_x^{\text{inert}} = \sum_{k=1}^{N_b} \left[ \left( M_\beta^{\text{inert}} + \bar{e} S_z^{\text{inert}} \right) \sin \psi^{(k)} \right]^{(k)} \quad (\text{A.47})$$

$$M_x^{\text{inert}} = \frac{N_b}{2} \left[ -I_0^* \left( \overset{\star\star}{\alpha}_x + 2 \overset{\star}{\alpha}_y \right) - I_0^* \left( \overset{\star\star}{\beta}_{Gs} - 2 \overset{\star}{\beta}_{Gc} \right) + S_\beta^* (\beta_P + \bar{\beta}_0) \overset{\star\star}{y} \right. \\ \left. - I_{\beta\alpha}^* \left( \overset{\star\star}{\beta}_{1s} - 2 \overset{\star}{\beta}_{1c} \right) + 2I_\beta^* (\beta_P + \bar{\beta}_0) \left( \overset{\star}{\zeta}_{1s} - \zeta_{1c} \right) \right] \quad (\text{A.48})$$

Pitching Moment:

$$M_y^{\text{inert}} = \sum_{k=1}^{N_b} \left[ - \left( M_\beta^{\text{inert}} + \bar{e} S_z^{\text{inert}} \right) \cos \psi^{(k)} \right]^{(k)} \quad (\text{A.49})$$

$$M_y^{\text{inert}} = \frac{N_b}{2} \left[ -I_0^* \left( \alpha_y^{**} - 2 \alpha_x^* \right) + I_0^* \left( \beta_{Gc}^{**} + 2 \beta_{Gs}^* \right) - S_\beta^* \left( \beta_P + \bar{\beta}_0 \right) \bar{x}^{**} \right. \\ \left. + I_{\beta\alpha}^* \left( \beta_{1c}^{**} + 2 \beta_{1s}^* \right) - 2I_\beta^* \left( \beta_P + \bar{\beta}_0 \right) \left( \zeta_{1c}^* + \zeta_{1s} \right) \right] \quad (\text{A.50})$$

## A.6 Rotor Aerodynamics

### A.6.1 Introduction

The rotor aerodynamic model is based on quasi-steady blade element theory. The rotor is assumed to operate in purely axial flow, which is a reasonable assumption for a tiltrotor in the high-speed airplane mode flight condition. The aerodynamic model used in the present analysis is derived from the formulation presented in Ref. 2. Aerodynamic forces and moments are expressed in terms of aerodynamic coefficients multiplying the perturbations in air velocity due to the rotor/hub degrees of freedom. These coefficients are functions of the steady tangential, perpendicular, and radial velocities seen by the blade, blade section pitch, and airfoil lift and drag coefficients, which are dependent on angle of attack and Mach number. In general, evaluating these coefficients requires a numerical integration over the length of the blade, to allow for arbitrary blade pitch settings, twist distribution, and airfoil properties. A detailed description of the aerodynamic model follows.

### A.6.2 Section aerodynamic forces

The lift and drag forces acting on a blade section are defined as

$$L = \frac{1}{2} \rho c (u_T^2 + u_P^2) c_l \quad (\text{A.51})$$

$$D = \frac{1}{2} \rho c (u_T^2 + u_P^2) c_d \quad (\text{A.52})$$

The section lift coefficient  $c_l$  and drag coefficient  $c_d$  are functions of the section angle of attack  $\alpha$  and Mach number  $M$ . Resolving the lift and drag forces into the hub plane gives the section out-of-plane, inplane, and radial aerodynamic forces, which can be expressed as (with the “bar” notation denoting a velocity nondimensionalized by tip speed  $\Omega R$ ):

$$F_z = \rho a c (\Omega R)^2 \bar{U} \left( \bar{u}_T \frac{c_l}{2a} - \bar{u}_P \frac{c_d}{2a} \right) \quad (\text{A.53})$$

$$F_x = \rho a c (\Omega R)^2 \bar{U} \left( \bar{u}_P \frac{c_l}{2a} + \bar{u}_T \frac{c_d}{2a} \right) \quad (\text{A.54})$$

$$F_r = \rho a c (\Omega R)^2 \bar{U} \bar{u}_R \frac{c_d}{2a} - \beta F_z \quad (\text{A.55})$$

Each velocity term in the above aerodynamic force equations may be expressed in terms of a steady part and a perturbation part. The steady parts of the tangential, perpendicular, and radial velocity components are given as:

$$\bar{u}_T = \frac{\Omega r}{\Omega R} = \bar{r} \quad (\text{A.56})$$

$$\bar{u}_P = \frac{V + v}{\Omega R} \approx \bar{V} \quad (\text{A.57})$$

$$\bar{u}_R = 0 \quad (\text{A.58})$$

For a tiltrotor in high-speed forward flight, the induced velocity  $v$  is very small compared to the aircraft’s forward velocity  $V$ , and has been neglected in this analysis. The perturbation parts of the velocity components are:

$$\delta \bar{u}_T = \bar{r}(\dot{\alpha}_z + \dot{\psi}_s) - \frac{(r-e)}{R} \dot{\zeta} - (\dot{x} - \bar{V} \alpha_y) \sin \psi_m + (\dot{y} + \bar{V} \alpha_x) \cos \psi_m \quad (\text{A.59})$$

$$\delta \bar{u}_P = \bar{r} \dot{\beta}_G + \frac{(r-e)}{R} \dot{\beta} + \dot{z} + \bar{r}(\dot{\alpha}_x \sin \psi_m - \dot{\alpha}_y \cos \psi_m) \quad (\text{A.60})$$

$$\delta \bar{u}_R = -(\dot{y} + \bar{V} \alpha_x) \sin \psi_m - (\dot{x} - \bar{V} \alpha_y) \cos \psi_m \quad (\text{A.61})$$

The terms in the tangential and perpendicular velocity components can be grouped to facilitate integration along the span of the blade. To simplify the expressions for rotor aerodynamics, the influence of hinge offset  $e$  in Eqs. A.59 and A.60 is neglected.

$$\delta \bar{u}_T = \bar{r} \delta \bar{u}_{TA} + \delta \bar{u}_{TB} \quad (\text{A.62})$$

$$\delta \bar{u}_P = \bar{r} \delta \bar{u}_{PB} + \delta \bar{u}_{PA} \quad (\text{A.63})$$

Perturbation values for the remaining sectional aerodynamic parameters are:

$$\delta c_l = \frac{\partial c_l}{\partial \alpha} \delta \alpha + \frac{\partial c_l}{\partial M} \delta M \quad (\text{A.64})$$

$$\delta c_d = \frac{\partial c_d}{\partial \alpha} \delta \alpha + \frac{\partial c_d}{\partial M} \delta M \quad (\text{A.65})$$

$$\delta \alpha = \delta \theta - \frac{\bar{u}_T \delta \bar{u}_P - \bar{u}_P \delta \bar{u}_T}{\bar{U}^2} \quad (\text{A.66})$$

$$\delta \bar{U} = \frac{\bar{u}_T \delta \bar{u}_T + \bar{u}_P \delta \bar{u}_P}{\bar{U}} \quad (\text{A.67})$$

$$\delta M = M_{\text{tip}} \delta \bar{U} \quad (\text{A.68})$$

$$\delta \theta = \phi - K_{PG} \beta_G - K_{P\beta} \beta - K_{P\zeta} \zeta \quad (\text{A.69})$$

### A.6.3 Rotor aerodynamic forces and moments

The aerodynamic forces and moments on the rotor are obtained by integrating the section aerodynamic forces along the span of the blade and summing over the total number of blades.

$$M_{\beta}^{\text{aero}} = \int_0^R F_z r \, dr \quad (\text{A.70})$$

$$M_{\zeta}^{\text{aero}} = \int_0^R F_x r \, dr \quad (\text{A.71})$$

$$T^{\text{aero}} = \sum_m^{N_b} \int_0^R F_z \, dr \quad (\text{A.72})$$

$$H^{\text{aero}} = \sum_m^{N_b} \left( \cos \psi_m \int_0^R F_r \, dr + \sin \psi_m \int_0^R F_x \, dr \right) \quad (\text{A.73})$$

$$Y^{\text{aero}} = \sum_m^{N_b} \left( \sin \psi_m \int_0^R F_r \, dr - \cos \psi_m \int_0^R F_x \, dr \right) \quad (\text{A.74})$$

$$Q^{\text{aero}} = \sum_m^{N_b} \int_0^R F_z r \, dr \quad (\text{A.75})$$

$$M_x^{\text{aero}} = \sum_m^{N_b} \left( \sin \psi_m \int_0^R F_z r \, dr \right) \quad (\text{A.76})$$

$$M_y^{\text{aero}} = \sum_m^{N_b} \left( -\cos \psi_m \int_0^R F_z r \, dr \right) \quad (\text{A.77})$$

Non-dimensionalizing the blade flap and lag moments by  $I_b \Omega^2$ , the hub forces by  $\frac{N_b I_b \Omega^2}{2R}$ , and the hub moments by  $\frac{N_b I_b \Omega^2}{2}$  yields the following:

$$\frac{M_\beta^{\text{aero}}}{I_b \Omega^2} = \gamma \int_0^1 \frac{F_z}{\rho a c (\Omega R)^2} \bar{r} d\bar{r} \quad (\text{A.78})$$

$$\frac{M_\zeta^{\text{aero}}}{I_b \Omega^2} = \gamma \int_0^1 \frac{F_x}{\rho a c (\Omega R)^2} \bar{r} d\bar{r} \quad (\text{A.79})$$

$$\frac{T^{\text{aero}}}{\frac{N_b I_b \Omega^2}{2} R} = \gamma \frac{2}{N_b} \sum_m^{N_b} \int_0^1 \frac{F_z}{\rho a c (\Omega R)^2} d\bar{r} \quad (\text{A.80})$$

$$\frac{H^{\text{aero}}}{\frac{N_b I_b \Omega^2}{2} R} = \gamma \frac{2}{N_b} \sum_m^{N_b} \left( \cos \psi_m \int_0^1 \frac{F_r}{\rho a c (\Omega R)^2} d\bar{r} + \sin \psi_m \int_0^1 \frac{F_x}{\rho a c (\Omega R)^2} d\bar{r} \right) \quad (\text{A.81})$$

$$\frac{Y^{\text{aero}}}{\frac{N_b I_b \Omega^2}{2} R} = \gamma \frac{2}{N_b} \sum_m^{N_b} \left( \sin \psi_m \int_0^1 \frac{F_r}{\rho a c (\Omega R)^2} d\bar{r} - \cos \psi_m \int_0^1 \frac{F_x}{\rho a c (\Omega R)^2} d\bar{r} \right) \quad (\text{A.82})$$

$$\frac{Q^{\text{aero}}}{\frac{N_b}{2} I_b \Omega^2} = \gamma \frac{2}{N_b} \sum_m^{N_b} \int_0^R \frac{F_x}{\rho a c (\Omega R)^2} r dr \quad (\text{A.83})$$

$$\frac{M_x^{\text{aero}}}{\frac{N_b}{2} I_b \Omega^2} = \gamma \frac{2}{N_b} \sum_m^{N_b} \left( \sin \psi_m \int_0^R \frac{F_z}{\rho a c (\Omega R)^2} r dr \right) \quad (\text{A.84})$$

$$\frac{M_y^{\text{aero}}}{\frac{N_b}{2} I_b \Omega^2} = \gamma \frac{2}{N_b} \sum_m^{N_b} \left( -\cos \psi_m \int_0^R \frac{F_z}{\rho a c (\Omega R)^2} r dr \right) \quad (\text{A.85})$$

To evaluate the above expressions, the following integrals must be calculated (neglecting the radial aerodynamic force ( $F_r$ )):

$$\int_0^1 \frac{F_z}{\rho a c (\Omega R)^2} d\bar{r} = \int_0^1 \bar{U} \left( \bar{u}_T \frac{c_l}{2a} - \bar{u}_P \frac{c_d}{2a} \right) d\bar{r} \quad (\text{A.86})$$

$$\int_0^1 \frac{F_z}{\rho a c (\Omega R)^2} \bar{r} d\bar{r} = \int_0^1 \bar{U} \left( \bar{u}_T \frac{c_l}{2a} - \bar{u}_P \frac{c_d}{2a} \right) \bar{r} d\bar{r} \quad (\text{A.87})$$

$$\int_0^1 \frac{F_x}{\rho a c (\Omega R)^2} d\bar{r} = \int_0^1 \bar{U} \left( \bar{u}_P \frac{c_l}{2a} + \bar{u}_T \frac{c_d}{2a} \right) d\bar{r} \quad (\text{A.88})$$

$$\int_0^1 \frac{F_x}{\rho a c (\Omega R)^2} \bar{r} d\bar{r} = \int_0^1 \bar{U} \left( \bar{u}_P \frac{c_l}{2a} + \bar{u}_T \frac{c_d}{2a} \right) \bar{r} d\bar{r} \quad (\text{A.89})$$

Substituting the perturbation quantities in Eqs. A.59–A.69 into these integral equations and performing the integration yields complicated expressions which may be written in a simple form by defining aerodynamic coefficient terms:

$$\int_0^1 \frac{F_z}{\rho ac(\Omega R)^2} d\bar{r} = T_0 + T_\mu \delta \bar{u}_{TB} + T_\zeta^* \delta \bar{u}_{TA} + T_\lambda \delta \bar{u}_{PA} + T_\beta^* \delta \bar{u}_{PB} + T_\theta \delta \theta \quad (\text{A.90})$$

$$\int_0^1 \frac{F_z}{\rho ac(\Omega R)^2} \bar{r} d\bar{r} = M_0 + M_\mu \delta \bar{u}_{TB} + M_\zeta^* \delta \bar{u}_{TA} + M_\lambda \delta \bar{u}_{PA} + M_\beta^* \delta \bar{u}_{PB} + M_\theta \delta \theta \quad (\text{A.91})$$

$$\int_0^1 \frac{F_x}{\rho ac(\Omega R)^2} d\bar{r} = H_0 + H_\mu \delta \bar{u}_{TB} + H_\zeta^* \delta \bar{u}_{TA} + H_\lambda \delta \bar{u}_{PA} + H_\beta^* \delta \bar{u}_{PB} + H_\theta \delta \theta \quad (\text{A.92})$$

$$\int_0^1 \frac{F_x}{\rho ac(\Omega R)^2} \bar{r} d\bar{r} = Q_0 + Q_\mu \delta \bar{u}_{TB} + Q_\zeta^* \delta \bar{u}_{TA} + Q_\lambda \delta \bar{u}_{PA} + Q_\beta^* \delta \bar{u}_{PB} + Q_\theta \delta \theta \quad (\text{A.93})$$

In the present analysis, the  $T, M, H,$  and  $Q$  terms in the above expressions are evaluated by numerically integrating the following equations:

$$T_0 = \frac{1}{2a} \int_0^1 \bar{U} (\bar{u}_T c_l - \bar{u}_P c_d) d\bar{r} \quad (\text{A.94})$$

$$T_\theta = \frac{1}{2a} \int_0^1 \bar{U} (\bar{u}_T c_{l\alpha} - \bar{u}_P c_{d\alpha}) d\bar{r} \quad (\text{A.95})$$

$$T_\mu = \frac{1}{2a} \int_0^1 \left[ \frac{\bar{u}_T \bar{u}_P}{\bar{U}} c_{l\alpha} + \frac{\bar{u}_T^2}{\bar{U}} M c_{lM} + \bar{U} c_l - \frac{\bar{u}_P^2}{\bar{U}} c_{d\alpha} - \frac{\bar{u}_T \bar{u}_P}{\bar{U}} M c_{dM} \right. \\ \left. + \frac{\bar{u}_T^2}{\bar{U}} c_l - \frac{\bar{u}_T \bar{u}_P}{\bar{U}} c_d \right] d\bar{r} \quad (\text{A.96})$$

$$T_\zeta^* = \frac{1}{2a} \int_0^1 \left[ \frac{\bar{u}_T \bar{u}_P}{\bar{U}} c_{l\alpha} + \frac{\bar{u}_T^2}{\bar{U}} M c_{lM} + \bar{U} c_l - \frac{\bar{u}_P^2}{\bar{U}} c_{d\alpha} - \frac{\bar{u}_T \bar{u}_P}{\bar{U}} M c_{dM} \right. \\ \left. + \frac{\bar{u}_T^2}{\bar{U}} c_l - \frac{\bar{u}_T \bar{u}_P}{\bar{U}} c_d \right] \bar{r} d\bar{r} \quad (\text{A.97})$$

$$T_\lambda = \frac{1}{2a} \int_0^1 \left[ -\frac{\bar{u}_T^2}{\bar{U}} c_{l\alpha} + \frac{\bar{u}_T \bar{u}_P}{\bar{U}} M c_{lM} - \bar{U} c_d + \frac{\bar{u}_T \bar{u}_P}{\bar{U}} c_{d\alpha} - \frac{\bar{u}_P^2}{\bar{U}} M c_{dM} \right. \\ \left. + \frac{\bar{u}_T \bar{u}_P}{\bar{U}} c_l - \frac{\bar{u}_P^2}{\bar{U}} c_d \right] d\bar{r} \quad (\text{A.98})$$

$$T_\beta^* = \frac{1}{2a} \int_0^1 \left[ -\frac{\bar{u}_T^2}{\bar{U}} c_{l\alpha} + \frac{\bar{u}_T \bar{u}_P}{\bar{U}} M c_{lM} - \bar{U} c_d + \frac{\bar{u}_T \bar{u}_P}{\bar{U}} c_{d\alpha} - \frac{\bar{u}_P^2}{\bar{U}} M c_{dM} \right. \\ \left. + \frac{\bar{u}_T \bar{u}_P}{\bar{U}} c_l - \frac{\bar{u}_P^2}{\bar{U}} c_d \right] \bar{r} d\bar{r} \quad (\text{A.99})$$



$$M_0 = \frac{1}{2a} \int_0^1 \bar{U} (\bar{u}_T c_l - \bar{u}_P c_d) \bar{r} \, d\bar{r} \quad (\text{A.100})$$

$$M_\theta = \frac{1}{2a} \int_0^1 \bar{U} (\bar{u}_T c_{l_\alpha} - \bar{u}_P c_{d_\alpha}) \bar{r} \, d\bar{r} \quad (\text{A.101})$$

$$M_\mu = \frac{1}{2a} \int_0^1 \left[ \frac{\bar{u}_T \bar{u}_P}{\bar{U}} c_{l_\alpha} + \frac{\bar{u}_T^2}{\bar{U}} M c_{l_M} + \bar{U} c_l - \frac{\bar{u}_P^2}{\bar{U}} c_{d_\alpha} - \frac{\bar{u}_T \bar{u}_P}{\bar{U}} M c_{d_M} \right. \\ \left. + \frac{\bar{u}_T^2}{\bar{U}} c_l - \frac{\bar{u}_T \bar{u}_P}{\bar{U}} c_d \right] \bar{r} \, d\bar{r} \quad (\text{A.102})$$

$$M_\zeta^* = \frac{1}{2a} \int_0^1 \left[ \frac{\bar{u}_T \bar{u}_P}{\bar{U}} c_{l_\alpha} + \frac{\bar{u}_T^2}{\bar{U}} M c_{l_M} + \bar{U} c_l - \frac{\bar{u}_P^2}{\bar{U}} c_{d_\alpha} - \frac{\bar{u}_T \bar{u}_P}{\bar{U}} M c_{d_M} \right. \\ \left. + \frac{\bar{u}_T^2}{\bar{U}} c_l - \frac{\bar{u}_T \bar{u}_P}{\bar{U}} c_d \right] \bar{r}^2 \, d\bar{r} \quad (\text{A.103})$$

$$M_\lambda = \frac{1}{2a} \int_0^1 \left[ -\frac{\bar{u}_T^2}{\bar{U}} c_{l_\alpha} + \frac{\bar{u}_T \bar{u}_P}{\bar{U}} M c_{l_M} - \bar{U} c_d + \frac{\bar{u}_T \bar{u}_P}{\bar{U}} c_{d_\alpha} - \frac{\bar{u}_P^2}{\bar{U}} M c_{d_M} \right. \\ \left. + \frac{\bar{u}_T \bar{u}_P}{\bar{U}} c_l - \frac{\bar{u}_P^2}{\bar{U}} c_d \right] \bar{r} \, d\bar{r} \quad (\text{A.104})$$

$$M_\beta^* = \frac{1}{2a} \int_0^1 \left[ -\frac{\bar{u}_T^2}{\bar{U}} c_{l_\alpha} + \frac{\bar{u}_T \bar{u}_P}{\bar{U}} M c_{l_M} - \bar{U} c_d + \frac{\bar{u}_T \bar{u}_P}{\bar{U}} c_{d_\alpha} - \frac{\bar{u}_P^2}{\bar{U}} M c_{d_M} \right. \\ \left. + \frac{\bar{u}_T \bar{u}_P}{\bar{U}} c_l - \frac{\bar{u}_P^2}{\bar{U}} c_d \right] \bar{r}^2 \, d\bar{r} \quad (\text{A.105})$$

$$H_0 = \frac{1}{2a} \int_0^1 \bar{U} (\bar{u}_P c_l + \bar{u}_T c_d) d\bar{r} \quad (\text{A.106})$$

$$H_\theta = \frac{1}{2a} \int_0^1 \bar{U} (\bar{u}_P c_{l_\alpha} + \bar{u}_T c_{d_\alpha}) d\bar{r} \quad (\text{A.107})$$

$$H_\mu = \frac{1}{2a} \int_0^1 \left[ \frac{\bar{u}_P^2}{\bar{U}} c_{l_\alpha} + \frac{\bar{u}_T \bar{u}_P}{\bar{U}} M c_{l_M} + \bar{U} c_d + \frac{\bar{u}_T \bar{u}_P}{\bar{U}} c_{d_\alpha} + \frac{\bar{u}_T^2}{\bar{U}} M c_{d_M} + \frac{\bar{u}_T \bar{u}_P}{\bar{U}} c_l + \frac{\bar{u}_T^2}{\bar{U}} c_d \right] d\bar{r} \quad (\text{A.108})$$

$$H_\zeta^* = \frac{1}{2a} \int_0^1 \left[ \frac{\bar{u}_P^2}{\bar{U}} c_{l_\alpha} + \frac{\bar{u}_T \bar{u}_P}{\bar{U}} M c_{l_M} + \bar{U} c_d + \frac{\bar{u}_T \bar{u}_P}{\bar{U}} c_{d_\alpha} + \frac{\bar{u}_T^2}{\bar{U}} M c_{d_M} + \frac{\bar{u}_T \bar{u}_P}{\bar{U}} c_l + \frac{\bar{u}_T^2}{\bar{U}} c_d \right] \bar{r} d\bar{r} \quad (\text{A.109})$$

$$H_\lambda = \frac{1}{2a} \int_0^1 \left[ -\frac{\bar{u}_T \bar{u}_P}{\bar{U}} c_{l_\alpha} + \frac{\bar{u}_P^2}{\bar{U}} M c_{l_M} + \bar{U} c_l - \frac{\bar{u}_T^2}{\bar{U}} c_{d_\alpha} + \frac{\bar{u}_T \bar{u}_P}{\bar{U}} M c_{d_M} + \frac{\bar{u}_P^2}{\bar{U}} c_l + \frac{\bar{u}_T \bar{u}_P}{\bar{U}} c_d \right] d\bar{r} \quad (\text{A.110})$$

$$H_\beta^* = \frac{1}{2a} \int_0^1 \left[ -\frac{\bar{u}_T \bar{u}_P}{\bar{U}} c_{l_\alpha} + \frac{\bar{u}_P^2}{\bar{U}} M c_{l_M} + \bar{U} c_l - \frac{\bar{u}_T^2}{\bar{U}} c_{d_\alpha} + \frac{\bar{u}_T \bar{u}_P}{\bar{U}} M c_{d_M} + \frac{\bar{u}_P^2}{\bar{U}} c_l + \frac{\bar{u}_T \bar{u}_P}{\bar{U}} c_d \right] \bar{r} d\bar{r} \quad (\text{A.111})$$

$$Q_0 = \frac{1}{2a} \int_0^1 \bar{U} (\bar{u}_P c_l + \bar{u}_T c_d) \bar{r} \, d\bar{r} \quad (\text{A.112})$$

$$Q_\theta = \frac{1}{2a} \int_0^1 \bar{U} (\bar{u}_P c_{l_\alpha} + \bar{u}_T c_{d_\alpha}) \bar{r} \, d\bar{r} \quad (\text{A.113})$$

$$Q_\mu = \frac{1}{2a} \int_0^1 \left[ \frac{\bar{u}_P^2}{\bar{U}} c_{l_\alpha} + \frac{\bar{u}_T \bar{u}_P}{\bar{U}} M c_{l_M} + \bar{U} c_d + \frac{\bar{u}_T \bar{u}_P}{\bar{U}} c_{d_\alpha} + \frac{\bar{u}_T^2}{\bar{U}} M c_{d_M} \right. \\ \left. + \frac{\bar{u}_T \bar{u}_P}{\bar{U}} c_l + \frac{\bar{u}_T^2}{\bar{U}} c_d \right] \bar{r} \, d\bar{r} \quad (\text{A.114})$$

$$Q_\zeta^* = \frac{1}{2a} \int_0^1 \left[ \frac{\bar{u}_P^2}{\bar{U}} c_{l_\alpha} + \frac{\bar{u}_T \bar{u}_P}{\bar{U}} M c_{l_M} + \bar{U} c_d + \frac{\bar{u}_T \bar{u}_P}{\bar{U}} c_{d_\alpha} + \frac{\bar{u}_T^2}{\bar{U}} M c_{d_M} \right. \\ \left. + \frac{\bar{u}_T \bar{u}_P}{\bar{U}} c_l + \frac{\bar{u}_T^2}{\bar{U}} c_d \right] \bar{r}^2 \, d\bar{r} \quad (\text{A.115})$$

$$Q_\lambda = \frac{1}{2a} \int_0^1 \left[ -\frac{\bar{u}_T \bar{u}_P}{\bar{U}} c_{l_\alpha} + \frac{\bar{u}_P^2}{\bar{U}} M c_{l_M} + \bar{U} c_l - \frac{\bar{u}_T^2}{\bar{U}} c_{d_\alpha} + \frac{\bar{u}_T \bar{u}_P}{\bar{U}} M c_{d_M} \right. \\ \left. + \frac{\bar{u}_P^2}{\bar{U}} c_l + \frac{\bar{u}_T \bar{u}_P}{\bar{U}} c_d \right] \bar{r} \, d\bar{r} \quad (\text{A.116})$$

$$Q_\beta^* = \frac{1}{2a} \int_0^1 \left[ -\frac{\bar{u}_T \bar{u}_P}{\bar{U}} c_{l_\alpha} + \frac{\bar{u}_P^2}{\bar{U}} M c_{l_M} + \bar{U} c_l - \frac{\bar{u}_T^2}{\bar{U}} c_{d_\alpha} + \frac{\bar{u}_T \bar{u}_P}{\bar{U}} M c_{d_M} \right. \\ \left. + \frac{\bar{u}_P^2}{\bar{U}} c_l + \frac{\bar{u}_T \bar{u}_P}{\bar{U}} c_d \right] \bar{r}^2 \, d\bar{r} \quad (\text{A.117})$$

Substituting Eqs. A.90–A.93 and Eqs. A.59–A.63 into the expressions for the aerodynamic forces and moments in Eqs. A.78–A.85, and transforming the blade flap and lag moments into the fixed frame completes the required aerodynamic expressions:

## A.7 Gimbal/Rotor Speed Degrees of Freedom

The equations of motion for the gimbal degrees of freedom equate the net pitching and yawing moments on the rotor to the elastic restoring moment in the gimbal spring:

$$\underline{\underline{\beta_{Gc}}} \quad \frac{M_y^{\text{aero}} + M_y^{\text{inert}}}{\frac{N_b}{2} I_b \Omega^2} = \frac{K_{\beta G}}{I_b \Omega^2} \beta_{Gc} = I_0^* (v_{\beta G}^2 - 1) \beta_{Gc} \quad (\text{A.118})$$

$$\underline{\underline{\beta_{Gs}}} \quad \frac{M_x^{\text{aero}} + M_x^{\text{inert}}}{\frac{N_b}{2} I_b \Omega^2} = \frac{K_{\beta G}}{I_b \Omega^2} \beta_{Gs} = I_0^* (v_{\beta G}^2 - 1) \beta_{Gs} \quad (\text{A.119})$$

For the case of a windmilling rotor, the equation of motion for the rotor speed degree of freedom simply states that the net torque on the rotor is zero:

$$\underline{\underline{\psi_s}} \quad \frac{Q^{\text{aero}} + Q^{\text{inert}}}{\frac{N_b}{2} I_b \Omega^2} = 0 \quad (\text{A.120})$$

## A.8 Rotor Equations of Motion

Assembling the structural and aerodynamic contributions to the equations of motion for the rotor degrees of freedom (including the gimbal and rotor speed DOFs), and the expressions for the hub forces and moments, the complete set of rotor equations of motion can be expressed in the form

$$[M^s] \underline{\underline{\ddot{q}}} + [C^s + C^a] \underline{\underline{\dot{q}}} + [K^s + K^a] \underline{\underline{q}} = 0 \quad (\text{A.121})$$

A listing of the structural and aerodynamic system matrices is presented below. The order of DOFs in the matrices is as follows:

$$\underline{\underline{q}} = \{ \beta_0 \ \beta_{1c} \ \beta_{1s} \ \zeta_0 \ \zeta_{1c} \ \zeta_{1s} \ \psi_s \ \beta_{Gc} \ \beta_{Gs} \ \bar{x} \ \bar{y} \ \bar{z} \ \alpha_x \ \alpha_y \ \alpha_z \} \quad (\text{A.122})$$

Any matrix element not listed below has a value of zero.

### Structural mass matrix

mrpi(1,1) = ibstar;

mrpi(1,12) = sbstar;

```
mrpi(2,2) = ibstar;  
mrpi(2,8) = ibastar;  
mrpi(2,10) = -sbstar*(beta0+betap);  
mrpi(2,14) = -ibastar;
```

```
mrpi(3,3) = ibstar;  
mrpi(3,9) = ibastar;  
mrpi(3,11) = -sbstar*(beta0+betap);  
mrpi(3,13) = ibastar;
```

```
mrpi(4,4) = izstar;  
mrpi(4,7) = -izastar;  
mrpi(4,15) = -izastar;
```

```
mrpi(5,5) = izstar;  
mrpi(5,11) = -szstar;
```

```
mrpi(6,6) = izstar;  
mrpi(6,10) = szstar;
```

```
mrpi(7,4) = -izastar;  
mrpi(7,7) = i0star;  
mrpi(7,15) = i0star;
```

```
mrpi(8,2) = ibastar;  
mrpi(8,8) = i0star;  
mrpi(8,10) = -sbstar*(beta0+betap);
```

mrpi(8,14) = -i0star;

mrpi(9,3) = ibastar;

mrpi(9,9) = i0star;

mrpi(9,11) = -sbstar\*(beta0+betap);

mrpi(9,13) = i0star;

mrpi(10,6) = szstar;

mrpi(10,10) = 2\*mstar;

mrpi(11,5) = -szstar;

mrpi(11,11) = 2\*mstar;

mrpi(12,1) = 2\*sbstar;

mrpi(12,12) = 2\*mstar;

mrpi(13,3) = ibastar;

mrpi(13,9) = i0star;

mrpi(13,11) = -sbstar\*(beta0+betap);

mrpi(13,13) = i0star;

mrpi(14,2) = -ibastar;

mrpi(14,8) = -i0star;

mrpi(14,10) = sbstar\*(beta0+betap);

mrpi(14,14) = i0star;

mrpi(15,4) = -2\*izastar;

mrpi(15,7) = 2\*i0star;

```
mrpi(15,15) = 2*i0star;
```

Structural damping matrix

```
crpi(1,4) = 2*ibstar*(beta0+betap);  
crpi(1,7) = 2*ibastar*(beta0+betap);  
crpi(1,15) = 2*ibastar*(beta0+betap);
```

```
crpi(2,3) = 2*ibstar;  
crpi(2,5) = -2*ibstar*(beta0+betap);  
crpi(2,9) = 2*ibastar;  
crpi(2,13) = 2*ibastar;
```

```
crpi(3,2) = -2*ibstar;  
crpi(3,6) = -2*ibstar*(beta0+betap);  
crpi(3,8) = -2*ibastar;  
crpi(3,14) = 2*ibastar;
```

```
crpi(4,1) = 2*ibstar*(beta0+betap);
```

```
crpi(5,2) = 2*ibstar*(beta0+betap);  
crpi(5,6) = 2*izstar;
```

```
crpi(6,3) = 2*ibstar*(beta0+betap);  
crpi(6,5) = -2*izstar;
```

```
crpi(7,1) = -2*ibastar*(beta0+betap);
```

```
crpi(8,3) = 2*ibastar;  
crpi(8,5) = -2*ibstar*(beta0+betap);  
crpi(8,9) = 2*i0star;  
crpi(8,13) = 2*i0star;  
  
crpi(9,2) = -2*ibastar;  
crpi(9,6) = -2*ibstar*(beta0+betap);  
crpi(9,8) = -2*i0star;  
crpi(9,14) = 2*i0star;  
  
crpi(10,3) = 2*sbstar*(beta0+betap);  
  
crpi(11,2) = -2*sbstar*(beta0+betap);  
  
crpi(13,2) = -2*ibastar;  
crpi(13,6) = -2*ibstar*(beta0+betap);  
crpi(13,8) = -2*i0star;  
crpi(13,14) = 2*i0star;  
  
crpi(14,3) = -2*ibastar;  
crpi(14,5) = 2*ibstar*(beta0+betap);  
crpi(14,9) = -2*i0star;  
crpi(14,13) = -2*i0star;  
  
crpi(15,1) = -4*ibastar*(beta0+betap);
```



Structural stiffness matrix

$$krpi(1,1) = ibstar*nubeta^2;$$

$$krpi(1,4) = dkbz;$$

$$krpi(2,2) = ibstar*(nubeta^2 - 1);$$

$$krpi(2,5) = dkbz;$$

$$krpi(2,6) = -2*ibstar*(beta0+betap);$$

$$krpi(3,3) = ibstar*(nubeta^2 - 1);$$

$$krpi(3,5) = 2*ibstar*(beta0+betap);$$

$$krpi(3,6) = dkbz;$$

$$krpi(4,1) = dkbz;$$

$$krpi(4,4) = izstar*nuzeta^2;$$

$$krpi(5,2) = dkbz;$$

$$krpi(5,3) = 2*ibstar*(beta0+betap);$$

$$krpi(5,5) = izstar*(nuzeta^2 - 1);$$

$$krpi(6,2) = -2*ibstar*(beta0+betap);$$

$$krpi(6,3) = dkbz;$$

$$krpi(6,6) = izstar*(nuzeta^2 - 1);$$

$$krpi(8,6) = -2*ibstar*(beta0+betap);$$

$$krpi(8,8) = i0star*(nubetg^2 - 1);$$

$$krpi(9,5) = 2*ibstar*(beta0+betap);$$

$$\text{krpi}(9,9) = i0\text{star} * (\text{nubetg}^2 - 1);$$

$$\text{krpi}(10,2) = -2 * \text{sbstar} * (\text{beta0} + \text{betap});$$

$$\text{krpi}(11,3) = -2 * \text{sbstar} * (\text{beta0} + \text{betap});$$

$$\text{krpi}(12,5) = 2 * \text{ibstar} * (\text{beta0} + \text{betap});$$

$$\text{krpi}(14,6) = 2 * \text{ibstar} * (\text{beta0} + \text{betap});$$

#### Aerodynamic damping matrix

$$\text{crpa}(1,1) = -\text{gamma} * \text{mbd};$$

$$\text{crpa}(1,4) = \text{gamma} * \text{mzd};$$

$$\text{crpa}(1,7) = -\text{gamma} * \text{mzd};$$

$$\text{crpa}(1,12) = -\text{gamma} * \text{mlam};$$

$$\text{crpa}(1,15) = -\text{gamma} * \text{mzd};$$

$$\text{crpa}(2,2) = -\text{gamma} * \text{mbd};$$

$$\text{crpa}(2,5) = \text{gamma} * \text{mzd};$$

$$\text{crpa}(2,8) = -\text{gamma} * \text{mbd};$$

$$\text{crpa}(2,11) = -\text{gamma} * \text{mmu};$$

$$\text{crpa}(2,14) = \text{gamma} * \text{mbd};$$

$$\text{crpa}(3,3) = -\text{gamma} * \text{mbd};$$

$$\text{crpa}(3,6) = \text{gamma} * \text{mzd};$$

$$\text{crpa}(3,9) = -\text{gamma} * \text{mbd};$$

$$\text{crpa}(3,10) = \text{gamma} * \text{mmu};$$

$$\text{crpa}(3,13) = -\text{gamma}*\text{mbd};$$

$$\text{crpa}(4,1) = -\text{gamma}*\text{qbd};$$

$$\text{crpa}(4,4) = \text{gamma}*\text{qzd};$$

$$\text{crpa}(4,7) = -\text{gamma}*\text{qzd};$$

$$\text{crpa}(4,12) = -\text{gamma}*\text{qlam};$$

$$\text{crpa}(4,15) = -\text{gamma}*\text{qzd};$$

$$\text{crpa}(5,2) = -\text{gamma}*\text{qbd};$$

$$\text{crpa}(5,5) = \text{gamma}*\text{qzd};$$

$$\text{crpa}(5,8) = -\text{gamma}*\text{qbd};$$

$$\text{crpa}(5,11) = -\text{gamma}*\text{qmu};$$

$$\text{crpa}(5,14) = \text{gamma}*\text{qbd};$$

$$\text{crpa}(6,3) = -\text{gamma}*\text{qbd};$$

$$\text{crpa}(6,6) = \text{gamma}*\text{qzd};$$

$$\text{crpa}(6,9) = -\text{gamma}*\text{qbd};$$

$$\text{crpa}(6,10) = \text{gamma}*\text{qmu};$$

$$\text{crpa}(6,13) = -\text{gamma}*\text{qbd};$$

$$\text{crpa}(7,1) = \text{gamma}*\text{qbd};$$

$$\text{crpa}(7,4) = -\text{gamma}*\text{qzd};$$

$$\text{crpa}(7,7) = \text{gamma}*\text{qzd};$$

$$\text{crpa}(7,12) = \text{gamma}*\text{qlam};$$

$$\text{crpa}(7,15) = \text{gamma}*\text{qzd};$$

$$\text{crpa}(8,2) = -\text{gamma}*\text{mbd};$$

$$\text{crpa}(8,5) = \text{gamma}*\text{mzd};$$

```
crpa(8,8) = -gamma*mbd;  
crpa(8,11) = -gamma*mmu;  
crpa(8,14) = gamma*mbd;  
  
crpa(9,3) = -gamma*mbd;  
crpa(9,6) = gamma*mzd;  
crpa(9,9) = -gamma*mbd;  
crpa(9,10) = gamma*mmu;  
crpa(9,13) = -gamma*mbd;  
  
crpa(10,3) = -gamma*hbd;  
crpa(10,6) = gamma*hzd;  
crpa(10,9) = -gamma*hbd;  
crpa(10,10) = gamma*hmu;  
crpa(10,13) = -gamma*hbd;  
  
crpa(11,2) = gamma*hbd;  
crpa(11,5) = -gamma*hzd;  
crpa(11,8) = gamma*hbd;  
crpa(11,11) = gamma*hmu;  
crpa(11,14) = -gamma*hbd;  
  
crpa(12,1) = -2*gamma*tbd;  
crpa(12,4) = 2*gamma*tzd;  
crpa(12,7) = -2*gamma*tzd;  
crpa(12,12) = -2*gamma*tlam;  
crpa(12,15) = -2*gamma*tzd;
```

$crpa(13,3) = -\gamma * mbd;$   
 $crpa(13,6) = \gamma * mzd;$   
 $crpa(13,9) = -\gamma * mbd;$   
 $crpa(13,10) = \gamma * mmu;$   
 $crpa(13,13) = -\gamma * mbd;$

$crpa(14,2) = \gamma * mbd;$   
 $crpa(14,5) = -\gamma * mzd;$   
 $crpa(14,8) = \gamma * mbd;$   
 $crpa(14,11) = \gamma * mmu;$   
 $crpa(14,14) = -\gamma * mbd;$

$crpa(15,1) = 2 * \gamma * qbd;$   
 $crpa(15,4) = -2 * \gamma * qzd;$   
 $crpa(15,7) = 2 * \gamma * qzd;$   
 $crpa(15,12) = 2 * \gamma * qlam;$   
 $crpa(15,15) = 2 * \gamma * qzd;$

#### Aerodynamic stiffness matrix

$krpa(1,1) = \gamma * kpb * mth;$   
 $krpa(1,4) = \gamma * kpz * mth;$

$krpa(2,2) = \gamma * kpb * mth;$   
 $krpa(2,3) = -\gamma * mbd;$   
 $krpa(2,5) = \gamma * kpz * mth;$   
 $krpa(2,6) = \gamma * mzd;$   
 $krpa(2,8) = \gamma * kpg * mth;$

$$\begin{aligned}
krpa(2,9) &= -\gamma * mbd; \\
krpa(2,13) &= -v * \gamma * mmu; \\
\\
krpa(3,2) &= \gamma * mbd; \\
krpa(3,3) &= \gamma * kpb * mth; \\
krpa(3,5) &= -\gamma * mzd; \\
krpa(3,6) &= \gamma * kpz * mth; \\
krpa(3,8) &= \gamma * mbd; \\
krpa(3,9) &= \gamma * kpg * mth; \\
krpa(3,14) &= -v * \gamma * mmu; \\
\\
krpa(4,1) &= \gamma * kpb * qth; \\
krpa(4,4) &= \gamma * kpz * qth; \\
\\
krpa(5,2) &= \gamma * kpb * qth; \\
krpa(5,3) &= -\gamma * qbd; \\
krpa(5,5) &= \gamma * kpz * qth; \\
krpa(5,6) &= \gamma * qzd; \\
krpa(5,8) &= \gamma * kpg * qth; \\
krpa(5,9) &= -\gamma * qbd; \\
krpa(5,13) &= -v * \gamma * qmu; \\
\\
krpa(6,2) &= \gamma * qbd; \\
krpa(6,3) &= \gamma * kpb * qth; \\
krpa(6,5) &= -\gamma * qzd; \\
krpa(6,6) &= \gamma * kpz * qth; \\
krpa(6,8) &= \gamma * qbd; \\
krpa(6,9) &= \gamma * kpg * qth;
\end{aligned}$$

$$\text{krpa}(6,14) = -v*\gamma*qu;$$

$$\text{krpa}(7,1) = -\gamma*qt*kp;$$

$$\text{krpa}(7,4) = -\gamma*qt*kpz;$$

$$\text{krpa}(8,2) = \gamma*kp*mt;$$

$$\text{krpa}(8,3) = -\gamma*mbd;$$

$$\text{krpa}(8,5) = \gamma*kpz*mt;$$

$$\text{krpa}(8,6) = \gamma*mzd;$$

$$\text{krpa}(8,8) = \gamma*kp*mt;$$

$$\text{krpa}(8,9) = -\gamma*mbd;$$

$$\text{krpa}(8,13) = -v*\gamma*mu;$$

$$\text{krpa}(9,2) = \gamma*mbd;$$

$$\text{krpa}(9,3) = \gamma*kp*mt;$$

$$\text{krpa}(9,5) = -\gamma*mzd;$$

$$\text{krpa}(9,6) = \gamma*kpz*mt;$$

$$\text{krpa}(9,8) = \gamma*mbd;$$

$$\text{krpa}(9,9) = \gamma*kp*mt;$$

$$\text{krpa}(9,14) = -v*\gamma*mu;$$

$$\text{krpa}(10,2) = \gamma*hb;$$

$$\text{krpa}(10,3) = \gamma*ht*kp;$$

$$\text{krpa}(10,5) = -\gamma*hz;$$

$$\text{krpa}(10,6) = \gamma*ht*kpz;$$

$$\text{krpa}(10,8) = \gamma*hb;$$

$$\text{krpa}(10,9) = \gamma*ht*kp;$$

$$\text{krpa}(10,14) = -v*\gamma*hu;$$

$$\text{krpa}(11,2) = -\text{gamma} \cdot \text{hth} \cdot \text{kp}b;$$

$$\text{krpa}(11,3) = \text{gamma} \cdot \text{h}b d;$$

$$\text{krpa}(11,5) = -\text{gamma} \cdot \text{hth} \cdot \text{kp}z;$$

$$\text{krpa}(11,6) = -\text{gamma} \cdot \text{h}z d;$$

$$\text{krpa}(11,8) = -\text{gamma} \cdot \text{hth} \cdot \text{kp}g;$$

$$\text{krpa}(11,9) = \text{gamma} \cdot \text{h}b d;$$

$$\text{krpa}(11,13) = v \cdot \text{gamma} \cdot \text{h}\mu;$$

$$\text{krpa}(12,1) = 2 \cdot \text{gamma} \cdot \text{kp}b \cdot \text{t}t h;$$

$$\text{krpa}(12,4) = 2 \cdot \text{gamma} \cdot \text{kp}z \cdot \text{t}t h;$$

$$\text{krpa}(13,2) = \text{gamma} \cdot \text{m}b d;$$

$$\text{krpa}(13,3) = \text{gamma} \cdot \text{kp}b \cdot \text{m}t h;$$

$$\text{krpa}(13,5) = -\text{gamma} \cdot \text{m}z d;$$

$$\text{krpa}(13,6) = \text{gamma} \cdot \text{kp}z \cdot \text{m}t h;$$

$$\text{krpa}(13,8) = \text{gamma} \cdot \text{m}b d;$$

$$\text{krpa}(13,9) = \text{gamma} \cdot \text{kp}g \cdot \text{m}t h;$$

$$\text{krpa}(13,14) = -v \cdot \text{gamma} \cdot \text{m}\mu;$$

$$\text{krpa}(14,2) = -\text{gamma} \cdot \text{kp}b \cdot \text{m}t h;$$

$$\text{krpa}(14,3) = \text{gamma} \cdot \text{m}b d;$$

$$\text{krpa}(14,5) = -\text{gamma} \cdot \text{kp}z \cdot \text{m}t h;$$

$$\text{krpa}(14,6) = -\text{gamma} \cdot \text{m}z d;$$

$$\text{krpa}(14,8) = -\text{gamma} \cdot \text{kp}g \cdot \text{m}t h;$$

$$\text{krpa}(14,9) = \text{gamma} \cdot \text{m}b d;$$

$$\text{krpa}(14,13) = v \cdot \text{gamma} \cdot \text{m}\mu;$$



```
krpa(15,1) = -2*gamma*kpb*qth;
krpa(15,4) = -2*gamma*kpz*qth;
```

## A.9 Wing Models

The formulation of the rotor equations of motion, hub forces, and hub moments in the present analysis has been carried out generally, with no assumptions made about the structure of the wing/pylon model to which it is attached. Two different types of wing models have been used successfully in the present study; a model developed using the finite element method (FEM), and a modal representation of the wing based upon experimental data. Both methods of representing the wing-pylon structure are described in this section.

### A.9.1 FEM wing structural model

The wing structure is represented by a simple Bernoulli-Euler beam undergoing vertical bending ( $w$ ), chordwise bending ( $v$ ), and torsion ( $\phi$ ) motions. The beam continuous degrees of freedom are thus:

$$\underline{u} = \{w \ v \ \phi\}^T \quad (\text{A.123})$$

The wing is modeled using the Finite Element Method, with each element having the following discrete degrees of freedom:

$$\underline{q} = \{w_1 \ v_1 \ \phi_1 \ v'_1 \ w'_1 \ w_2 \ v_2 \ \phi_2 \ v'_2 \ w'_2\}^T \quad (\text{A.124})$$

The beam continuous degrees of freedom are related to the discrete element degrees of freedom using a set of assumed shape functions. This relationship can be expressed in matrix form:

$$\begin{aligned} \underline{u} &= [H]\underline{q} \\ &= \begin{bmatrix} H_{1b} & 0 & 0 & 0 & H_{2b} & H_{3b} & 0 & 0 & 0 & H_{4b} \\ 0 & H_{1b} & 0 & H_{2b} & 0 & 0 & H_{3b} & 0 & H_{4b} & 0 \\ 0 & 0 & H_{1\phi} & 0 & 0 & 0 & 0 & H_{2\phi} & 0 & 0 \end{bmatrix} \underline{q} \quad (\text{A.125}) \end{aligned}$$

where  $H_{1b}$ ,  $H_{2b}$ ,  $H_{3b}$ , and  $H_{4b}$  are the standard cubic polynomial shape functions describing bending in a Bernoulli-Euler type beam element, and  $H_{1\phi}$  and  $H_{2\phi}$  are the linear shape functions used to describe the torsion deformation of the element.

### Structural stiffness matrix

The total strain energy stored in an element of length  $l$  can be expressed as:

$$V = \frac{1}{2} \int_0^l (\underline{u}'')^T \begin{bmatrix} EI_b & 0 & 0 \\ 0 & EI_c & 0 \\ 0 & 0 & GJ \end{bmatrix} \underline{u}'' dx \quad (\text{A.126})$$

Rewriting in terms of the discrete degrees of freedom:

$$\begin{aligned} V &= \frac{1}{2} \underline{q}^T \left( \int_0^l [H'']^T \begin{bmatrix} EI_b & 0 & 0 \\ 0 & EI_c & 0 \\ 0 & 0 & GJ \end{bmatrix} [H''] dx \right) \underline{q} \\ &= \frac{1}{2} \underline{q}^T [K^S] \underline{q} \quad (\text{A.127}) \end{aligned}$$

where  $[K^S]$  is the wing element structural stiffness matrix. Symbolically evaluating the integral in Eq. A.127, the  $10 \times 10$  element stiffness matrix may be written as follows (matrix entries not shown are zero):

$$\begin{aligned} \text{wing\_ks}(1,1) &= 12 \cdot \text{eif} / l^3; \\ \text{wing\_ks}(1,5) &= 6 \cdot \text{eif} / l^2; \end{aligned}$$

$$\text{wing\_ks}(1,6) = -12*\text{eif}/l^3;$$

$$\text{wing\_ks}(1,10) = 6*\text{eif}/l^2;$$

$$\text{wing\_ks}(2,2) = 12*\text{eic}/l^3;$$

$$\text{wing\_ks}(2,4) = 6*\text{eic}/l^2;$$

$$\text{wing\_ks}(2,7) = -12*\text{eic}/l^3;$$

$$\text{wing\_ks}(2,9) = 6*\text{eic}/l^2;$$

$$\text{wing\_ks}(3,3) = \text{gj}/l;$$

$$\text{wing\_ks}(3,8) = -\text{gj}/l;$$

$$\text{wing\_ks}(4,2) = 6*\text{eic}/l^2;$$

$$\text{wing\_ks}(4,4) = 4*\text{eic}/l;$$

$$\text{wing\_ks}(4,7) = -6*\text{eic}/l^2;$$

$$\text{wing\_ks}(4,9) = 2*\text{eic}/l;$$

$$\text{wing\_ks}(5,1) = 6*\text{eif}/l^2;$$

$$\text{wing\_ks}(5,5) = 4*\text{eif}/l;$$

$$\text{wing\_ks}(5,6) = -6*\text{eif}/l^2;$$

$$\text{wing\_ks}(5,10) = 2*\text{eif}/l;$$

$$\text{wing\_ks}(6,1) = -12*\text{eif}/l^3;$$

$$\text{wing\_ks}(6,5) = -6*\text{eif}/l^2;$$

$$\text{wing\_ks}(6,6) = 12*\text{eif}/l^3;$$

$$\text{wing\_ks}(6,10) = -6*\text{eif}/l^2;$$

$$\text{wing\_ks}(7,2) = -12*\text{eic}/l^3;$$

$$\text{wing\_ks}(7,4) = -6*\text{eic}/l^2;$$

$$\text{wing\_ks}(7,7) = 12*eic/l^3;$$

$$\text{wing\_ks}(7,9) = -6*eic/l^2;$$

$$\text{wing\_ks}(8,3) = -gj/l;$$

$$\text{wing\_ks}(8,8) = gj/l;$$

$$\text{wing\_ks}(9,2) = 6*eic/l^2;$$

$$\text{wing\_ks}(9,4) = 2*eic/l;$$

$$\text{wing\_ks}(9,7) = -6*eic/l^2;$$

$$\text{wing\_ks}(9,9) = 4*eic/l;$$

$$\text{wing\_ks}(10,1) = 6*eif/l^2;$$

$$\text{wing\_ks}(10,5) = 2*eif/l;$$

$$\text{wing\_ks}(10,6) = -6*eif/l^2;$$

$$\text{wing\_ks}(10,10) = 4*eif/l;$$

### Structural mass matrix

The kinetic energy of the element is formulated, assuming that the section center of gravity may be offset from the elastic axis by a distance  $y_{CG}$  in the chordwise direction (positive for CG forward of EA). The velocity of an arbitrary point on the beam cross-section can be expressed as:

$$\dot{\underline{u}} = \begin{bmatrix} \dot{u}_x \\ \dot{u}_y \\ \dot{u}_x \end{bmatrix} = \begin{bmatrix} 0 & 0 & 0 \\ 0 & 1 & 0 \\ 1 & 0 & y \end{bmatrix} \begin{bmatrix} \dot{w} \\ \dot{v} \\ \dot{\phi} \end{bmatrix} \quad (\text{A.128})$$

The kinetic energy of the element can then be written as:

$$\begin{aligned}
T &= \frac{1}{2} \int_V \rho \dot{\underline{u}}^T \dot{\underline{u}} dV \\
&= \frac{1}{2} \int_0^l \underline{\dot{u}}^T \left[ \int_A \rho \begin{bmatrix} 1 & 0 & y \\ 0 & 1 & 0 \\ y & 0 & y^2 \end{bmatrix} dA \right] \underline{\dot{u}} dx \\
&= \frac{1}{2} \int_0^l \underline{\dot{u}}^T \begin{bmatrix} m & 0 & S_\alpha \\ 0 & m & 0 \\ S_\alpha & 0 & I_\phi \end{bmatrix} \underline{\dot{u}} dx
\end{aligned} \tag{A.129}$$

Rewriting in terms of the discrete degrees of freedom:

$$\begin{aligned}
T &= \frac{1}{2} \underline{\dot{q}}^T \left( \int_0^l [H]^T \begin{bmatrix} m & 0 & S_\alpha \\ 0 & m & 0 \\ S_\alpha & 0 & I_\phi \end{bmatrix} [H] dx \right) \underline{\dot{q}} \\
&= \frac{1}{2} \underline{\dot{q}}^T [M^S] \underline{\dot{q}}
\end{aligned} \tag{A.130}$$

where  $[M^S]$  is the wing element structural mass matrix. Symbolically evaluating the integral in Eq. A.130, the  $10 \times 10$  element mass matrix can be written as follows:

$$\begin{aligned}
\text{wing\_ms}(1,1) &= 156/420*m*1; \\
\text{wing\_ms}(1,3) &= 147/420*Salf*1; \\
\text{wing\_ms}(1,5) &= 22/420*m*1^2; \\
\text{wing\_ms}(1,6) &= 54/420*m*1; \\
\text{wing\_ms}(1,8) &= 63/420*Salf*1; \\
\text{wing\_ms}(1,10) &= -13/420*m*1^2;
\end{aligned}$$

$$\begin{aligned}
\text{wing\_ms}(2,2) &= 156/420*m*1; \\
\text{wing\_ms}(2,4) &= 22/420*m*1^2;
\end{aligned}$$

```

wing_ms(2,7) = 54/420*m*l;
wing_ms(2,9) = -13/420*m*l^2;

wing_ms(3,1) = 147/420*Salf*l;
wing_ms(3,3) = 140/420*Iphi*l;
wing_ms(3,5) = 21/420*Salf*l^2;
wing_ms(3,6) = 63/420*Salf*l;
wing_ms(3,8) = 70/420*Iphi*l;
wing_ms(3,10) = -14/420*Salf*l^2;

wing_ms(4,2) = 22/420*m*l^2;
wing_ms(4,4) = 4/420*m*l^3;
wing_ms(4,7) = 13/420*m*l^2;
wing_ms(4,9) = -3/420*m*l^3;

wing_ms(5,1) = 22/420*m*l^2;
wing_ms(5,3) = 21/420*Salf*l^2;
wing_ms(5,5) = 4/420*m*l^3;
wing_ms(5,6) = 13/420*m*l^2;
wing_ms(5,8) = 14/420*Salf*l^2;
wing_ms(5,10) = -3/420*m*l^3;

wing_ms(6,1) = 54/420*m*l;
wing_ms(6,3) = 63/420*Salf*l;
wing_ms(6,5) = 13/420*m*l^2;
wing_ms(6,6) = 156/420*m*l;

wing_ms(6,8) = 147/420*Salf*l;

```

$$\text{wing\_ms}(6,10) = -22/420*m*l^2;$$

$$\text{wing\_ms}(7,2) = 54/420*m*l;$$

$$\text{wing\_ms}(7,4) = 13/420*m*l^2;$$

$$\text{wing\_ms}(7,7) = 156/420*m*l;$$

$$\text{wing\_ms}(7,9) = -22/420*m*l^2;$$

$$\text{wing\_ms}(8,1) = 63/420*Salf*l;$$

$$\text{wing\_ms}(8,3) = 70/420*Iphi*l;$$

$$\text{wing\_ms}(8,5) = 14/420*Salf*l^2;$$

$$\text{wing\_ms}(8,6) = 147/420*Salf*l;$$

$$\text{wing\_ms}(8,8) = 140/420*Iphi*l;$$

$$\text{wing\_ms}(8,10) = -21/420*Salf*l^2;$$

$$\text{wing\_ms}(9,2) = -13/420*m*l^2;$$

$$\text{wing\_ms}(9,4) = -3/420*m*l^3;$$

$$\text{wing\_ms}(9,7) = -22/420*m*l^2;$$

$$\text{wing\_ms}(9,9) = 4/420*m*l^3;$$

$$\text{wing\_ms}(10,1) = -13/420*m*l^2;$$

$$\text{wing\_ms}(10,3) = -14/420*Salf*l^2;$$

$$\text{wing\_ms}(10,5) = -3/420*m*l^3;$$

$$\text{wing\_ms}(10,6) = -22/420*m*l^2;$$

$$\text{wing\_ms}(10,8) = -21/420*Salf*l^2;$$

$$\text{wing\_ms}(10,10) = 4/420*m*l^3;$$

## A.9.2 FEM wing aerodynamics

The wing aerodynamic model presented in this section is a quasi-steady approximation. Chapter 5 describes a modification to this basic aerodynamic model which optionally adds unsteady aerodynamic effects.

The effective angle of attack at a given wing section is

$$\alpha_{\text{eff}} = \phi \cos \Lambda - w' \sin \Lambda - \frac{\dot{w}}{V} + b\left(\frac{1}{2} - a\right) \left( \frac{\dot{\phi}}{V} \cos \Lambda - \frac{\dot{w}'}{V} \sin \Lambda \right) \quad (\text{A.131})$$

where  $b$  is the wing semichord length,  $a$  is the location of the elastic axis, measured positive aft from the midchord point as a fraction of semichord, and  $\Lambda$  is the wing sweep angle, aft sweep positive. Because of the wing sweep, the aerodynamic formulation requires a continuous  $w'$  degree of freedom, so a new mapping between continuous and discrete degrees of freedom must be defined:

$$\begin{aligned} \underline{u}^A &= \begin{Bmatrix} w \\ v \\ \phi \\ v' \\ w' \end{Bmatrix} = [H^A] \underline{q} \\ &= \begin{bmatrix} H_{1b} & 0 & 0 & 0 & H_{2b} & H_{3b} & 0 & 0 & 0 & H_{4b} \\ 0 & H_{1b} & 0 & H_{2b} & 0 & 0 & H_{3b} & 0 & H_{4b} & 0 \\ 0 & 0 & H_{1\phi} & 0 & 0 & 0 & 0 & H_{2\phi} & 0 & 0 \\ 0 & H'_{1b} & 0 & H'_{2b} & 0 & 0 & H'_{3b} & 0 & H'_{4b} & 0 \\ H'_{1b} & 0 & 0 & 0 & H'_{2b} & H'_{3b} & 0 & 0 & 0 & H'_{4b} \end{bmatrix} \underline{q} \quad (\text{A.132}) \end{aligned}$$

where  $H'_{1b}$ ,  $H'_{2b}$ ,  $H'_{3b}$ , and  $H'_{4b}$  are the spatial derivatives of the cubic Bernoulli-Euler beam shape functions.

The aerodynamic forces on the wing cross section can be written as:



$$L_w = \rho V^2 b c_{l_\alpha} \alpha_{\text{eff}} \quad (\text{A.133})$$

$$L_v = 0 \quad (\text{A.134})$$

$$M_\phi = \rho V^2 b^2 \left( a + \frac{1}{2} \right) c_{l_\alpha} \alpha_{\text{eff}} \quad (\text{A.135})$$

$$M_{v'} = 0 \quad (\text{A.136})$$

$$M_{w'} = 0 \quad (\text{A.137})$$

Writing these forces in matrix form:

$$\begin{Bmatrix} L_w \\ L_v \\ M_\phi \\ M_{v'} \\ M_{w'} \end{Bmatrix} = [A_1] \begin{Bmatrix} w \\ v \\ \phi \\ v' \\ w' \end{Bmatrix} + [A_2] \begin{Bmatrix} \dot{w} \\ \dot{v} \\ \dot{\phi} \\ \dot{v}' \\ \dot{w}' \end{Bmatrix} \quad (\text{A.138})$$

where

$$[A_1] = \rho V^2 b c_{l_\alpha} \begin{bmatrix} 0 & 0 & \cos \Lambda & 0 & -\sin \Lambda \\ 0 & 0 & 0 & 0 & 0 \\ 0 & 0 & b \left( a + \frac{1}{2} \right) \cos \Lambda & 0 & -b \left( a + \frac{1}{2} \right) \sin \Lambda \\ 0 & 0 & 0 & 0 & 0 \\ 0 & 0 & 0 & 0 & 0 \end{bmatrix} \quad (\text{A.139})$$

$$[A_2] = \rho V b c_{l_\alpha} \begin{bmatrix} -1 & 0 & b \left( \frac{1}{2} - a \right) \cos \Lambda & 0 & -b \left( \frac{1}{2} - a \right) \sin \Lambda \\ 0 & 0 & 0 & 0 & 0 \\ -b \left( a + \frac{1}{2} \right) & 0 & b^2 \left( a + \frac{1}{2} \right) \left( \frac{1}{2} - a \right) \cos \Lambda & 0 & -b^2 \left( a + \frac{1}{2} \right) \left( \frac{1}{2} - a \right) \sin \Lambda \\ 0 & 0 & 0 & 0 & 0 \\ 0 & 0 & 0 & 0 & 0 \end{bmatrix} \quad (\text{A.140})$$

The work done by the aerodynamic forces on a wing element may be written as:

$$\begin{aligned}
 W &= \int_0^l (\underline{u}^A)^T \begin{Bmatrix} L_w \\ L_v \\ M_\phi \\ M_{v'} \\ M_{w'} \end{Bmatrix} dx \\
 &= \int_0^l \left[ (\underline{u}^A)^T [A_1] \underline{u}^A + (\underline{u}^A)^T [A_2] \dot{\underline{u}}^A \right] dx \quad (\text{A.141})
 \end{aligned}$$

Rewriting in terms of the discrete degrees of freedom:

$$\begin{aligned}
 W &= \underline{q}^T \left[ \left( \int_0^l [H^A]^T [A_1] [H^A] dx \right) \underline{q} \right. \\
 &\quad \left. + \left( \int_0^l [H^A]^T [A_2] [H^A] dx \right) \dot{\underline{q}} \right] \\
 &= \underline{q}^T \left[ [K^A] \underline{q} + [C^A] \dot{\underline{q}} \right] \quad (\text{A.142})
 \end{aligned}$$

where  $[K^A]$  and  $[C^A]$  are the aerodynamic stiffness and damping matrices, respectively. The integrations in Eq. A.142 are performed symbolically, producing  $10 \times 10$  element matrices, listed below:

**Stiffness matrix:**

$$\begin{aligned}
 \text{wing\_ka}(1,1) &= \rho * v^2 * b * c_l * \sin(\lambda) / 2; \\
 \text{wing\_ka}(1,3) &= \rho * v^2 * b * c_l * \cos(\lambda) * 7 * 1 / 20; \\
 \text{wing\_ka}(1,5) &= -\rho * v^2 * b * c_l * \sin(\lambda) * 1 / 10; \\
 \text{wing\_ka}(1,6) &= -\rho * v^2 * b * c_l * \sin(\lambda) / 2; \\
 \text{wing\_ka}(1,8) &= \rho * v^2 * b * c_l * \cos(\lambda) * 3 * 1 / 20; \\
 \text{wing\_ka}(1,10) &= \rho * v^2 * b * c_l * \sin(\lambda) * 1 / 10; \\
 \\ \\
 \text{wing\_ka}(3,1) &= \rho * v^2 * b^2 * (a + 1/2) * c_l * \sin(\lambda) / 2;
 \end{aligned}$$

$$\begin{aligned}
\text{wing\_ka}(3,3) &= \rho \cdot v^2 \cdot b^2 \cdot (a+1/2) \cdot \text{cla} \cdot \cos(\lambda) \cdot 1/3; \\
\text{wing\_ka}(3,5) &= -\rho \cdot v^2 \cdot b^2 \cdot (a+1/2) \cdot \text{cla} \cdot \sin(\lambda) \cdot 1/12; \\
\text{wing\_ka}(3,6) &= -\rho \cdot v^2 \cdot b^2 \cdot (a+1/2) \cdot \text{cla} \cdot \sin(\lambda) / 2; \\
\text{wing\_ka}(3,8) &= \rho \cdot v^2 \cdot b^2 \cdot (a+1/2) \cdot \text{cla} \cdot \cos(\lambda) \cdot 1/6; \\
\text{wing\_ka}(3,10) &= \rho \cdot v^2 \cdot b^2 \cdot (a+1/2) \cdot \text{cla} \cdot \sin(\lambda) \cdot 1/12;
\end{aligned}$$

$$\begin{aligned}
\text{wing\_ka}(5,1) &= \rho \cdot v^2 \cdot b \cdot \text{cla} \cdot \sin(\lambda) \cdot 1/10; \\
\text{wing\_ka}(5,3) &= \rho \cdot v^2 \cdot b \cdot \text{cla} \cdot \cos(\lambda) \cdot 1^2/20; \\
\text{wing\_ka}(5,6) &= -\rho \cdot v^2 \cdot b \cdot \text{cla} \cdot \sin(\lambda) \cdot 1/10; \\
\text{wing\_ka}(5,8) &= \rho \cdot v^2 \cdot b \cdot \text{cla} \cdot \cos(\lambda) \cdot 1^2/30; \\
\text{wing\_ka}(5,10) &= \rho \cdot v^2 \cdot b \cdot \text{cla} \cdot \sin(\lambda) \cdot 1^2/60;
\end{aligned}$$

$$\begin{aligned}
\text{wing\_ka}(6,1) &= \rho \cdot v^2 \cdot b \cdot \text{cla} \cdot \sin(\lambda) / 2; \\
\text{wing\_ka}(6,3) &= \rho \cdot v^2 \cdot b \cdot \text{cla} \cdot \cos(\lambda) \cdot 3 \cdot 1/20; \\
\text{wing\_ka}(6,5) &= \rho \cdot v^2 \cdot b \cdot \text{cla} \cdot \sin(\lambda) \cdot 1/10; \\
\text{wing\_ka}(6,6) &= -\rho \cdot v^2 \cdot b \cdot \text{cla} \cdot \sin(\lambda) / 2; \\
\text{wing\_ka}(6,8) &= \rho \cdot v^2 \cdot b \cdot \text{cla} \cdot \cos(\lambda) \cdot 7 \cdot 1/20; \\
\text{wing\_ka}(6,10) &= -\rho \cdot v^2 \cdot b \cdot \text{cla} \cdot \sin(\lambda) \cdot 1/10;
\end{aligned}$$

$$\begin{aligned}
\text{wing\_ka}(8,1) &= \rho \cdot v^2 \cdot b^2 \cdot (a+1/2) \cdot \text{cla} \cdot \sin(\lambda) / 2; \\
\text{wing\_ka}(8,3) &= \rho \cdot v^2 \cdot b^2 \cdot (a+1/2) \cdot \text{cla} \cdot \cos(\lambda) \cdot 1/6; \\
\text{wing\_ka}(8,5) &= \rho \cdot v^2 \cdot b^2 \cdot (a+1/2) \cdot \text{cla} \cdot \sin(\lambda) \cdot 1/12; \\
\text{wing\_ka}(8,6) &= -\rho \cdot v^2 \cdot b^2 \cdot (a+1/2) \cdot \text{cla} \cdot \sin(\lambda) / 2; \\
\text{wing\_ka}(8,8) &= \rho \cdot v^2 \cdot b^2 \cdot (a+1/2) \cdot \text{cla} \cdot \cos(\lambda) \cdot 1/3; \\
\text{wing\_ka}(8,10) &= -\rho \cdot v^2 \cdot b^2 \cdot (a+1/2) \cdot \text{cla} \cdot \sin(\lambda) \cdot 1/12;
\end{aligned}$$

$$\begin{aligned}
\text{wing\_ka}(10,1) &= -\rho \cdot v^2 \cdot b \cdot \text{cla} \cdot \sin(\lambda) \cdot 1/10; \\
\text{wing\_ka}(10,3) &= -\rho \cdot v^2 \cdot b \cdot \text{cla} \cdot \cos(\lambda) \cdot 1^2/30;
\end{aligned}$$

```
wing_ka(10,5) = -rho*v^2*b*cla*sin(lambda)*l^2/60;
wing_ka(10,6) = rho*v^2*b*cla*sin(lambda)*l/10;
wing_ka(10,8) = -rho*v^2*b*cla*cos(lambda)*l^2/20;
```

Damping matrix:

```
wing_ca(1,1) = -rho*v*b*cla*13*l/35 ...
              + rho*v*b^2*(1/2-a)*cla*sin(lambda)/2;
wing_ca(1,3) = rho*v*b^2*(1/2-a)*cla*cos(lambda)*7*l/20;
wing_ca(1,5) = -rho*v*b*cla*11*l^2/210 ...
              + -rho*v*b^2*(1/2-a)*cla*sin(lambda)*l/10;
wing_ca(1,6) = -rho*v*b*cla*9*l/70 ...
              + -rho*v*b^2*(1/2-a)*cla*sin(lambda)/2;
wing_ca(1,8) = rho*v*b^2*(1/2-a)*cla*cos(lambda)*3*l/20;
wing_ca(1,10) = rho*v*b*cla*13*l^2/420 ...
              + rho*v*b^2*(1/2-a)*cla*sin(lambda)*l/10;

wing_ca(3,1) = -rho*v*b^2*(a+1/2)*cla*7*l/20 ...
              + rho*v*b^3*(1/2-a)*(a+1/2)*cla*sin(lambda)/2;
wing_ca(3,3) = rho*v*b^3*(1/2-a)*(a+1/2)*cla*cos(lambda)*l/3;
wing_ca(3,5) = -rho*v*b^2*(a+1/2)*cla*l^2/20 ...
              + -rho*v*b^3*(1/2-a)*(a+1/2)*cla*sin(lambda)*l/12;
wing_ca(3,6) = -rho*v*b^2*(a+1/2)*cla*3*l/20 ...
              + -rho*v*b^3*(1/2-a)*(a+1/2)*cla*sin(lambda)/2;
wing_ca(3,8) = rho*v*b^3*(1/2-a)*(a+1/2)*cla*cos(lambda)*l/6;
wing_ca(3,10) = rho*v*b^2*(a+1/2)*cla*l^2/30 ...
              + rho*v*b^3*(1/2-a)*(a+1/2)*cla*sin(lambda)*l/12;
```

```

wing_ca(5,1) = -rho*v*b*cla*11*l^2/210 ...
              + rho*v*b^2*(1/2-a)*cla*sin(lambda)*l/10;
wing_ca(5,3) = rho*v*b^2*(1/2-a)*cla*cos(lambda)*l^2/20;
wing_ca(5,5) = -rho*v*b*cla*l^3/105;
wing_ca(5,6) = -rho*v*b*cla*13*l^2/420 ...
              + -rho*v*b^2*(1/2-a)*cla*sin(lambda)*l/10;
wing_ca(5,8) = rho*v*b^2*(1/2-a)*cla*cos(lambda)*l^2/30;
wing_ca(5,10)= rho*v*b*cla*l^3/140 ...
              + rho*v*b^2*(1/2-a)*cla*sin(lambda)*l^2/60;

wing_ca(6,1) = -rho*v*b*cla*9*l/70 ...
              + rho*v*b^2*(1/2-a)*cla*sin(lambda)/2;
wing_ca(6,3) = rho*v*b^2*(1/2-a)*cla*cos(lambda)*3*l/20;
wing_ca(6,5) = -rho*v*b*cla*13*l^2/420 ...
              + rho*v*b^2*(1/2-a)*cla*sin(lambda)*l/10;
wing_ca(6,6) = -rho*v*b*cla*13*l/35 ...
              + -rho*v*b^2*(1/2-a)*cla*sin(lambda)/2;
wing_ca(6,8) = rho*v*b^2*(1/2-a)*cla*cos(lambda)*7*l/20;
wing_ca(6,10)= rho*v*b*cla*11*l^2/210 ...
              + -rho*v*b^2*(1/2-a)*cla*sin(lambda)*l/10;

wing_ca(8,1) = -rho*v*b^2*(a+1/2)*cla*3*l/20 ...
              + rho*v*b^3*(1/2-a)*(a+1/2)*cla*sin(lambda)/2;
wing_ca(8,3) = rho*v*b^3*(1/2-a)*(a+1/2)*cla*cos(lambda)*l/6;
wing_ca(8,5) = -rho*v*b^2*(a+1/2)*cla*l^2/30 ...
              + rho*v*b^3*(1/2-a)*(a+1/2)*cla*sin(lambda)*l/12;
wing_ca(8,6) = -rho*v*b^2*(a+1/2)*cla*7*l/20 ...
              + -rho*v*b^3*(1/2-a)*(a+1/2)*cla*sin(lambda)/2;

```

```

wing_ca(8,8) = rho*v*b^3*(1/2-a)*(a+1/2)*cla*cos(lambda)*l/3;
wing_ca(8,10) = rho*v*b^2*(a+1/2)*cla*l^2/20 ...
               + -rho*v*b^3*(1/2-a)*(a+1/2)*cla*sin(lambda)*l/12;

wing_ca(10,1) = rho*v*b*cla*13*l^2/420 ...
               + -rho*v*b^2*(1/2-a)*cla*sin(lambda)*l/10;
wing_ca(10,3) = -rho*v*b^2*(1/2-a)*cla*cos(lambda)*l^2/30;
wing_ca(10,5) = rho*v*b*cla*l^3/140 ...
               + -rho*v*b^2*(1/2-a)*cla*sin(lambda)*l^2/60;
wing_ca(10,6) = rho*v*b*cla*11*l^2/210 ...
               + rho*v*b^2*(1/2-a)*cla*sin(lambda)*l/10;
wing_ca(10,8) = -rho*v*b^2*(1/2-a)*cla*cos(lambda)*l^2/20;
wing_ca(10,10) = -rho*v*b*cla*l^3/105;

```

### A.9.3 FEM Wing assembly and pylon inertial contribution

The wing model developed for the present analysis uses four elements to model a semi-span cantilevered wing, assembled using standard FEM techniques. To enforce the cantilevered boundary condition at the wing root, the rows and columns associated with the degrees of freedom at the root node are deleted from the assembled wing matrices.

The engine nacelle is assumed to be a rigid body, rigidly attached to the wingtip node. The nacelle center of gravity may be offset from the wingtip node by the distances  $\{x_p, y_p, z_p\}$ . Contributions due to the mass ( $m_p$ ) and inertia ( $I_{pitch}, I_{yaw}, I_{roll}$ ) of the nacelle are accounted for by adding the following matrix to the wingtip node location in the assembled wing mass matrix:

$$M_{\text{nacelle}} = \begin{bmatrix} m_p & 0 & m_p y_p & 0 & m_p x_p \\ 0 & m_p & -m_p z_p & m_p x_p & 0 \\ m_p y_p & -m_p z_p & I_{\text{pitch}} & 0 & 0 \\ 0 & m_p x_p & 0 & I_{\text{yaw}} & 0 \\ m_p x_p & 0 & 0 & 0 & I_{\text{roll}} \end{bmatrix} \quad (\text{A.143})$$

#### A.9.4 Modal wing representation

Another method of representing the wing structure in the present analysis uses wing modal properties, such as may be obtained from ground vibration tests. This approach was used in this study to model the WRATS wing and pylon. For each wing mode to be included in the analysis, the modal frequency  $\omega$  and damping ratio  $\zeta$  must be provided, along with the corresponding mode shape (displacements and rotations) at the rotor hub attachment point. The frequency and damping information is used to form modal mass, damping, and stiffness matrices (assuming a unity modal mass matrix):

$$M = \begin{bmatrix} 1 & 0 & \cdots & 0 \\ 0 & 1 & \cdots & 0 \\ \vdots & \vdots & \ddots & \vdots \\ 0 & 0 & \cdots & 1 \end{bmatrix} \quad (\text{A.144})$$

$$C = \begin{bmatrix} 2\zeta_1\omega_1 & 0 & \cdots & 0 \\ 0 & 2\zeta_2\omega_2 & \cdots & 0 \\ \vdots & \vdots & \ddots & \vdots \\ 0 & 0 & \cdots & 2\zeta_n\omega_n \end{bmatrix} \quad (\text{A.145})$$

$$K = \begin{bmatrix} \omega_1^2 & 0 & \cdots & 0 \\ 0 & \omega_2^2 & \cdots & 0 \\ \vdots & \vdots & \ddots & \vdots \\ 0 & 0 & \cdots & \omega_n^2 \end{bmatrix} \quad (\text{A.146})$$

The mode shapes are assembled into a modal transformation matrix  $\Phi$ , relating hub displacement and rotation to wing modal displacements  $\underline{q}_{\text{wing}}$ :

$$\begin{Bmatrix} \bar{x} \\ \bar{y} \\ \bar{z} \\ \alpha_x \\ \alpha_y \\ \alpha_z \end{Bmatrix} = \begin{bmatrix} \phi_1 & \phi_2 & \cdots & \phi_n \end{bmatrix} \begin{Bmatrix} q_{\text{wing}}(1) \\ q_{\text{wing}}(2) \\ \vdots \\ q_{\text{wing}}(n) \end{Bmatrix} \quad (\text{A.147})$$

$$= [\Phi] \underline{q}_{\text{wing}}$$

Care must be taken in the scaling of the mode shapes in  $\Phi$ . As discussed in the next section, the transformation matrix is used to convert the rotor hub degrees of freedom in the rotor equations into the wing degrees of freedom (the wing modes, in this case). The



scaling of the mode shapes must be such that the converted rotor equations are compatibly scaled with the wing modal equations.

## A.10 Wing/Rotor Coupling

The fully assembled wing/pylon equations must be divided by  $\frac{N_b}{2}I_b\Omega^2$ , in order to be non-dimensionalized in a manner compatible with the nondimensional rotor/hub equations of motion. The rows and columns corresponding to the  $w$  and  $v$  degrees of freedom are additionally non-dimensionalized by rotor radius  $R$ .

To couple the wing and rotor models, rotor hub motion must be expressed in terms of the wing motion at the hub attachment point, and the work done by the rotor on the wingtip must be expressed in terms of the rotor hub forces and moments. This process can be automated by first relating the hub degrees of freedom to the wing model degrees of freedom at the wingtip. For the modal wing representation, this information must be provided. For the FEM wing model, the corresponding transformation matrix is as follows:

$$\begin{aligned} \begin{Bmatrix} \bar{x} \\ \bar{y} \\ \bar{z} \\ \alpha_x \\ \alpha_y \\ \alpha_z \end{Bmatrix} &= \begin{bmatrix} 1 & 0 & \bar{h}\cos\Lambda & 0 & -\bar{h}\sin\Lambda \\ 0 & \sin\Lambda & 0 & -\bar{h} & 0 \\ 0 & \cos\Lambda & 0 & 0 & 0 \\ 0 & 0 & 0 & 1 & 0 \\ 0 & 0 & \cos\Lambda & 0 & -\sin\Lambda \\ 0 & 0 & -\sin\Lambda & 0 & -\cos\Lambda \end{bmatrix} \begin{Bmatrix} w_{\text{tip}} \\ v_{\text{tip}} \\ \phi_{\text{tip}} \\ v'_{\text{tip}} \\ w'_{\text{tip}} \end{Bmatrix} \\ &= [\Phi] \underline{q}_{\text{tip}} \end{aligned} \quad (\text{A.148})$$

where  $\bar{h}$  is distance of hub ahead of wingtip elastic axis, as a fraction of rotor radius, and  $\Lambda$  is the wing sweep angle, positive aft.

This matrix is used as a modal transformation matrix which converts the rotor/hub equations of motion to rotor/wingtip equations of motion. For example, for the rotor/hub mass matrix:

$$\left[ \begin{array}{c|c} M_{9 \times 9}^{rr} & M_{9 \times 5}^{rw} \\ \hline M_{5 \times 9}^{wr} & M_{5 \times 5}^{ww} \end{array} \right] = \left[ \begin{array}{c|c} M_{9 \times 9}^{rr} & M_{9 \times 6}^{rh} \Phi_{6 \times 5} \\ \hline \Phi_{5 \times 6}^T M_{6 \times 9}^{hr} & \Phi_{5 \times 6}^T M_{6 \times 6}^{hh} \Phi_{6 \times 5} \end{array} \right] \quad (\text{A.149})$$

After this transformation, the rotor/wingtip matrices may be added to the wing matrices using standard FEM techniques, yielding the complete equations of motion for the wing/nacelle/rotor system.

# Appendix B

## Wing Unsteady Aerodynamic Model

In Section 5.1.2, an unsteady aerodynamic model for the wing and flaperon was introduced. This model was developed using a Rational Function Approximation (RFA) to derive a time-domain, state-space aerodynamic model from frequency-domain oscillatory response data. This Appendix provides more specific details about how the RFA model is generated, and how the model is integrated with the present semispan tiltrotor stability analysis.

### B.1 Generating RFA model from frequency-domain data

The aerodynamic forces on a two-dimensional airfoil section can be written in a reduced Laplace domain ( $\bar{s} = \frac{sb}{U}$ ) as:

$$\mathbf{F}(\bar{s}) = \mathbf{Q}(\bar{s})\mathbf{H}(\bar{s}) \quad (\text{B.1})$$

where  $\mathbf{F}(\bar{s})$  is a vector of generalized loads represented by the airfoil lift coefficient, pitching moment, and flap hinge moment:

$$\mathbf{F}(\bar{s}) = \begin{Bmatrix} C_l \\ C_m \\ C_h \end{Bmatrix} \quad (\text{B.2})$$

and  $\mathbf{H}(\bar{s})$  is a vector of generalized airfoil motions, in the form of four chordwise velocity distributions, normalized by freestream velocity  $U$ :

$$\mathbf{H}(\bar{s}) = \begin{Bmatrix} \frac{W_0}{U} \\ \frac{W_1}{U} \\ \frac{D_0}{U} \\ \frac{D_1}{U} \end{Bmatrix} \quad (\text{B.3})$$

Any distribution of normal velocity experienced by an airfoil undergoing arbitrary pitching, plunging, and flap motions can be described by a combination of these velocity distributions. Figure B.1 illustrates the four generalized velocity distributions.

The aerodynamic transfer matrix  $\mathbf{Q}(\bar{s})$  can be obtained from experimental frequency response data, or from any suitable frequency-domain aerodynamic analysis. In the present analysis, the classical Theodorsen unsteady aerodynamic model [78] provides the frequency domain data used to generate the time-domain RFA model.

The RFA model approximates  $\mathbf{Q}(\bar{s})$  using the following rational function:

$$\tilde{\mathbf{Q}}(\bar{s}) = \mathbf{C}_0 + \mathbf{C}_1 \bar{s} + \sum_{n=1}^{n_L} \frac{\bar{s}}{\bar{s} + \gamma_n} \mathbf{C}_{n+1} \quad (\text{B.4})$$

The term  $\mathbf{C}_0$  in Eq. (B.4) represents the quasi-steady aerodynamic contribution. In the present analysis,  $\mathbf{C}_0$  is derived to match the steady-state airloads from Theodorsen. The airloads are re-written from Theodorsen's pitch, plunge, and flap degrees of freedom into the generalized motions of Eq. (B.3), resulting in the following:

$$\mathbf{C}_0 = \begin{bmatrix} 2\pi & 2\pi \left(\frac{1}{2} - a\right) & 2T_{10} & T_{11} \\ \pi \left(a + \frac{1}{2}\right) & \pi \left(a + \frac{1}{2}\right) \left(\frac{1}{2} - a\right) & \left(a + \frac{1}{2}\right) T_{10} & \left(a + \frac{1}{2}\right) \frac{T_{11}}{2} \\ \frac{T_{12}}{2} & \frac{T_{12}}{2} \left(\frac{1}{2} - a\right) & \frac{T_{12} T_{10}}{2\pi} & \frac{T_{12} T_{11}}{2 \cdot 2\pi} \end{bmatrix} \quad (\text{B.5})$$

The constants  $T_{10}$ ,  $T_{11}$ , and  $T_{12}$  are defined by Theodorsen in Ref. 78:

$$\begin{aligned} T_{10} &= \sqrt{1 - c^2} + \cos^{-1} c \\ T_{11} &= \cos^{-1} c(1 - 2c) + \sqrt{1 - c^2}(2 - c) \\ T_{12} &= \sqrt{1 - c^2}(2 + c) - \cos^{-1} c(2c + 1) \end{aligned} \quad (\text{B.6})$$

In Eqs. (B.5) and (B.6), the variable  $a$  is defined as the distance, measured positive aft, from the midchord of the airfoil to the center of rotation, and  $c$  is the distance from the midchord to the flap hinge location. Both quantities are normalized by the semichord  $b$ .

The next term in Eq. (B.4),  $\mathbf{C}_1 \bar{s}$ , is constrained to be zero, since it is desired to have a finite response even at infinite frequency. Therefore,

$$\mathbf{C}_1 = [\mathbf{0}]_{3 \times 4} \quad (\text{B.7})$$

The final summation term in Eq. (B.4) represents  $n_L$  aerodynamic lag states, with poles  $\gamma_n$  which lie on the negative real axis. Each of the aerodynamic lag terms has an associated aerodynamic transfer matrix  $C_{n+1}$ . The contents of each transfer matrix are chosen such that they provide a best fit, in a least squares sense, to tabulated oscillatory response data. This data can be represented in the form:

$$\mathbf{Q}(k_m), \quad m = 1, 2, \dots, n_{dp} \quad (\text{B.8})$$

In the present formulation, this data was generated using Theodorsen's aerodynamic model for 20 different reduced frequencies ( $n_{dp} = 20$ ), over the a reduced frequency range of  $k = 0 \rightarrow 4$ . This range of reduced frequencies covers all the rotor/wing modal frequencies at all airspeeds considered in the present analysis.

To solve for the unknown contents of the matrices  $\mathbf{C}_2 \rightarrow \mathbf{C}_{n+1}$ , the fitting process is performed in the reduced frequency domain, so the Laplace variable  $\bar{s}$  is replaced in Eq. (B.4) by  $ik$ :

$$\tilde{\mathbf{Q}}(ik) = \mathbf{C}_0 + \mathbf{C}_1 ik + \sum_{n=1}^{n_L} \frac{ik}{ik + \gamma_n} \mathbf{C}_{n+1} \quad (\text{B.9})$$

The real and imaginary parts of Eq. (B.9) are separated by multiplying and dividing by the complex conjugate of the denominator term, as shown here:

$$\frac{ik}{ik + \gamma_n} = \frac{ik}{ik + \gamma_n} \frac{(\gamma_n - ik)}{(\gamma_n - ik)} = \frac{k^2 + ik\gamma_n}{\gamma_n^2 + k^2} \quad (\text{B.10})$$

The real and imaginary parts of the oscillatory response data can then be approximated using the real and imaginary parts of Eq. (B.9) for the  $m^{\text{th}}$  reduced frequency:

$$\text{Re}[\mathbf{Q}(ik_m)] = \mathbf{C}_0 + \sum_{n=1}^{n_L} \frac{k_m^2}{\gamma_n^2 + k_m^2} \mathbf{C}_{n+1} \quad (\text{B.11})$$

$$\text{Im}[\mathbf{Q}(ik_m)] = \mathbf{C}_1 k_m + \sum_{n=1}^{n_L} \frac{k_m \gamma_n}{\gamma_n^2 + k_m^2} \mathbf{C}_{n+1} \quad (\text{B.12})$$

The matrix terms in Eqs. (B.11) and (B.12) can be split up, and the equations can be re-written individually for each terms in the matrices  $\mathbf{Q}$  and  $\mathbf{C}$ :

$$\text{Re}[Q_{ij}(ik_m)] = (C_0)_{ij} + \sum_{n=1}^{n_L} \frac{k_m^2}{\gamma_n^2 + k_m^2} (C_{n+1})_{ij} \quad (\text{B.13})$$

$$\text{Im}[Q_{ij}(ik_m)] = (C_1)_{ij} k_m + \sum_{n=1}^{n_L} \frac{k_m \gamma_n}{\gamma_n^2 + k_m^2} (C_{n+1})_{ij} \quad (\text{B.14})$$

Taking Eqs. (B.13) and (B.14) corresponding to a given row  $i$  and column  $j$  and re-writing in matrix form gives:

$$\begin{bmatrix} 0 & \frac{k_m^2}{\gamma_1^2 + k_m^2} & \cdots & \frac{k_m^2}{\gamma_{n_L}^2 + k_m^2} \\ k_m & \frac{k_m \gamma_1}{\gamma_1^2 + k_m^2} & \cdots & \frac{k_m \gamma_{n_L}}{\gamma_{n_L}^2 + k_m^2} \end{bmatrix} \begin{Bmatrix} (C_1)_{ij} \\ \vdots \\ (C_{n_L+1})_{ij} \end{Bmatrix} = \begin{Bmatrix} \operatorname{Re} [Q_{ij}(ik_m)] - (C_0)_{ij} \\ \operatorname{Im} [Q_{ij}(ik_m)] \end{Bmatrix} \quad (\text{B.15})$$

or simply:

$$[\mathbf{I}(k_m)]_{2 \times (n_L+1)} \{\mathbf{c}\}_{(n_L+1) \times 1} = \{\mathbf{r}(k_m)\}_{2 \times 1} \quad (\text{B.16})$$

Equation (B.16) can be written for each of the  $n_{dp}$  reduced frequencies being considered in the fitting process:

$$\begin{bmatrix} \mathbf{I}(k_1) \\ \mathbf{I}(k_2) \\ \vdots \\ \mathbf{I}(k_{n_{dp}}) \end{bmatrix} \mathbf{c} = \begin{Bmatrix} \mathbf{r}(k_1) \\ \mathbf{r}(k_2) \\ \vdots \\ \mathbf{r}(k_{n_{dp}}) \end{Bmatrix} \quad (\text{B.17})$$

or

$$[\mathbf{L}]_{2n_{dp} \times (n_L+1)} \{\mathbf{c}\}_{(n_L+1) \times 1} = [\mathbf{R}]_{2n_{dp} \times 1} \quad (\text{B.18})$$

As long as the number of reduced frequencies  $n_{dp}$  is greater than  $\frac{n_L+1}{2}$ , Eq. (B.18) contains more equations than unknowns. A standard least-squares fitting process is then used to solve for  $\mathbf{c}$ . This process is repeated for each entry  $(i, j)$  in the transfer matrices, until the entire rational function (Eq. (B.4)) has been defined.

### B.1.1 Optimal pole placement to improve fit

In order to achieve the best possible fit for the rational function, the locations of the poles of the aerodynamic lag states are selected using a numerical optimization process. The goal of the optimization is to minimize the fitting error between the oscillatory response data and the rational function approximation. The objective function that the optimization

process attempts to minimize can be written as the sum, over every row and column ( $i, j$ ) of the transfer matrices and all reduced frequencies  $k_m$  used for the fitting process, of a normalized error:

$$F(\gamma_1, \gamma_2, \dots, \gamma_{n_L}) = \sum_{ij} \frac{\sum_{m=1}^{n_{dp}} |\tilde{Q}_{ij}(ik_m) - Q_{ij}(ik_m)|^2}{\max_m \{1, |Q_{ij}(ik_m)|^2\}} \quad (\text{B.19})$$

A numerical optimization process is used to minimize the value of the function  $F$  in Eq. (B.19) by selecting optimal values for the pole locations  $\gamma$ . This optimization process constitutes an outer-loop, wrapped around the curve fit process used to create the rational function approximation for a given set of pole locations. For each function evaluation in the optimization routine, the least-squares fitting process is performed to revise the approximating function  $\tilde{Q}$ .

### B.1.2 Results of RFA fitting process

The algorithm described in this section for fitting a RFA model to oscillatory response data was used to create a model for use in the active control investigation described in Chapter 5. Frequency-domain unsteady aerodynamic data was generated using Theodorsen's model, described in Ref. 78. The fitting process was carried out over a reduced frequency range of 0 to 4. The RFA model developed uses five aerodynamic lag states. Table B.1 provides the resulting pole locations and components of the aerodynamic transfer matrices obtained in the fitting process. Figures B.2 – B.13 compare the resulting RFA model to the data used to perform the fit. The RFA model matches the original data very well, indicating the fitting process was successful.

## B.2 Integration of RFA aero model with FEM wing

In this section, the 2-dimensional unsteady aerodynamic model developed in Section B.1 is integrated with the FEM wing model developed in Appendix A, Section A.9. The



unsteady aerodynamic model developed here replaces the original quasi-steady model originally developed for the wing, when it is desired to include unsteady aerodynamic effects in the analysis.

### B.2.1 Conversion to time domain

By choosing a rational expression for the form of the approximate model in the Laplace domain, the model can be easily transformed to the time domain. For convenience, the summation term in Eq. (B.4) can be re-written using matrix notation, with the rational function taking the following form:

$$\tilde{\mathbf{Q}}(\bar{s}) = \mathbf{C}_0 + \mathbf{C}_1\bar{s} + \mathbf{D}(\mathbf{I}\bar{s} - \mathbf{R})^{-1}\mathbf{E}\bar{s} \quad (\text{B.20})$$

where the matrices  $\mathbf{D}$ ,  $\mathbf{R}$ , and  $\mathbf{E}$  are defined as

$$\mathbf{D} = [\mathbf{I} \quad \mathbf{I} \quad \cdots \quad \mathbf{I}] \quad (\text{B.21})$$

$$\mathbf{R} = - \begin{bmatrix} \gamma_1\mathbf{I} & & & \\ & \gamma_2\mathbf{I} & & \\ & & \ddots & \\ & & & \gamma_{n_L}\mathbf{I} \end{bmatrix} \quad (\text{B.22})$$

$$\mathbf{E} = \begin{bmatrix} \mathbf{C}_2 \\ \mathbf{C}_3 \\ \vdots \\ \mathbf{C}_{n_L+1} \end{bmatrix} \quad (\text{B.23})$$

Substituting the rational function approximation of the aerodynamic transfer matrix in Eq. (B.20) into Eq. (B.1), and defining a vector of aerodynamic states  $\mathbf{X}(\bar{s})$  as

$$\mathbf{X}(\bar{s}) = (\mathbf{I}\bar{s} - \mathbf{R})^{-1}\mathbf{E}\bar{s}\mathbf{H}(\bar{s}) \quad (\text{B.24})$$

yields the following expression for the aerodynamic loads in the Laplace domain:

$$\mathbf{F}(\bar{s}) = \mathbf{C}_0\mathbf{H}(\bar{s}) + \mathbf{C}_1\bar{s}\mathbf{H}(\bar{s}) + \mathbf{D}\mathbf{X}(\bar{s}) \quad (\text{B.25})$$

Equations (B.24) and (B.25) are then transformed from the reduced Laplace domain ( $\bar{s}$ ) to the time domain, resulting in the following expressions:

$$\dot{\mathbf{x}}(t) = \frac{U}{b}\mathbf{R}\mathbf{x}(t) + \mathbf{E}\dot{\mathbf{h}}(t) \quad (\text{B.26})$$

$$\mathbf{f}(t) = \mathbf{C}_0\mathbf{h}(t) + \mathbf{C}_1\frac{b}{U}\dot{\mathbf{h}}(t) + \mathbf{D}\mathbf{x}(t) \quad (\text{B.27})$$

Equation (B.27) gives the aerodynamic forces and moments on a 2-D airfoil section as a function of both the generalized airfoil motions  $\mathbf{h}(t)$  (pitch, plunge, and flap deflection and rate) and the aerodynamic states  $\mathbf{x}(t)$  in the time domain. The aerodynamic states, governed by Eq. (B.26), are in turn influenced by airfoil motion.

## B.2.2 Numerical integration across span of wing elements

Equations (B.26) and (B.27) provide the time-domain unsteady aerodynamic loading on a 2-dimensional airfoil section. To integrate this aerodynamic model with the FEM wing model developed in Appendix A, Section A.9, the spanwise distribution of airloads on a given wing element must be obtained.

First, the generalized motions in Eq. (B.3) are expressed in terms of the FEM wing degrees of freedom. Accounting for wing sweep  $\Lambda$ , and adding a flap degree of freedom  $\delta$  to the FEM wing degrees of freedom  $\underline{u}^A$ , the relationship may be expressed as:

$$\begin{aligned}
\mathbf{h}(t) = \begin{Bmatrix} \frac{w_0(t)}{U} \\ \frac{w_1(t)}{U} \\ \frac{d_0(t)}{U} \\ \frac{d_1(t)}{U} \end{Bmatrix} &= \begin{bmatrix} 0 & 0 & \cos\Lambda & 0 & -\sin\Lambda & 0 \\ 0 & 0 & 0 & 0 & 0 & 0 \\ 0 & 0 & 0 & 0 & 0 & 1 \\ 0 & 0 & 0 & 0 & 0 & 0 \end{bmatrix} \begin{Bmatrix} w \\ v \\ \phi \\ v' \\ w' \\ \delta \end{Bmatrix} \\
&+ \begin{bmatrix} -\frac{1}{U} & 0 & 0 & 0 & 0 & 0 \\ 0 & 0 & \frac{b}{U} \cos\Lambda & 0 & -\frac{b}{U} \sin\Lambda & 0 \\ 0 & 0 & 0 & 0 & 0 & 0 \\ 0 & 0 & 0 & 0 & 0 & \frac{b}{U} \end{bmatrix} \begin{Bmatrix} \dot{w} \\ \dot{v} \\ \dot{\phi} \\ \dot{v}' \\ \dot{w}' \\ \dot{\delta} \end{Bmatrix} \quad (\text{B.28}) \\
&= [\mathbf{TM1}] \begin{Bmatrix} \underline{u}^A \\ \delta \end{Bmatrix} + [\mathbf{TM2}] \begin{Bmatrix} \underline{\dot{u}}^A \\ \dot{\delta} \end{Bmatrix}
\end{aligned}$$

Substituting Eq. (B.28) into Eqs. (B.26) and (B.27) yields equations for the airloads and aerodynamic lag states at one spanwise location on the wing:

$$\dot{\mathbf{x}} = \frac{U}{b} \mathbf{R}\mathbf{x} + \mathbf{E} \left( \mathbf{TM1} \begin{Bmatrix} \dot{u}^A \\ \dot{\delta} \end{Bmatrix} + \mathbf{TM2} \begin{Bmatrix} \ddot{u}^A \\ \ddot{\delta} \end{Bmatrix} \right) \quad (\text{B.29})$$

$$= \frac{U}{b} \mathbf{R}\mathbf{x} + [\mathbf{E1}^{\text{wing}} \mathbf{E1}^{\text{flap}}] \begin{Bmatrix} \dot{u}^A \\ \dot{\delta} \end{Bmatrix} + [\mathbf{E2}^{\text{wing}} \mathbf{E2}^{\text{flap}}] \begin{Bmatrix} \ddot{u}^A \\ \ddot{\delta} \end{Bmatrix}$$

$$\mathbf{f} = \mathbf{C}_0 \left( \mathbf{TM1} \begin{Bmatrix} u^A \\ \delta \end{Bmatrix} + \mathbf{TM2} \begin{Bmatrix} \dot{u}^A \\ \dot{\delta} \end{Bmatrix} \right) + \mathbf{D}\mathbf{x} \quad (\text{B.30})$$

$$= \mathbf{C1} \begin{Bmatrix} u^A \\ \delta \end{Bmatrix} + \mathbf{C2} \begin{Bmatrix} \dot{u}^A \\ \dot{\delta} \end{Bmatrix} + \mathbf{D}\mathbf{x}$$

The first two terms in the final version of Eq. B.30 give the quasi-steady aerodynamic contribution to the airloads. The unsteady contribution comes from the lag states through the term  $\mathbf{D}\mathbf{x}$ .

In the present model, the airloads  $\mathbf{f}$  and lag states  $\mathbf{x}$  are calculated at each of the FEM nodal locations on the wing. The airloads are assumed to vary linearly across the element. With this assumption, the total load on the FEM element can be numerically integrated as a function of the airloads at nodal points 1 and 2 on the element.

Recall that the load vector  $\mathbf{f}$  contains the section lift, pitching moment, and hinge moment coefficients (see Eq. (B.2)). The aerodynamic forces and moments acting on the the wing cross-section can be written as:

$$\begin{aligned}
& \begin{pmatrix} L_w \\ L_v \\ M_\phi \\ M_{v'} \\ M_{w'} \\ M_\delta \end{pmatrix} = \rho U^2 b \begin{pmatrix} \mathbf{f}(1) \\ 0 \\ 2b\mathbf{f}(2) \\ 0 \\ 0 \\ 2b\mathbf{f}(3) \end{pmatrix} \\
& = \rho U^2 b \left( \begin{bmatrix} \mathbf{C1}(1,:) \\ 0 \\ 2b\mathbf{C1}(2,:) \\ 0 \\ 0 \\ 2b\mathbf{C1}(3,:) \end{bmatrix} \begin{Bmatrix} \underline{u}^A \\ \delta \end{Bmatrix} + \begin{bmatrix} \mathbf{C2}(1,:) \\ 0 \\ 2b\mathbf{C2}(2,:) \\ 0 \\ 0 \\ 2b\mathbf{C2}(3,:) \end{bmatrix} \begin{Bmatrix} \underline{\dot{u}}^A \\ \dot{\delta} \end{Bmatrix} + \begin{bmatrix} \mathbf{D}(1,:) \\ 0 \\ 2b\mathbf{D}(2,:) \\ 0 \\ 0 \\ 2b\mathbf{D}(3,:) \end{bmatrix} \mathbf{x} \right) \quad (\text{B.31})
\end{aligned}$$

If the forces and moments are assumed to vary linearly across the element, the work done by the airloads on a wing element can be written as:

$$\begin{aligned}
W &= \int_0^l \begin{Bmatrix} \underline{u}^A \\ \delta \end{Bmatrix}^T \begin{Bmatrix} L_w \\ L_v \\ M_\phi \\ M_{v'} \\ M_{w'} \end{Bmatrix} dx \\
&= \int_0^l \begin{Bmatrix} \underline{u}^A \\ \delta \end{Bmatrix}^T \left( \begin{Bmatrix} L_w \\ L_v \\ M_\phi \\ M_{v'} \\ M_{w'} \end{Bmatrix}_{x=0} + (1-x) \begin{Bmatrix} L_w \\ L_v \\ M_\phi \\ M_{v'} \\ M_{w'} \end{Bmatrix}_{x=l} \right) dx \quad (\text{B.32})
\end{aligned}$$

Expressing the continuous degrees of freedom  $\underline{u}$  in terms of the discrete FEM degrees of freedom  $\underline{q}$  using the standard FEM shape functions and carrying out the integration gives:

$$W = \left\{ \begin{array}{c} \underline{q} \\ \delta \end{array} \right\}^T \left[ [K^A \ D_0] \left\{ \begin{array}{c} \underline{q} \\ \delta \end{array} \right\} + [C^A \ D_1] \left\{ \begin{array}{c} \dot{\underline{q}} \\ \dot{\delta} \end{array} \right\} + [Q^{\text{unsteady}}] \left\{ \begin{array}{c} \mathbf{x}_{x=0} \\ \mathbf{x}_{x=l} \end{array} \right\} \right] \quad (\text{B.33})$$

The wing can now be assembled, using standard finite element assembly techniques. The final system equations of motion, including a flap degree of freedom  $\delta$  and the aerodynamic lag states  $\mathbf{x}$ , (which now should be taken to mean a vector containing all the lag states for all nodes), can be written as follows:

$$\begin{bmatrix} M & 0 & 0 & 0 & 0 \\ 0 & I & 0 & 0 & 0 \\ 0 & 0 & I & 0 & 0 \\ 0 & 0 & 0 & I & 0 \\ -E2^{\text{wing}} & -E2^{\text{flap}} & 0 & 0 & 1 \end{bmatrix} \left\{ \begin{array}{c} \underline{q}^{**} \\ \delta^{**} \\ \underline{q}^* \\ \delta^* \\ \mathbf{x}^* \end{array} \right\} = \begin{bmatrix} -C & D_1 & -K & D_0 & Q^{\text{unsteady}} \\ 0 & 0 & 0 & 0 & 0 \\ I & 0 & 0 & 0 & 0 \\ 0 & I & 0 & 0 & 0 \\ E1^{\text{wing}} & E1^{\text{flap}} & 0 & 0 & R \end{bmatrix} \left\{ \begin{array}{c} \underline{q}^* \\ \delta^* \\ \underline{q} \\ \delta \\ \mathbf{x} \end{array} \right\} + \begin{bmatrix} 0 \\ 1 \\ 0 \\ 0 \\ 0 \end{bmatrix} \delta^{**} \quad (\text{B.34})$$

Other terms in Eq. B.34, such as  $E1^{\text{wing}}$  should also be understood as the total assembled contributions of each FEM element's own  $E1^{\text{wing}}$ , as defined in Eq. B.29. Equation B.34 can be rendered into the familiar form  $\dot{x} = Ax + Bu$  by multiplying both sides of the equation by the inverse of the matrix on the left hand side.

Table B.1: RFA model curve-fit results

<b>Lag State 1</b>				
Pole Location $\gamma_1$ :		$s = -0.004383$ rad/sec		
Aerodynamic Transfer Matrix Component $C_2$ :				
	$W_0$	$W_1$	$D_0$	$D_1$
$C_l$	-0.1453	-0.1312	-0.08912	-0.03030
$C_m$	-0.007789	-0.006938	-0.004560	-0.001572
$C_h$	0.0007959	0.0007175	0.0005033	0.0001670
<b>Lag State 2</b>				
Pole Location $\gamma_2$ :		$s = -0.083217$ rad/sec		
Aerodynamic Transfer Matrix Component $C_3$ :				
	$W_0$	$W_1$	$D_0$	$D_1$
$C_l$	-1.412	-1.248	-0.8436	-0.2854
$C_m$	-0.06223	-0.05733	-0.04263	-0.01385
$C_h$	0.008501	0.007553	0.004701	0.001700
<b>Lag State 3</b>				
Pole Location $\gamma_3$ :		$s = -0.3477$ rad/sec		
Aerodynamic Transfer Matrix Component $C_4$ :				
	$W_0$	$W_1$	$D_0$	$D_1$
$C_l$	-1.493	-1.372	-0.9353	-0.3192
$C_m$	-0.09204	-0.08030	-0.04834	-0.01742
$C_h$	0.007477	0.006847	0.005329	0.001639
<b>Lag State 4</b>				
Pole Location $\gamma_4$ :		$s = -9.033$ rad/sec		
Aerodynamic Transfer Matrix Component $C_5$ :				
	$W_0$	$W_1$	$D_0$	$D_1$
$C_l$	-5.715	-2.514	-1.316	-0.3090
$C_m$	1.017	0.7198	-0.01490	0.07812
$C_h$	0.1076	0.08560	0.001654	0.01467
<b>Lag State 5</b>				
Pole Location $\gamma_5$ :		$s = -67.02$ rad/sec		
Aerodynamic Transfer Matrix Component $C_6$ :				
	$W_0$	$W_1$	$D_0$	$D_1$
$C_l$	247.8	99.79	49.41	10.32
$C_m$	-48.74	-34.68	0.07185	-3.876
$C_h$	-4.933	-3.912	-0.008001	-0.6644

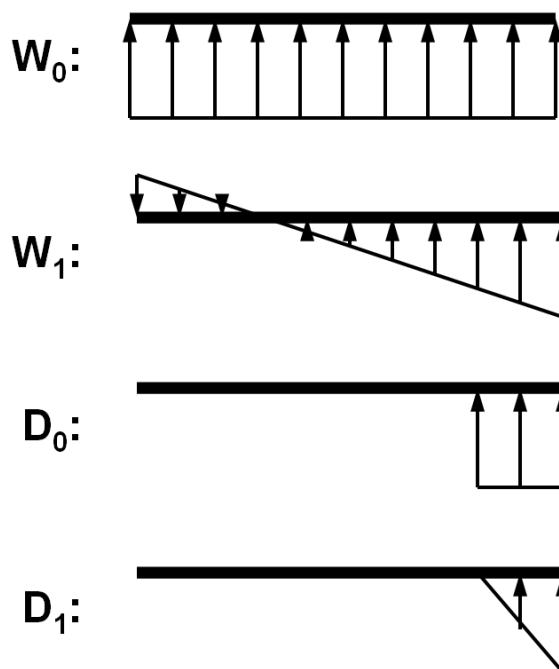


Figure B.1: Velocity distributions corresponding to the generalized airfoil and flap motions used in unsteady aerodynamics formulation

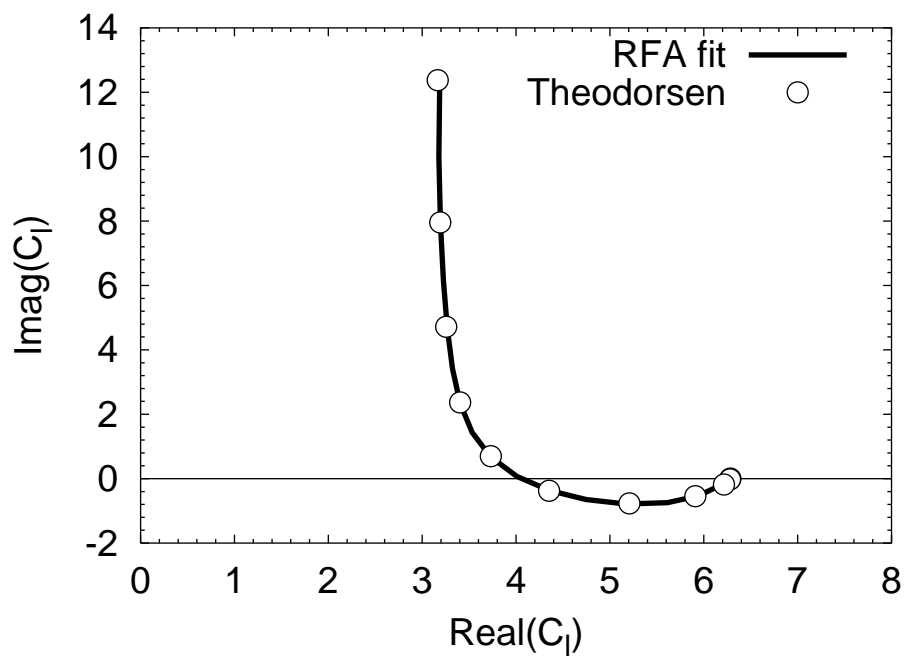


Figure B.2: Comparison of state-space RFA model to frequency-domain aerodynamic model, coefficient of lift due to  $W_0$



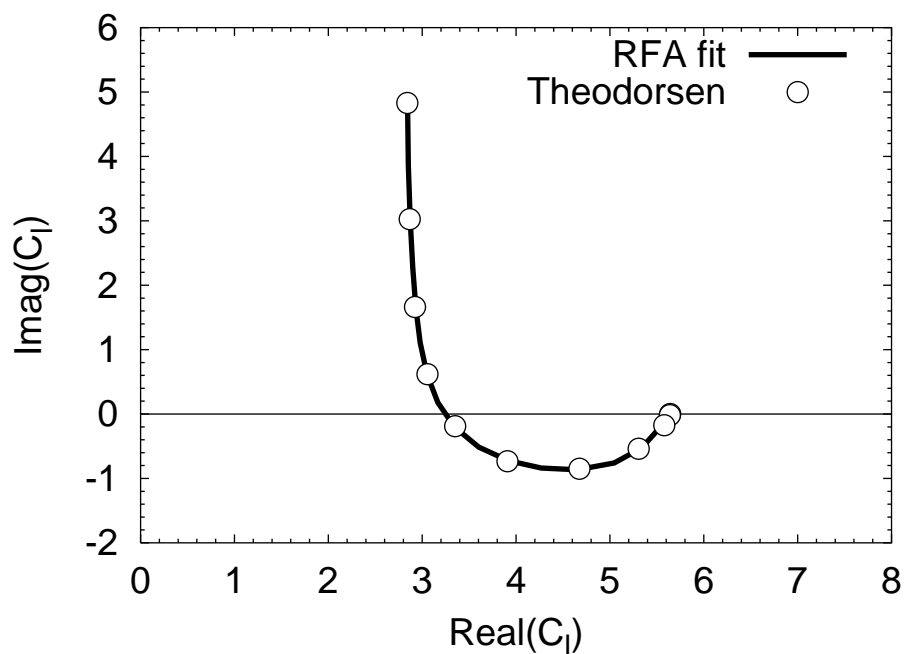


Figure B.3: Comparison of state-space RFA model to frequency-domain aerodynamic model, coefficient of lift due to  $W_1$

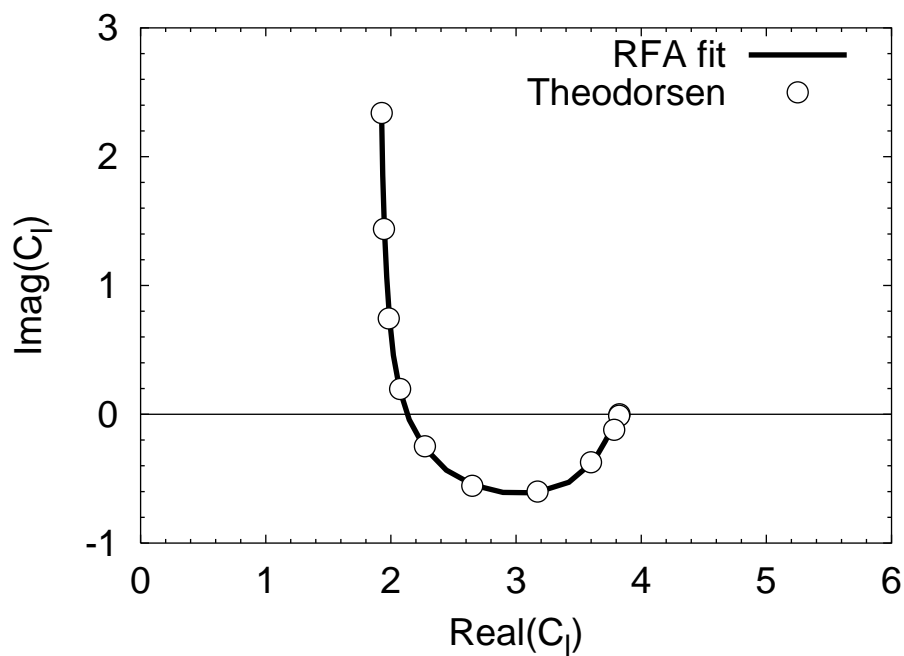


Figure B.4: Comparison of state-space RFA model to frequency-domain aerodynamic model, coefficient of lift due to  $D_0$

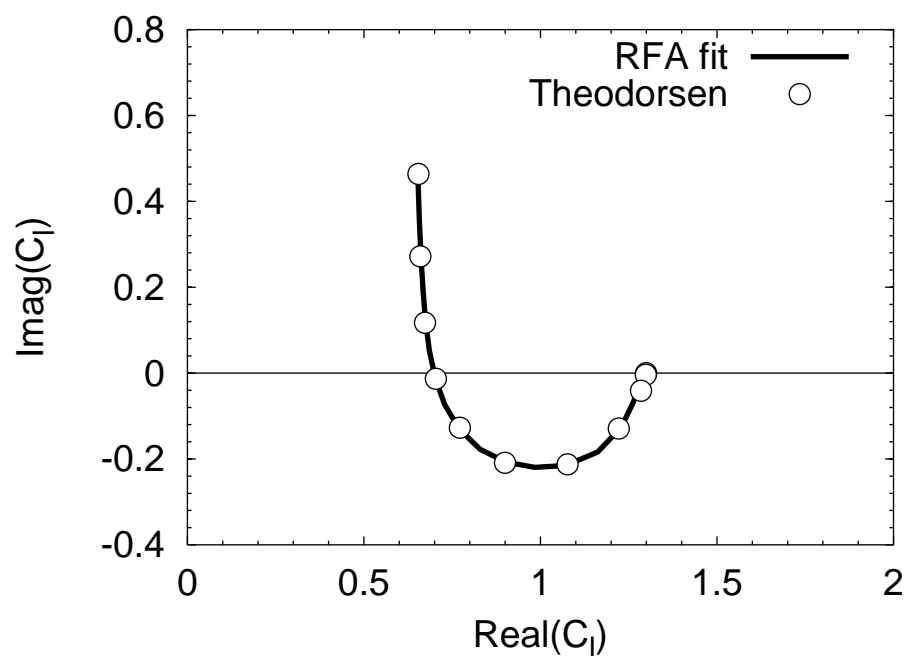


Figure B.5: Comparison of state-space RFA model to frequency-domain aerodynamic model, coefficient of lift due to  $D_1$

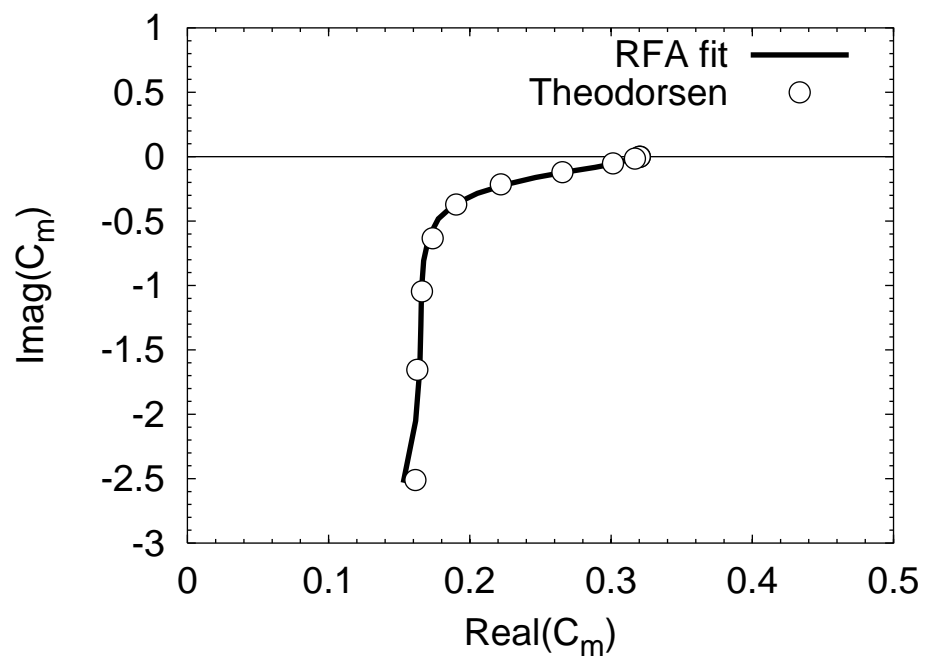


Figure B.6: Comparison of state-space RFA model to frequency-domain aerodynamic model, pitching moment coefficient due to  $W_0$

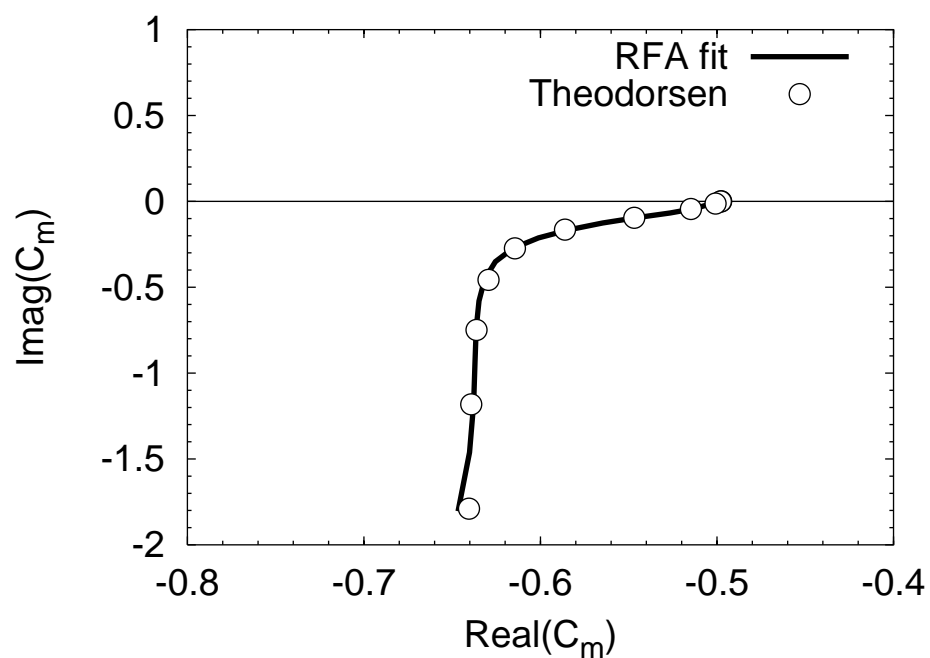


Figure B.7: Comparison of state-space RFA model to frequency-domain aerodynamic model, pitching moment coefficient due to  $W_1$

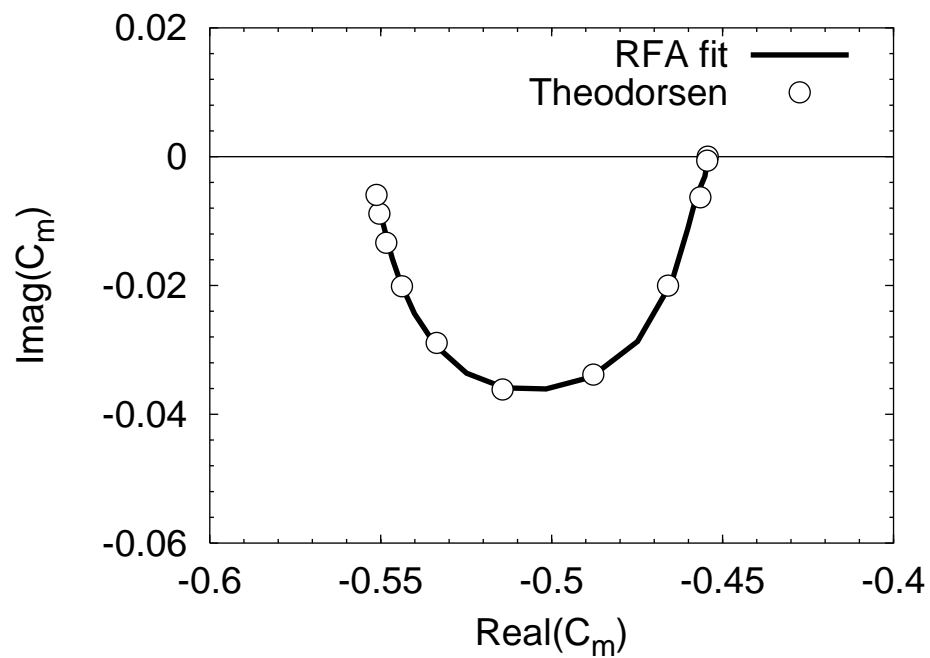


Figure B.8: Comparison of state-space RFA model to frequency-domain aerodynamic model, pitching moment coefficient due to  $D_0$

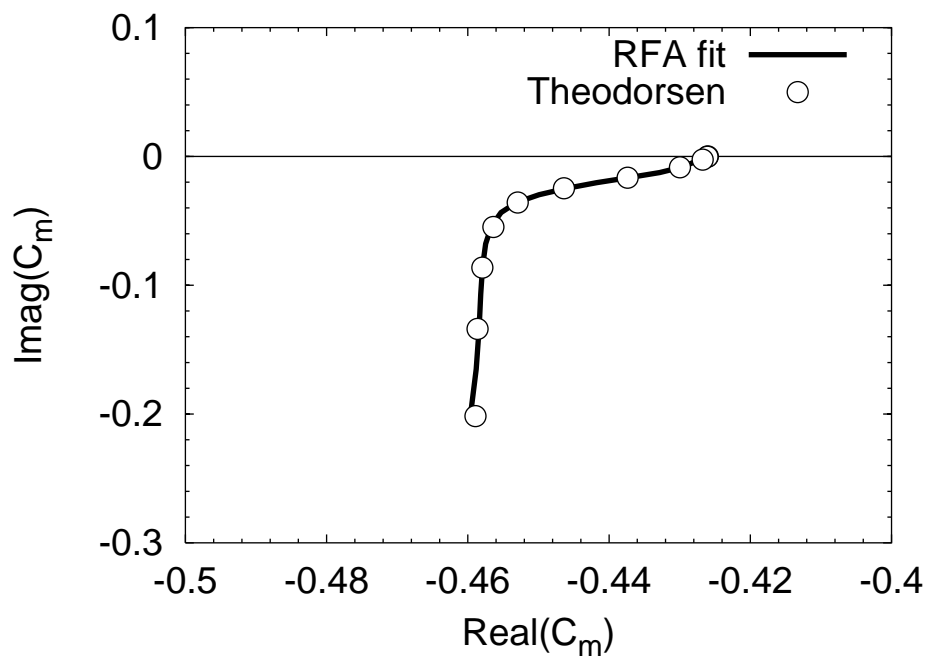


Figure B.9: Comparison of state-space RFA model to frequency-domain aerodynamic model, pitching moment coefficient due to  $D_1$

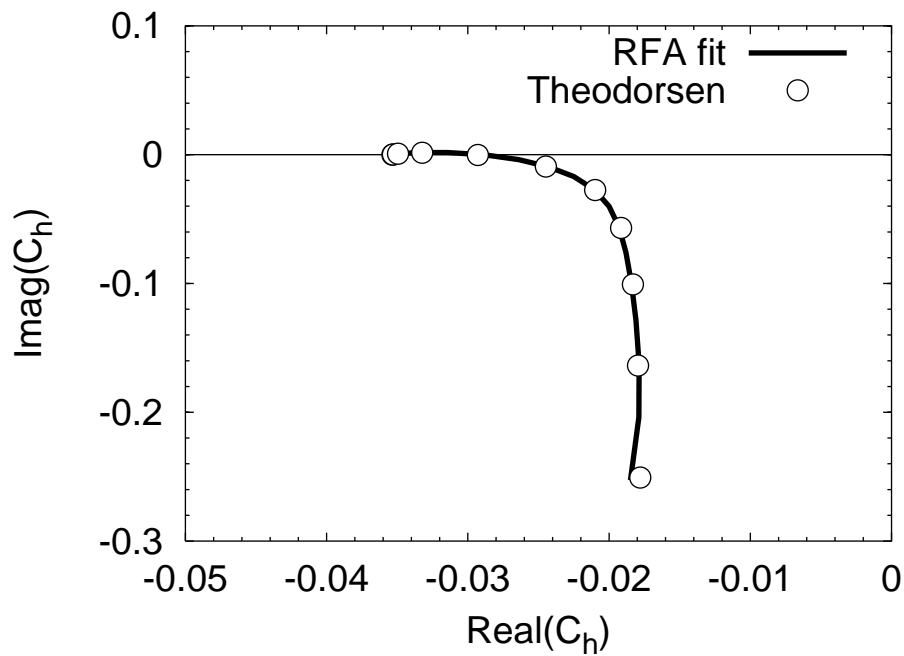


Figure B.10: Comparison of state-space RFA model to frequency-domain aerodynamic model, hinge moment coefficient due to  $W_0$

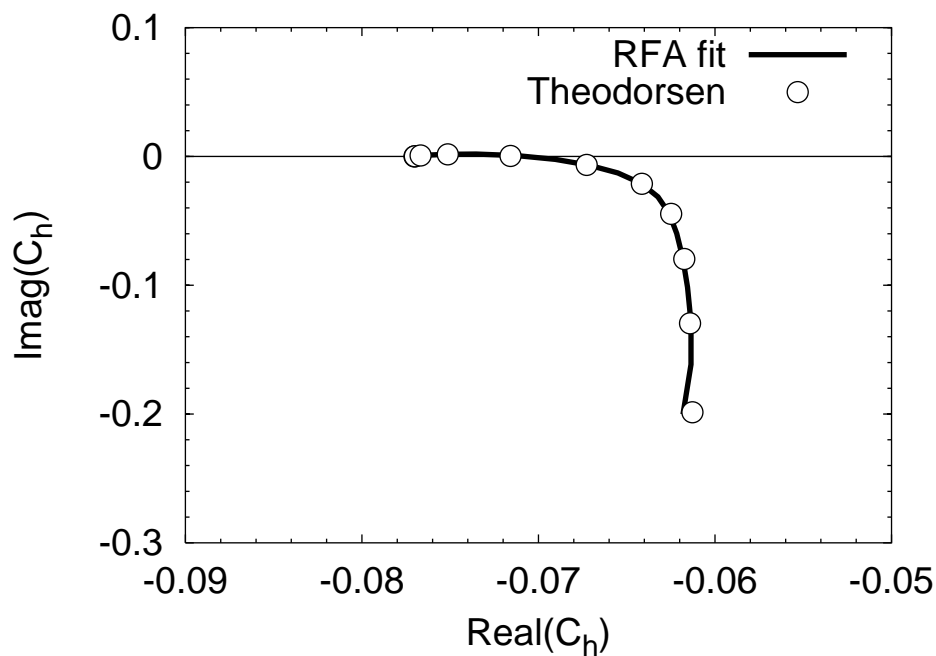


Figure B.11: Comparison of state-space RFA model to frequency-domain aerodynamic model, hinge moment coefficient due to  $W_1$

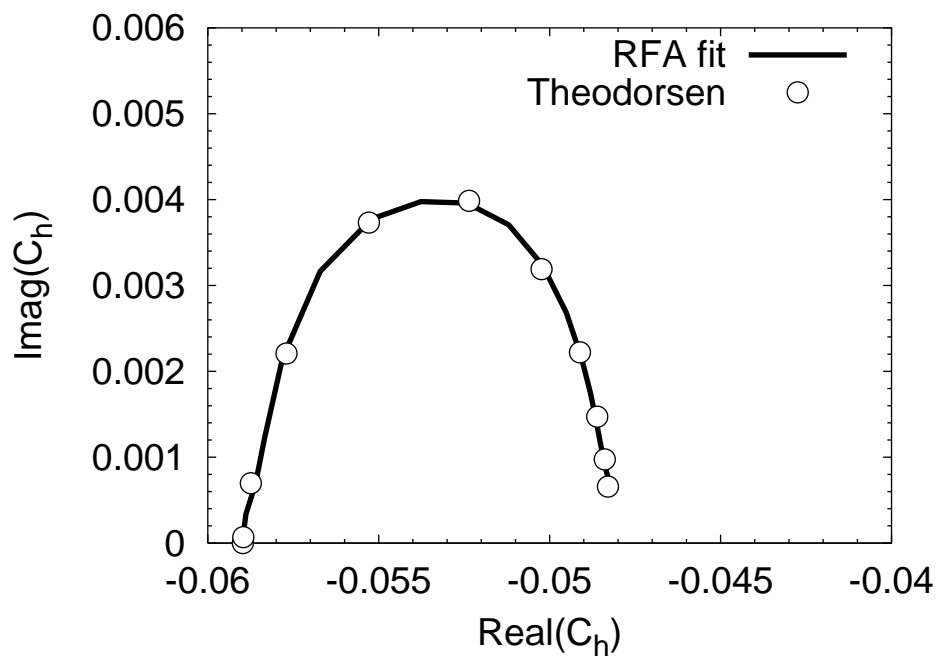


Figure B.12: Comparison of state-space RFA model to frequency-domain aerodynamic model, hinge moment coefficient due to  $D_0$

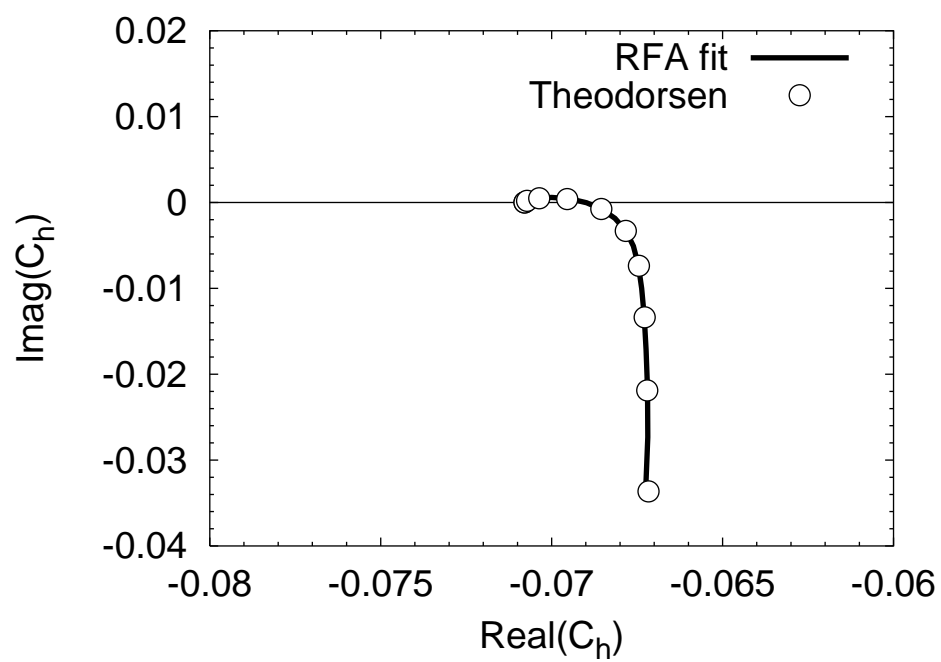


Figure B.13: Comparison of state-space RFA model to frequency-domain aerodynamic model, hinge moment coefficient due to  $D_1$

# Vita

**Eric L. Hathaway**

## Contact Information

### Work Address

The Boeing Company  
M/S 23-03  
Ridley Park, PA 19078  
(610) 591-8584  
Email: eric.l.hathaway@boeing.com

### Home Address

218 Parham Road  
Springfield, PA 19064  
(610) 543-0399  
Email: hathaway@psualum.com  
Citizenship: USA

## Education

Doctor of Philosophy in Aerospace Engineering, expected August 2005, The Pennsylvania State University

Thesis Title: Active and Passive Techniques for Tiltrotor Aeroelastic Stability Augmentation

Master of Science in Aerospace Engineering, August 1999, The Pennsylvania State University

Thesis Title: Use of Aeroelastic Couplings for Alleviation of Helicopter Aeromechanical Instability

Bachelor of Science with Honors in Aerospace Engineering, May 1997, The Pennsylvania State University

## Honors and Awards

Rotorcraft Center Graduate Fellowship, 1999–2003

AHS Vertical Flight Foundation Scholarship, 1997

Penn State Engineering Society Scholarship, 1993–1997

## Work Experience

Flying Qualities Engineer, The Boeing Company, August 2003 – present

Graduate Teaching Assistant, Department of Aerospace Engineering, Penn State University, 1999–2001

Undergraduate Research Assistant, Penn State Applied Research Laboratory, 1995–1996

## Publications and Presentations

“Tiltrotor Whirl Flutter Alleviation Using Actively Controlled Wing Flaperons”, presented at 60th Annual AHS Forum, Baltimore, Maryland, June 7–10, 2004.

“Design Optimization for Improved Tiltrotor Whirl Flutter Stability”, presented at 29th European Rotorcraft Forum, Friedrichshafen, Germany, 16–18 September, 2003.

“Modeling Refinements in Simple Tiltrotor Whirl Flutter Analyses”, *Journal of the American Helicopter Society*, Vol. 48, No. 3, July 2003, pp. 186–198.

“Modeling Refinements in Simple Tiltrotor Aeroelastic Stability Analyses”, presented at 43rd AIAA/ASME/ASCE/AHS/ASC Structures, Structural Dynamics, and Materials Conference, Denver, CO, April 22–25, 2002.

“Concurrently Optimized Aeroelastic Couplings and Rotor Stiffness for Alleviation of Helicopter Aeromechanical Instability”, *AIAA Journal of Aircraft*, Vol. 38, No. 1, January–February 2001, pp. 69–80.

“Concurrent Optimization of Aeroelastic Couplings and Rotor Stiffness for the Alleviation of Helicopter Aeromechanical Instability”, presented at 55th annual AHS Forum, Montreal, Canada, May 25–27, 1999.

“Optimized Aeroelastic Couplings for Alleviation of Helicopter Ground Resonance”, *AIAA Journal of Aircraft*, Vol. 35, No. 4, July–August 1998, pp. 582–589.

“Individual Blade Control for Alleviation of Helicopter Ground Resonance”, presented at 38th AIAA/ASME/ASCE/AHS/ASC Structures, Structural Dynamics, and Materials Conference, Long Beach, CA, April 20–23, 1998.